Complementarity of Searches for Dark Matter

Felix Kahlhoefer

St Catherine's College, Oxford

Thesis submitted in fulfilment of the requirements for the degree of
Doctor of Philosophy at the University of Oxford

Trinity Term 2014

Complementarity of Searches for Dark Matter

Felix Kahlhoefer, St Catherine's College, Oxford

Thesis submitted in fulfilment of the requirements for the degree of
Doctor of Philosophy at the University of Oxford
Trinity Term 2014

Abstract

The striking evidence for the existence of dark matter in the Universe implies that there is new physics to be discovered beyond the Standard Model. To identify the nature of this dark matter is a key task for modern astroparticle physics, and a large number of experiments pursuing a range of different search strategies have been developed to solve it. The topic of this thesis is the complementarity of these different experiments and the issue of how to combine the information from different searches independently of experimental and theoretical uncertainties. The first part focuses on the direct detection of dark matter scattering in nuclear recoil detectors, with a special emphasis on the impact of the assumed velocity distribution of Galactic dark matter particles. By converting experimental data to variables that make the astrophysical unknowns explicit, different experiments can be compared without implicit assumptions concerning the dark matter halo. We extend this framework to include annual modulation signals and apply it to recent experimental hints for dark matter, showing that the tension between these results and constraints from other experiments is independent of astrophysical uncertainties. We explore possible ways of ameliorating this tension by changing our assumptions on the properties of dark matter interactions. In this context, we propose a new approach for inferring the properties of the dark matter particle, which does not require any assumptions about the structure of the dark matter halo. A particularly interesting option is to study dark matter particles that couple differently to protons and neutrons (so-called isospin-violating dark matter). Such isospin-violation arises naturally in models where the vector mediator is the gauge boson of a new $U(1)$ that mixes with the Standard Model gauge bosons. In the second part, we first discuss the case where both the Z' and the dark matter particle have a mass of a few GeV and then turn to the case where the Z' is significantly heavier. While the former case is most strongly constrained by precision measurements from LEP and B-factories, the latter scenario can be probed with great sensitivity at the LHC using monojet and monophoton searches, as well as searches for resonances in dijet, dilepton and diboson final states. Finally, we study models of dark matter where loop contributions are important for a comparison of LHC searches and direct detection experiments. This is the case for dark matter interactions with Yukawa-like couplings to quarks and for interactions that lead to spin-dependent or momentum suppressed scattering cross sections at tree level. We find that including the contribution from heavy-quark loops can significantly alter the conclusions obtained from a tree-level analysis.

Statement of Originality

This thesis is based on original research comprising the work published in Refs. [1–7] and contains no material that has already been accepted, or is concurrently being submitted, for any degree or diploma or certificate or other qualification at the University of Oxford or elsewhere.

Chapters 1 and 2 contain background information on dark matter.

Chapter 3 contains original research based on *JCAP* **1201** (2012) 024, *JCAP* **1307** (2013) 023 and `arXiv:1403.4606` in collaboration with Brian Feldstein, Mads Frandsen, Christopher McCabe, Kai Schmidt-Hoberg and Subir Sarkar. I provided the initiative and several key ideas for this work and wrote most of the code used to obtain numerical results.

Chapter 4 contains original research based on *JHEP* **1109** (2011) 128 and *JHEP* **1207** (2012) 123 performed in collaboration with Mads Frandsen, Anthony Preston, Kai Schmidt-Hoberg and Subir Sarkar. I carried out large parts of the calculations and the data analysis.

Chapter 5 contains original research based on *JHEP* **1307** (2013) 125 and *JCAP* **1304** (2013) 050 performed in collaboration with Ulrich Haisch and James Unwin. I provided the initiative and several key ideas for this work and have written large parts of the code used to obtain numerical results.

To the best of my knowledge this thesis contains no material previously published or written by another person, except where due reference is made in the text.

Oxford, 17th December 2014

(Felix Kahlhoefer)

Whenever a theory appears to you as the only possible one, take this as a sign that you have neither understood the theory nor the problem which it was intended to solve.

(Karl Popper, Objective Knowledge: An Evolutionary Approach, 1972)

Contents

Acronyms vii

Acknowledgements ix

1 Introduction 1

1.1 Observational evidence for dark matter . . . 1

1.2 Dark matter properties . . . 4

1.3 Thermal production of dark matter . . . 5

1.4 Candidates for dark matter . . . 8

1.4.1 WIMPs . . . 8

1.4.2 Asymmetric dark matter . . . 9

1.4.3 SuperWIMPs and FIMPs . . . 10

1.4.4 Axions . . . 11

1.4.5 Sterile neutrinos . . . 11

1.5 Outline . . . 12

2 Detection of dark matter 14

2.1 Direct detection . . . 14

2.1.1 The velocity integral . . . 16

2.1.2 Experimental signatures . . . 17

2.1.3 Hints for light dark matter . . . 19

2.2 Indirect detection . . . 21

2.3 Collider searches . . . 22

2.4 Comparing different searches using effective operators . . . 23

3 Astrophysical uncertainties and halo-independent methods **29**

3.1 Resolving astrophysical uncertainties . . . 30

3.1.1 Measuring the velocity integral . . . 31

3.1.2 Constraining the velocity integral . . . 32

3.1.3 Measuring the modulation amplitude . . . 33

3.1.4 Constraining the modulation fraction . . . 34

3.2 Halo-independent methods: Results . . . 37

3.2.1 A consistent description of CoGeNT and CRESST-II . . . 38

3.2.2 A consistent description of DAMA, CoGeNT and CRESST-II . . . 40

3.3 CDMS versus XENON . . . 44

3.3.1 Astrophysical uncertainties . . . 46

3.3.2 Non-standard momentum and velocity dependence . . . 48

3.3.3 Reducing the tension between CDMS-Si and XENON10/100 . . . 49

3.4 A new halo-independent approach . . . 52

3.4.1 Finding the optimum velocity integral . . . 53

3.4.2 Example: hypercharged dark matter . . . 56

3.4.3 Applications and future directions . . . 59

4 Phenomenology and collider constraints for vector mediators **61**

4.1 Interactions of a vector mediator . . . 62

4.2 Effective Lagrangian for a light Z' . . . 64

4.3 Mixing parameters for a light Z' . . . 68

4.4 Mixing parameters for a heavy Z' . . . 72

4.4.1 Production and decay of a heavy Z' at colliders . . . 72

4.4.2 Interactions with SM bosons . . . 73

4.4.3 Experimental constraints . . . 74

4.5 LHC and Tevatron bounds for general vector mediators . . . 78

5 The importance of heavy-quark loops for LHC monojet searches **86**

5.1 Yukawa-like interactions . . . 87

5.1.1 Limits from monojet searches . . . 87

5.1.2 Bounds from relic density and direct searches . . . 91
5.2 Spin-dependent and momentum-suppressed interactions . . . 94
5.2.1 Tensor and pseudotensor operators . . . 95
5.2.2 Axialvector and anapole operators . . . 100

6 Conclusions **106**

Appendices **111**

A.1 Various descriptions of the Galactic dark matter halo . . . 111
A.1.1 Isotropic models . . . 111
A.1.2 Anisotropic models . . . 113
A.1.3 Additional contributions to the local dark matter density . . . 114
A.2 Overview of direct detection experiments . . . 115
A.3 The extended maximum likelihood method . . . 120
A.4 Studying the velocity integral with multiple-element targets . . . 122
A.4.1 Constraining the velocity integral . . . 122
A.4.2 Measuring the velocity integral . . . 123
A.5 Scattering cross sections for the scalar operator . . . 126
A.6 Decay widths of a vector mediator . . . 128
A.7 Calculation of one-loop amplitudes . . . 129

Bibliography **131**

Acronyms

ADM	asymmetric dark matter, page 10
APV	atomic parity violation, page 70
BBN	Big Bang nucleosynthesis, page 4
BSM	(Physics) Beyond the Standard Model, page 5
CDM	cold dark matter, page 5
CL	confidence level, page 32
CMB	Cosmic Microwave Background, page 4
D-Y	Drell-Yan (production), page 72
DM	dark matter, page 1
EFT	effective field theory, page 91
EWPT	electroweak precision tests, page 68
FIMP	feebly interacting massive particle, page 11
ISR	initial state radiation, page 23
LHC	Large Hadron Collider, page 22
LO	leading order, page 72
M-B	Maxwell-Boltzmann (distribution), page 16
MACHO	massive compact halo object, page 4

MOND Modified Newtonian Dynamics, page 2

NFW Navarro-Frenk-White (profile), page 112

NLO next-to-leading order, page 75

NWA narrow width approximation, page 72

PDF parton distribution function, page 72

PDG Particle Data Group, page 25

SD spin-dependent, page 15

SHM Standard Halo Model, page 16

SI spin-independent, page 15

SM Standard Model (of particle physics), page 5

SUSY supersymmetry, page 9

UV ultraviolet, page 26

VBF vector boson fusion, page 72

WIMP weakly interacting massive particle, page 8

Acknowledgements

Above all, I would like to express my deepest gratitude towards Subir Sarkar for all the guidance, stimulation and support he has given me over the course of my time in Oxford. He has not only been a devoted and diligent supervisor, but he has been a mentor and an inspiring example. I would also like to express my great appreciation towards Mads T. Frandsen, Ulrich Haisch, Christopher McCabe and Kai Schmidt-Hoberg, who have shared with me their knowledge and experience. This thesis would not have been possible without everything that I have learned from and together with them. Moreover, I am grateful to Brian Feldstein, John March-Russell, Matthew McCullough, Philipp Mertsch, Emanuele Re and James Unwin for fruitful collaboration.

I thank Kyle Allison, Alan Barr, David Berge, Celine Boehm, Andrew Brown, Matthew Dolan, Patrick Fox, Rhorry Gauld, Edward Hardy, Joachim Kopp, Robert Lasenby, Tongyan Lin, John Magorrian, Paul McMillan, Paolo Panci, Andrew Pontzen, Raoul Rontsch, Graham Ross, Steven Schramm, Thomas Schwetz-Mangold, Tim Tait, Lian-Tao Wang, Stephen West, Stephen Worm and Giulia Zanderighi for many helpful comments and discussions. For proof-reading this thesis I am indebted to Subir Sarkar, Ulrich Haisch, Kai Schmidt-Hoberg and Inés Usandizaga.

I would like to thank the organisers and participants of the ISAPP 2011 in Heidelberg, the UNILHC 2012 school in Valencia and the TAUP 2013 summer school in Asilomar, CA for many interesting lectures and conversations. Furthermore, I would like to thank KITP Santa Barbara, KICP Chicago, NORDITA Stockholm and CERN Geneva for hospitality. I gratefully acknowledge financial support from DAAD, Studienstiftung des deutschen Volkes and a Leathersellers' Company Scholarship at St Catherine's College Oxford.

To conclude, I wish to give very special thanks to my parents and my sister, whose unfaltering support and encouragement have been the foundation of this thesis. Finally, I thank Inés. She has been my first reason to come to Oxford and remained my best.

CHAPTER 1

Introduction

Almost everything we know about the Universe and its past has been deduced from observing the sky and measuring the light and electromagnetic radiation emitted from astrophysical and cosmic sources. Ironically, it is precisely these observations that have led us to the conclusion that around 80% of the matter in the Universe is non-luminous, meaning that it does not emit, absorb or reflect light. The clear evidence for the gravitational interactions of this so-called dark matter (DM) is confronted with an almost complete ignorance of its properties. Identifying the nature of DM is therefore a key challenge for modern astroparticle physics.

The aim of this chapter is to present the case for DM and review its theoretical interpretation. In Sec. 1.1 we give an overview of the evidence for DM based on astrophysical measurements and cosmology. We then use these observations in Sec. 1.2 to infer the basic properties that any DM particle candidate must fulfil. In Sec. 1.3 a particular emphasis will be placed on the calculation of the DM relic density from the thermal freeze-out mechanism. Finally, we present an overview of popular particle physics models for DM in Sec. 1.4. In Sec. 1.5 we conclude this chapter with an outline of the remainder of this thesis.

1.1 Observational evidence for dark matter

On galactic scales the central piece of evidence for DM comes from measurements of the rotational velocity $v_{\rm rot}$ of stars and gas in the outer regions of spiral galaxies. These velocities are observed to be so large that the gravitational attraction of the visible mass alone would be insufficient to support stable orbits. More precisely, the rotational velocity at a distance r from the centre of a

galaxy should obey the relation

$$v_{\rm rot}(r) = \sqrt{\frac{G_{\rm N}\, M(r)}{r}}\ , \tag{1.1}$$

where $G_{\rm N}$ is Newton's constant and $M(r)$ is the total mass contained within radius r. In the absence of an invisible contribution to the mass, $M(r)$ is expected to be approximately constant beyond the optical disk and consequently circular velocities should fall off as $v_{\rm rot}(r) \propto r^{-1/2}$. Instead, rotation curves are observed to be approximately constant up to very large radii [8, 9]. This discrepancy between the observed rotation curves and the prediction based on the visible matter alone implies that there must be an additional contribution from a halo of non-luminous matter such that $M(r) \propto r$ at large distances.

There are reasons to be uncomfortable with this line of reasoning, since there is no way of knowing whether Newtonian dynamics remain accurate at galactic scales to the required precision. Indeed, an alternative way to explain the observation of constant rotation curves is proposed by a theory called Modified Newtonian Dynamics (MOND) [10], which changes the acceleration of particles in very weak gravitational fields. To distinguish the DM hypothesis from MOND, it is therefore crucial to find additional evidence for a missing mass component in other kinds of systems using different observational techniques [11].

In galaxy clusters, measurements of the velocity dispersion of galaxies can be used to infer the presence of DM in a way similar to the observation of galactic rotation curves. It was indeed in the Coma cluster where evidence for DM was inferred for the first time: by applying the virial theorem Fritz Zwicky concluded that the mass-to-light ratio of this cluster must be two orders of magnitude larger than that of the Sun [12]. The same conclusion can be obtained from measuring the temperature of the hot X-ray emitting gas, which in the absence of DM would give the dominant contribution to the total mass of a galaxy cluster.

A more impressive method to infer — and even map — the total gravitating mass of a galaxy cluster is to use gravitational lensing, i.e. the fact that gravitational fields affect the propagation of light. For strong gravitational fields, General Relativity predicts that the resulting deflection of light can lead to multiple images of a single bright background object. But even for weaker gravitational fields a statistical analysis of the distortion of the images of background objects can be used to infer the size and shape of the gravitational potential along the line of sight. This approach

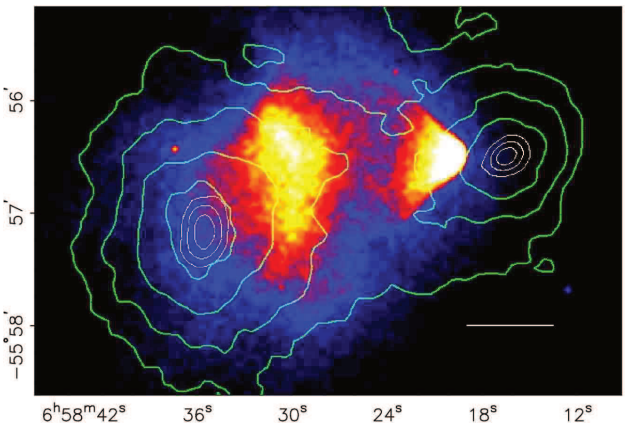

FIG. 1.1. Observation of the Bullet Cluster from Ref. [13]. The coloured regions show the distribution of gas, inferred from its X-ray emission. The green contours show the distribution of gravitating matter, which is reconstructed using weak gravitational lensing. Clearly, the total mass of this system is dominated by a non-luminous component that has not been affected by the cluster collision.

can be used not only to determine the mass-to-light ratio of galaxy clusters, but also to study whether the DM profile traces the distribution of baryonic matter.

Systems of particular interest in this context are colliding galaxy clusters. In a cluster collision, the hot gas of both systems will dissipate energy because of electromagnetic interactions and will therefore be held up at the point of the collision. Provided DM is collisionless, on the other hand, DM halos can pass straight through one another and will consequently be separated from the gas. This expectation indeed agrees with observations. The most famous example is the 'Bullet Cluster' (1E0657-558) [13] where gravitational lensing can be used to demonstrate a clear mismatch between the distribution of luminous and gravitating matter (see Fig. 1.1).

Finally, DM plays a crucial role in our understanding of how the first structures formed in the early Universe. In the absence of DM, structure could only have begun to form after recombination, when the photon pressure was no longer large enough to prevent baryons from forming overdense regions. The amount and age of the observed large-scale structure in the Universe, however, implies that matter must have begun to collapse into structures much earlier. This observation can only be explained if the dominant part of non-relativistic matter is DM, which does not interact with photons, so that perturbations can already begin to grow before recombination. Once the Universe becomes matter dominated, baryons can then fall into the potential wells created by DM and

rapidly form structures that match the DM perturbations. Indeed, numerical N-body simulations of the growth of DM structure agree well with observations [14].

A precise confirmation of these processes can be obtained from the Cosmic Microwave Background (CMB), which contains an anisotropy due to the acoustic oscillations of the baryon-photon plasma in the early Universe. Measuring the temperature distribution of the CMB therefore enables us to determine the total contribution of DM and baryons to the energy density of the Universe, called Ω_χ and Ω_b, respectively. In the framework of the standard concordance model of cosmology, the most recent measurements of the Planck satellite have been used to infer [15]

$$\Omega_\chi \approx 0.265 \,, \quad \Omega_b \approx 0.0487 \,, \tag{1.2}$$

implying that although non-relativistic matter accounts for almost a third of the energy density of the Universe, only about 15% of this matter is baryonic. This spectacular observation can be confirmed independently by comparing the predictions from Big Bang nucleosynthesis (BBN) with the observed abundances of elements [16]. We are led to the conclusion that the largest part of the matter density of the Universe is in a form of matter that is different from all the matter we know.

1.2 Dark matter properties

All of the evidence for DM presented above results exclusively from its gravitational interactions. Nevertheless, given the success of particle physics in describing the early Universe, it is well motivated to assume that DM is composed of elementary particles. Astrophysical and cosmological observations then provide a number of constraints that any viable candidate for the DM particle must satisfy. The most obvious constraint is that DM must be electrically neutral and stable on cosmological time scales, i.e. it must have a lifetime large compared to the age of the Universe. In addition, we can derive several more non-trivial requirements for the DM particles.

First of all, we know that most of the DM must be non-baryonic [17], because the baryon fraction of the Universe determined from BBN and the CMB is far too small to account for the observed DM relic density. Moreover, gravitational microlensing of Milky Way satellites allows to directly constrain the amount of DM in baryonic dark objects such as brown dwarfs or gas giants, collectively referred to as massive compact halo objects (MACHOs). These searches show that the number

of MACHOs in the Milky Way is too small to account for the missing mass inferred from the Galactic rotation curve [18]. Similarly, one can directly constrain the amount of diffuse baryons from observations of the Lyman alpha forest of the intergalactic medium [19].

Furthermore, it is possible to constrain the DM self-interaction cross section by measuring the central density [20, 21] and ellipticity [22] of DM halos, or by studying colliding galaxy clusters such as the Bullet Cluster [23, 24]. To be consistent with observations, the rate of momentum transfer due to self-interactions should not significantly exceed the expansion rate of the Universe. In terms of the self-interaction cross section, however, the resulting constraints are rather weak, requiring typically $\sigma_{\text{self}}/m_\chi \lesssim 10^{-24}\,\text{cm}^2\,\text{GeV}^{-1}$. In other words, while very strong self-interactions are excluded, DM particles do by no means have to be completely collisionless.

Finally, observations require cold DM (CDM), i.e. that DM particles should be non-relativistic at matter-radiation equality. The reason is that relativistic DM particles tend to wash out density perturbations at scales below the free-streaming length of about $0.1\,\text{Mpc}\,(1\,\text{keV}/m_\chi)$. If the free-streaming length is large compared to galactic scales, the resulting suppression of small-scale structures would be in tension with the observed amount of structure. These considerations typically rule out DM particles with $m_\chi \lesssim 1\,\text{keV}$. In particular, we conclude that ordinary neutrinos, which are constrained to have masses $m_\nu \lesssim 1\,\text{eV}$, cannot be the dominant component of DM. Consequently, the Standard Model (SM) of particle physics does not contain a viable candidate for the DM particle. In other words, the evidence for DM presented in this chapter is at the same time evidence for Beyond the Standard Model (BSM) physics.

1.3 Thermal production of dark matter

A further fundamental requirement for any DM candidate is that it is produced in the early Universe with the correct abundance to account for the observed relic density $\Omega_\chi = 0.265$. In this section, we present the standard approach of calculating the DM relic density from thermal freeze-out, following Refs. [25–27]. Some alternative ways to obtain the observed relic abundance will be discussed in Sec. 1.4.

A general assumption for many models of DM is that DM particles were in thermal equilibrium in the early Universe, i.e. that they interacted frequently with SM particles in the plasma. In such

a setup the production of DM particles from SM particles is efficient as long as the temperature T is above the DM mass m_χ. Moreover, DM production is in equilibrium with the annihilation of DM into SM particles, with a rate given by $\Gamma_{\rm prod} = \Gamma_{\rm ann} = \langle \sigma_{\rm ann}\, v \rangle n_{\rm eq}$, where $\sigma_{\rm ann}$ is the total annihilation cross section of DM, v is the relative velocity of the annihilating particles and the brackets denote a thermal average. The equilibrium number density $n_{\rm eq}$ for g_χ degrees of freedom is given by

$$n_{\rm eq} = g_\chi \left(\frac{m_\chi T}{2\pi} \right)^{3/2} \exp(-m_\chi/T) \; . \tag{1.3}$$

As long as DM remains in thermal equilibrium, its density per comoving volume therefore decreases exponentially as the Universe expands and cools down to temperatures below the DM mass.

To describe the evolution of the Universe, one introduces the scale factor $a(t)$ and defines the Hubble parameter $H(t) = \dot{a}(t)/a(t)$. The Friedman equation then determines the time evolution of H in terms of the mass-energy density ρ:

$$H^2 = \frac{8\pi}{3 M_{\rm P}^2}\, \rho \; , \tag{1.4}$$

where $M_{\rm P} \equiv (G_{\rm N})^{-1/2} = 1.22 \times 10^{19}$ GeV is the Planck mass and we assume that the Universe is flat. During radiation domination

$$\rho = \frac{\pi^2}{30}\, g_*(T)\, T^4 \tag{1.5}$$

and therefore $H = 1.66 \sqrt{g_*}\, T^2/M_{\rm P}$, where g_* is the effective number of relativistic degrees of freedom.

Once the temperature of the plasma drops below the DM mass, the number density of DM particles becomes Boltzmann suppressed. As a consequence, DM annihilations become rapidly less frequent, until the annihilation rate drops below the Hubble expansion rate, $\Gamma_{\rm ann} \lesssim H$. At this point, the processes which keep DM in thermal equilibrium become inoperative and the number of DM particles per comoving volume becomes constant. This thermal decoupling is referred to as freeze-out.

Assuming that DM is its own anti-particle (as is the case in many of the models that we will discuss below), the number density n after freeze-out can be obtained from the Boltzmann equation

$$\frac{{\rm d}n}{{\rm d}t} = -3\, H\, n - \langle \sigma_{\rm ann} v \rangle \left(n^2 - n_{\rm eq}^2 \right) \; . \tag{1.6}$$

Introducing the entropy density

$$s = \frac{2\pi^2}{45}\, g_*^s(T)\, T^3 \,, \tag{1.7}$$

with g_*^s being the effective degrees of freedom for the entropy density, we can rewrite Eq. (1.6) in terms of $Y \equiv n/s$ and $x \equiv m_\chi/T$ to obtain

$$\frac{\mathrm{d}Y}{\mathrm{d}x} = -\sqrt{\frac{\pi g_*}{45}}\, \frac{M_\mathrm{P} m_\chi}{x^2}\, \langle \sigma_\mathrm{ann} v \rangle \left(Y^2 - Y_\mathrm{eq}^2 \right) \,. \tag{1.8}$$

From this equation, the freeze-out temperature T_fo can be found numerically. In terms of x_fo the present DM abundance Y_0 is approximately given by [26]

$$Y_0 = \sqrt{\frac{45}{\pi g_*}}\, \frac{1}{m_\chi M_\mathrm{P}}\, \frac{x_\mathrm{fo}}{\langle \sigma_\mathrm{ann} v \rangle} \,. \tag{1.9}$$

Instead of Y_0 it is common to quote the DM relic density $\Omega_\chi \equiv \rho_\chi/\rho_c$, where $\rho_\chi = m_\chi\, Y\, s$ and $\rho_c = 3\, H^2\, M_\mathrm{P}^2/(8\pi)$ is the critical density. Substituting the present values of H, s and T (called H_0, s_0 and T_0), one finds approximately

$$\Omega_\chi\, h^2 = \frac{1.07 \times 10^9\ \mathrm{GeV}^{-1}}{M_\mathrm{P}}\, \frac{x_\mathrm{fo}}{\sqrt{g_*}\langle \sigma_\mathrm{ann} v \rangle} \,, \tag{1.10}$$

where $h = H_0/100\,\mathrm{km\,s^{-1}} \approx 0.67$ [15]. The freeze-out temperature depends only weakly on the details of the model and is typically $20 \lesssim x_\mathrm{fo} \lesssim 30$. The corresponding number of relativistic degrees of freedom is $80 \lesssim g_* \lesssim 90$.[1] Substituting these values, one finds the approximate expression

$$\Omega_\chi\, h^2 = \frac{3 \times 10^{-27}\ \mathrm{cm^3\,s^{-1}}}{\langle \sigma_\mathrm{ann} v \rangle} \,. \tag{1.11}$$

The cross section $\langle \sigma_\mathrm{ann} v \rangle \approx 3 \times 10^{-26}\ \mathrm{cm^3\,s^{-1}}$ required to match the observed DM relic density $\Omega_\chi\, h^2 = 0.1199 \pm 0.0027$ [15] is often referred to as the *thermal cross section*.

To calculate $\langle \sigma_\mathrm{ann} v \rangle$, we can use the partial wave expansion $\sigma v = a + b v^2 + \mathcal{O}(v^4)$, giving $\langle \sigma v \rangle \simeq a + 6b/x_\mathrm{fo}$. To good approximation Eq. (1.8) can then be integrated analytically, to give [25]

$$\Omega_\chi\, h^2 \simeq \frac{1.07 \times 10^9}{\mathrm{GeV}}\, \frac{x_\mathrm{fo}}{M_\mathrm{Pl}\sqrt{g_*}\left(a + \frac{3b}{x_\mathrm{fo}}\right)} \,. \tag{1.12}$$

The calculations above still hold if DM particles are distinct from their anti-particles, provided there is no asymmetry between the two. In this case, $\rho_\chi = 2\, m_\chi\, Y\, s$, so for the same annihilation

[1] This approximation assumes that freeze-out occurs between the electroweak phase transition and the QCD phase transition and should therefore be valid for DM masses between a few GeV and a few TeV.

cross section the final relic abundance is larger by a factor of 2.

1.4 Candidates for dark matter

As discussed in Sec. 1.2, the SM does not contain a suitable candidate for the DM particle. While it is not difficult in principle to extend the SM so that it contains an additional particle with the required properties, it is desirable that such an extension also address other open problems in particle physics. In fact, the SM, while being extremely successful experimentally, has various shortcomings from the theoretical perspective. In particular, it contains a number of free parameters, which cannot be explained or predicted within the model. Well-motivated extensions of the SM therefore often aim to account for the smallness of certain parameters compared to others by introducing additional symmetries or dynamical mechanisms. Remarkably, it turns out that many models developed for these reasons automatically contain a suitable DM candidate. Here we review some of the most popular proposals.

1.4.1 WIMPs

Of all hypothetical DM candidates, none have been studied in more detail than weakly interacting massive particles (WIMPs). This interest is based on the remarkable observation that for a particle with weak interactions (characterised by Fermi's constant $G_\mathrm{F} \approx 1.166 \times 10^{-5}\,\mathrm{GeV}^{-2}$) the DM annihilation cross section is parametrically given by $\langle \sigma_\mathrm{ann} v \rangle \sim G_\mathrm{F}^2\, m_\chi^2/(4\pi)$, which yields the thermal cross section for $m_\chi \sim 10\,\mathrm{GeV}$ [28]. The simplest example for such a particle, a Dirac neutrino with mass of a few GeV, has been excluded by direct detection experiments (see Sec. 2.1). Nevertheless, the term WIMP has been generalised to refer to any kind of stable particle with a mass close to the electroweak scale, i.e. $10\,\mathrm{GeV} \lesssim m_\chi \lesssim 1\,\mathrm{TeV}$, and an interaction strength comparable to the SM weak interactions.

New stable particles at the electroweak scale are in fact a generic feature of extensions of the SM that aim to address the so-called hierarchy problem, i.e. the large separation between the electroweak scale and the Planck scale. In order to protect the former against large contributions from radiative corrections, one typically needs to introduce new states below the TeV scale. The lightest such state can be stable — for example due to a discrete symmetry that forbids all possible

decay channels — and would then be a perfect WIMP candidate. The most well-known example is weak scale supersymmetry (SUSY) with conserved R-parity, where the lightest SUSY particle in many models is either the neutralino or the sneutrino (see Refs. [29, 30] and Sec. 2.3). Another possibility is the first Kaluza-Klein excitation of the SM hypercharge gauge boson in models of universal extra dimensions [31].

While the term WIMP has been used for a wide range of different models, all these models have in common that the relic abundance is determined from thermal freeze-out. In practice, however, the calculation of Ω_χ is often more involved than outlined in Sec. 1.3, for example due to the presence of thresholds or resonances, or because additional unstable particles with mass close to m_χ can lead to co-annihilations [32]. Note also, that a particle does not necessarily have to be a WIMP in order to obtain the required abundance from the freeze-out mechanism. In fact, an annihilation cross section close to the thermal cross section can be obtained for a wide range of masses and couplings [33].

1.4.2 Asymmetric dark matter

Although the idea of thermal freeze-out is an attractive framework to explain the observed abundance of matter, it actually fails to predict the relic density of baryons Ω_B. The reason is that baryons ought to stay in thermal equilibrium until $T \lesssim m_N/50$, at which point $\Omega_B \lesssim 10^{-10}$, i.e. 9 orders of magnitude below the observed value $\Omega_B \sim 0.05$. To explain this discrepancy, as well as the apparent absence of anti-baryons in the Universe, one must invoke an initial asymmetry

$$\eta_B \equiv \frac{n_B - n_{\bar{B}}}{n_\gamma} \,. \tag{1.13}$$

Such an asymmetry can only be generated by out-of-equilibrium processes violating C and CP [34]. It has been subsequently recognised that these conditions necessitate BSM physics, since the SM has insufficient CP violation and cannot accommodate the necessary departure from thermal equilibrium.

The idea of asymmetric DM (ADM) is based on the observation that Ω_B and Ω_χ are similar in magnitude, a coincidence that cannot be explained if DM is a thermal relic. If, on the other hand, the DM particle is a new electroweak-scale particle that shares in the generation of the baryon asymmetry, there is a natural link between the respective abundances [35–39]. Provided that the

DM particles stay in thermal equilibrium sufficiently long, almost all anti-particles will annihilate away and their number density is exponentially suppressed. Consequently, the DM number density n_χ is entirely determined by the asymmetry η_χ, and we obtain the relation

$$\frac{\Omega_\chi}{\Omega_B} = \frac{m_\chi \, \eta_\chi}{m_N \, \eta_B} \, , \tag{1.14}$$

where m_N is the nucleon mass.

Assuming comparable asymmetries, the observed cosmological abundance is therefore realised for $m_\chi \sim 5\,\text{GeV}$, providing an attractive framework for relatively light DM particles. Models for ADM often invoke new strong dynamics, such as technicolour [35, 40], where the conservation of technibaryon number explains the stability of the DM particle. Nevertheless, candidates for ADM can also arise in SUSY models [39].

1.4.3 SuperWIMPs and FIMPs

SuperWIMPs are particles that have only 'super weak' interactions and are produced non-thermally by the decay of a heavier state. If this heavier state can decay only to the superWIMP, it will naturally have a very long lifetime due to the smallness of the couplings. Consequently, this particle can act as a WIMP in the early Universe and obtain its relic density from thermal freeze-out. The relic density of the superWIMP is then given by

$$\Omega_{\text{SWIMP}} = \frac{m_{\text{SWIMP}}}{m_{\text{WIMP}}} \Omega_{\text{WIMP}} \, . \tag{1.15}$$

The freeze-out mechanism can therefore still be exploited to account for the observed relic density, but the resulting DM particles would be almost impossible to detect [41].

The most common example for a superWIMP is the gravitino, which is the supersymmetric partner of the graviton. Note, however, that gravitinos can also be produced thermally via non-renormalisable interactions. While these interactions are strongly suppressed today, they may have been efficient in the early Universe, if the reheat temperature T_R after inflation was sufficiently high [42, 43]. Particles that are produced thermally in spite of highly suppressed interactions are often referred to as feebly interacting massive particles (FIMPs). Since these particles never reach thermal equilibrium themselves, this generation mechanism is sometimes referred to as freeze-in [44].

1.4.4 Axions

An important shortcoming of the SM is its failure to explain the absence of sizeable CP violation in the strong sector (in particular the smallness of the neutron electric dipole moment). The most attractive solution to this so-called 'strong CP problem' is the postulation of a new global quasi-symmetry (called $U_{\rm PQ}(1)$ after the original proponents [45, 46]), which is broken both spontaneously and by non-perturbative effects. The breakdown of $U_{\rm PQ}(1)$ leads to a new degree of freedom, the axion field, with a classical potential that dynamically sets the CP-violating term to zero.

It was pointed out subsequently that this solution of the strong CP problem implies the presence of a new light state, the axion [47, 48]. In terms of the scale f_a at which $U_{\rm PQ}(1)$ is broken, the axion mass is given by

$$m_a \sim m_\pi \, f_\pi / f_a \sim 0.6 \, \text{eV} \, \frac{10^7 \, \text{GeV}}{f_a} \, , \tag{1.16}$$

where m_π and f_π are the mass and decay constant of the pion, respectively. The couplings of the axion to SM particles is similarly suppressed by the scale f_a. While thermal production of axions in the early Universe is therefore completely negligible, a sizeable relic abundance can arise from the 'mis-alignment mechanism' [49–51]. This non-thermal production mechanism guarantees that axions are produced non-relativistically, i.e. as CDM. Consequently, axions are consistent with large-scale structure formation in spite of their very small mass. In particular, for $10^{-6} \, \text{eV} \lesssim m_a \lesssim 10^{-3} \, \text{eV}$ the observed relic abundance can be reproduced while avoiding astrophysical constraints from consideration of energy loss by stars and supernovae.

1.4.5 Sterile neutrinos

The motivation for sterile neutrinos comes from the necessity to augment the SM in order to account for the non-zero neutrino masses that are inferred from neutrino oscillations. It would be desirable that this new mechanism also explains the smallness of the neutrino masses m_ν compared to all other fermions. The most attractive solution to this problem is the see-saw mechanism [52, 53], which is based on the introduction of a new set of singlet Majorana fermions. These so-called sterile neutrinos can have both a Dirac mass term m_D and a Majorana mass term m_M. Diagonalisation of the neutrino mass matrix then gives $m_\nu \sim m_D^2 / m_M$, i.e. a suppression of the active neutrino

masses if m_M is sufficiently larger than m_D. An attractive option is that m_D is at the keV scale, while m_M is at the electroweak scale (sometimes referred to as the νMSM [54]). The lightest sterile neutrino then has a mass of around 10 keV and can play the role of the DM.

In the νMSM, the lightest sterile neutrino can decay into an active neutrino and a photon, but its lifetime is sufficiently large that it appears stable on cosmological timescales and avoids direct constraints from X-ray observations. Sterile neutrinos can be produced in the early Universe either by mixing with the active neutrinos or from the decay of a heavier state in a similar way as a superWIMP [55]. Interestingly, keV sterile neutrinos can be warm DM, i.e. they can have a free-streaming length comparable to the size of dwarf spheroidal galaxies. In this case they would suppress the formation of structure at the smallest scales and potentially explain various discrepancies between N-body simulations of CDM and observations (see e.g. Refs. [56–58]).

1.5 Outline

Given the large number of different candidates for the DM particle presented in the previous section and the vast range of conceivable properties, it should be clear that a comprehensive treatment of all options is difficult. Nevertheless, the aim of this thesis is to study the experimental signatures of DM that are relevant to large classes of DM models. Rather than exploring any specific model in detail we will only make the basic assumption that the couplings between DM and SM particles are sufficiently large that interactions like DM scattering and annihilation can lead to observable signals. This assumption also ensures that DM particles were in thermal equilibrium in the early Universe, provided the Universe once had a temperature exceeding the DM mass. We will not limit ourselves to WIMPs, however, but also consider the possibility that DM carries an initial asymmetry that determines the DM relic density. The latter option is particularly interesting, since we will often focus on the possibility that the DM particle has a mass of about 10 GeV (see Sec. 2.1.3).

We will discuss possible ways to search for DM particles with these properties in Chapter 2. In particular, we will point out the complementarity between the different search strategies and review some recent experimental results. In the process, we will introduce the basic framework and relevant notation for the remainder of this thesis. Chapter 3 then focuses on the direct detection of DM scattering in nuclear recoil detectors, in particular on the uncertainties related to the assumed

velocity distribution of Galactic DM particles. By converting experimental data to new variables, we can make the astrophysical unknowns explicit and thus compare different experiments without the need to make implicit assumptions concerning the DM halo. We will apply this method to recent experimental results to show that some of them can be brought into mutual agreement, while others remain in tension independently of astrophysical uncertainties. We will explore possible ways of reducing this tension by altering the properties of DM interactions. In this context, we will propose a new approach for inferring the properties of the DM particle, which does not require any assumptions about the structure of the DM halo.

In Chapter 4 we will discuss the experimental signatures of DM interacting with nuclei via a vector mediator, such as the gauge boson of a new $U(1)$. We will first discuss the case where this new Z' as well as the DM particle have a mass of a few GeV and then turn to the case where the Z' is significantly heavier. While the former case is most strongly constrained by precision measurements, the latter scenario can be probed with great sensitivity at hadron colliders. Finally, Chapter 5 explores in more detail the subtleties of DM searches at colliders, with a particular focus on cases where loop contributions are important for a comparison of collider searches and direct detection experiments. Of particular interest are models where the dominant contribution to the DM production cross section arises from heavy-quark loops and models where the direct detection cross section is spin-dependent or momentum suppressed. Our conclusions are presented in Chapter 6 together with an outlook and perspectives for future work.

CHAPTER 2

Detection of dark matter

The overwhelming amount of evidence for the gravitational interactions of DM and the large variety of viable particle candidates makes the identification of DM a key challenge for modern astroparticle physics. There are three different experimental strategies that promise to shed light on this puzzle [30, 59, 60]. Direct detection experiments attempt to observe the interactions of DM particles with nuclei in shielded underground detectors. Indirect detection experiments look for the products of DM annihilations with satellites, balloons and ground based telescopes. Finally, accelerator experiments aim to actually produce DM by colliding SM particles at high energies. We present a discussion of these different approaches in Secs. 2.1–2.3 and introduce the framework and notation for the remainder of this thesis. A particular focus will be on the calculation of differential event rates in direct detection experiments. We review some recent experimental results and emphasise the complementarity of different types of experiments. Finally, we discuss the idea of using effective operators to compare different search strategies in Sec. 2.4.

2.1 Direct detection

As DM particles from the DM halo of the Milky Way pass through the Earth, they can scatter off nuclei and transfer some of their kinetic energy. Direct detection experiments aim to observe these interactions by measuring the resulting nuclear recoil energy E_R in dedicated low-background detectors [61–63] (see Ref. [64] for a recent review). In the laboratory frame the differential event rate with respect to recoil energy is given by

$$\frac{\mathrm{d}R}{\mathrm{d}E_\mathrm{R}} = \frac{\rho}{m_\mathrm{N}\, m_\chi} \int_{v_\mathrm{min}}^{\infty} v f(\boldsymbol{v} + \boldsymbol{v}_\mathrm{E}(t)) \frac{\mathrm{d}\sigma}{\mathrm{d}E_\mathrm{R}} \mathrm{d}^3 v \,, \tag{2.1}$$

where ρ is the local DM density, m_χ and m_N are the DM and target nucleus mass, $f(\mathbf{v})$ is the local DM velocity distribution evaluated in the Galactic rest frame, $\boldsymbol{v}_\mathrm{E}(t)$ is the velocity of the Earth relative to the Galactic rest frame [65, 66] and $v = |\boldsymbol{v}|$. For elastic scattering the *minimum velocity* required for a DM particle to transfer the energy E_R to a given nucleus N is

$$v_\mathrm{min}(E_\mathrm{R}) = \sqrt{\frac{m_\mathrm{N} E_\mathrm{R}}{2\,\mu_{\mathrm{N}\chi}^2}}\,, \tag{2.2}$$

where $\mu_{\mathrm{N}\chi} = m_\mathrm{N}\, m_\chi/(m_\mathrm{N} + m_\chi)$ is the reduced mass of the DM-nucleus system.

The differential cross section $\mathrm{d}\sigma/\,\mathrm{d}E_\mathrm{R}$ depends on the underlying properties of the DM-quark interaction, in particular on whether the interactions are spin-independent (SI) or spin-dependent (SD), see e.g. Refs. [67–69]. For SI scattering, one finds

$$\frac{\mathrm{d}\sigma}{\mathrm{d}E_\mathrm{R}} = C_\mathrm{T}^2(A,Z)\,F^2(E_\mathrm{R})\frac{m_\mathrm{N}\,\sigma_n}{2\,\mu_{n\chi}^2\,v^2}\,, \tag{2.3}$$

where $\mu_{n\chi}$ is the reduced DM-neutron mass and $C_\mathrm{T}(A,Z) \equiv [f_p/f_n Z + (A-Z)]$ with A and Z being the mass and charge number of the target nucleus and $f_{n,p}$ denoting the effective DM coupling to neutrons and protons, respectively. Furthermore, $F(E_\mathrm{R})$ is the nuclear form factor and σ_n is the DM-neutron scattering cross section at zero momentum transfer. The above parameterisation of the cross section holds e.g. for DM-nucleus scattering mediated by a heavy CP-even scalar boson or by a heavy vector mediator coupling to the vector current (see Sec. 2.4). While the factor C_T^2 encodes the coherent enhancement of the DM interactions for zero momentum transfer, the form factor $F^2(E_\mathrm{R})$ reflects the loss of this coherence for $E_\mathrm{R} > 0$ due to the finite size of the nucleus. For $f_p = f_n$ one finds that the differential cross section at zero momentum transfer is proportional to A^2, because the contributions from all nucleons interfere constructively.

For SD scattering, the corresponding expression for the differential cross section is

$$\frac{\mathrm{d}\sigma}{\mathrm{d}E_\mathrm{R}} = \frac{4\pi}{3(2J+1)}\left[a_0^2 S_{00}(E_\mathrm{R}) + a_0 a_1 S_{01}(E_\mathrm{R}) + a_1^2 S_{11}(E_\mathrm{R})\right]\frac{m_\mathrm{N}\,\sigma_n^\mathrm{SD}}{2\,\mu_{n\chi}^2\,v^2}\,, \tag{2.4}$$

where J is the nucleus spin and S_{ij} are nuclear form factors. The effective couplings a_0 and a_1 are defined as $a_0 \equiv a_n + a_p$ and $a_1 \equiv a_n - a_p$ with $a_{n,p}$ denoting the effective DM coupling to neutrons and protons, respectively. SD interactions can arise for example from the exchange of a heavy vector mediator coupling only to the axial current (see Sec. 2.4).

Unless otherwise stated, we adopt for the astrophysical parameters the Standard Halo Model (SHM),

i.e. a truncated Maxwell-Boltzmann (M-B) distribution for $f(v)$ with velocity dispersion $v_0 = 220\ \mathrm{km\,s^{-1}}$ and escape velocity $v_{\rm esc} = 544\ \mathrm{km\,s^{-1}}$ (see also Appendix A.1), and take $\rho = 0.3\ \mathrm{GeV\,cm^{-3}}$. For SI scattering, we use the Helm form factor [70], for SD scattering we take the form factors from Ref. [71] for xenon, from Ref. [72] for caesium and from Ref. [73] for all other target materials.

The number of events $P(E_1, E_2)$ expected in the energy range $[E_1, E_2]$ is

$$P(E_1, E_2) = \kappa \int \mathrm{Res}(E_1, E_2, E_{\rm R})\, \epsilon(E_{\rm R})\, \frac{\mathrm{d}R}{\mathrm{d}E_{\rm R}}\, \mathrm{d}E_{\rm R}\ , \tag{2.5}$$

where κ is the exposure of the detector, $\epsilon(E_{\rm R})$ is the detector acceptance and

$$\mathrm{Res}(E_1, E_2, E_{\rm R}) \equiv \frac{1}{2}\left[\mathrm{erf}\left(\frac{E_2 - E_{\rm R}}{\sqrt{2}\Delta E_{\rm R}}\right) - \mathrm{erf}\left(\frac{E_1 - E_{\rm R}}{\sqrt{2}\Delta E_{\rm R}}\right)\right] \tag{2.6}$$

is the detector response function for a detector with energy resolution $\Delta E_{\rm R}$ [74].

2.1.1 The velocity integral

Substituting the standard parameterisation for either SI or SD scattering into Eq. (2.1), we see that direct detection experiments do not directly probe the local velocity distribution $f(v)$, but rather the velocity integral

$$g(v_{\rm min}, t) \equiv \int_{v_{\rm min}}^{\infty} \frac{f(\boldsymbol{v} + \boldsymbol{v}_{\rm E}(t))}{v}\, \mathrm{d}^3 v\ . \tag{2.7}$$

For our purposes, it will be convenient to absorb the DM mass, cross section and density into this definition and consider the *rescaled velocity integral*

$$\tilde{g}(v_{\rm min}) \equiv \frac{\rho\, \sigma_n}{m_\chi}\, g(v_{\rm min})\ , \tag{2.8}$$

which has typical values in the range $(10^{-30}$–$10^{-22})\ \mathrm{day}^{-1}$. The differential event rate for SI scattering can then be written in the very simple way

$$\frac{\mathrm{d}R}{\mathrm{d}E_{\rm R}} = \frac{C_{\rm T}^2(A, Z)\, F^2(E_{\rm R})}{2\, \mu_{n\chi}^2}\, \tilde{g}(v_{\rm min})\ . \tag{2.9}$$

At this point, it is worth developing some intuition for $\tilde{g}(v_{\rm min})$ and elucidating its relation to the more familiar DM velocity distribution $f(v)$. In the left panel of Fig. 2.1, we show the canonical M-B velocity distribution of the SHM, along with a sharply peaked function which could arise from

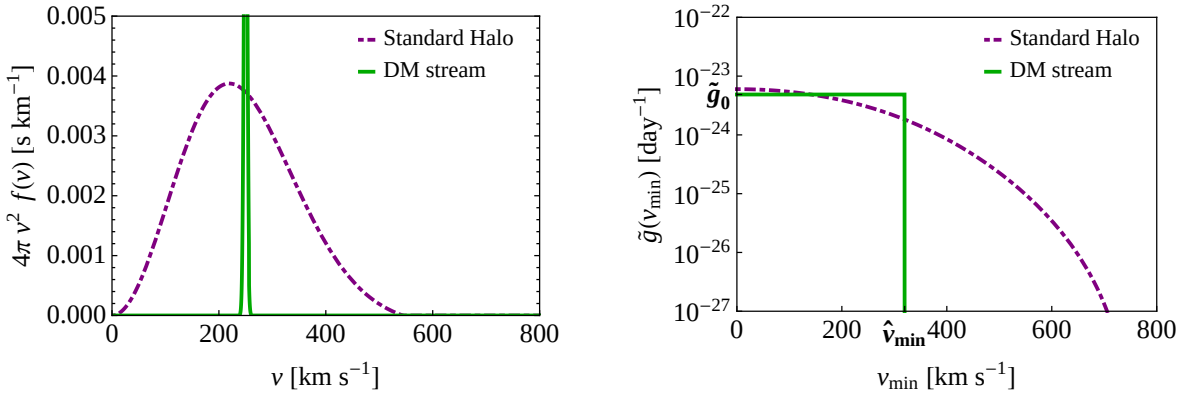

FIG. 2.1. The one-dimensional velocity distribution $4\pi\, v^2\, f(v)$ (left) and the rescaled velocity integral $\tilde{g}(v_{\rm min})$ (right) for the SHM (purple, dot-dashed) and a sharply peaked DM stream (green, solid). In order to calculate $\tilde{g}(v_{\rm min})$, we have assumed $\sigma_n = 10^{-40}$ cm^2, $\rho = 0.3$ GeV cm^{-3} and $m_\chi = 15$ GeV. The velocity of the DM stream is $\boldsymbol{v}_{\rm s} = (250,\, 0,\, 0)$ km s^{-1}, giving $\hat{v}_{\rm min} = |\boldsymbol{v}_{\rm s} - \boldsymbol{v}_{\rm E}| \approx 330$ km s^{-1}.

a stream of DM or alternatively can be thought of as a shifted M-B distribution in the limit of small velocity dispersion. In the right panel we show the corresponding $\tilde{g}(v_{\rm min})$.[1] Since $f(v)$ is positive everywhere, $\tilde{g}(v_{\rm min})$ has the important property that for *any* velocity distribution it is a decreasing function of $v_{\rm min}$ [75]. As the velocity dispersion decreases, $\tilde{g}(v_{\rm min})$ becomes more like a step function, which is the minimal form consistent with this property.

In Fig. 2.2 we examine the range of predictions for $g(v_{\rm min})$ from a variety of reasonable models for the Galactic halo. First of all we note that $g(v_{\rm min})$ can change considerably even in the context of the SHM if we vary v_0 and $v_{\rm esc}$ within their observational bounds (see the left panel of Fig. 2.2). Moreover, the SHM is unlikely to be an accurate description and many alternative models and parameterisations for the halo exist in the literature. We present an overview in Appendix A.1 and show the corresponding velocity integrals in the right panel of Fig. 2.2. Even for a fixed choice of $v_{\rm esc}$ and v_0 there is a large spread in the predictions of the velocity integral, especially near the cut-off.

2.1.2 Experimental signatures

We observe from Fig. 2.1 that the velocity integral decreases rapidly for increasing $v_{\rm min}$, in particular for velocities close to the escape velocity. The corresponding recoil energy spectrum in a given

[1] We neglect the time dependence of $g(v_{\rm min})$ here, which would lead to a slight smearing of the step function.

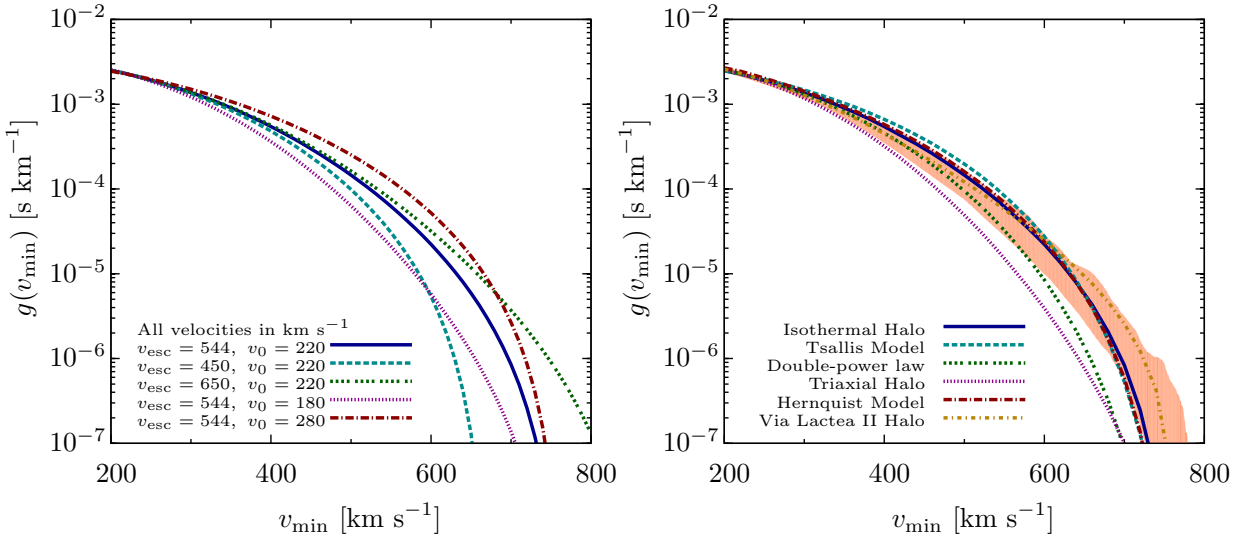

FIG. 2.2. The velocity integral $g(v_{\rm min})$ for the SHM with different parameters (left) and alternative descriptions of the DM halo introduced in Appendix A.1 (right). The shaded region corresponds to the values of $g(v_{\rm min})$ observed in the GHALO$_{\rm s}$ simulation [76].

detector will fall even faster because of the contribution of the nuclear form factor, which reflects the loss of coherence for large momentum transfer. Furthermore, since $g(v_{\rm min}) = 0$ for $v_{\rm min} > v_{\rm esc} + v_{\rm E}$, there will be no events above the maximum recoil energy

$$E_{\rm R}^{\rm max} = \frac{2\,\mu_{{\rm N}\chi}^2}{m_{\rm N}}(v_{\rm esc} + v_{\rm E})^2\ . \tag{2.10}$$

The lighter the DM particles, the smaller the possible recoil energies. In fact, for $m_{\rm N} = 120\,\text{GeV}$ and $m_\chi = 50\,\text{GeV}$ on obtains $E_{\rm R}^{\rm max} \sim 130\,\text{keV}$, for $m_\chi = 10\,\text{GeV}$ only $E_{\rm R}^{\rm max} \sim 9\,\text{keV}$.

Current direct detection experiments are able to reduce known backgrounds to the point where they are sensitive to less than 1 event per kg target material per year. Nevertheless, the expected recoil spectrum is essentially featureless and close to the low-energy threshold of the detector and therefore difficult to distinguish from potential unknown backgrounds. Isolating a DM signal and convincingly rejecting possible background contributions is therefore a great experimental challenge.

The expected DM signal does, however, have some characteristic features that can be used to improve experimental sensitivity and confirm the nature of an observed excess. In particular, the event rate is expected to show an annual modulation due to the motion of the Earth around the Sun [77, 78]. In summer, when the velocity of the Earth relative to the Sun is mostly aligned with the velocity of the Sun relative to the DM halo, incoming DM particles will on average have larger

velocities, leading to a harder recoil spectrum compared to winter, when the velocity of the Earth is mostly anti-aligned with the velocity of the Sun. An experiment observing only the high-energy tail of the recoil spectrum is therefore expected to observe more events in summer, with the peak around 2 June. We will discuss these annual modulations in more detail in Chapter 3.

The motion of the Earth relative to the DM halo also implies that the nuclear recoils will not have an isotropic distribution but instead point preferentially in the backward direction. Consequently, if the direction of nuclear recoils can be observed, there should be a strong correlation with the motion of the Earth [79]. In practice, directional detection is extremely challenging, since a relatively low-density target is required in order to obtain observable track lengths. Since it is very difficult to achieve a target mass with competitive sensitivity, we will not consider directional detection further in this thesis.

2.1.3 Hints for light dark matter

The majority of direct detection experiments have focussed on DM particles with a mass of $100\,\text{GeV} \lesssim m_\chi \lesssim 1\,\text{TeV}$, motivated simultaneously by the WIMP paradigm and by the existence of a natural particle candidate in SUSY extensions of the SM (see Chapter 1). With an impressive increase of sensitivity over the past few years, direct detection experiments such as XENON100 [80] and LUX [81] have pushed down the bounds on the SI scattering cross section on nuclei for such particles to the point where they significantly constrain the relevant SUSY parameter space (see e.g. Ref. [82]).

Less attention has been paid to searching for lighter particles, not only because of fewer theoretical motivations, but also because the typical energy deposited in the scattering of light DM particles is close to the detector threshold, making it very difficult to distinguish nuclear recoils from background [83]. For these reasons, an ideal experiment to probe the low-mass region should have target nuclei with low mass number and a low energy threshold. Unfortunately, it is hard to reliably determine the detector response to a potential DM signal at such low recoil energies [84, 85] and the interpretation of the data becomes very sensitive to the assumed velocity distribution of the DM halo [86–89]. With increasing interest amongst theorists in developing particle physics models for light DM (see Sec. 1.4), the experimental community is nevertheless becoming more and more aware of the importance of looking in this mass region.

Indeed, over the past years several experiments have observed hints for DM particles with $m_\chi \sim 10\,\text{GeV}$. This mass region (and a cross section of $\sigma_p \sim 10^{-40}\,\text{cm}^2$) is favoured by an excess of events over the expected background observed by CoGeNT [90] and CRESST-II [91], the latter quoting a statistical significance of over 4σ. Moreover, the CDMS-II collaboration has observed 3 events in the DM search region of their silicon detectors (CDMS-Si for short), compared to a background expectation of only 0.62 events [92]. Considering only the number of events this signal is compatible with background at the 2σ level, but taking into account their distribution, a background+DM interpretation of the data is preferred over the background-only hypothesis with a probability of 99.8%. The highest likelihood is found for a DM particle with mass 8.6 GeV, but the favoured cross section is $1.9 \times 10^{-41}\,\text{cm}^2$, i.e. significantly below the value obtained from CoGeNT and CRESST-II.

Two DM direct detection experiments, namely DAMA [93] and CoGeNT [94], have published data with evidence for an annual modulation consistent with the expectation for a DM signal. The combined results from DAMA/NaI and DAMA/LIBRA have a statistical significance exceeding 8σ, the annual modulation observed by CoGeNT has a significance of 2.8σ. Again, the simplest explanation of these experiments in terms of DM is SI elastic scattering of a DM particle with $m_\chi \sim 10\,\text{GeV}$ [95]. However, although favouring a similar mass range, the scattering cross section required to explain the DAMA signal (assuming the modulation fraction predicted by the SHM) is too large to be brought into agreement with the other experimental claims. It is therefore very difficult to find a consistent interpretation of all these 'anomalies'.

Moreover, an interpretation of the observed signals in terms of elastic SI scattering of DM is strongly disfavoured by other null results, such as CDMS-II [96], SuperCDMS [97], XENON10 [98], XENON100 [80] and LUX [81] (see e.g. [99–104]). A more detailed discussion of these experimental results will be provided in Chapter 3 and Appendix A.2. The main focus of our discussion will be whether the tension between different experiments can be reduced by accounting for experimental and astrophysical uncertainties, and if better agreement is found for different assumptions concerning the underlying nature of DM scattering.

2.2 Indirect detection

The key idea of DM indirect detection is to study regions in space where large DM densities are expected, such as the Galactic centre or the centre of the Sun, and search for an excess of SM particles produced from the annihilation or decay of DM. Here we briefly review the different kinds of indirect searches and comment on the respective challenges.

Among the most important search channels for the indirect detection of DM are γ-rays, because they travel in straight lines and suffer from very little absorption. Moreover, if two DM particles annihilate directly into two photons, one expects to observe a mono-energetic γ-ray line with an energy equal to the DM mass. Since DM cannot carry electric charge, however, annihilation into two photons can only be induced at the loop level and may therefore be undetectably small (see e.g. Ref. [105]). Nevertheless, other processes can lead to distinctive γ-ray spectra, such as internal bremsstrahlung [106] or diffuse γ-rays resulting from the bremsstrahlung and Inverse Compton scattering of electrons and positrons produced in DM annihilation or decay processes [107]. The strongest bounds on the γ-ray flux currently come from Fermi-LAT [108, 109]. Note that, since the astrophysical backgrounds at the Galactic centre are often difficult to model, the best constraints often come from observations of Milky Way dwarf spheroidals, which are strongly DM dominated [110].

Another interesting possibility for indirect detection is to search for an anomalous component of antimatter in cosmic rays, in particular positrons and antiprotons, but also heavier anti-nuclei. The two great challenges for these searches are to model the transport of charged particles through the interstellar medium (see e.g. Ref. [111]) and to model alternative sources for cosmic rays like nearby supernova remnants [112]. Such astrophysical foregrounds could plausibly explain the positron excess observed by PAMELA [113] and later confirmed by AMS-2 [114]. A way to test the various explanations for this excess is to measure the boron-to-carbon ratio in cosmic rays [112]. A very promising alternative is to search for light anti-nuclei, which would provide a better discrimination between DM annihilation and astrophysical contributions [115].

While being much more difficult to detect than photons or charged particles, neutrinos nevertheless have great potential in the search for DM. The reason is that neutrinos offer the unique possibility to look for DM annihilation in the centre of the Sun, for example using IceCube [116]. The Sun is

expected to accumulate DM as the Solar System moves through the Galactic halo, because DM particles can become gravitationally bound to the Sun if they scatter with nuclei and lose some of their momentum [117]. Even if DM does not directly annihilate into neutrinos, the annihilation into heavy quarks and charged leptons will produce an excess of high-energy neutrinos, which can easily escape from the Sun [118]. Since no other process in the Sun can produce neutrinos with energies of a GeV or more, observation of such an excess would provide unambiguous evidence for DM. Note that, in contrast to most other indirect searches, bounds on the neutrino flux from the Sun typically do not constrain the DM annihilation cross section, but the DM scattering cross section, which determines the capture rate and therefore the DM density inside the Sun.

For ADM, annihilation processes are usually absent and consequently most indirect searches do not give relevant constraints. Nevertheless, since in these models DM particles would continuously accumulate in stars, other indirect signatures are expected. For example, ADM may alter the heat transfer in stars [119–121] or even lead to the collapse of neutron stars to black holes [122].

2.3 Collider searches

It is a remarkable fact that one of the leading experiments for DM detection is the CERN Large Hadron Collider (LHC). Although any DM particles produced at the LHC will escape from the detector unnoticed, we may observe large amounts of missing transverse energy ($\not{E}_T$) if one or more SM particles are produced in association with the DM particles.

This experimental signature occurs naturally in the case where the DM particle is the lightest of a set of new particles that are odd under a new $\mathbb{Z}_2$ symmetry while all SM particles are even. Such a $\mathbb{Z}_2$ symmetry not only ensures the stability of the DM particle, but it also guarantees that any other odd particle produced at a collider must ultimately decay into the DM particle together with a number of SM particles. In contrast to the DM particle, the heavier odd particles can in principle participate in the strong interactions, so they may be produced at hadron colliders much more easily. The decay to the colour-neutral lightest state must then necessarily involve strongly-interacting SM particles, which lead to easily observable jets of hadrons in combination with large $\not{E}_T$ from the escaping DM particles. The most common example for this setup is SUSY with R-parity conservation, which is imposed to suppress proton decay.

If we do not want to assume the presence of new heavier states, however, the only way to produce DM is via its direct couplings to SM particles [123], i.e. by inverting the annihilation of DM that occurred in the early Universe (see Sec. 1.3). In this case, we only obtain an observable signal if additional SM particles are produced via SM interactions, for example a single jet from initial state radiation (ISR). Experimental searches for such monojet events have been performed at the Tevatron [124] as well as at the LHC by both CMS [125] and ATLAS [126]. Unfortunately, the SM backgrounds in these searches are large and the transverse momentum (p_{T}) spectrum of the signal — although slightly harder than the background — is essentially featureless.

Consequently, these search channels typically do not provide sufficient information to determine the mass of the DM particles. Nevertheless, the resulting bounds on the production cross section allow to directly constrain the couplings of DM particles to quarks, which also determine the DM scattering cross section in direct detection experiments [127–129]. Similar, although typically weaker, constraints can be obtained from other search channels, such as mono-photons [130], mono-leptons [131], mono-Z [132, 133] or mono-Higgs [134].

LHC searches for DM are complementary to the other search strategies described above in the sense that they are better suited to probe certain mass regions and types of DM interactions. In particular, collider searches do not suffer from a limitation for light DM, since in the low-mass region the monojet cross sections as well as the kinematic distributions become essentially independent of the DM mass. On the other hand, present collider searches cease to be constraining for DM particles with mass of a TeV or more simply because of kinematics, making direct and indirect searches the most promising detection strategies for these parameter regions. We will now discuss the comparison of different search strategies in more detail.

2.4 Comparing different searches using effective operators

Clearly, all of the search strategies described above are related in the sense that they probe the interactions between DM and SM particles, in particular quarks. Therefore, if a DM signal is observed in one experiment, it should be possible to predict the corresponding experimental signatures arising from related processes in other searches. Conversely, there should be a way of comparing the bounds on the DM interaction strength obtained from different search strategies. A

naive comparison, however, is complicated by the fact that different search strategies probe DM interactions at very different energies. In direct searches, DM particles are non-relativistic with $v/c \sim 10^{-3}$ and the typical momentum transfer is of the order of a few MeV. DM particles in the Galactic centre are equally non-relativistic, but the energy available in DM annihilation is twice the rest mass of the DM particle. At the LHC, on the other hand, DM particles may be produced with energies of up to several TeV.

This separation of scales implies that different experiments probe different aspects of the DM interactions [135]. For example, direct detection experiments cannot probe the coupling of DM particles to individual quarks, but only the coherent interaction with the entire nucleus, which can be enhanced or suppressed depending on how the contributions from individual quarks interfere. Moreover, interactions between DM particles and quarks can be such that they vanish in the non-relativistic limit, i.e. they are suppressed by powers of either v, q/m_χ or q/m_N (so-called momentum suppression). Similarly, annihilation cross sections may be suppressed by powers of the DM velocity if the conservation of angular momentum requires the annihilating DM particles to have non-zero angular momentum (i.e. if s-wave annihilation is forbidden).

To discuss a particularly striking example, let us consider the case where the DM particle is a Dirac fermion χ and the interactions between DM and quarks are mediated by a vector boson R. The most general (renormalisable) way to couple R to DM and quarks is then given by (see also Sec. 4.1)

$$\mathcal{L} = \sum_q \bar{q} \left(g_q^{\mathrm{V}} \gamma^\mu + g_q^{\mathrm{A}} \gamma^\mu \gamma^5 \right) q \, R_\mu + \bar{\chi} \left(g_\chi^{\mathrm{V}} \gamma^\mu + g_\chi^{\mathrm{A}} \gamma^\mu \gamma^5 \right) \chi \, R_\mu \, . \tag{2.11}$$

At the LHC it is impossible to distinguish whether R couples predominantly to the axial current ($g^{\mathrm{V}} \approx 0$) or to the vector current ($g^{\mathrm{A}} \approx 0$), since monojet cross sections are almost identical for the two cases. In direct detection, however, the two cases give vastly different predictions. If R couples to the vector current, one obtains SI scattering with

$$\sigma_N^{\mathrm{SI}} = f_N^2 \frac{\mu_{N\chi}^2}{\pi \, M_R^4} \, , \tag{2.12}$$

where N stands for either p or n, M_R is the mass of the vector mediator and the effective DM-nucleon couplings are given by $f_p = g_\chi^{\mathrm{V}}(2g_u^{\mathrm{V}} + g_d^{\mathrm{V}})$ and $f_n = g_\chi^{\mathrm{V}}(g_u^{\mathrm{V}} + 2g_d^{\mathrm{V}})$.

If, on the other hand, R couples to the axial current, one obtains SD interactions with

$$\sigma_N^{\rm SD} = a_N^2 \frac{3\,\mu_{N\chi}^2}{\pi\, M_R^4} \,. \tag{2.13}$$

The effective SD couplings are given by

$$a_{p,n} = g_\chi^{\rm A} \sum_{q=u,d,s} \Delta q^{(p,n)}\, g_q^{\rm A} \,, \tag{2.14}$$

where the coefficients $\Delta q^{(N)}$ encode the contributions of the light quarks to the nucleon spin, which can be extracted from polarised deep inelastic scattering. The Particle Data Group (PDG) values are [136]

$$\begin{aligned} \Delta u^{(p)} &= \Delta d^{(n)} = 0.84 \pm 0.03 \,, \\ \Delta d^{(p)} &= \Delta u^{(n)} = -0.43 \pm 0.03 \,, \\ \Delta s^{(p)} &= \Delta s^{(n)} = -0.09 \pm 0.03 \,. \end{aligned} \tag{2.15}$$

For SD interactions there is no coherent enhancement proportional to the square of the nucleus mass and typically not all isotopes of a given target element carry spin. Consequently, expected event rates are suppressed by several orders of magnitude compared to SI interactions with similar couplings.

Finally, if R has mixed couplings (e.g. $g_q^{\rm A} = 0$ and $g_\chi^{\rm V} = 0$), DM scattering is momentum suppressed and vanishes in the non-relativistic limit. Because of this suppression such interactions are very difficult to probe in direct detection experiments (see Sec. 5.2). Similarly, DM annihilation into quarks is unsuppressed for vector couplings, helicity suppressed (i.e. proportional to m_q^2) for axial couplings, and velocity suppressed (i.e. p-wave) for mixed couplings [137].

This simple example clearly demonstrates that we can only compare different searches once we have specified the Lorentz structure of the assumed DM-quark interactions. However, it is not necessary to also specify the details of the mediator of the interaction. Indeed, for sufficiently large mediator mass, we can integrate out the heavy mediator to obtain effective four-fermion interactions. The three examples discussed above then correspond to the vector operator

$$\mathcal{O}_{\rm V} \equiv \frac{1}{\Lambda_{\rm V}^2} \left(\bar{\chi}\gamma_\mu \chi\right) \left(\bar{q}\gamma^\mu q\right) \,, \tag{2.16}$$

the axialvector operator

$$\mathcal{O}_{\rm AX} \equiv \frac{1}{\Lambda^2_{\rm AX}} \left(\bar{\chi}\gamma_\mu\gamma_5\chi\right)\left(\bar{q}\gamma^\mu\gamma_5 q\right) \tag{2.17}$$

and the so-called anapole operator [138, 139]

$$\mathcal{O}_{\rm AN} \equiv \frac{1}{\Lambda^2_{\rm AN}} \left(\bar{\chi}\gamma_\mu\gamma_5\chi\right)\left(\bar{q}\gamma^\mu q\right) \ . \tag{2.18}$$

The suppression scale Λ is associated with the scale of new physics. In terms of the ultraviolet (UV) completion discussed above it is given by $\Lambda^2 = M_R^2/(g_q\, g_\chi)$.

If the mediator is sufficiently heavy ($m_R \gg 1$ TeV), the effective interactions introduced above remain valid even at LHC energies. Both monojet cross sections and direct detection cross sections will then be proportional to Λ^{-4}, so that we can directly translate bounds from one kind of search to the other. For the vector operator and light DM, for example, current LHC searches find $\Lambda \gtrsim 900$ GeV, corresponding to $\sigma_N \lesssim 10^{-39}$ cm^2 [125, 126]. This bound implies that LHC searches are superior to direct detection experiments for $m_\chi \lesssim 5$ GeV and inferior for heavier DM. A similar bound is found for the axialvector operator, which is stronger than the typical constraints on SD interactions from direct detection experiments over the entire DM mass range.

Nevertheless, there are reasons to be cautious when applying effective operators to LHC searches for DM. In particular, the UV completion should have perturbative couplings, meaning that $g_{q,\chi} \lesssim \sqrt{4\pi}$. Consequently, for $\Lambda = 900$ GeV, the mediator mass has to be smaller than about 3.2 TeV.[1] Once the centre-of-mass energy $\sqrt{s}$ becomes comparable to this scale, we can no longer rely on an effective operator description, because the mediator may be produced on-shell (see e.g. Refs. [140, 141]).

Similarly, effective operators run into problems with unitarity [142]. In order for all predicted probabilities to be smaller than unity, we must impose partial wave unitarity, which corresponds to the inequality

$$\left|\frac{1}{32\pi}\int\limits_{-1}^{1} \mathrm{d}(\cos\theta)\, \mathrm{P}_J(\cos\theta)\, \mathcal{M}(s,\cos\theta)\right| < 1 \tag{2.19}$$

for all J, where P_J is the Jth Legendre polynomial and $\mathcal{M}$ is the amplitude under consideration. For the vector operator and the process $q\bar{q} \to \chi\bar{\chi}$ we find $\mathcal{M} = 2\sqrt{3}\, s/\Lambda^2$, so the inequality above is

[1] In fact, one could even argue that for a perturbative UV completion the width of the mediator, Γ, should satisfy $\Gamma/M_R < 1$. This requirement would imply $g_q \lesssim 1$ and therefore $M_R \lesssim 1.7$ TeV.

violated for $\sqrt{s} > 1.9\,\text{TeV}$, implying that new physics must appear below this scale. The conclusion is that effective operators may not be valid at the LHC, because the mediator may be accessible for LHC energies. We will discuss this case in more detail in Chapter 4.

Nevertheless, bearing the caveats discussed above in mind, effective operators can be very valuable tools to study the qualitative behaviour of different types of DM interactions and to develop an intuition for the relevant effects in monojet searches and direct detection experiments. For these reasons, there is an extensive literature on the interpretation of DM searches using effective operators [60, 68, 125–130, 137–139, 143–156]. We now define all effective operators that will be studied in this thesis for future reference.

In analogy to the operators obtained by integrating out a vector mediator, we can study interactions that arise from the exchange of a heavy scalar or pseudoscalar state Φ that connects SM quarks to DM. If this mediator is a SM singlet, it can only couple to quarks via mixing with the Higgs. The induced quark couplings will then be proportional to the SM Yukawa couplings. Consequently, we write the scalar and pseudoscalar operators as

$$\mathcal{O}_{\text{S}} \equiv \frac{m_q}{\Lambda_{\text{S}}^3}\,\bar{q}q\,\bar{\chi}\chi\,, \qquad\qquad \mathcal{O}_{\text{P}} \equiv \frac{m_q}{\Lambda_{\text{P}}^3}\,\bar{q}\gamma^5 q\,\bar{\chi}\gamma^5\chi\,, \tag{2.20}$$

where the scale Λ is related to the fundamental couplings by $\Lambda^3 = v\,M_\Phi^2/(g_q g_\chi)$ with $v = 246\,\text{GeV}$ being the SM Higgs vacuum expectation value. Like the vector operator, the operator $\mathcal{O}_{\text{S}}$ leads to SI scattering in direct detection experiments and one obtains an expression analogous to Eq. (2.12). The calculation of the effective DM-nucleon couplings f_p and f_n is however more involved, since there is a non-vanishing contribution from sea quarks and gluons. The details of this calculation are presented in Appendix A.5. For the pseudoscalar operator, on the other hand, direct detection signals are both SD and momentum suppressed and hence unobservably small.

Further operators of interest are the tensor and pseudotensor operator [68]

$$\mathcal{O}_{\text{T}} \equiv \frac{1}{\Lambda_{\text{T}}^2}\,(\bar{\chi}\sigma_{\mu\nu}\chi)\,(\bar{q}\sigma^{\mu\nu}q)\,, \qquad\qquad \mathcal{O}_{\text{PT}} \equiv \frac{i}{\Lambda_{\text{PT}}^2}\,(\bar{\chi}\sigma_{\mu\nu}\gamma_5\chi)\,(\bar{q}\sigma^{\mu\nu}q)\,. \tag{2.21}$$

These operators do not typically arise from integrating out a heavy mediator. They can, however, be obtained (together with other effective four-fermion operators) from Fierz rearrangements of effective operators like $(\bar{\chi}q)(\bar{q}\chi)$ and $(\bar{\chi}\gamma_5 q)(\bar{q}\gamma_5\chi)$, which in turn result from integrating out a t-channel mediator (such as the heavy coloured particles present in models of top-flavoured minimal

flavour violating DM [157]). The operator $\mathcal{O}_{\rm T}$ induces SD interactions with

$$\sigma_N^{\rm SD} = a_N^2 \frac{12}{\pi} \frac{\mu_{N\chi}^2}{\Lambda_{\rm T}^4} \,, \tag{2.22}$$

which differs from the corresponding formula for the axialvector operator by a factor of 4 [144]. For $\mathcal{O}_{\rm PT}$ on the other hand the direct detection cross section is momentum-suppressed (see Sec. 5.2).

Finally, SI scattering can also result from the magnetic and electric dipole-type interactions [146, 147] encoded in

$$\mathcal{O}_{\rm M} \equiv \frac{1}{\Lambda_{\rm M}^2} \mathcal{C}_{\rm M} \left(\bar{\chi}\sigma_{\mu\nu}\chi\right) F^{\mu\nu} \,, \qquad \mathcal{O}_{\rm E} \equiv= \frac{i}{\Lambda_{\rm E}^2} \mathcal{C}_{\rm E} \left(\bar{\chi}\sigma_{\mu\nu}\gamma_5\chi\right) F^{\mu\nu} \,, \tag{2.23}$$

with $F^{\mu\nu}$ denoting the regular electromagnetic field strength tensor. The coefficient $\mathcal{C}_{\rm M}$ ($\mathcal{C}_{\rm E}$) carries the dimension of a mass and can be interpreted as the magnetic (electric) dipole moment of the DM particle in units of Λ^2. As we shall see in Sec. 5.2.1, the resulting cross sections for DM-nucleon scattering via photon exchange are *enhanced* for small momentum transfer, due to the propagator from the massless mediator, i.e. the photon.

Our discussion above has been limited to the case where the DM particle is a Dirac fermion. For the case of Majorana fermions the vector, tensor and pseudotensor operators vanish. The qualitative behaviour of the remaining operators is unchanged, but predicted cross sections will change by numerical factors of order unity. Wherever applicable, we will quote the final results for both cases. Operators analogous to the ones above can also be written down for a scalar DM particle ϕ. In the following, only two cases will be of interest, namely the scalar and vector operators

$$\mathcal{O}_{\rm S}^{\phi} \equiv \frac{m_q}{\Lambda_{\rm S}^2} \bar{q}q \, \phi^*\phi \,, \qquad \mathcal{O}_{\rm V}^{\phi} \equiv \frac{i}{\Lambda_{\rm V}^2} (\phi^* \, \partial^\mu \phi - \phi \, \partial^\mu \phi^*) \, (\bar{q}\gamma_\mu q) \,, \tag{2.24}$$

both of which lead to SI scattering.

To conclude this section, we point out that for our discussion here we have only considered tree-level processes. This treatment suggests that LHC searches involving $\not{E}_T$ provide the strongest constraints on $\mathcal{O}_{\rm T}$ and $\mathcal{O}_{\rm AX}$ and the *only* constraint on the operators $\mathcal{O}_{\rm PT}$ and $\mathcal{O}_{\rm AN}$. As we shall see in Chapter 5, this naive expectation is however not necessarily correct, because each of these operators induces one of the SI operators given above at the one-loop level.

CHAPTER 3

Astrophysical uncertainties & halo-independent methods

In this chapter we study the impact of the assumed DM velocity distribution $f(\boldsymbol{v})$ on the interpretation of results from direct detection experiments. Our poor knowledge of this quantity strongly affects the conclusions we can draw from the data, for example whether the results of different experiments are mutually consistent [76, 86, 88, 89, 158–164]. The standard approach of showing bounds on the DM scattering cross section as a function of the DM mass is not suitable for studying these uncertainties, because the exclusion bounds have to be reproduced separately for every velocity distribution under consideration.

One might wonder if the experimental data can itself be used to infer the DM velocity distribution. Unfortunately, this turns out to be rather difficult [165–167] because a nuclear recoil of energy E_{R} can originate from any DM particle which has a velocity larger than the minimum velocity $v_{\mathrm{min}}(E_{\mathrm{R}})$. Consequently, rather than probing the velocity distribution, direct detection experiments actually measure the velocity integral $g(v_{\mathrm{min}})$ defined in Eq. (2.7). Based on this observation it was suggested by Fox et al. [168] that results from one experiment be converted into v_{min}-space in order to predict the event rate in a second experiment without having to make any assumptions concerning astrophysics. While this approach works well in comparing two experiments that are sensitive to a similar range of DM velocities, it is difficult to compare a large number of experiments or experiments that probe different regions of v_{min}-space. It would therefore be preferable to have a framework in which the astrophysical unknowns are made explicit so that one can assess their impact on the extraction of DM properties.

In Sec. 3.1 we investigate in detail the idea, also suggested in Ref. [168], of mapping *all* experimental results into v_{min}-space. To do so, we must make an assumption on the mass of the DM

particles, so the approach is complementary to the usual analysis of direct detection experiments, where the astrophysical parameters are held fixed and the DM mass and cross section are allowed to vary. Just as the usual presentation of results shows whether all experiments are consistent for some range of DM mass and scattering cross section, our treatment will illustrate whether it is possible to find a DM velocity distribution that can reconcile all experimental results. We extend the existing framework to include annual modulation signals, as well as experiments with multiple target elements.

In Sec. 3.2 we illustrate this idea by focussing on the DM mass range (6–15) GeV motivated by claims of signals from DAMA, CoGeNT and CRESST-II (see Sec. 2.1.3), and show that $g(v_{\rm min})$ can indeed be chosen in such a way that a consistent description of these experiments is possible. However, upper limits on signals from XENON10/100 and CDMS-II *cannot* be evaded by appealing to astrophysical uncertainties alone. We explore this tension in more detail in Sec. 3.3 with a focus on the results from CDMS-Si and XENON10/100. While the amount of disagreement between these experiments is independent of astrophysical uncertainties, there are possible ways of ameliorating the tension by altering the properties of DM interactions.

Finally, in Sec. 3.4 we propose a new approach for determining DM parameters, which does not involve any assumptions about the structure of the DM halo. Given a DM model, our method yields the velocity distribution which best describes a set of direct detection data as a finite sum of streams with optimised speeds and densities. We give an explicit example in which the method is applied to determining the ratio of proton to neutron couplings of DM from a hypothetical set of future data.

3.1 Resolving astrophysical uncertainties

In this section we discuss how information on $\tilde{g}(v_{\rm min})$, defined in Eqs. (2.7) and (2.8), can be extracted from direct detection experiments.[1] First we consider experiments that observe a signal that can be interpreted in terms of DM scattering, such as CoGeNT and CRESST-II. In this case, the measured signal can be directly translated into a measurement of $\tilde{g}(v_{\rm min})$. Then there are experiments that do not observe a DM signal above their expected background and thus give a

[1] A similar discussion is presented in the appendix of Ref. [168].

constraint on the differential DM scattering rate, which can be converted into a bound on $\tilde{g}(v_{\min})$. Since $\tilde{g}(v_{\min})$ is time-dependent, the resulting limit strictly speaking applies to the *time average* of $\tilde{g}(v_{\min})$ over the period of data taking. The modulating part of $\tilde{g}(v_{\min})$ — and how to constrain it — will be discussed separately.

3.1.1 Measuring the velocity integral

It is straightforward to infer the value of $\tilde{g}(v_{\min})$ at $v_{\min}(E_{\mathrm{R}})$ from a nuclear recoil detector such as CoGeNT that consists of a single element and measures the differential event rate $\mathrm{d}R/\mathrm{d}E_{\mathrm{R}}$ at the recoil energy E_{R}. Inverting Eq. (2.9), we find

$$\tilde{g}(v_{\min}) = 2\,\mu_{n\chi}^2\,\frac{1}{C_{\mathrm{T}}^2(A,Z)\,F^2(E_{\mathrm{R}})}\,\frac{\mathrm{d}R}{\mathrm{d}E_{\mathrm{R}}}\,. \tag{3.1}$$

For a realistic treatment we must take the detector resolution ΔE and the detector acceptance $\epsilon(E_{\mathrm{R}})$ into account. If the detector measures the differential event rate in the interval $[E_1, E_2]$, we can infer the value of $\tilde{g}(v_{\min})$ for $v_{\min}$ in the interval $[v_{\min}(E_1 - \Delta E), v_{\min}(E_2 + \Delta E)]$:

$$\tilde{g}(v_{\min}) = 2\,\mu_{n\chi}^2\,\frac{1}{C_{\mathrm{T}}^2(A,Z)\,F^2(\hat{E}_{\mathrm{R}})\,\epsilon(\hat{E}_{\mathrm{R}})}\,\frac{\mathrm{d}R}{\mathrm{d}E_{\mathrm{R}}}\,. \tag{3.2}$$

The recoil energy $\hat{E}_{\mathrm{R}}$, where the nuclear form factor and the acceptance are evaluated, should lie in the range $E_1 < \hat{E}_{\mathrm{R}} < E_2$. We assume that the energy bin is sufficiently small that these quantities do not vary significantly with $\hat{E}_{\mathrm{R}}$ over the bin range.[1] For rapidly varying form factors or efficiencies, a somewhat different approach is needed [169].

Additional care is required for experiments like DAMA and CRESST-II, which have targets with more than one element. The target of the DAMA detector comprises sodium and iodine nuclei, the latter being much heavier than the former ($m_{\mathrm{I}} \approx 5.5\,m_{\mathrm{Na}}$). If we focus on light DM, however, the possible momentum transfer is so small that the kinetic energy of the recoiling iodine nucleus is always below the energy threshold of the detector. Consequently, it is a good approximation to assume that all contributions to $\mathrm{d}R/\mathrm{d}E_{\mathrm{R}}$ come from scattering on sodium, and use Eq. (3.2) taking the mass fraction of sodium in the detector into account (see Sec. 3.1.3).

For CRESST-II, which contains oxygen, calcium and tungsten, the situation is more complicated.

[1] This assumption is good for CoGeNT and light DM. However it is not necessarily a good approximation for CRESST-II where $\epsilon(E_{\mathrm{R}})$ can change rapidly within a single bin if it contains the onset of a new detector module. This problem can however be avoided by an appropriate binning of the data (see Appendix A.2).

Since tungsten is much heavier than oxygen and calcium, we can again ignore it. Oxygen and calcium however are relatively close in mass, so extracting information on $\tilde{g}(v_{\rm min})$ becomes more complicated. We discuss these difficulties — and how to deal with them — in Appendix A.4.

3.1.2 Constraining the velocity integral

Next we consider experiments that do not measure the differential event rate but rather place a bound on $\mathrm{d}R/\mathrm{d}E_{\rm R}$ over some energy range. This is usually converted into a constraint on σ_n for a given DM mass, assuming a Galactic halo model such as the SHM. Instead we wish to use the bound on $\mathrm{d}R/\mathrm{d}E_{\rm R}$ to constrain $\tilde{g}(v_{\rm min})$ for different values of $v_{\rm min}$.[1]

Since $f(v) \geq 0$, the following inequality holds for any value of $v_{\rm min}$:

$$\tilde{g}(v_{\rm min}) \geq \tilde{g}(\hat{v}_{\rm min})\, \Theta(\hat{v}_{\rm min} - v_{\rm min})\,, \tag{3.3}$$

where $\hat{v}_{\rm min}$ is an arbitrary constant and $\Theta(x)$ is the Heaviside step function. Of all velocity integrals that have $\tilde{g}(\hat{v}_{\rm min}) = \tilde{g}_0$, the one defined by $\tilde{g}(v_{\rm min}) = \tilde{g}_0\, \Theta(\hat{v}_{\rm min} - v_{\rm min})$ thus predicts the smallest number of events in any given experiment. Of course $g(v_{\rm min}) \propto \Theta(\hat{v}_{\rm min} - v_{\rm min})$ is not a realistic model for the Galactic halo, but it nevertheless is a valid velocity integral that can be used to predict the event rate for a given experiment. A more realistic halo must satisfy Eq. (3.3) and will therefore necessarily predict a *larger* event rate. Consequently, if we can reject the case when $\tilde{g}(v_{\rm min}) = \tilde{g}_0\, \Theta(\hat{v}_{\rm min} - v_{\rm min})$, we can also reject any other halo model with $\tilde{g}(\hat{v}_{\rm min}) = \tilde{g}_0$.

If an experiment places an upper bound on $\mathrm{d}R/\mathrm{d}E_{\rm R}$, we can hence bound $\tilde{g}(v_{\rm min})$ by fixing $v_{\rm min} = \hat{v}_{\rm min}$ and finding the smallest value of $\tilde{g}(\hat{v}_{\rm min})$ such that the predicted event rate for $\tilde{g}(v_{\rm min}) = \tilde{g}(\hat{v}_{\rm min})\, \Theta(\hat{v}_{\rm min} - v_{\rm min})$ *exceeds* the allowed value at a given confidence level (CL). Repeating this procedure for all $\hat{v}_{\rm min}$, we obtain a continuous upper bound on $\tilde{g}(\hat{v}_{\rm min})$, as illustrated in Fig. 3.1. If the exclusion curve thus obtained touches (or crosses) the $\tilde{g}(v_{\rm min})$ curve for a particular $f(v)$, this model will be excluded by the experimental data at the same CL used to construct the exclusion bound. In other words, if the bound on $\tilde{g}(v_{\rm min})$ lies below (some of) the values of $\tilde{g}(v_{\rm min})$ implied by the measured recoil spectra from CoGeNT or CRESST-II, it will not be possible to find a halo model that consistently describes all measurements and evades all experimental bounds.

[1] Again, difficulties arising for experiments with more than one type of target nuclei are discussed in Appendix A.4.

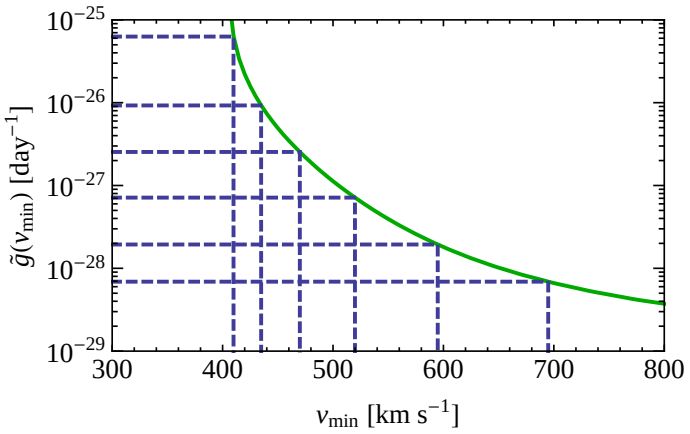

FIG. 3.1. An illustration of the method used to constrain the rescaled velocity integral. The blue dashed lines correspond to velocity integrals of the form $\tilde{g}_0\,\Theta(\hat{v}_{\rm min} - v_{\rm min})$ for different choices of $\tilde{g}_0$ and $\hat{v}_{\rm min}$. The predicted event rate in the XENON100 detector for each of these velocity integrals can be rejected by the data from XENON100. The green line shows the resulting bound on $\tilde{g}(v_{\rm min})$.

Note that the converse of this statement is not necessarily true: even if $\tilde{g}(v_{\rm min})$ stays below a given exclusion curve for all values of $v_{\rm min}$, this does not imply that the model is *not* excluded by the corresponding experiment. By construction, we have only ensured that the predicted differential event rate in each individual energy bin is below the respective experimental limit. However, if the measured velocity integral remains close to the exclusion limit over a wide range of $v_{\rm min}$, the predicted total event rate, i.e. the integral of the differential event rate over several bins, may be excluded at the chosen CL.

3.1.3 Measuring the modulation amplitude

We now turn to the annual modulation of DM signals due to the motion of the Earth relative to the Galactic rest frame. We wish to include these annual modulations into our analysis of the velocity integral to determine whether the modulation signals observed by DAMA and CoGeNT are compatible with the null results from other experiments.[1] We first discuss how constraints can be obtained without making any assumptions about the modulation fraction and then discuss how the modulation fraction can be constrained in order to obtain stronger experimental bounds.

[1] It is already known [102] that the two modulation signals are (marginally) compatible with each other, independent of astrophysics.

The time dependence of $g(v_{\rm min}, t)$ can be approximately parameterised as

$$g(v_{\rm min}, t) = g(v_{\rm min}) \left[1 + A(v_{\rm min}) \cdot \cos\left(2\pi \frac{t - t_0(v_{\rm min})}{1\ \text{yr}}\right)\right] \ , \tag{3.4}$$

where $g(v_{\rm min})$ is the time average of $g(v_{\rm min}, t)$. Note that, as emphasised in Ref. [76], *both* the modulation fraction A and the peak date t_0 can in general depend on $v_{\rm min}$. For future use we define the modulation amplitude $\Delta g(v_{\rm min})$ as

$$\Delta g(v_{\rm min}) \equiv \frac{1}{2}\left[g(v_{\rm min}, t_0(v_{\rm min})) - g(v_{\rm min}, t_0(v_{\rm min}) + 0.5\ \text{yr})\right] = A(v_{\rm min})\, g(v_{\rm min}) \tag{3.5}$$

and introduce the rescaled modulation amplitude $\Delta\tilde{g}(v_{\rm min}) = \Delta g(v_{\rm min})\, \sigma_n\, \rho/m_\chi$ in analogy to Eq. (2.8).

First we need to constrain the function $t_0(v_{\rm min})$. CoGeNT and DAMA probe largely the same region of $v_{\rm min}$-space, so it would be inconsistent to assume different phases for the two experiments. It was shown [102] that the phase measured by DAMA and by CoGeNT are consistent at the 90% CL for sufficiently low DM mass. We will therefore take $t_0(v_{\rm min}) = 146$ days which is the best-fit value from DAMA. Varying t_0 within the 1σ region allowed by DAMA changes the best-fit value for the CoGeNT modulation amplitude by about 20%, which does not significantly affect any of our conclusions.

In complete analogy to Sec. 3.1.1 we can infer measurements of $\Delta\tilde{g}(v_{\rm min})$ from the modulation of the event rate, $\Delta \mathrm{d}R/\mathrm{d}E_{\rm R}$, seen by DAMA and CoGeNT

$$\Delta\tilde{g}(v_{\rm min}) = 2\,\mu_{n\chi}^2 \frac{1}{C_{\rm T}^2(A,Z)\, F^2(E_{\rm R})} \Delta\frac{\mathrm{d}R}{\mathrm{d}E_{\rm R}} \ . \tag{3.6}$$

As the modulation fraction must satisfy $A(v_{\rm min}) \leq 1$, we see from Eq. (3.5) that $\Delta\tilde{g}(v_{\rm min}) \leq \tilde{g}(v_{\rm min})$. We can therefore trivially obtain a bound on $\Delta\tilde{g}(v_{\rm min})$ from the constraints for $\tilde{g}(v_{\rm min})$ obtained using the method introduced above. We can then compare the values for $\Delta\tilde{g}(v_{\rm min})$ obtained from DAMA and CoGeNT with the bounds on $\Delta\tilde{g}(v_{\rm min})$ obtained from null results.

3.1.4 Constraining the modulation fraction

We will now discuss what can reasonably be assumed about the modulation fraction $A(v_{\rm min})$ given known models of the Galactic halo, and how it can be constrained once the velocity integral is measured. The predicted modulation fractions for various halo models are shown in the left panel of

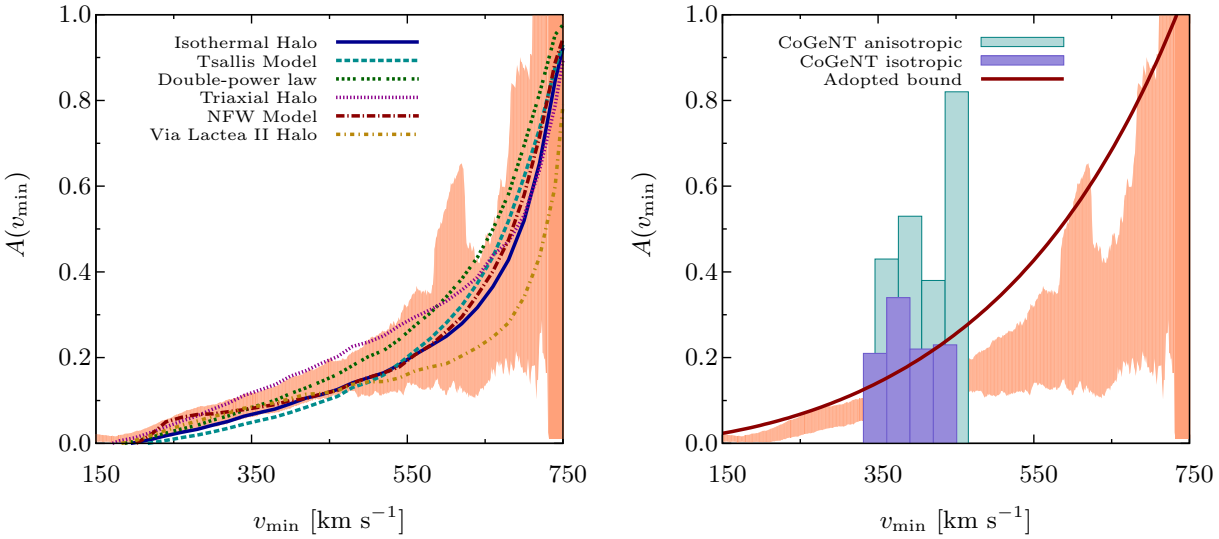

FIG. 3.2. Left: The modulation fraction $A(v_{\rm min})$ for different descriptions of the Galactic DM halo. Right: The constraint for the modulation fraction extracted from the CoGeNT data (boxes) together with the bound that we will adopt (red solid line). The shaded region in both panels corresponds to the modulation fractions observed in the GHALO$_{\rm s}$ simulation [76].

Fig. 3.2. We observe that $A(v_{\rm min})$ is almost everywhere significantly smaller than 100%. Indeed, a modulation fraction of 100% would imply that no signal is observed at $t_0 + 0.5$ yr, which is possible only if $v_{\rm min} > v_{\rm esc} + v_{\rm E}(t_0 + 0.5\ {\rm yr})$.

It therefore appears sensible to analyse experimental data not only using the trivial requirement $A(v_{\rm min}) \leq 1$, but to impose a stronger constraint on the modulation fraction. If we require that the modulation fraction satisfies $A(v_{\rm min}) \leq A^{\rm max}(v_{\rm min})$, any direct detection experiment that constrains $\tilde{g}(v_{\rm min}) \leq \tilde{g}^{\rm max}(v_{\rm min})$ will also constrain $\Delta\tilde{g}(v_{\rm min})$ according to

$$\Delta\tilde{g}(v_{\rm min}) = A(v_{\rm min})\,\tilde{g}(v_{\rm min}) \leq A^{\rm max}(v_{\rm min})\,\tilde{g}^{\rm max}(v_{\rm min})\ . \tag{3.7}$$

The empirical bound that we will adopt is shown as the red line in the right panel of Fig. 3.2. Note that this is a weak bound in the sense that we allow modulation fractions much larger than the value expected in any reasonable description of the DM halo.

Of course it would be desirable to actually use measurements of $\tilde{g}(v_{\rm min})$ to place a bound on $A(v_{\rm min})$ rather than having to make an ad-hoc assumption. Comparing the left panel of Fig. 3.2 to the right panel of Fig. 2.2, we observe that there is indeed a direct correspondence between the velocity integral and the modulation fraction: the steeper the slope of the velocity integral, the larger

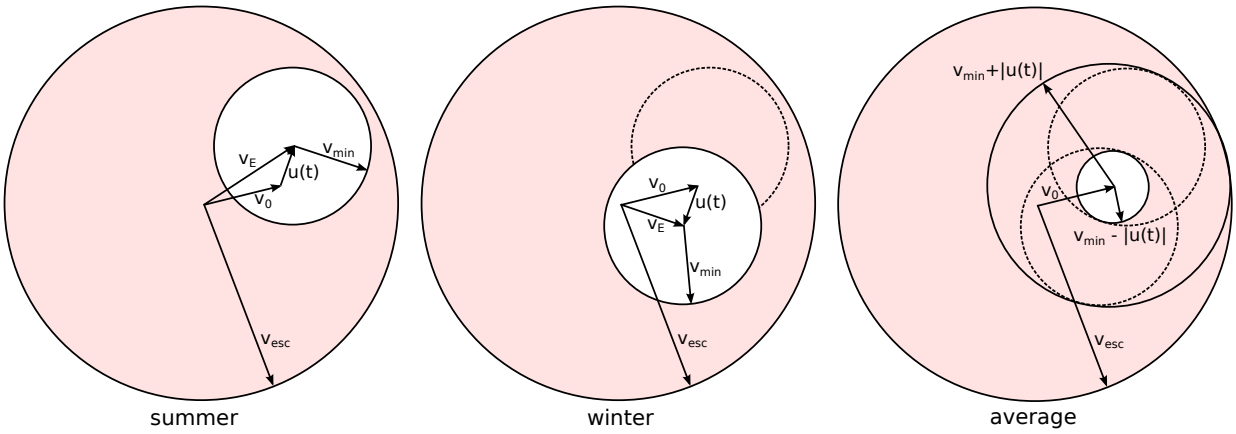

FIG. 3.3. A graphical representation of the velocity integral. The red shaded region is the region of velocity space that is being integrated over, while the white regions are excluded by the requirement $v > v_{\min}$. Note that the relative magnitude of the different velocities are not drawn to scale.

the modulation fraction. This result is intuitively clear: If $g(v_{\min})$ falls steeply with increasing $v_{\min}$ we can also expect large changes between the rates observed in summer and winter. This observation can in fact be used to constrain the modulation fraction once the velocity integral is known. The basic idea is that we can place an upper bound on the maximum value, $\tilde{g}(v_{\min}, \text{summer})$, and a lower bound on the minimum value, $\tilde{g}(v_{\min}, \text{winter})$, using only the time average $\tilde{g}(v_{\min})$.

How such bounds can be obtained is sketched in Fig. 3.3. We observe that

$$\tilde{g}(v_{\min}, \text{summer}) < \tilde{g}(v_{\min} - u) \,, \quad \tilde{g}(v_{\min}, \text{winter}) > \tilde{g}(v_{\min} + u) \,, \tag{3.8}$$

where $u = 29.8\,\mathrm{km\,s^{-1}}$ is the velocity of the Earth around the Sun. It then follows that

$$\Delta\tilde{g}(v_{\min}) = \tilde{g}(v_{\min}, \text{summer}) - \tilde{g}(v_{\min}, \text{winter}) < \tilde{g}(v_{\min} - u) - \tilde{g}(v_{\min} + u) \tag{3.9}$$

and therefore that the modulation fraction is bounded by

$$A(v_{\min}) = \frac{\tilde{g}(v_{\min}, \text{summer}) - \tilde{g}(v_{\min}, \text{winter})}{\tilde{g}(v_{\min}, \text{summer}) + \tilde{g}(v_{\min}, \text{winter})} < \frac{\tilde{g}(v_{\min} - u) - \tilde{g}(v_{\min} + u)}{2\,\tilde{g}(v_{\min})} \,, \tag{3.10}$$

where we have used $\tilde{g}(v_{\min}, \text{summer}) + \tilde{g}(v_{\min}, \text{winter}) \approx 2\,\tilde{g}(v_{\min})$.

An even stronger constraint can be obtained under the assumption of an isotropic DM halo. In this case, only the seasonal change in the *radial* component of $\boldsymbol{u}$, u_r, matters, because the halo will look the same for any value of u_ϕ and u_θ. We can then replace u in the equation above by

$u_r = u \cos\gamma = 15.0\,\mathrm{km\,s^{-1}}$, where γ is the inclination angle between the Galactic and Ecliptic plane.

As an example, we use the CoGeNT data to derive a bound on the modulation fraction for a given DM mass. For this purpose, we need to bin the measured events in such a way that the resulting bin width in v_{min}-space is equal to u (see Appendix A.2). The resulting constraints for $m_\chi = 9\,\mathrm{GeV}$ are shown in the right panel of Fig. 3.2. We observe that assuming an isotropic halo, these constraints are actually quite severe, limiting the modulation fraction to 20% at $v_{\mathrm{min}} = 400\,\mathrm{km\,s^{-1}}$, which in fact coincides with our adopted bound for $A(v_{\mathrm{min}})$. For an anisotropic halo, modulation fractions of up to 40% may be possible in the same range.

This observation is also relevant for a self-consistent DM interpretation of the CoGeNT experiment. To bring the modulation observed by CoGeNT into agreement with the measured event rate, a relatively large modulation fraction is required [99]. If a significant part of the signal observed in CoGeNT were to be rejected as surface events, as suggested in Refs. [90, 170], the required modulation fractions would be even larger. In this case, the constraint on the modulation fraction derived above can be used to conclude that a consistent description is only possible if the DM halo is highly anisotropic.

3.2 Halo-independent methods: Results

We now apply the methods developed in the previous section to analyse recent results from direct detection experiments (see Appendix A.2 for details). First of all, we use the event rates reported by CoGeNT and CRESST-II to measure $\tilde{g}(v_{\mathrm{min}})$ and the null results from XENON, CDMS-II, SIMPLE and the CRESST-II commissioning run to constrain it. Our results are shown in Fig. 3.4 for various values of the DM mass m_χ. As we increase m_χ the exclusion curves as well as the CoGeNT data points move according to $v_{\mathrm{min}} \propto 1/m_\chi$ (which holds when $m_\chi \ll m_{\mathrm{N}}$). The CRESST-II data points and exclusion curves scale differently because in the lower panels m_χ becomes comparable to the mass of oxygen nuclei.

For all DM masses considered, one can see the obvious conflict between the measurements by CoGeNT and CRESST-II and the exclusion bounds from other experiments. In each case, most of the measured points lie above one or more of the exclusion curves. We conclude that a consistent description of all experiments is not possible for *any* model of the DM halo if the DM particles

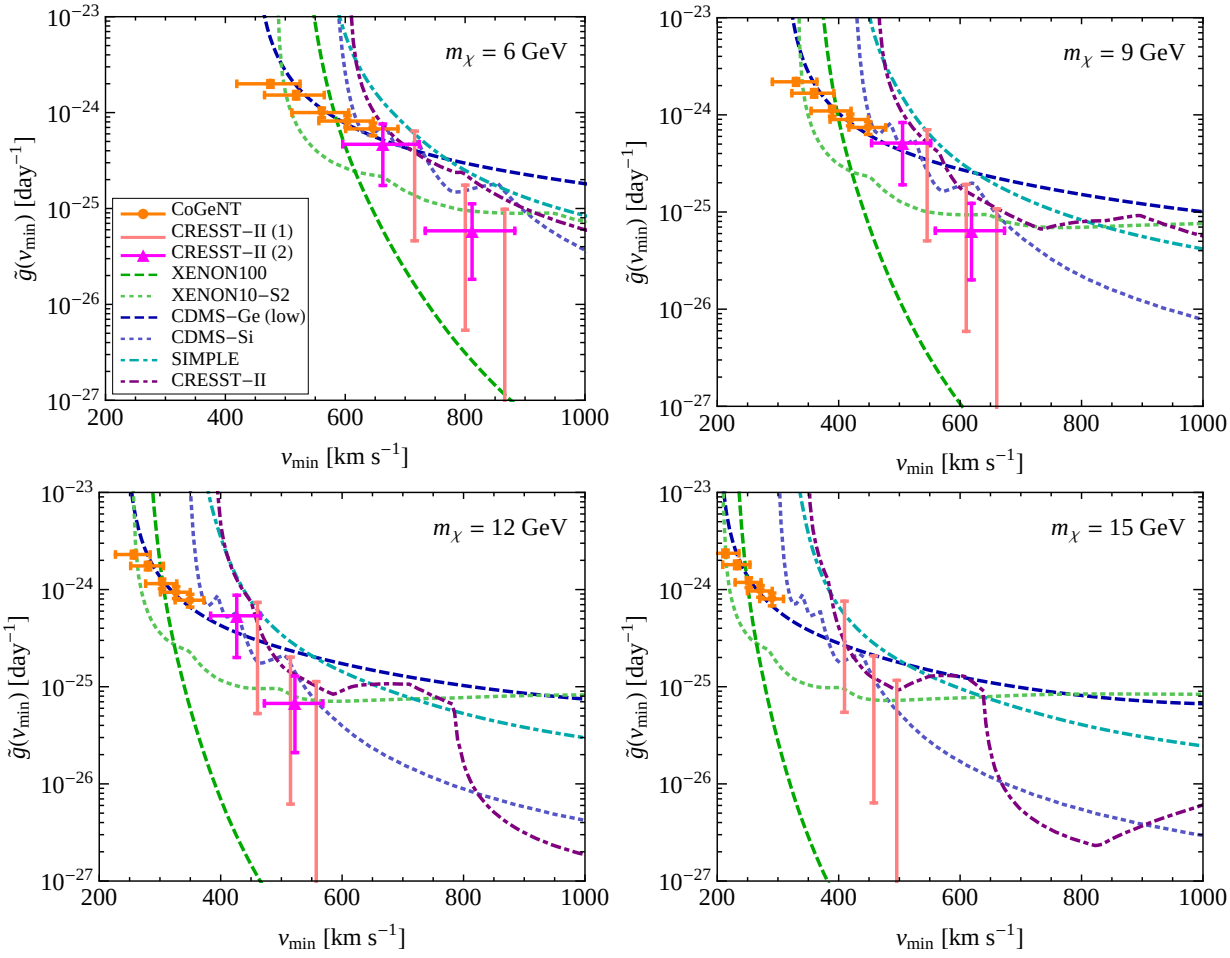

FIG. 3.4. Measurements and exclusion bounds of the velocity integral $\tilde{g}(v_{\rm min})$ for different DM masses m_χ. Values of $\tilde{g}(v_{\rm min})$ above the lines are excluded with at least 90% confidence. For $m_\chi = 6$, 9 and 12 GeV the data points for CRESST-II have been obtained using two different methods, as described in Appendix A.4. It is not possible to find any model for the DM halo that provides a consistent description of all experiments.

undergo elastic SI scattering with $f_n/f_p = 1$. There is no functional form for $\tilde{g}(v_{\rm min})$ that would allow a DM interpretation of the CoGeNT or CRESST-II data that is consistent with all other experiments.

3.2.1 A consistent description of CoGeNT and CRESST-II

Even though we cannot find a halo model that provides a consistent description of *all* experiments, it can be seen in Fig. 3.4 that CRESST-II and CoGeNT probe $\tilde{g}(v_{\rm min})$ at different ranges of $v_{\rm min}$. Therefore it should be possible to choose $\tilde{g}(v_{\rm min})$ such that we obtain a consistent description for these two experiments. This choice must be different from the SHM for which the best-fit DM

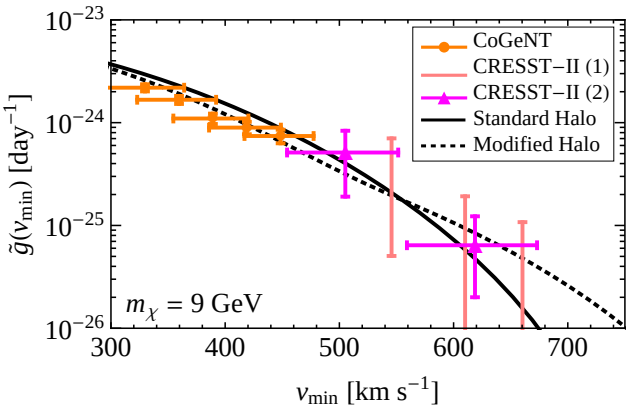

FIG. 3.5. Measurements of the rescaled velocity integral $\tilde{g}(v_{\rm min})$ compared to the predictions of the SHM and the Modified Halo Model assuming $\sigma_n = 10^{-40}\,\mathrm{cm}^2$ and $\rho = 0.3\,\mathrm{GeV\,cm}^{-3}$. The Modified Halo Model provides a consistent description of the data from CoGeNT and CRESST-II for a DM particle with $m_\chi = 9\,\mathrm{GeV}$.

regions of CRESST-II and CoGeNT do *not* overlap, because CRESST-II favours larger DM masses than CoGeNT [91, 104].

To understand the origin of this discrepancy, we show the SHM prediction for $\tilde{g}(v_{\rm min})$ in Fig. 3.5 together with the measurements from CoGeNT and CRESST-II for $m_\chi = 9\,\mathrm{GeV}$. We observe that the SHM prediction of the rescaled velocity integral below $500\,\mathrm{km\,s}^{-1}$ is slightly too flat to fit the CoGeNT data, which therefore favours smaller DM masses. Moreover there is an additional constraint (which is not apparent in Fig. 3.5) from the fact that CoGeNT does not observe a signal at higher energies. This constraint additionally disfavours the case $m_\chi \geq 9\,\mathrm{GeV}$ if the rescaled velocity integral is too flat. Consequently, if we want to push the CoGeNT region to larger DM mass, we need to make the rescaled velocity integral steeper below $500\,\mathrm{km\,s}^{-1}$. As a result our new velocity integral will predict fewer events from oxygen in the lowest bins of CRESST-II because $\tilde{g}(v_{\rm min})$ becomes smaller around $500\,\mathrm{km\,s}^{-1}$. To compensate, we must increase the contribution from calcium in the lowest bins, corresponding to larger values of $\tilde{g}(v_{\rm min})$ around $600\,\mathrm{km\,s}^{-1}$ (see also the discussion in Appendix A.4).

We can easily achieve this goal by adding two SHM-like contributions, one with relatively small velocity dispersion and low cut-off which dominates at low values of $v_{\rm min}$, and a second one with much larger v_0 and $v_{\rm esc}$. Of course, the resulting velocity distribution is *not* a self-consistent model of the DM halo; it is only a convenient parameterisation to illustrate how the velocity integral can be changed to simultaneously accommodate several direct detection experiments. Nevertheless, it

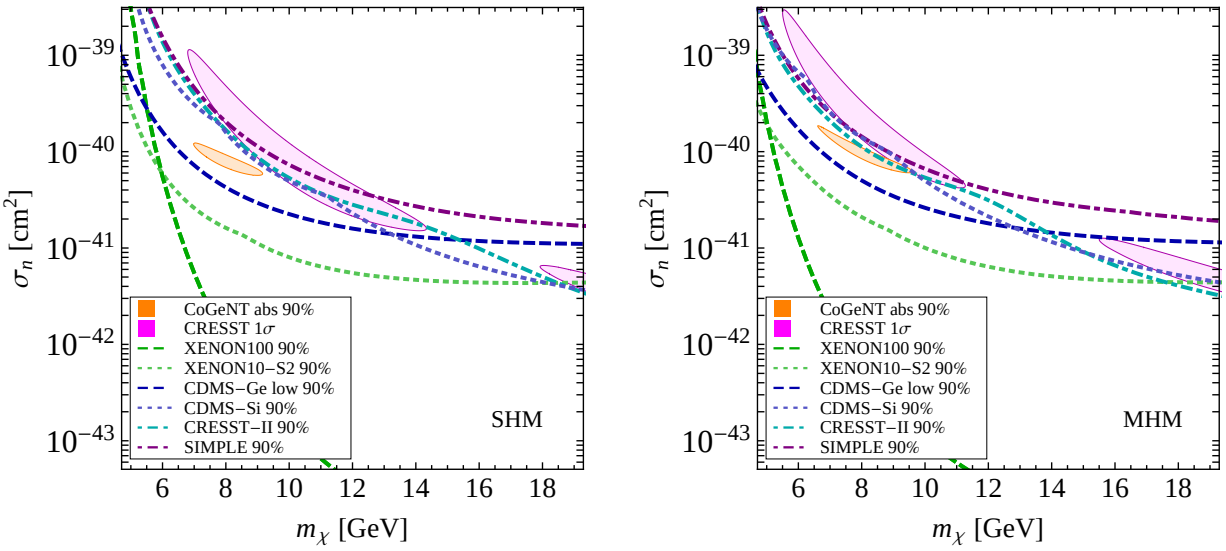

FIG. 3.6. 90% confidence regions inferred from the absolute rate observed by CoGeNT and 1σ regions from CRESST-II as well as the 90% exclusion limits from other experiments for the SHM (left) and the Modified Halo Model (right). By construction, the Modified Halo Model leads to an overlap of the CoGeNT and CRESST-II regions.

is not inconceivable that such a velocity integral can be realised in models with a strong anisotropy, where the tangential component with low velocity dispersion dominates at low energies and the radial component with high dispersion dominates at high energies. We shall refer to this new velocity integral as the Modified Halo Model (or MHM for short).

We show the corresponding best-fit regions and exclusion limits in the m_χ-σ_n plane in Fig. 3.6. As desired, the CoGeNT and CRESST-II[1] regions now overlap at $m_\chi \sim 9$ GeV. The common parameter region is, nevertheless, clearly excluded by XENON10/100 and CDMS-II, an observation which we have already made from Fig. 3.4.

3.2.2 A consistent description of DAMA, CoGeNT and CRESST-II

Now we include annual modulations in our halo-independent analysis. The values of $\Delta\tilde{g}(v_{\rm min})$ inferred from CoGeNT and DAMA are shown in Fig. 3.7 together with constraints from experimental null results. For the upper panels, *no* assumptions on the modulation fraction have been made,

[1]Note that for CRESST-II we show the 1σ best-fit region using the publicly available data as stated in Appendix A.2. The region we obtain corresponds roughly to the 2σ region published by the CRESST collaboration [91].

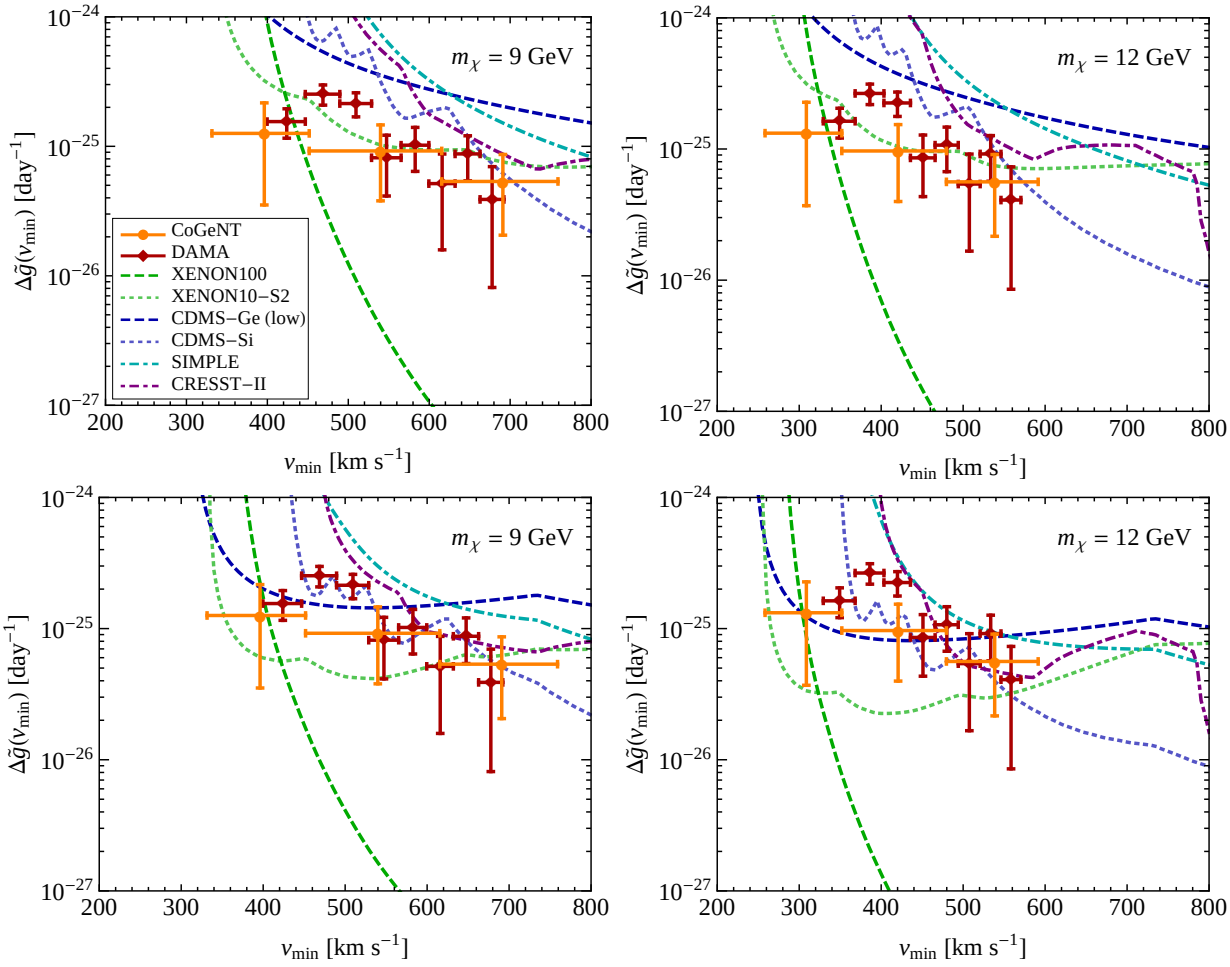

FIG. 3.7. Measured values of $\Delta\tilde{g}(v_{\rm min})$ from DAMA and CoGeNT compared to the exclusion limits from other experiments. For the upper panels, *no* assumptions on the modulation fraction have been made, for the lower panels, we assume that the modulation fraction is bounded by the red line in the right panel of Fig. 3.2. Even for such weak assumptions on the modulation fraction there is significant tension between the different experiments, most notably it is impossible to find a DM velocity distribution that describes the observed modulations and evades the bound from XENON100.

for the lower panels, we assume that the modulation fraction is bounded by the red line in the right panel of Fig. 3.2. We observe that even in the most conservative case the bounds from the XENON10 and XENON100 experiments remain strong. Other experiments, however, do not significantly constrain $\Delta\tilde{g}(v_{\rm min})$. Once we include our (rather weak) assumption on the modulation fraction, the bounds on $\Delta\tilde{g}(v_{\rm min})$ become significantly more constraining. Decreasing the mass of the DM particle can reduce this tension considerably because at high values of $v_{\rm min}$ larger modulation fractions are allowed so the exclusion limits become less stringent. On the other hand,

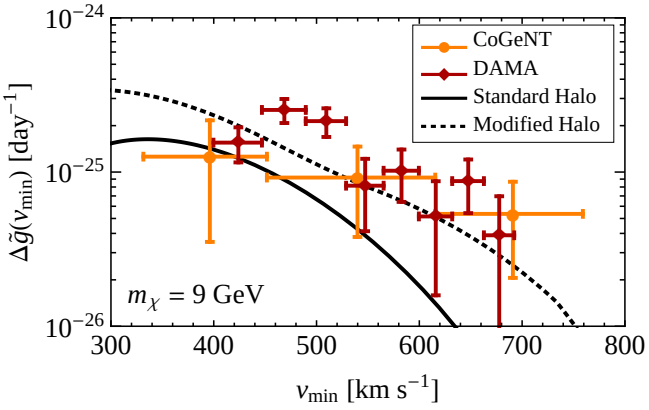

FIG. 3.8. Measurements of the modulation amplitude $\Delta\tilde{g}(v_{\rm min})$ compared to the predictions of the SHM and the Modified Halo Model. In both cases, we have assumed $\sigma_n = 10^{-40}\,\mathrm{cm}^2$ and $\rho = 0.3\,\mathrm{GeV\,cm}^{-3}$. While in the SHM the predicted modulation amplitude for these parameters is too small to explain the observed modulations, we can get a sufficiently large modulation amplitude in the Modified Halo Model.

for small masses it becomes increasingly difficult to explain the modulation observed by CoGeNT above 2 keVee because these recoil energies correspond to very large velocities, where we expect $\tilde{g}(v_{\rm min})$ — and therefore $\Delta\tilde{g}(v_{\rm min})$ — to be small.

As can be seen from Fig. 3.7, DAMA and CoGeNT probe the same region of $v_{\rm min}$-space, so it is not possible to improve their agreement by changing the halo model as we did for CoGeNT and CRESST-II. Fortunately, such a modification is not necessary because DAMA and CoGeNT favour roughly the same modulation amplitude. The more interesting question is whether this modulation amplitude is compatible with the average value of $\tilde{g}(v_{\rm min})$ inferred from CRESST-II and the CoGeNT unmodulated event rate.

For a cross section of $\sigma_n \approx 10^{-40}\,\mathrm{cm}^2$, as favoured by the combination of CoGeNT and CRESST-II (see Fig. 3.6) the SHM prediction of the modulation amplitude is too small to account for the modulation seen by DAMA and CoGeNT [69, 99–102]. This is obvious from plotting the SHM prediction for $\Delta\tilde{g}(v_{\rm min})$ together with the measured modulation amplitudes (see Fig. 3.8). However, we have already noted in Sec. 3.2.1 that the velocity integral must be modified if we want to simultaneously explain CoGeNT and CRESST-II. Now we consider whether we can bring these experiments into agreement with DAMA (and therefore also with the CoGeNT modulation) by additionally allowing a larger modulation fraction. Of course, for a given velocity integral the modulation fraction must satisfy Eq. (3.10), so we cannot choose arbitrarily large values.

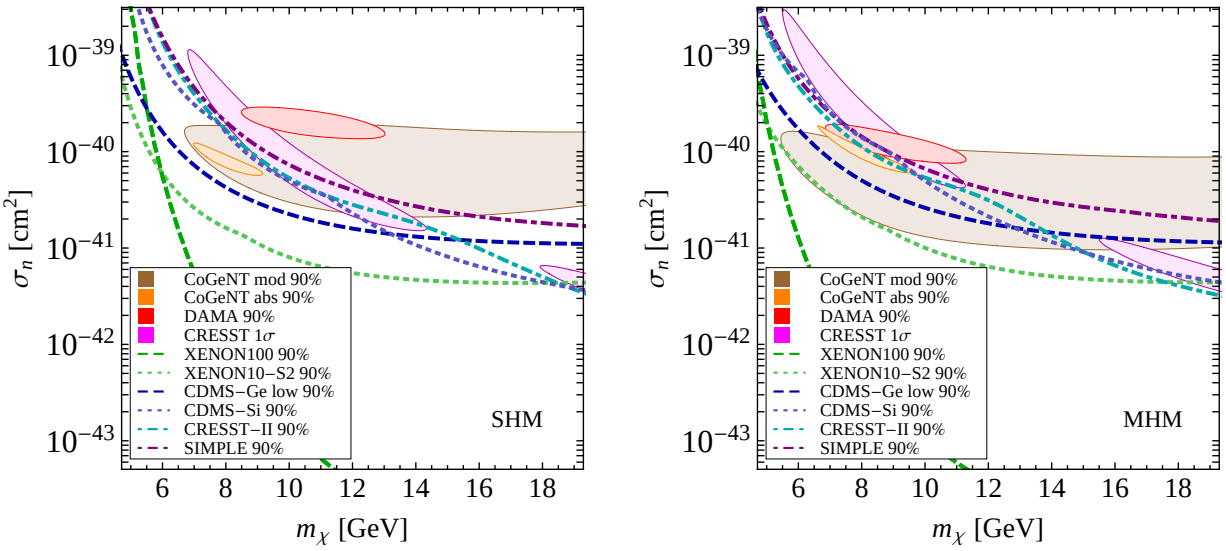

FIG. 3.9. 90% confidence regions from CoGeNT (inferred separately from the modulation and the absolute rate) and DAMA as well as the 1σ region from CRESST-II for the SHM (left) and the Modified Halo Model (right). The 90% exclusion limits from other experiments are also shown. By construction, the Modified Halo Model brings the four best-fit regions into good agreement.

To explore one possible option, we assume that $g(v_{\rm min})$ is given by the Modified Halo Model (see Fig. 3.5) and that the modulation fraction saturates the bound $A^{\rm max}(v_{\rm min})$ shown in Fig. 3.2. By the reasoning in Sec. 3.1.4 these two assumptions are compatible *only* if the DM halo is highly anisotropic. As can be seen in Fig. 3.8, we then obtain a sufficiently large modulation amplitude to describe the DAMA and CoGeNT modulations. Consequently, the four best-fit regions in the traditional σ_n-m_χ parameter plane are now in good agreement (Fig. 3.9). However these are of course excluded by XENON10/100 and CDMS-II. Because of this obvious contradiction we wish to emphasise again that we do not consider present data sufficient to actually determine the velocity integral or the modulation amplitude. We use it only to illustrate how our method can be applied to bring future, more reliable, data sets into agreement.

For the entire analysis above, we have assumed standard interactions between DM and nuclei, i.e. we have performed all calculations only for elastic SI scattering with equal couplings to protons and neutrons. Nevertheless, there are many well-motivated models where DM couples to quarks in a more complicated way (some possible options will be discussed in Chapters 4 and 5). It is therefore an interesting question to study whether the halo-independent tension between the

different experiments can be alleviated by modifying the assumed particle physics properties of DM [103, 104, 171–173]. We will now study this question in the context of the tension between experimental results from XENON10/100 and CDMS-Si.

3.3 CDMS versus XENON

In this section, we will discuss the tension between the exclusion bounds obtained from XENON10 and XENON100 and the best-fit parameter region from CDMS-Si. We provide the details of our analysis in Appendix A.2 and present our results in Fig. 3.10. For the analysis of CDMS-Si we use the extended maximum likelihood method [174], which is described in detail in Appendix A.3. The contours we show correspond to 68% and 90% CL — these agree well with the ones shown by the CDMS-II collaboration [92]. In excellent agreement with their analysis, we find that the best-fit point is $m_\chi = 8.55\,\text{GeV}$ with $\sigma_n = 2 \times 10^{-41}\,\text{cm}^2$. Assuming that the log-likelihood follows a χ^2-distribution, we determine the p-value of the background-only hypothesis to be 0.38%.[1]

For XENON10, we consider the S2-only analysis [98]. The sensitivity of this analysis depends strongly on the behaviour of the ionisation yield $\mathcal{Q}_\text{y}$ at low energies [84, 85]. To calculate the central bound (thick dashed blue line) in Fig. 3.10 we adopt the original choice of $\mathcal{Q}_\text{y}$ made in Ref. [98], assuming that $\mathcal{Q}_\text{y}$ vanishes for $E_\text{R} < 1.4\,\text{keV}$, and use the 'maximum gap method' [175] to set a bound. We have checked that the 'p_max method' [175] and the 'binned Poisson method' [74, 176] give comparable bounds. In every case, we find bounds that are *significantly weaker* than the published one [98] — even when we assume exactly the same values of $\mathcal{Q}_\text{y}$ — but in good agreement with other independent analyses [85, 100].[2]

We also consider values of $\mathcal{Q}_\text{y}$ that have recently been determined by the XENON100 collaboration by comparing calibration data to Monte Carlo simulations [177]. We adopt the range of values given in fig. 3 of Ref. [177], which we have reproduced together with the choice of $\mathcal{Q}_\text{y}$ from [98] in Fig. 3.10 (inset). Most of the sensitivity for detecting low-mass DM relies on recoil energies below 3 keV, where $\mathcal{Q}_\text{y}$ cannot be reliably extracted from the data. We therefore extrapolate $\mathcal{Q}_\text{y}$ in two

[1] As argued in Appendix A.3, the assumption of a χ^2-distribution for the log-likelihood function is not necessarily good. Indeed, running a Monte Carlo simulation of background events in CDMS-Si, we find a somewhat smaller p-value of 0.12%.

[2] The XENON10 collaboration has subsequently issued an erratum acknowledging the error. The corrected limit is in good agreement with our result.

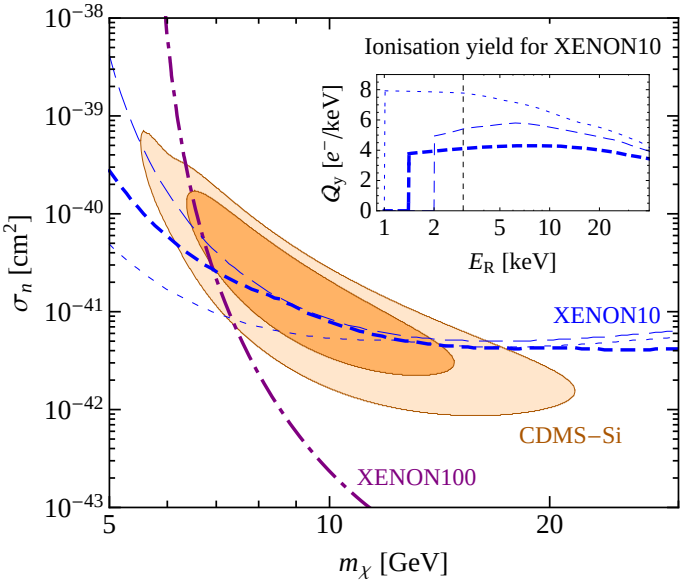

FIG. 3.10. CDMS-Si confidence region (68% and 90% CL) together with the 90% exclusion curves from XENON10 and XENON100 from our analysis, assuming standard elastic SI scattering and equal coupling to protons and neutrons. Our CDMS-Si confidence region and XENON100 bound agree well with the results from the respective collaborations [80, 92]. Our XENON10 bound, however, is significantly weaker than the published one [98]. We consider three choices of the ionisation yield $\mathcal{Q}_y$ to illustrate the corresponding variation of the extracted bound.

different ways that bracket the range of possibilities: the pessimistic choice (light dashed blue line in Fig. 3.10) assumes that $\mathcal{Q}_y$ follows the lower bound of the range given in Ref. [177] and then drops to zero at 2 keV. The optimistic choice (light dotted blue line) assumes that $\mathcal{Q}_y$ follows the upper bound of the range, continuing to rise up to $8\,e^-\,\mathrm{keV}^{-1}$ below 3 keV, and then drops to 0 at 1 keV. Even for the optimistic case we do not extrapolate $\mathcal{Q}_y$ below 1 keV, i.e. we neglect upward fluctuations. Changing $\mathcal{Q}_y$ also changes the energy scale shown in fig. 2 of Ref. [98], so we convert the energies of the observed events appropriately when setting the bound. It is clear from Fig. 3.10 that although the XENON10 S2-only analysis does constrain the CDMS-Si parameter region, an unambiguous bound cannot be placed at low mass because of the uncertainty in the value of the ionisation yield $\mathcal{Q}_y$ at low energy.

Henceforth we present only one XENON10 bound, adopting the original choice of $\mathcal{Q}_y$ from Ref. [98]. As this bound is significantly weaker than the published one [98], CDMS-Si and XENON10/100 are actually *consistent* at about 90% CL. Nevertheless there is some tension between these results. We will now explore possible ways to ameliorate this tension.

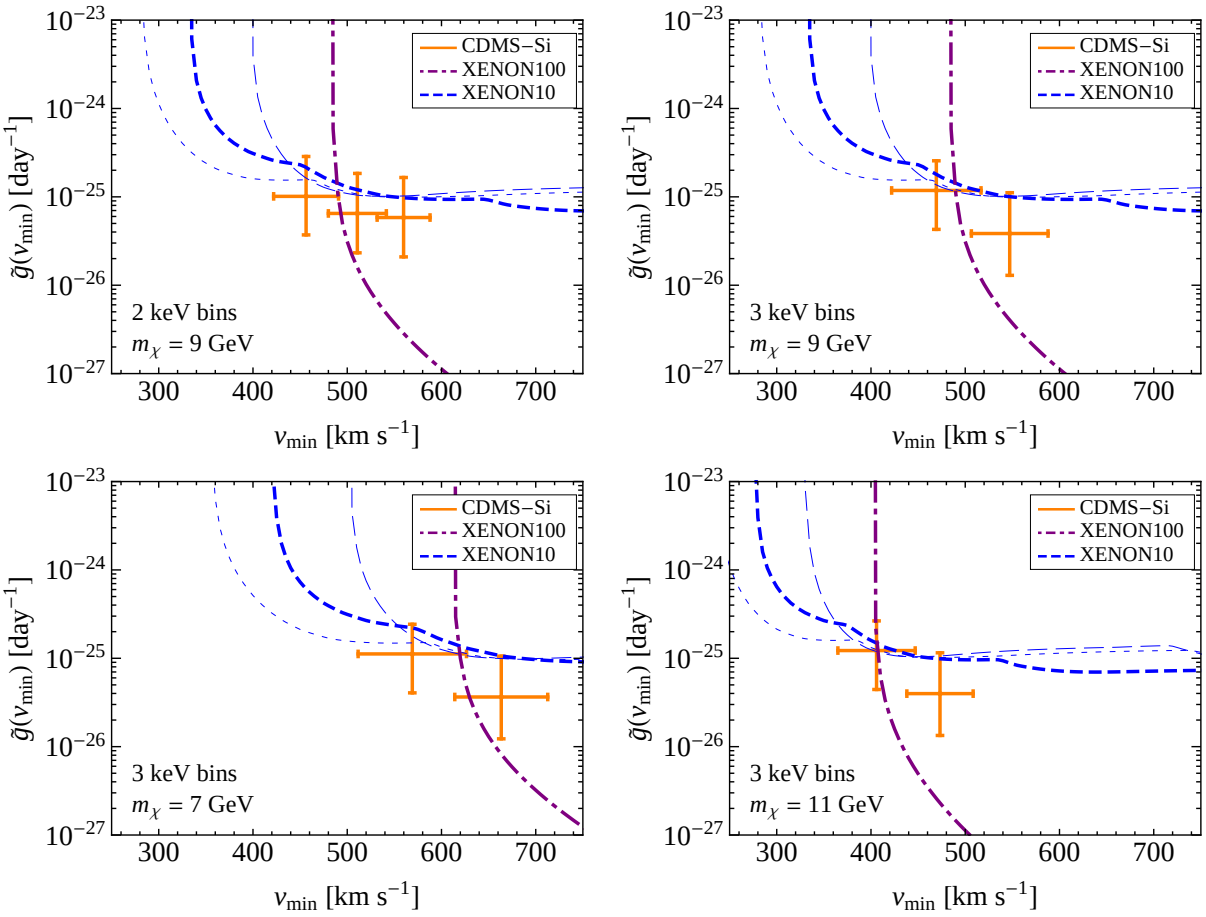

FIG. 3.11. The CDMS-Si and XENON10/100 results translated into $v_{\rm min}$-space. The upper panels show the case $m_\chi = 9\,\text{GeV}$ for two choices of binning, the lower panels show alternative assumptions for the DM mass. For all the cases considered, the region of $v_{\rm min}$-space probed by CDMS-Si is constrained by XENON10/100.

3.3.1 Astrophysical uncertainties

First of all, we perform the analysis introduced in Sec. 3.1 in order to map XENON10/100 and CDMS-Si into $v_{\rm min}$-space. The resulting bounds from XENON10 and XENON100 are shown as the blue (dashed) and purple (dot-dashed) lines in Fig. 3.11, respectively. For CDMS-Si the differential event rate is found most easily by binning both the observed events and the background expectation.[1] We subtract the background using the Feldman-Cousins technique [179], which allows us to calculate an upper and lower bound on the signal event rate at 1σ CL. The orange data points in Fig. 3.11 show the result of this procedure for $m_\chi = 9\,\text{GeV}$ (upper panels) and $m_\chi = 7\,\text{GeV}$ and

[1] An alternative method that uses the extended maximum likelihood method to avoid the need for binning has been proposed recently in Ref. [178].

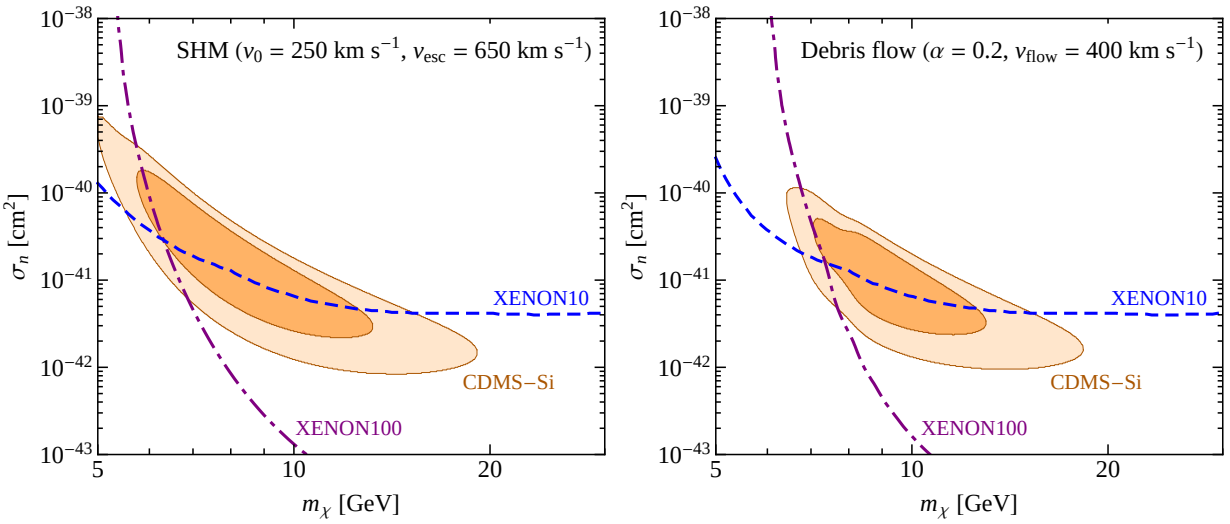

FIG. 3.12. The CDMS-Si region and XENON10/100 bounds calculated for different astrophysical parameters. The left panel shows the SHM, but with higher values of v_0 and v_{esc}. The right panel shows the effect of a debris flow which contributes 20% to the local DM density. Although the signal region and bounds move by a few GeV, the consistency of CDMS-Si and XENON10/100 is unchanged in either case, since all experiments probe the same region of v_{min}-space.

$m_\chi = 11\,\text{GeV}$ (lower-left and lower-right panel, respectively). Binning the data introduces a certain arbitrariness so we check the robustness of our results by considering two choices of the bin width: 2 keV and 3 keV for the upper-left and the upper-right panel of Fig. 3.11, respectively. The inferred values for $\tilde{g}(v_{min})$ agree well, implying that our conclusions are largely independent of the choice of bin width. In all cases, the highest bin is in significant tension with the XENON100 bound except for the case $m_\chi = 7\,\text{GeV}$, corresponding to the least constrained mass in Fig. 3.10.

We observe from Fig. 3.11 that all three experiments probe essentially the same region of v_{min}-space. This suggests that it will *not* be possible to significantly improve the consistency of CDMS-Si and XENON10/100 by varying astrophysical parameters. To explicitly confirm this expectation, we consider two variations in astrophysical parameters. In the left panel of Fig. 3.12 we keep the usual M-B velocity distribution but choose $v_0 = 250\,\text{km}\,\text{s}^{-1}$ and $v_{esc} = 650\,\text{km}\,\text{s}^{-1}$, which are at the upper end of the allowed range for these parameters (see Appendix A.1). Although we see that the CDMS-Si region and XENON10/100 bounds move towards lower masses by about 1 GeV, the tension between the experiments remains essentially unchanged. As a more radical modification we consider the effect of a *debris flow* (described in detail in Appendix A.1). We see again that although the preferred mass changes, the overall agreement does not.

3.3.2 Non-standard momentum and velocity dependence

We have seen that CDMS-Si and XENON10/100 probe the same region of $v_{\rm min}$-space so the tension between these experiments is independent of astrophysical uncertainties. We now consider the effect of modifying the particle physics in such a way that we introduce an additional momentum- or velocity-dependence of the cross section which can change the recoil energy spectrum.

Non-trivial momentum dependence can be studied using the simple parameterisation [180]

$$\frac{\mathrm{d}\sigma}{\mathrm{d}E_{\rm R}} = \left(\frac{\mathrm{d}\sigma}{\mathrm{d}E_{\rm R}}\right)_0 \left(\frac{q^2}{q_{\rm ref}^2}\right)^n \,, \tag{3.11}$$

where $(\mathrm{d}\sigma/\mathrm{d}E_{\rm R})_0$ is the differential cross section introduced in Eq. (2.3), $q = \sqrt{2\,m_{\rm N}\,E_{\rm R}}$ is the momentum transfer and $q_{\rm ref}$ is an arbitrary normalisation. The crucial observation is that the momentum transfer q is related to the minimum velocity $v_{\rm min}$ by

$$v_{\rm min} = \frac{q}{2\,\mu_{{\rm N}\chi}} \,. \tag{3.12}$$

For DM with $m_\chi \ll m_{\rm N}$, however, the reduced mass is approximately given by $\mu_{{\rm N}\chi} \approx m_\chi$ independent of $m_{\rm N}$. Consequently, experiments that probe the same range of $v_{\rm min}$ will also probe the same range of q (see also Ref. [181]). We cannot therefore significantly shift the parameter region favoured by CDMS-Si relative to the XENON10/100 bounds by introducing a momentum dependence. This is illustrated in the left panel of Fig. 3.13 for $q_{\rm ref} = 10\,\mathrm{MeV}$ and $n = -2$, which corresponds to long-range interactions arising from a (nearly) massless mediator. As expected, no significant improvement is found.

In many realistic models, the cross section depends not only on the momentum transfer but also on the velocity v of the incoming DM particle. This is the case e.g. for dipole interactions [146, 147, 182] and anapole interactions [138, 139]. Since we know already that both CDMS-Si and XENON10/100 probe the same part of the DM velocity distribution, such an additional velocity dependence is not expected to change the picture significantly. We confirm this expectation for the case of anapole interactions, which lead to a differential scattering cross section [139]

$$\frac{\mathrm{d}\sigma}{\mathrm{d}E_{\rm R}} = \frac{m_{\rm N}\,\sigma_{\rm ref}}{2\,\mu_{{\rm N}\chi}^2}\frac{Z^2}{v^2}\left[v^2 + \frac{q^2}{2\,m_{\rm N}^2}\left(1 - \frac{m_{\rm N}^2}{2\,\mu^2}\right)\right] F(E_{\rm R})^2 \,. \tag{3.13}$$

Our results are shown in the right panel of Fig. 3.13. As expected, because of the momentum-

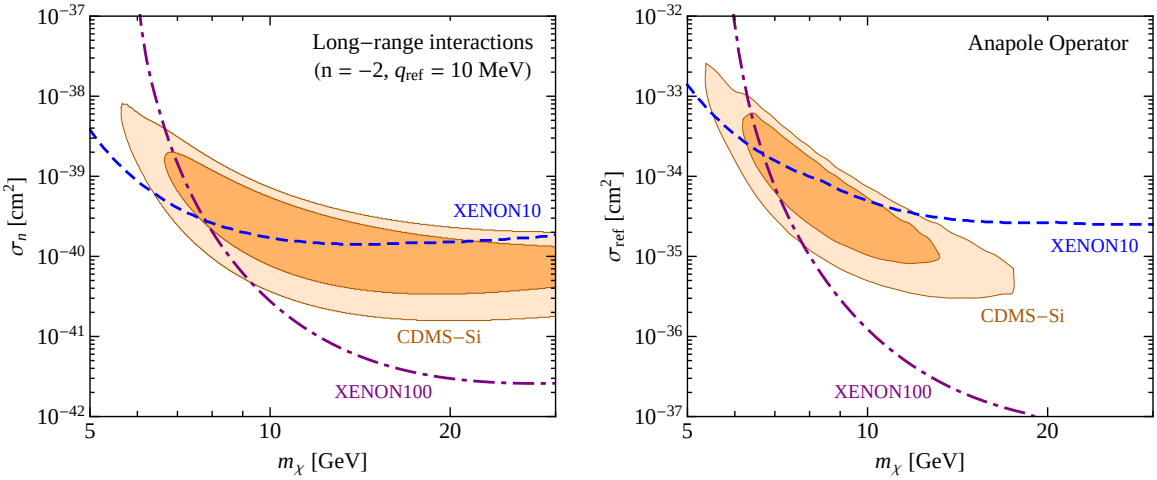

FIG. 3.13. Two examples for modifications of the momentum- and velocity-dependence of the differential cross section. Left: Long-range interactions, which enhance the cross section for small momentum transfer. Right: Anapole interactions, which suppress the cross section for small momentum transfer and small velocity (note the change of vertical scale).

and velocity-suppression, the CDMS-Si favoured parameter region and the XENON10/100 bounds are moved to much larger cross sections, but their relative position remains largely unchanged. Nevertheless, we do observe a slight shift of the CDMS-Si region compared to the XENON10/100 bounds, which can be traced back to the fact that for anapole interactions DM particles couple to protons only, leading to a factor of Z^2 rather than A^2 in the cross section. We explore the effect of different DM couplings to protons and neutrons in more detail in the next section.

3.3.3 Reducing the tension between CDMS-Si and XENON10/100

CDMS-Si and XENON10/100 cannot be brought into better agreement by modifying either the DM velocity distribution or the velocity/momentum dependence of the cross section. To weaken the constraints from XENON10/100, we need to reduce the enhancement of the cross section for heavy nuclei. In this section, we discuss two possible modifications of DM interactions that can increase the sensitivity of light targets compared to heavy ones: inelastic DM [183] and isospin-dependent couplings [184–187].

In the former case, DM-nucleon interactions require the transition between two DM states of

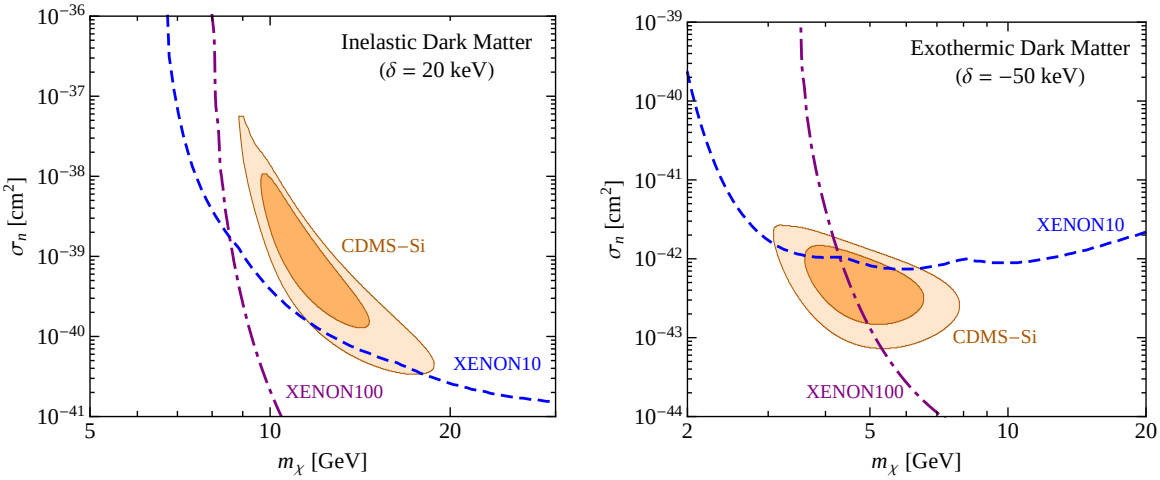

FIG. 3.14. Two examples for inelastic scattering. Left: Inelastic interactions with $\delta > 0$, which suppress the scattering rate on light target nuclei. Right: Exothermic interactions with $\delta < 0$, which enhance the scattering rate on light target nuclei. Note the change of scales in these figures.

slightly different mass. The minimum velocity required for a recoil of energy E_R is then

$$v_\mathrm{min} = \left| \delta + \frac{m_\mathrm{N}\, E_\mathrm{R}}{\mu} \right| \frac{1}{\sqrt{2\, E_\mathrm{R}\, m_\mathrm{N}}} \,, \tag{3.14}$$

where δ is the mass splitting between incoming and outgoing DM state. If the incoming DM particle is lighter ($\delta > 0$), scattering will be enhanced for heavy targets. However, if the heavier state is also populated initially, scattering with $\delta < 0$ will favour lighter targets. This second case, referred to as exothermic DM [188, 189], thus seems a promising option to fully reconcile CDMS-Si and XENON10/100. We present our results in Fig. 3.14. As expected, the XENON10/100 bounds are strengthened for inelastic DM and weakened for exothermic DM. In fact, a relatively small splitting of $\delta = -50\,\mathrm{keV}$ is sufficient to bring CDMS-Si and XENON10/100 into good agreement.

Another possible route is based on the observation that the strength of the XENON10/100 bounds results partially from the factor A^2 in the cross section, following from the assumption that DM couples equally to protons and neutrons. If DM couples to protons only (as for anapole interactions), the cross section will be proportional to Z^2, thus reducing the enhancement of neutron-rich targets. If the coupling to neutrons is slightly negative, $f_n/f_p < 0$, targets with a large fraction of neutrons will suffer even more strongly, because of the destructive interference between protons and neutrons. Such negative values of f_n/f_p (often referred to as isospin-dependent or isospin-violating couplings) can arise e.g. in theories with a light Z' that mixes with the SM gauge bosons (see Chapter 4).

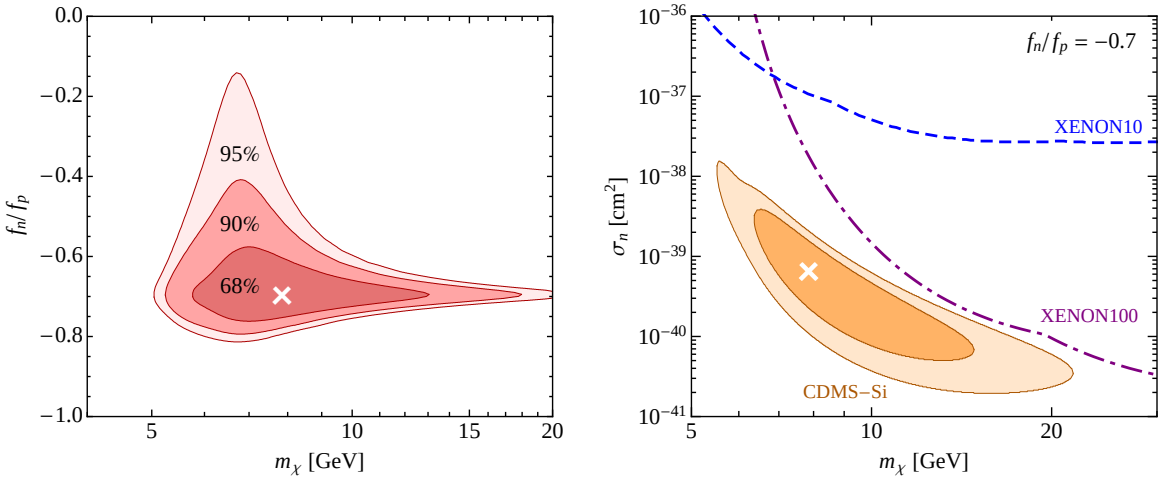

FIG. 3.15. Isospin-dependent couplings. Left: Combined parameter estimation of f_n/f_p, m_χ and σ_n (not shown) using a global maximum likelihood method (see text for details). As expected, there is a preference for $f_n/f_p = -0.7$ but the 2σ confidence region extends up to $f_n/f_p \approx -0.2$. Right: CDMS-Si allowed parameter region and XENON10/100 bounds for $f_n/f_p = -0.7$. In both plots, the best-fit point is indicated with a white cross.

To study this possibility, we scan simultaneously over f_n/f_p, σ_n and m_χ and calculate the likelihood for each set of parameters, using the maximum likelihood method described in Ref. [100]. In particular, we assume that the likelihood for XENON10 and XENON100 for a given set of parameters are given by $\mathcal{L}_{\rm Xe} = \exp(-N_{\rm max})$, where $N_{\rm max}$ is the number of events expected in the largest interval determined using the maximum gap method. Since we use an unbinned maximum likelihood method for CDMS-Si, the minimum value of the likelihood depends on an arbitrary normalisation constant and does not carry physical significance. We cannot therefore perform a goodness-of-fit analysis, but we can infer confidence regions for parameter estimation.

The results of this analysis are shown in the left panel of Fig. 3.15. As expected [184–187], the best fit is found for $f_n/f_p \approx -0.7$, which strongly suppresses the bounds from XENON10/100, as shown in the right panel of Fig. 3.15. Note that in this particular case, the strongest constraints on CDMS-Si arise from SIMPLE and the CRESST-II commissioning run (not shown). For $f_n/f_p = -0.7$ these experiments require $\sigma_n \lesssim 10^{-39}\,\text{cm}^2$ at $m_\chi \approx 10\,\text{GeV}$ [1] and therefore do not significantly constrain the CDMS-Si preferred region.

In spite of the preference for $f_n/f_p \approx -0.7$, we observe that much larger values of f_n/f_p are still allowed by the data. At 1σ CL, we find $-0.76 < f_n/f_p < -0.58$ and the 2σ confidence

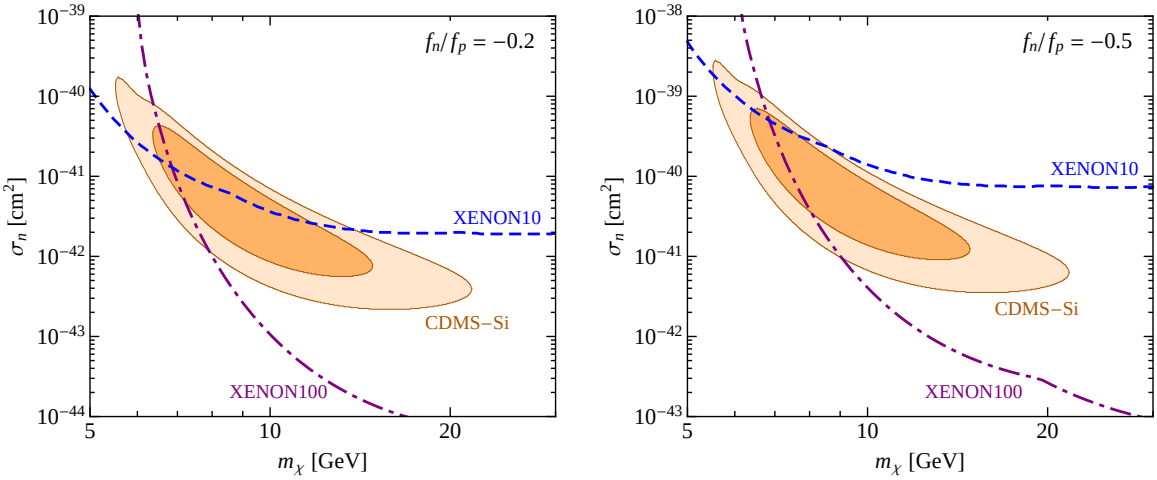

FIG. 3.16. Alternative choices for isospin-dependent couplings. No significant fine-tuning of f_n/f_p is required to weaken the XENON10/100 bounds relative to CDMS-Si. Note the change of scales in these figures.

region extends up to $f_n/f_p \approx -0.2$. To illustrate this point, we show the cases $f_n/f_p = -0.5$ and $f_n/f_p = -0.2$ in Fig. 3.16. We conclude that little fine-tuning is required to suppress the bounds from XENON10/100, in particular we do not require a precise cancellation of proton and neutron contributions and are therefore not sensitive to potential differences in the form factors as discussed in Ref. [190]. We also emphasise that even though $f_n = f_p$ is strongly disfavoured compared to $f_n/f_p = -0.7$ when performing a parameter estimation, this does not imply that such a value cannot give a good fit to the data. In fact, as we have shown above, CDMS-Si and XENON10/100 *are* compatible at the 90% CL even for $f_n = f_p$.

3.4 A new halo-independent approach

In this section we address the question of how strongly astrophysical uncertainties affect the potential to determine the DM properties from future direct detection experiments. It is known that, since changes in the halo structure can mimic changes in the DM parameters, a single direct detection experiment is insufficient to determine even the DM mass [191]. To make progress, one has to find a way to combine information from different target materials and quantify the impact of astrophysical uncertainties [64, 192, 193].

The standard approach to this problem is to parameterise the uncertainties in $f(\mathbf{v})$ and scan (or

marginalise) over the associated parameters [163–165, 194–196]. This approach suffers from the problem that it is unclear whether the chosen parameterisation of the halo is sufficiently general. Moreover, it is typically necessary to perform large numbers of numerical integrations over the DM velocity distribution, making this method numerically slow. Efficient scans then often require a Bayesian approach with the need to motivate prior distributions for DM parameters.

We therefore propose a new method for dealing with uncertainties in the DM velocity distribution, where instead of parameterising $f(\mathbf{v})$, we directly parameterise $\tilde{g}(v_{\min})$, so that predicted event rates depend on the parameters in a very simple way. In analogy to the treatment of the DM speed distribution $f(v) = \int f(\mathbf{v})\,\mathrm{d}\Omega_v$ in Ref. [166], we will write the velocity integral as a sum of step functions. This approach allows us to have a large number of free parameters and removes the need to make any assumptions about the form of $f(\mathbf{v})$. Consequently, any conclusions drawn from it will be completely robust in the face of astrophysical uncertainties. Moreover, our method involves a frequentist rather than a Bayesian approach, so that no prior distributions for any of the parameters need to be proposed.

3.4.1 Finding the optimum velocity integral

Our goal is to find the function $\tilde{g}(v_{\min})$ that best describes a given set of data from direct detection experiments for a proposed DM model. We want to make *no assumptions on the functional form* of $\tilde{g}(v_{\min})$ apart from it being monotonically decreasing [75]. We therefore proceed as follows:

- We determine the region of $v_{\min}$-space probed by the experiments under consideration by converting recoil energies into $v_{\min}$-values. We then divide this region into N_{s} evenly spaced intervals of the form $[v_j,\, v_{j+1}]$.

- We take the ansatz that $\tilde{g}(v_{\min})$ is a monotonically decreasing sum of N_{s} steps, i.e. we introduce N_{s} constants g_j, such that $\tilde{g}(v_{\min}) = g_j$ for $v_{\min} \in [v_j,\, v_{j+1}]$ (see Fig. 3.17). The monotonicity requirement implies that $0 \leq g_j \leq g_{j-1}$ for all j.[1]

- Using this ansatz and given an experiment with energy bins of the form $\left[E^{(i)},\, E^{(i+1)}\right]$ we now predict the expected number of events, $P_i(\mathbf{g})$, in each bin. Defining E_j implicitly by

[1] Note that the overall normalisation of $\tilde{g}(v_{\min})$ is unconstrained, because we allow σ_n to take arbitrary values for a given m_χ. For more restricted model hypotheses, we would have to include an additional constraint on the normalisation of $\tilde{g}(v_{\min})$.

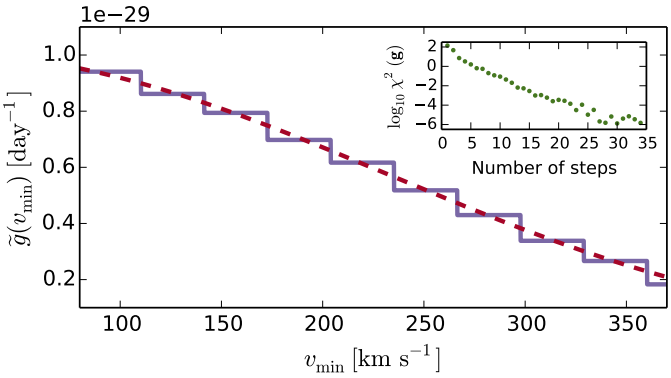

FIG. 3.17. The red (dashed) line shows the SHM prediction for $\tilde{g}(v_{\rm min})$, the purple line shows our best-fit approximation using 10 steps. Increasing the number of steps leads to a rapid decrease of $\chi^2(\mathbf{g})$, which quickly converges to zero (see inset).

$v_j = v_{\rm min}(E_j)$ and using Eq. (2.5) we obtain the simple expression $P_i(\mathbf{g}) = \sum_j C_{ij}\, g_j$, where

$$C_{ij} \equiv \frac{C_{\rm T}^2(A,Z)}{2\,\mu_{n\chi}^2}\,\kappa \int_{E_j}^{E_{j+1}} {\rm Res}\left(E^{(i)},\, E^{(i+1)}, E_{\rm R}\right)\,\epsilon(E_{\rm R})\,F^2(E_{\rm R})\,{\rm d}E_{\rm R} \tag{3.15}$$

are calculable constants that depend only on the experimental details and the assumed DM properties, but are independent of astrophysics.

- We now define the usual χ^2 test statistic

$$\chi^2(\mathbf{g}) \equiv \sum_i \frac{(P_i(\mathbf{g}) - N_i)^2}{P_i(\mathbf{g})}\,, \tag{3.16}$$

where N_i is the experimentally observed number of events in the ith bin.

- Now, we numerically find the step heights g_j that minimise $\chi^2(\mathbf{g})$, maintaining the requirement of monotonicity $0 \leq g_j \leq g_{j-1}$. Although $N_{\rm s}$ can be rather large (see below), it is nevertheless easily possible to find the global minimum of $\chi^2(\mathbf{g})$. The reason is that the allowed region of $\mathbf{g}$ is convex and the Hessian of $\chi^2(\mathbf{g})$ is positive semi-definite everywhere within. Consequently, any local minimum of $\chi^2(\mathbf{g})$ is automatically a global minimum.

- Finally, we take $N_{\rm s} \to \infty$. In practice, we take $N_{\rm s}$ so large that further increases yield negligible improvements to χ^2. In typical examples of interest, we find that $N_{\rm s} \gtrsim 30$ is sufficient for this purpose. For such values of $N_{\rm s}$ the minimisation takes roughly a few seconds on a standard desktop computer.

Effectively, we decompose the DM velocity distribution into a large number of streams with different densities and speeds. Since any continuous function may be approximated arbitrarily well by a sum of step functions, this method effectively finds the *best possible form* for $\tilde{g}(v_{\rm min})$ for a given set of data and model parameters.

Interestingly, we have found that, even in the limit that $N_{\rm s} \to \infty$, the number of *non-zero* steps in the optimised halos (i.e. the number of steps with $g_j \neq g_{j+1}$) always remains smaller than the number of bins of data. This follows from the fact that, if we divide an optimised $\tilde{g}(v_{\rm min})$ into 'flat' sections with differing heights h_i, then these must all satisfy $\partial\chi^2/\partial h_i = 0$. It may be checked that these equations can only all be satisfied if either the number of flat sections is smaller than the number of bins, or if the predictions P_i can be made to perfectly match the observations N_i. The latter possibility, however, is extremely unlikely for realistic cases including Poisson fluctuations. As a result, taking the limit $N_{\rm s} \to \infty$ does not actually lead to more and more steps being added to the optimised halos, but rather allows for finer adjustments of the *endpoints* of the flat sections. Taking large $N_{\rm s}$ thus turns out to be a useful trick for determining the optimal endpoints for the flat sections in a numerically efficient way.

We can now repeat our procedure for different sets of DM parameters and thereby find the minimum of $\chi^2(\mathbf{g})$, called $\hat{\chi}^2$, for every point in parameter space. The best-fit values for the DM parameters are then determined by finding the global minimum of $\hat{\chi}^2$, which we call $\hat{\chi}^2_{\rm min}$. We then define the test statistic $\Delta\chi^2 \equiv \hat{\chi}^2 - \hat{\chi}^2_{\rm min}$, which we have confirmed to follow a χ^2-distribution with the degrees of freedom given by the number of fitted DM parameters. Consequently, $\Delta\chi^2$ can be used to define confidence intervals as usual.

To illustrate this method, we have generated mock data for a set of future experiments (taken from Ref. [192], see below). Two particular examples are shown in Fig. 3.18, where we use non-standard DM velocity distributions (see Appendix A.1) to generate a total of about 700 events across three different targets. For the left plot, we assume a 10% contribution from a DM stream with a velocity of $600\,{\rm km\,s^{-1}}$ in the laboratory frame and take $m_\chi = 50\,{\rm GeV}$, $f_p/f_n = 1$ and $\sigma_n = 8\times10^{-46}\,{\rm cm^2}$. For the right plot we consider the case that the DM velocity distribution contains a 25% contribution from a dark disk with velocity dispersion and lag relative to the baryonic disk both equal to $50\ {\rm km\,s^{-1}}$ [197], and have assumed $m_\chi = 800$ GeV, $f_p/f_n = 1$ and $\sigma_n = 7\times10^{-45}$ cm^2. In both cases we neglect Poisson fluctuations.

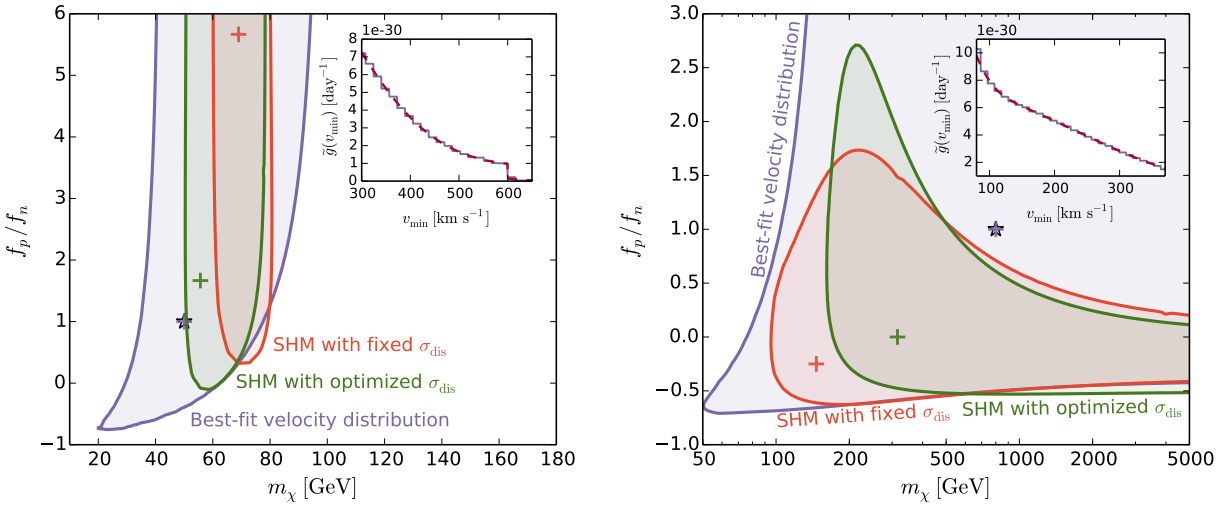

FIG. 3.18. DM parameter estimation using mock data for different non-standard DM velocity distributions. For the left plot it is assumed that 10% of the local DM density is in a DM stream, for the right plot it is assumed that 25% of the local DM density is in a dark disk. The crosses (shaded regions) correspond to the best-fit values (90% confidence regions) for three different methods (see text). The best-fit values for the DM parameters obtained from our new method (purple cross) perfectly coincide with the true values (white star). The insets show the best-fit halo that we obtain at the global minimum of $\chi^2(\mathbf{g})$ (solid purple line), compared to the assumed halo used to generate the data (red dashed line).

We observe that in both scenarios (as well as in all other cases that we have considered) the best-fit values for the DM parameters obtained from our method (purple cross) perfectly coincide with the true values (white star) and the best-fit $\tilde{g}(v_{\rm min})$ matches perfectly the assumed velocity integral (see insets). For comparison, we also show the best-fit values and 90% confidence regions obtained from two alternative methods, namely simply assuming the SHM with fixed parameters and optimising the fit over σ_n only (red) or assuming the SHM, but optimising the fits over both σ_n and the velocity dispersion $\sigma_{\rm dis}$ (green). It may be seen that both of these methods *incorrectly exclude* the true DM parameters at 90% CL.[1]

3.4.2 Example: hypercharged dark matter

We will now focus on a concrete model to show how our method is used in practice. If DM carries SM hypercharge (and is in an appropriate representation of $SU(2)_L$ so that it has an electrically neutral component), then it will generically interact with nuclei via tree-level Z-boson exchange, which

[1] It should be noted that other methods exist in the literature, such as the very general parameterisation of $f(v)$ discussed in Refs. [195, 196, 198], that are well suited for reconstructing the DM parameters for non-standard velocity distributions. We leave a comparison of these methods with our approach to future work.

results in a coupling ratio of $f_p/f_n \approx -0.04$. As discussed in Ref. [199], current direct detection constraints on such DM particles require masses greater than about $10^8\,\text{GeV}$, and future experiments will be able to see a signal for m_χ up to $(10^{10}\text{–}10^{11})\,\text{GeV}$. Such heavy DM particles most simply obtain an appropriate relic abundance by having masses close to the reheating temperature of the Universe. Since the coupling strength of hypercharged DM is fixed, detection of a signal would immediately reveal the DM mass through the scattering rate, and this would then give otherwise unobtainable information about the thermal history of the Universe. In this scenario it would be of crucial importance to confirm that DM-nucleon scattering is mediated by Z-bosons. We will therefore use hypercharged DM as an example to show how our method may be used to determine f_p/f_n in a halo-independent way.

The most likely target materials for ton-scale future direct detection experiments are xenon, germanium and argon [192]. Since their neutron to proton number ratios differ by less than 15%, determining f_p/f_n by looking at the relative rates of a signal on these elements will not be easy. Moreover, planned experiments using these elements will probe different regions of v_{min}-space, not only because the energy thresholds may differ, but also because for $m_\chi \gg m_N$ heavier target nuclei are sensitive to smaller velocities.

Consequently, astrophysical uncertainties severely affect the determination of f_p/f_n. If, for example, future data shows an excess of events in Xe-based experiments compared to Ar-based experiments, this observation could either be due to preferential coupling of DM to neutrons, as in the hypercharged scenario, or due to the DM velocity distribution decreasing more rapidly than in the SHM. Nevertheless, as long as there is non-negligible *overlap* between the regions of v_{min}-space probed by different experiments, it will be possible to determine f_p/f_n in a halo-independent way, given sufficient exposure.

This situation is illustrated in the left panel of Fig. 3.19. The data points correspond to hypothetical measurements from future experiments employing Xe (blue), Ge (green) and Ar (purple) targets, assuming fermionic DM with hypercharge 1/2 and $m_\chi = 7 \times 10^7\,\text{GeV}$, compatible with the constraint from LUX, as well as a DM velocity distribution given by the SHM. For this plot, we have chosen a bin width of 10 keV and taken all experimental details from Ref. [192]. In particular, we take energy-independent effective exposures of 2, 2.16, and 6.4 ton yr and low energy thresholds of 10, 10 and 30 keV at Xe, Ge and Ar, respectively.

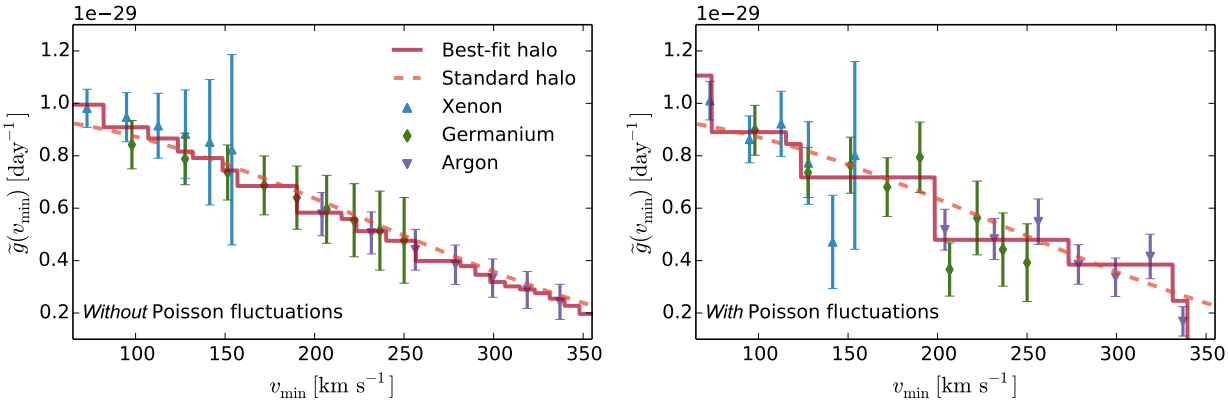

FIG. 3.19. Hypothetical measurements of the velocity integral $\tilde{g}(v_{\rm min})$ from future experiments together with the best-fit velocity integral and the SHM velocity integral. For the left panel, the shown data points correspond to the prediction for hypercharged DM with $m_\chi = 7 \times 10^7$ GeV, but are interpreted under the *incorrect* assumption that $f_p = f_n$. In the right panel, we show the same setup but additionally include a set of possible Poisson fluctuations.

For Xe we only include the lowest 6 bins, because its rapidly decreasing form factor cuts off the event rate at higher energies. We have checked that changing the number of bins or the bin size has negligible impact on our results. We map the experimental data onto $\tilde{g}(v_{\rm min})$-values bin by bin using Eq. (3.2) and test the *incorrect* model hypothesis that $f_p/f_n = 1$.

Because of this incorrect hypothesis the data points from Xe predict values of $\tilde{g}(v_{\rm min})$ that are large compared to the SHM prediction with best-fit normalisation (orange dashed line), while the Ar predictions are comparatively small. The optimum velocity integral $\tilde{g}(v_{\rm min})$ as obtained from our method (red solid line), therefore clearly deviates from the SHM prediction and falls more steeply to reproduce this trend. In the absence of Poisson fluctuations, the value of $\hat{\chi}^2$ associated to the best-fit velocity integral in this example is $\hat{\chi}^2 = 1.05$. Had we made the 'correct' hypothesis that $f_p/f_n = -0.04$, the best-fit velocity integral would be identical to the SHM prediction used to generate the data, giving $\hat{\chi}^2_{\rm min} \approx 0$ (see Fig. 3.17).

The difference $\Delta\chi^2 = 1.05$ describes the extent to which $f_p/f_n = 1$ is disfavoured by the data. In this particular example, the hypothesis is excluded at the 69% CL. Of course, Poisson fluctuations are expected to modify our conclusions. Nevertheless, our method still enables us to find the best-fit velocity integral even when the data points would favour an increasing velocity integral in some regions of $v_{\rm min}$-space. One possible example for the effect of such fluctuations is shown in the right panel of Fig. 3.19, together with the corresponding best-fit velocity integral. If we include Poisson

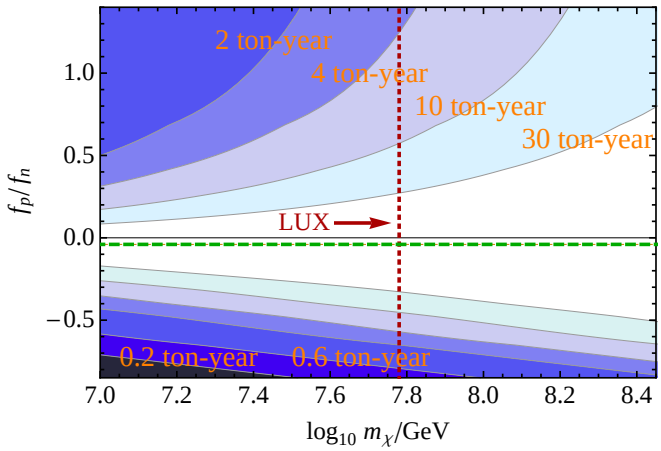

FIG. 3.20. Expected 90% confidence intervals on the ratio of DM couplings for different experimental exposures without making any assumptions about the DM velocity distribution. The underlying data was generated assuming hypercharged DM with mass given on the horizontal axis. The vertical dashed line indicates the lower bound on m_χ from the LUX experiment [81], the horizontal dashed line corresponds to $f_p/f_n = -0.04$.

fluctuations, we find a median exclusion of the hypothesis that $f_p/f_n = 1$ at the 66% CL. With a probability of about 22%, the fluctuations are such that we can exclude $f_p/f_n = 1$ with at least 90% confidence.

In Fig. 3.20 we show the 90% confidence limits on f_p/f_n which may be obtained from various exposures at Xe (rescaling the exposures at Ge and Ar from Ref. [192] correspondingly). The data is generated assuming the same parameters for hypercharged DM as above, and we have minimised χ^2 over both $\mathbf{g}$ and the hypothesised DM mass. In order to show what may be accomplished in a typical case, we have again ignored Poisson fluctuations for this plot.

To conclude this section, we note that the power to exclude $f_p/f_n = 1$ comes largely from the fact that Ge-based experiments have overlap in $v_{\min}$-space with both Xe and Ar targets. In the absence of a Ge target, we find (neglecting Poisson fluctuations) $\Delta\chi^2 < 0.001$. We come to the important conclusion that for heavy DM essentially *no* information can be inferred about f_p/f_n in a halo-independent way when using only Xe and Ar targets.

3.4.3 Applications and future directions

The method we have presented here is extremely general and — given a data set — can be used to determine the best-fit velocity distribution for a wide variety of possible model hypotheses. There

is no obstacle to performing analyses of many more complicated particle physics models, such as inelastic or exothermic DM or DM with long-range or momentum-suppressed interactions. Similarly, our method could also be applied to $\Delta g(v_{\rm min})$ in order to compare annually modulating signals of DM and to constraining the modulation fraction.

Another exciting prospect is to apply our method to experimental results that give contradictory information when interpreted in terms of the SHM (such as CoGeNT, CDMS-Si, LUX and SuperCDMS) to understand if a different DM velocity distribution can bring these experiments into agreement. Here, however, there are two important complications. The first issue is that, for experiments with unclear compatibility, one would be interested in determining the goodness of fit at the actual best-fit point in addition to the determination of confidence intervals in DM parameter space. Typically, the value of the χ^2 statistic at a best fit point follows a χ^2 distribution with number of degrees of freedom given by the number of observations (i.e. bins) minus the number of free parameters. Our requirement of monotonicity, however, makes the notion of the number of free parameters in our halo fits somewhat unclear. In particular, we know that it generally remains impossible for us to fit data arbitrarily well even in the limit of an infinite number of $\tilde{g}(v_{\rm min})$ steps. The second issue is that, for experiments observing small event rates, binning the data and using χ^2-methods becomes unreliable. In principle, there is no obvious obstacle to using an unbinned extended maximum likelihood method [174] to determine the optimum $\tilde{g}(v_{\rm min})$, but doing so would appear to make future progress on the goodness-of-fit question difficult. We leave these problems to future work.

CHAPTER 4

Phenomenology and collider constraints for vector mediators

In this chapter we turn to the discussion of particle physics models that can account for the potential DM signals discussed in the previous chapter. For this purpose we study the interactions of a new spin-1 mediator that connects the SM to DM. We will show that it is possible to achieve sufficiently large DM-nucleon scattering cross sections while allowing naturally for $f_n/f_p \neq 1$. In particular, it is possible to obtain $f_n/f_p \sim -0.7$ using a single mediator. For models that obtain isospin-violating couplings from the interference of several independent mediators, we refer to Refs. [171, 200] but note the problems arising from radiative corrections [190, 201].

In Sec. 4.1 we present the effective Lagrangian describing the interactions of a general spin-1 mediator with SM fermions and DM particles and calculate the ratio f_n/f_p for DM-nucleon scattering that results from the mixing of the mediator with the neutral gauge bosons of the SM. We then consider a specific example for such a vector mediator, namely a Z' with kinetic mixing and mass mixing in Sec. 4.2. We first focus on the case of mediators with a mass small compared to the Z boson and show that large direct detection cross sections are compatible with all experimental constraints (Sec. 4.3). For the case of a heavy Z' we study the constraints from collider experiments, including monojet and monophoton searches but also constraints that arise from the couplings of Z' to leptons, SM gauge bosons and the Higgs (Sec. 4.4). Finally, in Sec. 4.5 we return to the general case of a vector mediator with arbitrary couplings and demonstrate that using experimental searches for dijet resonances it is still possible (under certain assumptions) to constrain the direct detection cross section.

4.1 Interactions of a vector mediator

In this section we discuss the general calculation of the effective couplings for DM scattering on neutrons and protons via the exchange of a neutral spin-1 mass eigenstate R. We write the Lagrangian for interactions between R and SM fermions as well as DM particles as

$$\mathcal{L}^R \supset \mathcal{L}^R_{\rm DM} + \mathcal{L}^R_{f\bar{f}} \,. \tag{4.1}$$

If DM is a Dirac fermion χ

$$\mathcal{L}^R_{\rm DM} = R_\mu \, \bar{\chi} \, \gamma^\mu (g^V_{\chi R} - g^A_{\chi R} \gamma^5) \chi \,, \tag{4.2}$$

while for a complex scalar ϕ

$$\mathcal{L}^R_{\rm DM} = g_{\phi R} \, R_\mu \, J^\mu_\phi \,, \tag{4.3}$$

where $J^\mu_\phi \equiv i(\phi^* \, \partial^\mu \phi - \phi \, \partial^\mu \phi^*)$. For a Majorana fermion, the vector coupling $g^V_{\chi R}$ vanishes, while a real scalar can only couple to R via the CP-odd operator $\partial_\mu R^\mu \, \phi^2$, which we do not consider further here (for a discussion see e.g. Ref. [202]).

The interactions of R with the SM fermions are described by

$$\mathcal{L}^R_{f\bar{f}} = \sum_{f=q,\ell,\nu} R_\mu \, \bar{f} \, \gamma^\mu (g^V_{fR} - g^A_{fR} \, \gamma^5) f \,, \tag{4.4}$$

where q, ℓ, ν denote SM quarks, charged leptons and neutrinos, respectively.

We assume that the mass eigenstate R arises from the mixing of an interaction eigenstate vector X with the SM $U(1)_Y$ B field and the neutral component W^3 of the $SU(2)_{\rm L}$ weak fields

$$\begin{pmatrix} B_\mu \\ W^3_\mu \\ X_\mu \end{pmatrix} = \begin{pmatrix} N_{11} & N_{12} & N_{13} \\ N_{21} & N_{22} & N_{23} \\ N_{31} & N_{32} & N_{33} \end{pmatrix} \begin{pmatrix} A_\mu \\ Z_\mu \\ R_\mu \end{pmatrix} \,, \tag{4.5}$$

where A and Z are the physical photon and neutral massive gauge boson fields of the SM. We will show below that by an appropriate redefinition of the fields both kinetic mixing and mass mixing can be written in this way.

In addition to any direct couplings of X to SM fermions, denoted by $f_f^{\rm V,A}$, the mixing will introduce additional contributions, so that the overall couplings of R to light quarks will be given

by[1]

$$
\begin{aligned}
g^{\mathrm{V}}_{uR} &= -\frac{1}{12}(5\hat{g}'N_{13} + 3\hat{g}N_{23}) - f^{\mathrm{V}}_u N_{33} \ , & g^{\mathrm{A}}_{uR} &= \frac{1}{4}(\hat{g}'N_{13} - \hat{g}N_{23}) - f^{\mathrm{A}}_u N_{33} \ , \\
g^{\mathrm{V}}_{dR} &= \frac{1}{12}(\hat{g}'N_{13} + 3\hat{g}N_{23}) - f^{\mathrm{V}}_d N_{33} \ , & g^{\mathrm{A}}_{dR} &= -\frac{1}{4}(\hat{g}'N_{13} - \hat{g}N_{23}) - f^{\mathrm{A}}_d N_{33} \ , \\
g^{\mathrm{V}}_{eR} &= \frac{1}{4}(3\hat{g}'N_{13} + \hat{g}N_{23}) - f^{\mathrm{V}}_e N_{33} \ , & g^{\mathrm{A}}_{eR} &= -\frac{1}{4}(\hat{g}'N_{13} - \hat{g}N_{23}) - f^{\mathrm{A}}_e N_{33} \ , \\
g^{\mathrm{V}}_{\nu R} &= \frac{1}{4}(\hat{g}'N_{13} - \hat{g}N_{23}) - f^{\mathrm{V}}_\nu N_{33} \ , & g^{\mathrm{A}}_{\nu R} &= \frac{1}{4}(\hat{g}'N_{13} - \hat{g}N_{23}) - f^{\mathrm{A}}_\nu N_{33} \ ,
\end{aligned}
\tag{4.6}
$$

where the numerical coefficients are determined from the hypercharge and weak quantum numbers of the SM fermions. Similarly, the effective vector and axial couplings of R to the DM particle are given by $g^{\mathrm{V}}_{\chi R} = f^{\mathrm{V}}_\chi N_{33}$ and $g^{\mathrm{A}}_{\chi R} = f^{\mathrm{A}}_\chi N_{33}$, or $g_{\phi R} = f_\phi N_{33}$, depending on whether the DM particle is a fermion or a scalar.

A mixing as in Eq. (4.5) not only induces couplings of R to the SM fermions, but also couplings of Z (and in some cases A) to the DM particle. The corresponding coupling constants can be calculated analogously by examining the corresponding column of the mixing matrix. The effective coupling constants for A are obtained from the first column, i.e. replacing N_{i3} by N_{i1}, and the effective coupling constants for Z are obtained from the second column. Note that if $N_{31} = 0$, there is no coupling of the physical photon to the DM state and hence *no DM millicharge*. Because of the strong constraints on such millicharges, we limit our discussion to this case and show below that indeed N_{31} remains zero in the scenario we are interested in.

In this case, the photon does not mediate DM-nucleon interactions and we can therefore study these interactions by integrating out the vector mediator R and the SM Z-boson. We then obtain the effective four-fermion interactions (see Sec. 2.4)

$$
\begin{aligned}
\mathcal{L}^{\mathrm{eff}}_R = {} & b^{\mathrm{V}}_f \, \bar{\chi}\gamma_\mu\chi \, \bar{f}\gamma^\mu f \ + \ b^{\mathrm{A}}_f \, \bar{\chi}\gamma_\mu\gamma^5\chi \, \bar{f}\gamma^\mu\gamma^5 f \\
& + c^1_f \, \bar{\chi}\gamma_\mu\gamma^5\chi \, \bar{f}\gamma^\mu f \ + \ c^2_f \, \bar{\chi}\gamma_\mu\chi \, \bar{f}\gamma^\mu\gamma^5 f \ ,
\end{aligned}
\tag{4.7}
$$

where

$$
b^{\mathrm{A,V}}_f \equiv b^{\mathrm{A,V}}_{fR} + b^{\mathrm{A,V}}_{fZ} \equiv \frac{g^{\mathrm{A,V}}_{\chi R}\, g^{\mathrm{A,V}}_{fR}}{m^2_R} + \frac{g^{\mathrm{A,V}}_{\chi Z}\, g^{\mathrm{A,V}}_{fZ}}{m^2_Z} \ . \tag{4.8}
$$

As discussed in Sec. 2.4, the mixing terms proportional to c^i_f are suppressed in the non-relativistic

[1] We use $\hat{g}$ and $\hat{g}'$ to denote the fundamental gauge couplings of $SU(2)_{\mathrm{L}}$ and $U(1)_Y$, which may be different from the observed ones, g and g', due to the effects of mixing.

limit, so we neglect them in our analysis. Unless $b^{\rm V}$ is very small compared to $b^{\rm A}$, the direct detection cross section will be dominated by the effective vector-vector interaction between the DM particle and nucleons (p, n) given by

$$\mathcal{L}_\chi^{\rm V} = f_p^\chi\, \bar\chi\gamma_\mu\chi\, \bar p\gamma^\mu p + f_n^\chi\, \bar\chi\gamma_\mu\chi\, \bar n\gamma^\mu n\,; \quad f_p^\chi = 2\, b_u^{\rm V} + b_d^{\rm V}\,,\ f_n^\chi = 2\, b_d^{\rm V} + b_u^{\rm V}\,. \tag{4.9}$$

Because of the conservation of the vector current, there is no contribution of sea quarks or gluons to the effective couplings. In the case of the complex scalar DM we have similarly

$$\mathcal{L}_\phi^{\rm eff} = a_f^{\rm V}\, J_\phi^\mu\, \bar f\gamma_\mu f\,, \quad \mathcal{L}_\phi^{\rm V} = f_p^\phi\, J_\phi^\mu\, \bar p\gamma_\mu p + f_n^\phi\, J_\phi^\mu\, \bar n\gamma_\mu n\,, \tag{4.10}$$

where

$$a_f^{\rm V} \equiv a_{fR}^{\rm V} + a_{fZ}^{\rm V} \equiv \frac{g_{\phi R}\, g_{fR}^{\rm V}}{m_R^2} + \frac{g_{\phi Z}\, g_{fZ}^{\rm V}}{m_Z^2}\,; \quad f_p^\phi = 2\, a_u^{\rm V} + a_d^{\rm V}\,, \quad f_n^\phi = 2a_d^{\rm V} + a_u^{\rm V}\,. \tag{4.11}$$

At this point, it is instructive to look at a few familiar cases:

1. For a mediator coupling to the baryonic current we have $b_u^{\rm V}/b_d^{\rm V} = f_n/f_p = 1$.
2. For a mediator coupling to the weak isospin current we have $b_u^{\rm V}/b_d^{\rm V} = f_n/f_p = -1$.
3. For a coupling to the EM current we have $b_u^{\rm V}/b_d^{\rm V} = -2$ and thus $f_n/f_p = 0$.
4. Finally, a coupling to the vectorial part of the SM Z current gives $b_u^{\rm V}/b_d^{\rm V} \approx -1/2$ and thus $f_p/f_n = (f_n/f_p)^{-1} \approx -0.04$, corresponding to a coupling dominantly to neutrons.

We have seen in Sec. 3.3 that experimental bounds from xenon-based experiments can be weakened considerably if $-0.8 < f_n/f_p < -0.5$. In isolation, none of the possibilities above yields such a ratio of f_n/f_p. As we will show in the following section, however, a single light vector mediator which mixes with the neutral SM gauge bosons can generate $f_n/f_p \approx -0.7$ with sufficiently large cross sections to explain the CDMS-Si signal *and* be in agreement with all other experimental constraints.

4.2 Effective Lagrangian for a light Z'

From now on we will take the interaction eigenstate X to be the new gauge boson corresponding to an additional $U(1)_X$ symmetry [203–206]. The corresponding mass eigenstate Z' is then a

specific realisation of the vector mediator R. The general possibility of DM (in particular light DM) coupling to the SM via a Z' has been considered before in Refs. [172, 207–212].

We consider an effective Lagrangian that includes kinetic mixing and mass mixing [204]:[1]

$$\begin{aligned}\mathcal{L} = \; & \mathcal{L}_{SM} - \frac{1}{4}\hat{X}^{\mu\nu}\hat{X}_{\mu\nu} + \frac{1}{2}m_{\hat{X}}^2\,\hat{X}_\mu\hat{X}^\mu + \bar{\chi}\left(i\hat{\partial\!\!\!/} - m_\chi\right)\chi \\ & - \frac{1}{2}\sin\epsilon\,\hat{B}_{\mu\nu}\hat{X}^{\mu\nu} + \delta m^2\,\hat{Z}_\mu\hat{X}^\mu - \sum_f f_f^{\mathrm{V}}\,\hat{X}^\mu\,\bar{f}\gamma_\mu f - f_\chi^{\mathrm{V}}\,\hat{X}^\mu\,\bar{\chi}\gamma_\mu\chi\,, \end{aligned} \tag{4.12}$$

where $\hat{X}^{\mu\nu} = \partial^\mu\hat{X}^\nu - \partial^\nu\hat{X}^\mu$ and the $U(1)_X$ is assumed to be broken, leading to a vector boson mass of $m_{\hat{X}}$. We denote fields in the original basis with hats $(\hat{B}, \hat{W}^3, \hat{X})$ and define $\hat{Z} \equiv \hat{c}_{\mathrm{W}}\hat{W}^3 - \hat{s}_{\mathrm{W}}\hat{B}$, where $\hat{s}_{\mathrm{W}}$ $(\hat{c}_{\mathrm{W}})$ is the sine (cosine) of the Weinberg angle and $\hat{g}'$, $\hat{g}$ are the corresponding gauge couplings. Canonically normalised interaction eigenstates after kinetic diagonalisation and normalisation are denoted without hats, while the mass eigenstates after mass diagonalisation are denoted by (A, Z, Z'). In the following we will abbreviate $s_\theta \equiv \sin\theta$, $c_\theta \equiv \cos\theta$ and $t_\theta \equiv \tan\theta$.

The diagonalisation of the above Lagrangian is discussed in detail for example in Ref. [204]. The field strengths are diagonalised and canonically normalised by two consecutive transformations:

$$\begin{pmatrix} \hat{B}_\mu \\ \hat{W}_\mu^3 \\ \hat{X}_\mu \end{pmatrix} = \begin{pmatrix} 1 & 0 & -t_\epsilon \\ 0 & 1 & 0 \\ 0 & 0 & 1/c_\epsilon \end{pmatrix} \begin{pmatrix} B_\mu \\ W_\mu^3 \\ X_\mu \end{pmatrix}\,, \tag{4.13}$$

$$\begin{pmatrix} B_\mu \\ W_\mu^3 \\ X_\mu \end{pmatrix} = \begin{pmatrix} \hat{c}_{\mathrm{W}} & -\hat{s}_{\mathrm{W}}c_\xi & \hat{s}_{\mathrm{W}}s_\xi \\ \hat{s}_{\mathrm{W}} & \hat{c}_{\mathrm{W}}c_\xi & -\hat{c}_{\mathrm{W}}s_\xi \\ 0 & s_\xi & c_\xi \end{pmatrix} \begin{pmatrix} A_\mu \\ Z_\mu \\ Z'_\mu \end{pmatrix}\,, \tag{4.14}$$

where

$$t_{2\xi} = \frac{-2\,c_\epsilon(\delta m^2 + m_{\hat{Z}}^2\,\hat{s}_{\mathrm{W}}\,s_\epsilon)}{m_{\hat{X}}^2 - m_{\hat{Z}}^2\,c_\epsilon^2 + m_{\hat{Z}}^2\,\hat{s}_{\mathrm{W}}^2\,s_\epsilon^2 + 2\,\delta m^2\,\hat{s}_{\mathrm{W}}\,s_\epsilon}\,. \tag{4.15}$$

Multiplying the two matrices, we obtain the effective couplings between the Z' and quarks

$$\begin{aligned} g_u^{\mathrm{V}} &= \frac{5}{12}\frac{e\,c_\xi\,t_\epsilon}{\hat{c}_{\mathrm{W}}} + \frac{1}{4}\frac{e\,s_\xi\,t_\epsilon}{\hat{c}_{\mathrm{W}}\,\hat{s}_{\mathrm{W}}} - \frac{2}{3}\frac{e\,\hat{s}_{\mathrm{W}}\,s_\xi}{\hat{c}_{\mathrm{W}}} - \frac{c_\xi}{c_\epsilon}\,f_u^{\mathrm{V}}\,, \\ g_d^{\mathrm{V}} &= -\frac{1}{12}\frac{e\,c_\xi\,t_\epsilon}{\hat{c}_{\mathrm{W}}} - \frac{1}{4}\frac{e\,s_\xi\,t_\epsilon}{\hat{c}_{\mathrm{W}}\,\hat{s}_{\mathrm{W}}} + \frac{2}{3}\frac{e\,\hat{s}_{\mathrm{W}}\,s_\xi}{\hat{c}_{\mathrm{W}}} - \frac{c_\xi}{c_\epsilon}\,f_d^{\mathrm{V}}\,. \end{aligned} \tag{4.16}$$

[1] There could also be a mass mixing term between Z' and B, which arises e.g. in Stückelberg models. However, we consider here only such mass mixing as can be induced by a Higgs vacuum expectation value, which mixes only Z and Z'.

Note also that in the case we consider, $N_{31} = 0$, which implies that there is *no DM-photon coupling*. This result is due to the fact that we only consider mass mixing between $\hat{X}$ and the $\hat{Z}$ interaction eigenstate. If the mass mixing were to include a component with the interaction eigenstate photon $\hat{A}$, then millicharges for the DM would result [213]. In our case, an important consequence is that even if the SM fermions are charged under X as in Ref. [204], the electric charge remains *unchanged*, such that $\hat{e} = e$.

The physical Z and Z' masses after diagonalisation are given by

$$m_Z^2 = m_{\hat{Z}}^2(1 + \hat{s}_\mathrm{W}\, t_\xi\, t_\epsilon) + \delta m^2\, c_\epsilon^{-1}\, t_\xi \,, \tag{4.17}$$

$$m_{Z'}^2 = \frac{m_{\hat{X}}^2 + \delta m^2(\hat{s}_\mathrm{W}\, s_\epsilon - c_\epsilon\, t_\xi)}{c_\epsilon^2\,(1 + \hat{s}_\mathrm{W}\, t_\xi\, t_\epsilon)} \,. \tag{4.18}$$

For the 'physical' weak angle, we adopt the definition

$$s_\mathrm{W}^2\, c_\mathrm{W}^2 = \frac{\pi\, \alpha(m_Z)}{\sqrt{2}\, G_\mathrm{F}\, m_Z^2} \,, \tag{4.19}$$

where $\alpha = e^2/(4\pi)$. Eq. (4.19) is also true with the replacements $s_\mathrm{W} \to \hat{s}_\mathrm{W}$, $c_\mathrm{W} \to \hat{c}_\mathrm{W}$ and $m_Z \to m_{\hat{Z}}$, leading to the identity $s_\mathrm{W}\, c_\mathrm{W}\, m_Z = \hat{s}_\mathrm{W}\, \hat{c}_\mathrm{W}\, m_{\hat{Z}}$. From these equations we fix $\hat{s}_\mathrm{W}$ and $m_{\hat{Z}}$ such that the experimentally well-measured quantities G_F (or alternatively s_W) and m_Z come out correctly. Finally, from the mixing matrix N_{ij}, the nucleon-DM couplings can be calculated using the formulae from Sec. 4.1 [209]

$$\begin{aligned}
f_p =& \frac{\hat{g}\, f_\chi^\mathrm{V}}{4\,\hat{c}_W}\frac{c_\xi^2}{c_\epsilon} t_\xi \left[(1 - 4\hat{s}_\mathrm{W}^2)\left(\frac{1}{m_Z^2} - \frac{1}{m_{Z'}^2}\right) - 3\,\hat{s}_\mathrm{W}\frac{t_\epsilon}{t_\xi}\left(\frac{t_\xi^2}{m_Z^2} + \frac{1}{m_{Z'}^2}\right)\right] - \frac{c_\xi^2}{c_\epsilon^2} f_\chi^\mathrm{V}\frac{2\, f_u^\mathrm{V} + f_d^\mathrm{V}}{m_{Z'}^2} \,, \\
f_n =& -\frac{\hat{g}\, f_\chi^\mathrm{V}}{4\,\hat{c}_W}\frac{c_\xi^2}{c_\epsilon} t_\xi \left[\left(\frac{1}{m_Z^2} - \frac{1}{m_{Z'}^2}\right) + \hat{s}_\mathrm{W}\frac{t_\epsilon}{t_\xi}\left(\frac{t_\xi^2}{m_Z^2} + \frac{1}{m_{Z'}^2}\right)\right] - \frac{c_\xi^2}{c_\epsilon^2} f_\chi^\mathrm{V}\frac{f_u^\mathrm{V} + 2\, f_d^\mathrm{V}}{m_{Z'}^2} \,.
\end{aligned} \tag{4.20}$$

In the equations above, we have allowed for the possibility that SM fermions are charged under the new $U(1)_X$ gauge group. Couplings to leptons, however, have to be very small for the Z' masses we are interested in. The simplest way to accommodate this constraint is to assume that the Z' couples to the baryon current and hence arises from a gauged version of $U(1)_B$. Anomaly-free models for such a baryonic Z' have been considered e.g. in Refs. [214, 215]. In these models, kinetic mixing between the Z' and the SM gauge bosons is naturally induced by quark loops [215]. However, these mixing effects will typically be small compared to the direct couplings of Z' to quarks, and since up and down quarks have equal charges under the baryonic $U(1)$, one then obtains $f_n/f_p \approx 1$.

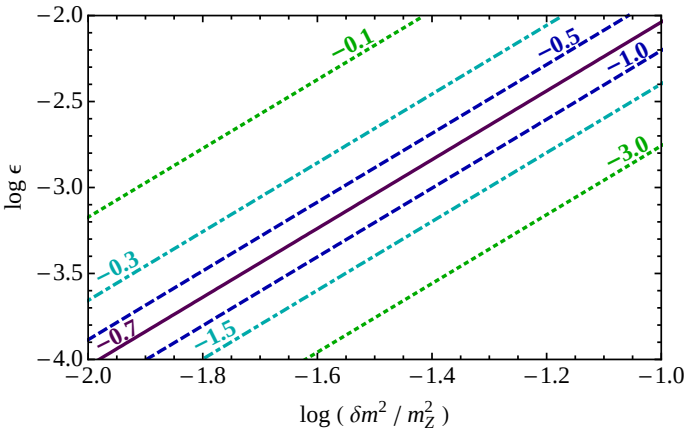

FIG. 4.1. Lines of constant f_n/f_p in the plane of kinetic and mass mixing parameters ϵ and δm. The solid purple line corresponds to $f_n/f_p \approx -0.7$. We have fixed $m_{Z'} = 4\,\text{GeV}$.

We will therefore focus on the case that the SM is completely uncharged under the $U(1)_X$. Of course, in this case the question arises how any mixing terms can be generated at all. It is known that kinetic mixing will be zero at tree level if both $U(1)$s arise from the breaking of a simple group [216]. However, if there is matter which is charged under both $U(1)$s, kinetic mixing will in general be induced at the 1-loop level. Similarly, the mass mixing term can also be generated, e.g. via the operator $\frac{1}{\Lambda^2} h^\dagger D_\mu h\, h'^\dagger D^\mu h' \to \frac{v^2 v'^2}{\Lambda^2} Z Z'$, where h' is the additional Higgs field which gives mass to the Z'. Note however that while the kinetic mixing term is renormalisable, we have to invoke higher dimensional operators to generate a mass mixing term.

If we set $\delta m^2 = 0$, i.e. consider kinetic mixing alone, the mass eigenstate Z' has photon-like couplings to quarks leading to $f_n/f_p = 0$. On the other hand, for $\epsilon = 0$, i.e. considering only mass mixing, the resulting Z' has Z-like coupling to quarks which leads to $f_n/f_p \ll -1$. If both parameters are non-zero, f_n/f_p is naturally negative, as is shown in Fig. 4.1 for $m_{Z'} = 4\,\text{GeV}$. Indeed, the value $f_n/f_p \approx -0.7$ required to evade the XENON10/100 constraints can be achieved for $\epsilon \approx \delta m^2/m_Z^2$. For this choice of parameters, and assuming $\epsilon \ll 1$, we find $\xi \approx \epsilon(1+\hat{s}_W)$, which leads to the couplings

$$f_p \simeq -\frac{\hat{g}\, f_\chi^V}{4\,\hat{c}_W} \frac{c_\xi^2}{c_\epsilon} t_\xi \frac{1}{m_{Z'}^2} \frac{3\,\hat{s}_W}{(1+\hat{s}_W)}\,, \quad f_n \simeq \frac{\hat{g}\, f_\chi^V}{4\,\hat{c}_W} \frac{c_\xi^2}{c_\epsilon} t_\xi \frac{1}{m_{Z'}^2} \left(1 - \frac{\hat{s}_W}{1+\hat{s}_W}\right)\,. \tag{4.21}$$

We therefore obtain the simple expression $f_n/f_p \approx -1/(3\hat{s}_W) \approx -0.7$.

4.3 Mixing parameters for a light Z'

In this section we discuss various constraints on a Z' with $m_{Z'} \ll m_Z$ that couples the SM to DM. In Sec. 4.4 we will then discuss constraints on a heavy Z' with $m_{Z'} \gg m_Z$. Note that we do not require the Z' interactions with the SM to yield the correct thermal relic density for χ. For a light Z', DM annihilation can be very efficient, leading to a depletion of the DM density. However, the observed relic abundance may still be obtained if there is an initial asymmetry in the dark sector (see Sec. 1.4). Conversely, for a heavy Z' but low mass DM, the interactions are typically so weak that they predict an overproduction of DM in the early universe. To obtain the required DM relic density in this scenario, one must assume either a contribution from additional mediators in the early Universe or additional couplings of the Z' to new hidden sector states.

Before discussing experimental bounds, let us determine the interesting parameter values for direct detection experiments. We have seen in Sec. 3.3 that assuming elastic SI scattering with $f_n/f_p = -0.7$, experimental hints for DM imply $m_\chi \sim 10\,\text{GeV}$ and $\sigma_{\text{SI}} \sim (10^{-39}\text{–}10^{-38})\ \text{cm}^2$. If we fix the kinetic mixing ϵ by the requirement $f_n/f_p \approx -0.7$, there are three remaining free parameters in our model:[1] $m_{Z'}$, δm and f_χ^{V}. As an example we take $m_{Z'} = 4\,\text{GeV}$, $\delta m = 8\,\text{GeV}$ and $m_\chi = 8\,\text{GeV}$, leading to $\epsilon = 0.007$ and $\xi = 0.011$. Using Eqs. (2.12) and (4.9), the resulting SI scattering cross section is

$$\sigma_n \simeq 8 \times 10^{-37}\,(f_\chi^{\text{V}})^2\,\text{cm}^2\,. \tag{4.22}$$

Thus, a sufficiently large cross section can easily be achieved for $f_\chi^{\text{V}} \sim 0.1$. Even for smaller mixing parameters or a somewhat heavier Z' larger values of f_χ^{V} could still lead to cross sections of the required magnitude. In fact, there is no reason why f_χ^{V} cannot be as large as its perturbative bound $f_\chi^{\text{V}} \lesssim \sqrt{4\pi}$. Note however, that since $\sigma_n \propto m_{Z'}^{-4}$, the cross section quickly becomes too small if $m_{Z'}$ is larger than about 15 GeV.

Electroweak precision tests

The constraints from electroweak precision tests (EWPT) are encoded in the S and T parameters. To determine these parameters, we use the effective Lagrangian formulation of the interaction

[1] Note that ξ is fixed as soon as δm and $m_{Z'}$ are determined and that the DM-neutron cross section is largely independent of the DM mass as long as $m_\chi \gg m_n$.

between the Z boson and the SM fermions [204, 217]:

$$\mathcal{L}_Z = -\frac{e}{2\,s_{\rm W}\,c_{\rm W}}\left(1+\frac{\alpha\,T}{2}\right) \times \bar{f}\gamma^\mu\left[\left(T_3^f - 2Q^f\left(s_{\rm W}^2 + \frac{\alpha\,S - 4c_{\rm W}^2\,s_{\rm W}^2\,\alpha\,T}{4(c_{\rm W}^2 - s_{\rm W}^2)}\right)\right) - T_3^f\gamma^5\right] f\,Z_\mu\,. \tag{4.23}$$

We can then determine S and T to quadratic order in ξ and ϵ, finding[1]

$$\alpha\,S = 4\,c_{\rm W}^2\,s_{\rm W}\,\xi\,(\epsilon - s_{\rm W}\xi)\,, \quad \alpha\,T = \xi^2\left(\frac{m_{Z'}^2}{m_Z^2} - 2\right) + 2\,s_{\rm W}\,\xi\,\epsilon\,. \tag{4.24}$$

In the framework that we consider, one typically has $\epsilon > s_{\rm W}\,\xi$ so that the S parameter is slightly positive. On the other hand, for $m_{Z'} < m_Z$ the T parameter will generally be negative. In this direction, S and T are tightly constrained. Nevertheless, given that our preferred parameter region corresponds to $\xi \sim \epsilon \sim 0.01$, we find $S \approx 0.01$ and $T \approx -0.015$, which is within the 95% CL PDG constraints [136].

Similarly we find that the ρ parameter, given by

$$\rho = \frac{m_{\rm W}^2}{m_Z^2\,c_{\rm W}^2} = \frac{s_{\rm W}^2}{\hat{s}_{\rm W}^2}\,, \tag{4.25}$$

is in slight tension but still reasonable agreement with experimental constraints. To quadratic order in ξ and ϵ we obtain

$$\rho - 1 = \frac{c_{\rm W}^2\,\xi^2}{c_{\rm W}^2 - s_{\rm W}^2}\left(\frac{m_{Z'}^2}{m_Z^2} - 1\right)\,, \tag{4.26}$$

which gives $\rho - 1 = -3\times10^{-4}$ for $\xi = 0.015$ in comparison with a measured value [136] of $\rho - 1 = 4^{+8}_{-4}\times10^{-4}$.

Z decay width

The induced coupling of the Z to the DM particle increases the invisible Z decay width. The contribution is approximately

$$\Gamma(Z\to\bar{\chi}\chi) = \frac{m_Z}{12\pi}\left(|g_{\chi Z}^{\rm V}|^2 + |g_{\chi Z}^{A}|^2\right) = \frac{m_Z}{12\pi}s_\xi^2\left(|f_\chi^{\rm V}|^2 + |f_\chi^{A}|^2\right)\,. \tag{4.27}$$

[1] Note that due to the requirement $f_n/f_p \approx -0.7$, ϵ must be of the same order of magnitude as ξ. We therefore have a term -2 appearing in the expression for T as opposed to a -1 in Ref. [204].

Consequently, as long as $s_\xi < 0.015$, we satisfy the experimental limit $\Gamma(Z \to \bar{\chi}\chi) < 1.5\,\text{MeV}$ even for $f_\chi \sim 1$.

Muon $g-2$

In the presence of a new vector mediator the anomalous magnetic moment of the muon will generally change. In the case of a dark Z' with $m_{Z'} \ll m_Z$, the contribution to $a_\mu = (g_\mu - 2)/2$ can be estimated to be [209]

$$\delta a_\mu \simeq \frac{\alpha\,\xi^2}{3\pi\,c_\text{W}^2\,s_\text{W}^2}\frac{m_\mu^2}{m_{Z'}^2} \tag{4.28}$$

up to a factor of order unity.[1] The requirement $\delta a_\mu \sim 4 \times 10^{-9}$ then implies an approximate limit of $m_{Z'} \gtrsim 1\,\text{GeV}$ for $\xi \sim 10^{-2}$.

Atomic parity violation

The contribution of the Z' to atomic parity violation (APV) is proportional to the product of the axial coupling of the Z' to electrons, $g_{eZ'}^A$, and the vector coupling to quarks, $g_{qZ'}^\text{V}$. In practice, however, one can only measure the vector coupling to an entire nucleus, which is proportional to $Zf_p + (A-Z)f_n$. Since f_p and f_n have different signs in all the cases that we consider, the two contributions nearly cancel, so that no relevant constraint arises from APV. In fact, the strongest bounds on APV come from measurements of cesium, which has almost the same ratio of protons to neutrons as xenon. Consequently, if indeed $f_n/f_p \approx -0.7$, the Z' will give almost no contribution to APV in cesium.

Hadronic decays

Measurements of the decays of ψ and Υ strongly constrain the axial coupling of the Z' to c and b quarks. According to Ref. [218], these limits are

$$|g_c^A| \lesssim 1.5 \times 10^{-3}\frac{m_{Z'}}{\text{GeV}}\,, \tag{4.29}$$

$$|g_b^A| \lesssim 0.8 \times 10^{-3}\frac{m_{Z'}}{\text{GeV}}\,. \tag{4.30}$$

[1] Here we assume that there are no cancellations between the axial and the vectorial part.

In our model, there is no direct axial coupling of the Z' to quarks, so that such a coupling can only arise from Z-Z' mixing. The resulting coupling constants are proportional to ξ, but can nevertheless become too large unless $m_{Z'} \gtrsim 1\,\text{GeV}$. The constraint for vector couplings is significantly weaker (especially if the decay of the Υ into two DM particles is kinematically not possible). In fact, according to Ref. [219] it is easily possible to have $|g_q^{\text{V}}| \sim 0.1$. Ongoing and forthcoming searches for a light Z' at collider experiments such as BaBar, Belle, BEPC and LHCb will be able to constrain these parameters more tightly [220].

Spin-dependent interactions

If the Z' couples to the axial DM current, one obtains an effective axial-axial coupling between the DM particle and quarks given by

$$b_q^{\text{A}} = \frac{g_\chi^{\text{A}}\, g_q^{\text{A}}}{m_{Z'}^2}\,, \tag{4.31}$$

neglecting the contribution of the Z, which gives a correction of order 1%. From Eq. (4.6) it follows that $b_d^{\text{A}} = b_s^{\text{A}} = -b_u^{\text{A}}$. Consequently, we obtain from Eq. (2.15)

$$\begin{aligned} a_p &= -1.36\, b_d^{\text{A}}\,, \\ a_n &= 1.18\, b_d^{\text{A}}\,, \end{aligned} \tag{4.32}$$

implying that the DM particle couples with roughly the same strength but *opposite* sign to the proton and neutron spin.

Using the results from Sec. 4.2 and Eq. (2.13), we find

$$\begin{aligned} \sigma_{p,n}^{\text{SD}} &\simeq 0.1 \frac{\mu_\chi^2}{m_{Z'}^4} \hat{g}'^2 (f_\chi^{\text{A}})^2 \left(\frac{c_\xi}{c_\epsilon}\right)^2 \left(\hat{s}_{\text{W}} s_\xi - c_\xi t_\epsilon + \frac{\hat{c}_{\text{W}}^2}{\hat{s}_{\text{W}}} s_\xi\right)^2 \\ &\simeq 3 \times 10^{-36}\,\text{cm}^2 (f_\chi^{\text{A}})^2\,, \end{aligned} \tag{4.33}$$

where in the second line we have substituted the same benchmark parameters as for the calculation of the SI cross section. For $f_\chi^{\text{A}} \sim f_\chi^{\text{V}}$, the SD cross section therefore is significantly larger than the SI one. Furthermore, for $f_n/f_p \sim -0.7$, SI interactions do not benefit from a large coherent enhancement, so that for comparable vector and axial couplings of the Z' both types of interactions should give similar signals in direct detection experiments. Consequently, both contributions should

be included when interpreting direct detection experiments in the context of this model. We leave such a study to future work.

4.4 Mixing parameters for a heavy Z'

We now turn to the case of a Z' with $m_{Z'} \gg m_Z$. In this case, most of the constraints discussed above will become weak. The notable exception are the constraints arising from measurements of the Z-pole, which directly constrain the magnitude of the mixing between Z and Z' independent of $m_{Z'}$. In addition, there will be a large number of additional constraints arising from the fact that a heavy Z' will be resonantly produced at colliders and its decays into SM particles can lead to observable signals. We will now consider these constraints in detail, beginning with a discussion of Z' production.

4.4.1 Production and decay of a heavy Z' at colliders

We can decompose the cross section for the production of a Z' in association with additional particles Y and subsequent decay of Z' into xy as follows:

$$\sigma(q\bar{q} \to Z' + Y \to xy + Y) = \sigma(q\bar{q} \to Z' + Y) \cdot \mathrm{BR}(Z' \to xy) \,, \tag{4.34}$$

where we have used the narrow width approximation (NWA), applicable if $\Gamma_{Z'}/m_{Z'} \ll 1$. Possible ways to produce a heavy Z' at colliders are Drell-Yan (D-Y) production, vector boson fusion (VBF) or 'Z'-Strahlung' from a SM gauge boson. Here, we will focus on D-Y production.

As a consequence of the NWA, the D-Y cross section $\sigma(q\bar{q} \to Z' \to xy)$ can be written in terms of the couplings $g_{u,d} \equiv \sqrt{(g^V_{qR})^2 + (g^A_{qR})^2}$ of the Z' to quarks as [221, 222]

$$\sigma_{xy} \propto \left[g_u^2 \, w_u(\sqrt{s}, m^2_{Z'}) + g_d^2 \, w_d(\sqrt{s}, m^2_{Z'}) \right] \cdot \mathrm{BR}(Z' \to xy) \,, \tag{4.35}$$

where $w_{u,d}$ parameterise the parton distribution functions (PDFs) of the proton. The coefficients $w_{u,d}$ are known and for a narrow resonance depend only on the centre-of-mass energy $\sqrt{s}$ and $m_{Z'}$. In Fig. 4.2 we show the leading order (LO) cross section for $\sigma(pp \to Z')$ with the couplings $g_{u,d}$ set equal to those of the SM Z boson, as well as the individual contributions from u- and d-quarks. For different quark couplings the production cross section of the Z' may then be found by a simple rescaling. Note that QCD corrections can enhance the D-Y production significantly. In

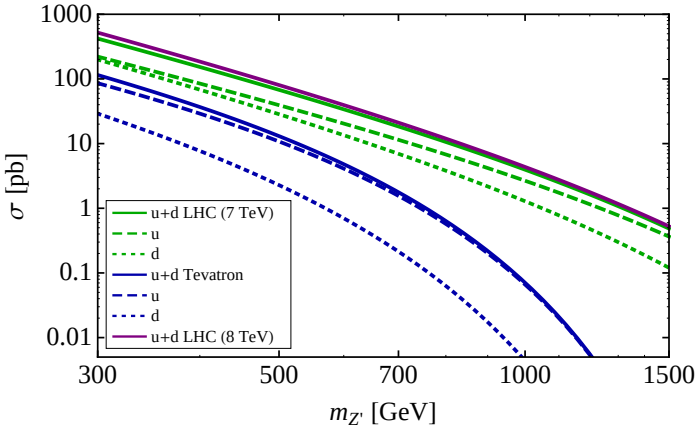

FIG. 4.2. Cross section for the D-Y production of a Z' as a function of $m_{Z'}$ at the LHC (with $\sqrt{s} = 7\,\text{TeV}$ and $\sqrt{s} = 8\,\text{TeV}$) and at the Tevatron for $g_{u,d}^{A,V}$ equal to those of the SM Z boson (solid lines). We also show the production cross section for the case that the Z' couples either only to u-quarks or only to d-quarks.

the following, we take the K-factors for the `MSTW2008NNLO` PDF from Ref. [222].

In order to calculate the total cross section for a given process, the remaining task is to calculate the branching ratios. Since $\text{BR}(Z' \to xy) = \Gamma^{xy}/\Gamma_{Z'}$, we need to calculate the partial decay widths Γ^{xy} and the total decay width $\Gamma_{Z'}$. Let us therefore now discuss all possible decay channels of a heavy Z' into SM particles. We will present this discussion in full generality first, and then determine the relevant terms subsequently.

4.4.2 Interactions with SM bosons

In addition to the couplings of the Z' to SM fermions and to DM discussed above, we now also consider terms in the Lagrangian that represent couplings to SM gauge bosons and the Higgs:

$$\mathcal{L}^{Z'} = \mathcal{L}^{Z'}_{\text{DM}} + \mathcal{L}^{Z'}_{f\bar{f}} + \mathcal{L}^{Z'}_{\text{gauge}} + \mathcal{L}^{Z'}_{H} \ . \tag{4.36}$$

Neglecting non-renormalisable operators and CP-violating terms (see e.g. Refs. [223, 224] for a more complete discussion) the couplings of a general vector mediator R to SM gauge fields can be written as

$$\begin{aligned}\mathcal{L}^{R}_{\text{gauge}} =& g^{R}_{WW1}[[RW^+W^-]]_1 + g^{R}_{WW2}[[RW^+W^-]]_2 \\ &+ g^{R}_{ZWW1}((RZW^+W^-)) + g^{R}_{\gamma WW1}((R\gamma W^+W^-))\end{aligned}$$

$$+ g^R_{ZZ}[[RZZ]]_\epsilon + g^R_{Z\gamma}[[RZ\gamma]]_\epsilon + g^R_{WW3}[[RW^+W^-]]_\epsilon$$
$$+ g^R_{ZWW2}\epsilon^{\mu\nu\rho\sigma}R_\mu Z_\nu W^+_\rho W^-_\sigma + g^R_{\gamma WW2}\epsilon^{\mu\nu\rho\sigma}R_\mu\gamma_\nu W^+_\rho W^-_\sigma \ , \tag{4.37}$$

where

$$\begin{aligned}
[[RW^+W^-]]_1 &\equiv i\left[(\partial_\mu W^+_\nu - \partial_\nu W^+_\mu)W^{\mu-}R^\nu - (\partial_\mu W^-_\nu - \partial_\nu W^-_\mu)W^{\mu+}R^\nu\right] \ , \\
[[RW^+W^-]]_2 &\equiv \frac{i}{2}(\partial_\mu R_\nu - \partial_\nu R_\mu)(W^{\mu+}W^{\nu-} - W^{\mu-}W^{\nu+}) \ , \\
[[RV_1V_2]]_\epsilon &\equiv \epsilon^{\mu\nu\rho\sigma}(V_{1\mu}\partial_\rho V_{2\nu} - \partial_\rho V_{1\mu}V_{2\nu})R_\sigma \ , \\
((RVW^+W^-)) &\equiv 2R_\mu V^\mu W^-_\nu W^{\nu+} - R_\mu W^{\mu+}V_\nu W^{\nu-} - R_\mu W^{\mu-}V_\nu W^{\nu+}
\end{aligned} \tag{4.38}$$

for appropriate combinations of $V_i = \{\gamma, Z, W^+, W^-\}$. The operators in the first two lines of Eq. (4.37) conserve C and P separately, while the operators in the last two lines are CP even but violate parity. The operators in the second and fourth line lead to decays into three gauge bosons. For comparable couplings these decays are suppressed compared to diboson final states due to smaller available phase space [225]. We will therefore neglect triboson decays in the following.

Couplings of R to the SM Higgs are of the form

$$\mathcal{L}^R_H = \ g^R_{ZH}R_\mu Z^\mu H + g^R_{ZHH}R_\mu Z^\mu H^2 \ . \tag{4.39}$$

Again, we expect decays into ZHH to be significantly suppressed compared to decays into ZH so we neglect them from now on. Since H is a real scalar and terms proportional to $\partial_\mu R^\mu$ are CP violating we do not consider decays of R into HH [223].

Let us now return to the case of a Z' with mixing. In terms of the mixing matrix in Eq. (4.5), the couplings of Z' to SM bosons are given by [209]

$$g^{Z'}_{WW1} = g^{Z'}_{WW2} = \hat{g}N_{23} \ , \qquad g^{Z'}_{ZH} = \frac{v}{2}(\hat{g}'N_{12} - \hat{g}N_{22})(\hat{g}'N_{13} - \hat{g}N_{23}) \ . \tag{4.40}$$

Note that, since P-violating couplings of gauge bosons are absent in the SM, the corresponding couplings of the Z' cannot be introduced by mixing alone.

4.4.3 Experimental constraints

Using the results from Sec. 4.2, we can calculate all couplings of the Z' as a function of $m_{Z'}$, δm, $\sin\epsilon$ and f^V_χ. As an example, we show the couplings $g_{u,d}$, which determine the Z' production cross

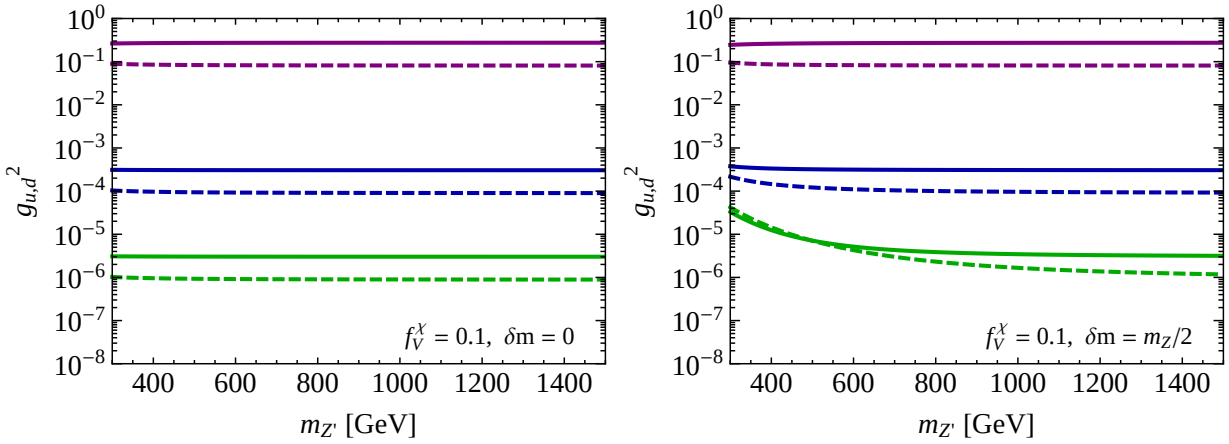

FIG. 4.3. The couplings g_u^2 (solid lines) and g_d^2 (dashed lines) as a function of $m_{Z'}$ for $\epsilon = 0.01$ (green), $\epsilon = 0.1$ (blue) and $\epsilon = 1$ (purple). In the left plot, interactions are induced by kinetic mixing only via the Lagrangian given in Eq. (4.12), while in the right plot we have included a mass mixing of $\delta m = m_Z/2$.

section, in Fig. 4.3 as a function of $m_{Z'}$ for different values of the kinetic mixing parameter ϵ and the mass mixing parameter δm. The partial decay widths in terms of the various couplings are summarised in Appendix A.6. For example, we are now in the position to calculate the invisible branching ratio of the Z', which is given by $BR(Z' \to \text{inv}) = (\Gamma^{\chi\bar{\chi}} + \Gamma^{\nu\bar{\nu}})/\Gamma_{Z'}$. Although invisible Z' decays are not directly observable, one can obtain monojet events if the Z' is produced in association with a jet ($j = q, g$), which can result for example from ISR (see Sec. 2.3).

To derive constraints on such invisible decays — and therefore on f_χ^V — we use the monojet search from CMS based on an integrated luminosity of $5.0\,\text{fb}^{-1}$ at $\sqrt{s} = 7$ TeV [125]. CMS considered events with $\not{E}_T > 350$ GeV, provided there was a primary jet (j_1) with transverse momentum $p_T > 110$ GeV and pseudorapidity $|\eta| < 2.4$. A secondary jet (j_2) with $p_T > 30$ GeV was also permitted if the two jets are not back-to-back: $|\Delta\phi(j_1, j_2)| < 2.5$. Events with high-$p_T$ tertiary jets, electrons or muons were vetoed. This null result excludes new contributions to the production cross section in excess of 32 fb at 95% CL. The corresponding ATLAS search [126] employs very similar cuts and finds a comparable bound on the cross section.

We compare this experimental bound with the predicted monojet signal from the invisible decays of a Z' simulated at parton-level using `CalcHEP` [226]. Since the experimental searches impose a cut on the number of additional jets, including parton showering and hadronisation typically leads to a slight reduction in the predicted cross sections even after including next-to-leading order (NLO)

Channel (Exp)	L [fb^{-1}]	Mass range	Couplings	Reference
$pp \to j\,j$ (CMS)	4.0 (8 TeV)	$1000 - 4000$	g_q	[232]
$pp \to j\,j$ (CMS)	0.13 (7 TeV)	$600 - 1000$	g_q	[233]
$pp \to j\,j$ (CDF)	1.13 (1.96 TeV)	$250 - 1400$	g_q	[234]
$pp \to t\,\bar{t}$ (CMS)	19.7 (8 TeV)	$500 - 3000$	$g_q\,g_t$	[235]
$pp \to \ell\ell$ (ATLAS)	20 (8 TeV)	$200 - 3500$	$g_q\,g_\ell$	[236]
$pp \to \tau\tau$ (CMS)	4.9 (7 TeV)	$350 - 1700$	$g_q\,g_\tau$	[237]
$pp \to j + \not{E}_T$ (CMS)	5.0 (7 TeV)	$*$	$g_q\,g_\chi$	[125]
$pp \to j + \not{E}_T$ (ATLAS)	4.7 (7 TeV)	$*$	$g_q\,g_\chi$	[126]
$pp \to j + \not{E}_T$ (CDF)	1.0 (1.96 TeV)	$*$	$g_q\,g_\chi$	[124]
$pp \to \gamma + \not{E}_T$ (CMS)	5.0 (7 TeV)	$*$	$g_q\,g_\chi\,,\ g_q\,g^R_{Z\gamma}$	[230]
$pp \to Z\,Z$ (ATLAS)	7.2 (8 TeV)	$300 - 2000$	$g_q\,g^R_{ZZ}$	[238]
$pp \to Z\,Z$ (CMS)	19.8 (8 TeV)	$600 - 2500$	$g_q\,g^R_{ZZ}$	[239]
$pp \to W\,W$ (ATLAS)	4.7 (7 TeV)	$300 - 1500$	$g_q\,g^R_{WW}$	[240]
$pp \to W\,W$ (CMS)	19.8 (8 TeV)	$800 - 2500$	$g_q\,g^R_{WW}$	[241]
$pp \to ZH$ (ATLAS)	4.7 (7 TeV) 20.3 (8 TeV)	$*$	$g_q\,g^R_{ZH}$	[242]

TABLE 4.1. Collider searches for various final states that constrain the couplings of a vector mediator. For resonance searches the mass range of the search is given, other searches are marked with a $*$. These searches can be applied to a wide range of mediator masses. In the case of scalar DM g_χ should be replaced by g_ϕ.

corrections [227]. For our purposes, however, these effects can be neglected. We have also checked explicitly that using the ATLAS data instead of the CMS data does not modify our results within errors.

In a similar way, one can constrain invisible decays of the Z' using searches for monophoton events, where instead of a jet a single photon is produced from ISR. The recoil of this photon against the invisible decay products of the Z' then leads to large amounts of $\not{E}_T$. Monophoton searches were first performed at LEP [228] and subsequently at the LHC by ATLAS [229] and CMS [230].

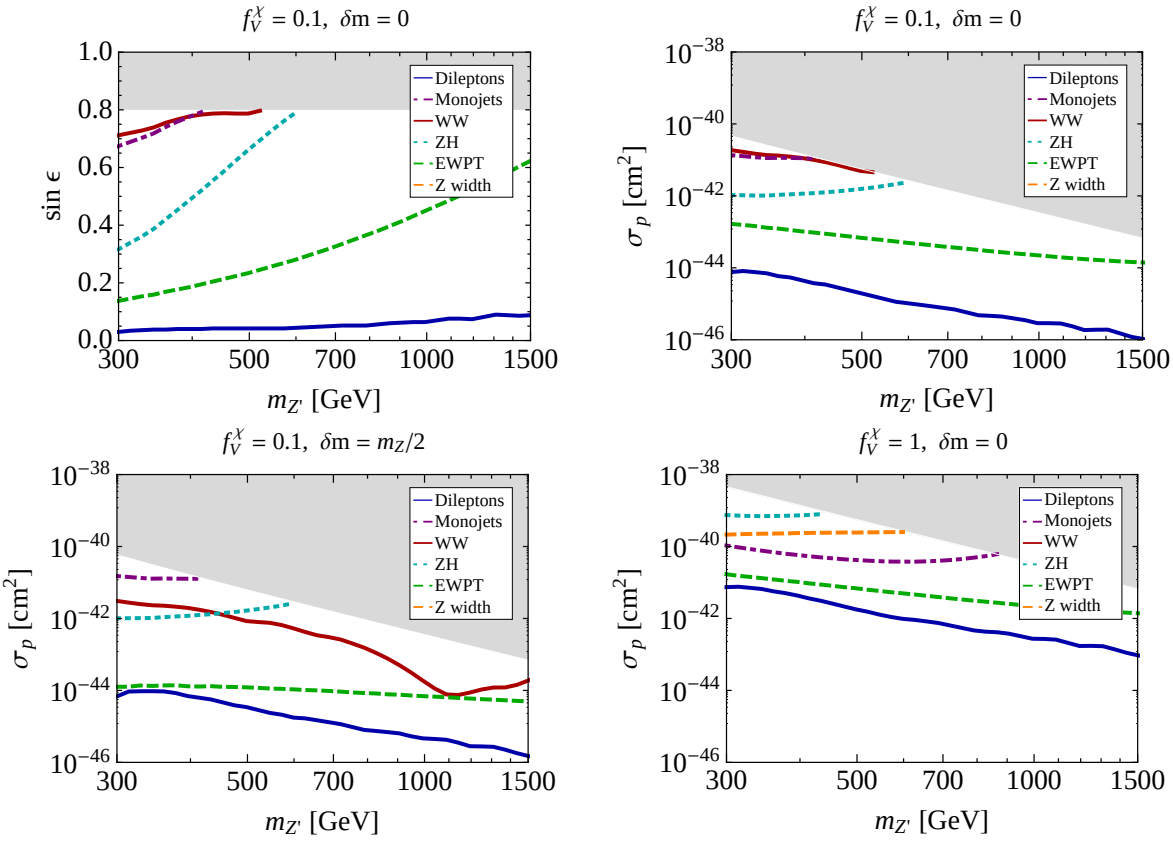

FIG. 4.4. Upper row: Bounds on the mixing parameter $\sin\epsilon$ and the direct detection cross section σ_p for $f_\chi^V = 0.1$ and $\delta m = 0$. Lower row: Bounds on the direct detection cross section for different choices of f_χ^V and δm. The grey shaded regions correspond to $\sin\epsilon > 0.8$. The parameter region above each line is excluded at 95% CL.

These searches are particularly interesting for a leptophilic Z' [130, 231]. If the Z' has comparable couplings to quarks and to leptons, however, monojet searches typically provide stronger constraints on the invisible branching ratio of the Z', since the ISR of a photon is suppressed compared to a jet.

In addition to monojet and monophoton searches, there are three further interesting search channels at the LHC: Dilepton resonances, WW resonances and ZH production. A summary of the experimental searches is given in Table 4.1. The resulting bounds directly constrain the mixing parameters ϵ and ξ. For fixed mass mixing and fixed direct couplings, these constraints can thus be interpreted as bounds on $\sin\epsilon$ as a function of $m_{Z'}$, which in turn can be translated into bounds on the DM direct detection cross section using Eqs. (2.12) and (4.9). Our results are presented in Fig. 4.4. Note that we do not consider values of $\sin\epsilon$ larger than 0.8.

For $f_\chi^V = 0.1$ and $\delta m = 0$, the LHC gives strong constraints on the direct detection cross

section, comparable to the best bounds from current direct detection experiments. In fact, searches for dilepton resonances are even more constraining than the EWPT discussed in Sec. 4.3. This conclusion does not change significantly, if we include a mass mixing term (see lower-left panel of Fig. 4.4). However, such a mass mixing will enhance ξ compared to ϵ, so the bound from WW resonance searches becomes stronger compared to the bound from dileptons and monojets. In fact, the limit from WW searches becomes very constraining for large $m_{Z'}$, because the interaction between the gauge bosons involves a derivative and is therefore enhanced for large masses.[1]

Increasing f_χ^V relaxes all bounds from the LHC since now smaller quark couplings — and therefore smaller mixing parameters — are sufficient to obtain similar direct detection cross section. At the same time the invisible partial width of Z' is increased so that decays of Z' into SM particles are additionally suppressed. Monojet searches, on the other hand, become significantly more constraining. Thus, even for $f_\chi^V = 1$, direct detection cross section above 10^{-41} cm^2 are excluded by dilepton and monojet searches as well as EWPT. Clearly, it is very difficult in this context to achieve direct detection cross sections large enough to explain recent experimental anomalies and impossible to do so if also imposing $f_n/f_p = -0.7$.

4.5 LHC and Tevatron bounds for general vector mediators

As we have seen above, there are strong constraints on a heavy spin-1 mediator that obtains its couplings to SM particles from kinetic mixing and mass mixing due to its interactions with SM leptons and gauge bosons. However, none of these interactions are actually required to obtain large DM scattering cross sections, and the direct couplings of the mediator to SM quarks are not very strongly constrained by collider searches. In this section, we will therefore study how much the constraints discussed above can be weakened if we consider less restrictive models, where the couplings to different types of particles can be varied independently. To make this change of perspective explicit, we will go back to denoting the spin-1 mediator by R rather than Z'.

We are particularly interested in the case where R has large couplings to SM quarks. We allow for the ratio $y \equiv g_{uR}^V/g_{dR}^V$ to take arbitrary values, so that $f_n/f_p = (y+2)/(2y+1)$ can differ

[1] Note, however, that for small kinetic mixing, the coupling of Z' to quarks and leptons is proportional to $c_\xi\, t_\epsilon \approx \epsilon$, while the coupling of Z' to WW is proportional to $s_\xi \approx \epsilon \sin\theta_W M_Z^2/m_R^2$. Thus, the partial width Γ^{WW} picks up an additional factor of $m_Z^4/m_{Z'}^4$ which reduces the enhancement from the derivative interaction.

significantly from the coupling ratio for Z exchange. A possible example for such a mediator is a new resonance associated with a strongly interacting extension of the SM [243, 244], e.g. an analogue of the neutral isospin zero ω resonance in QCD. Another possibility (although without isospin violation) would be a baryonic Z' as discussed in Ref. [245]. We will show that, in spite of the very general treatment, it is still possible to constrain the direct detection cross section in a *model independent* way by combining the limits from all relevant collider searches.

The key assumption that we have to make is that R decays either directly into SM particles or into new states that remain invisible, i.e. escape the detector without decaying into visible particles. In other words, decays into other hidden sector states are either kinematically forbidden or give a negligible contribution to the total width. This assumption is necessary because if we were to allow decays into new states that give complicated (and hence unobservable) experimental signatures, we could make Γ_R arbitrarily large and thereby completely hide the resonance at the LHC. Instead, making use of our assumption, we can write

$$\Gamma_R = \Gamma^{\chi\bar{\chi}} + \sum_q \Gamma^{q\bar{q}} + \sum_\ell \Gamma^{\ell\bar{\ell}} + \sum_\nu \Gamma^{\nu\bar{\nu}} + \Gamma^{WW} + \Gamma^{ZZ} + \Gamma^{\gamma Z} + \Gamma^{ZH} \,. \tag{4.41}$$

The formulae for the partial widths in terms of the couplings are given in Appendix A.6.

From Eq. (2.12) we obtain

$$\sigma_p \simeq (2y+1)^2 \, \frac{\mu_{\chi n}^2}{\pi} \, \frac{\left(g_{dR}^V\right)^2 \left(g_{\chi R}^V\right)^2}{m_R^4} \leq (2y+1)^2 \, \frac{\mu_{\chi n}^2}{\pi} \, \frac{g_d^2 \, g_\chi^2}{m_R^4} \,, \tag{4.42}$$

where we have introduced $g_f^2 \equiv \left(g_{fR}^V\right)^2 + \left(g_{fR}^A\right)^2$. For $m_\chi \ll m_R$ we can use the formula for $\Gamma^{\chi\bar{\chi}}$ given in Eq. (A.33) to express g_χ^2 in terms of the partial decay width:

$$\sigma_p \leq 12 \, (2y+1)^2 \, \frac{\mu_{\chi n}^2}{m_R^5} \, g_d^2 \, \Gamma^{\chi\bar{\chi}} \,. \tag{4.43}$$

We can then use the fact that $\Gamma^{\chi\bar{\chi}} \leq \Gamma_R \cdot \mathrm{BR}(R \to \mathrm{inv})$ to obtain

$$\sigma_p \leq 12 \, (2y+1)^2 \, \frac{\mu_{\chi n}^2 \, \Gamma_R}{m_R^5} \, g_d^2 \cdot \mathrm{BR}(R \to \mathrm{inv}) \,. \tag{4.44}$$

As discussed in Sec. 4.4, monojet and monophoton searches at the LHC provide a limit on the combination $g_q^2 \cdot \mathrm{BR}(R \to \mathrm{inv})$. Consequently, if we can constrain Γ_R, Eq. (4.44) gives a bound on the direct detection cross section as a function of m_R.

In order to obtain such a bound, let us assume that we can constrain $g_q^2 \cdot \mathrm{BR}(R \to xy) \leq s_{xy}$ for

all possible final states. We can then sum these bounds to obtain an upper limit

$$g_q^2 \leq s_{\text{tot}} = \sum_{xy} s_{xy} \,, \tag{4.45}$$

since the branching ratios must sum to unity. In other words, for $g_q^2 > s_{\text{tot}}$ the total number of R produced would be so large that its decays would *have to* leave an observable signal in at least one search channel. As we will now show, it is indeed possible to combine the information from a large number of different LHC searches to make sure that R has no place to hide.

We have already discussed a number of possible decay channels in the context of a Z' with mixing. Now that we allow for arbitrary couplings, we also need to constrain the remaining decay channels, in particular decays into quarks. Searches for resonances in the invariant mass distribution of dijet events have been carried out at Tevatron [234] and at the LHC [232, 233, 246]. For invariant masses below 600 GeV, the sensitivity of the LHC is compromised by large QCD backgrounds. We therefore use the CDF limit [234] for $300\,\text{GeV} < m_R < 600\,\text{GeV}$. Above 1000 GeV, we use the most recent full analysis from CMS [232]. The intermediate range from 600 GeV to 1000 GeV has been studied by CMS using a dedicated search based on an alternative analysis strategy with modified triggers [233]. The comparison of all these bounds is shown in Fig. 4.5. The bounds from the CMS searches are shown as bands, reflecting how the limit changes depending on the precise width and shape of the resonance. We take the upper end of both bands shown in Fig. 4.5 as a conservative bound for all widths.

Searches for dijet resonances constrain the decays of R into the five lightest quarks. To constrain $g_q^2 \cdot \text{BR}(R \to t\bar{t})$ independently, we use the dedicated CMS searches [235] for $t\bar{t}$ resonances. The resulting bounds are shown in Fig. 4.6. For family independent couplings and assuming $m_R > 2m_t$ one can use a bound on $g_q^2 \cdot \text{BR}(R \to jj)$ to infer a bound on $g_q^2 \cdot \text{BR}(R \to t\bar{t})$ via the relation

$$\text{BR}(R \to t\bar{t}) = \frac{\sqrt{1 - 4m_t^2/m_R^2}}{2 + 3g_d^2/g_u^2} \cdot \text{BR}(R \to jj) \,. \tag{4.46}$$

For $g_u \sim g_d$, the resulting bound on $g_q^2 \cdot \text{BR}(R \to t\bar{t})$ inferred from the dijet limit is comparable to the direct bound from top pair searches. As expected, for $g_u \ll g_d$, the inferred bound on $g_q^2 \cdot \text{BR}(R \to t\bar{t})$ is much stronger than the direct one, while for $g_u \gg g_d$, we can actually invert the equation above to obtain a bound on $g_q^2 \cdot \text{BR}(R \to jj)$ from the bounds on $g_q^2 \cdot \text{BR}(R \to t\bar{t})$.

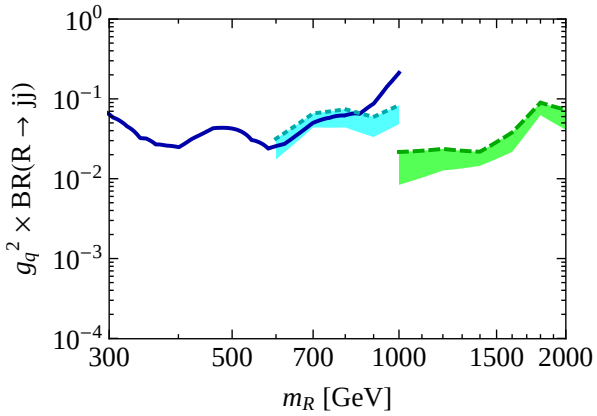

FIG. 4.5. Dijet limits from CDF [234] (blue), from CMS [232] (green, dashed) and from the CMS low-mass analysis [233] (cyan, dotted).

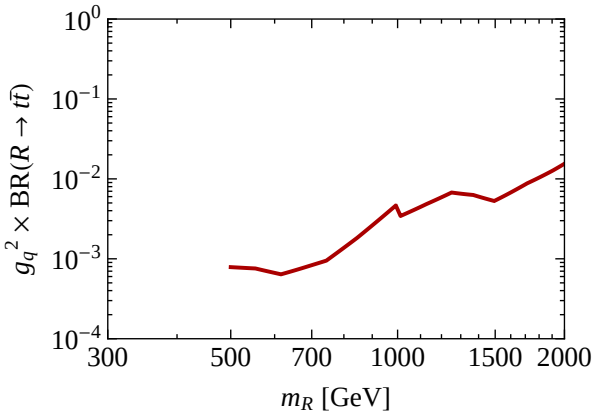

FIG. 4.6. Limit on $g_q^2 \cdot \mathrm{BR}(R \to t\bar{t})$ from CMS [235]. Note that CMS studies different topologies for $m_R < 1$ TeV and $m_R > 1$ TeV.

Finally, we also need to constrain decays of R into ZZ and $Z\gamma$, which were absent for the Z' because of their parity violating nature. The former decay is strongly constrained by searches for ZZ resonances [238, 239]. For the latter decay, there are no dedicated searches, but we can obtain a sufficiently strong constraint from monophoton searches. We have previously discussed monophoton searches in the context of constraining invisible decays of R. However, another way to obtain a single photon in association with $\not{E}_T$ is D-Y production of R followed by the direct decay of R into $Z\gamma$, with subsequent decay of Z to neutrinos $\sigma(pp \to R \to \gamma Z \to \gamma\, \nu\bar{\nu})$. Note, however, that such monophoton searches are only sensitive to these decays if $m_R/2$ is sufficiently larger than any cut on $\not{E}_T$ or the photon p_T. We use the data from CMS [230] and `CalcHEP` for the signal prediction. Note that the limits on the direct decay $R \to Z\gamma$ have been calculated without including the contribution of invisible decays of R together with a photon from ISR. For sizeable invisible branching of R the bounds would therefore become even stronger.

A summary of all limits is shown in Fig. 4.7. We observe that there is indeed a bound for every decay channel mentioned in Eq. (4.41). We are therefore in the position to sum all experimental bounds in order to infer a bound on g_q^2 using Eq. (4.45). The result is shown in Fig. 4.8. The final step in order to constrain direct detection cross sections, is now to extract an upper bound on Γ_R. However, it is not necessarily true that maximising g_q^2 will also maximise Γ_R. In particular, if the quark couplings satisfy $g_q^2 < s_{xy}$ for one particular channel with final state xy, we can increase the couplings of R to xy — and thereby the width Γ_R — arbitrarily without being excluded

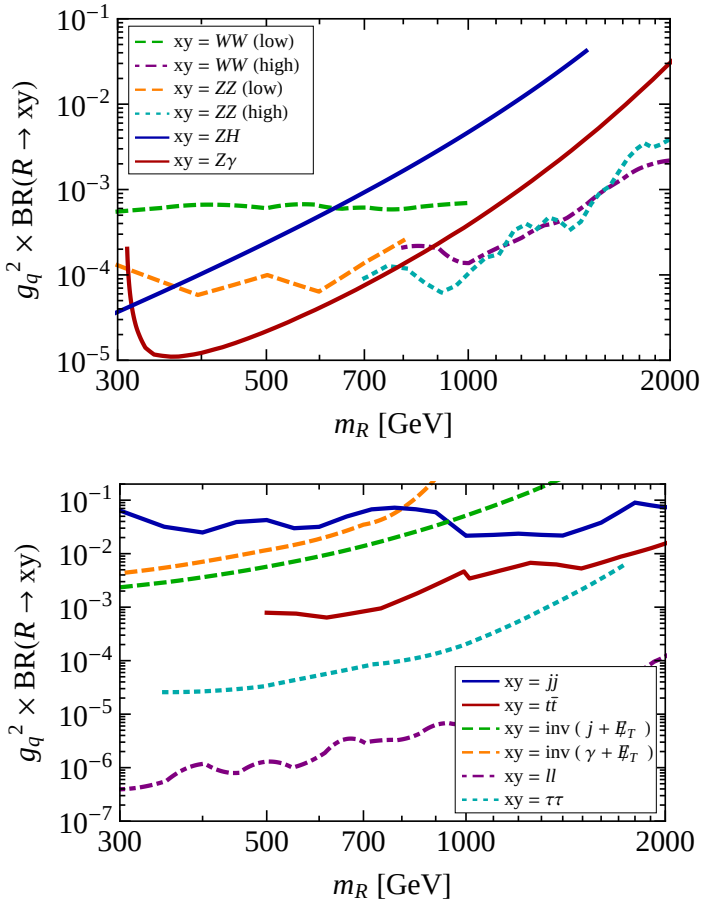

FIG. 4.7. Bounds on $g_q^2 \cdot \mathrm{BR}(R \to xy)$ as a function of m_R, with xy being SM gauge bosons or ZH (upper panel) or SM fermions or DM particles (lower panel).

experimentally. By similar reasoning, if $g_q^2 < s_{\mathrm{tot}} - s_{qq}$ we can simultaneously increase all couplings of R apart from its coupling to quarks without violating experimental constraints.

We observe from Fig. 4.7, however, that of all possible decay channels, the branching into dijets is least tightly constrained. Consequently, $s_{\mathrm{tot}} \approx s_{qq}$ and therefore $s_{\mathrm{tot}} - s_{qq} \ll s_{\mathrm{tot}}$. The case $g_q^2 < s_{\mathrm{tot}} - s_{qq}$ would therefore lead to a scenario similar to the one discussed in the previous section, where R has large couplings to DM, but strongly suppressed couplings to SM quarks. Since we have already discussed this case in detail, we will here focus on the case where direct quark couplings are large, i.e. we assume that $g_q^2 > s_{\mathrm{tot}} - s_{qq}$. In this case, Γ_R is indeed maximised by pushing g_q, as well as all other couplings of R, to their experimental limit. The total width must then satisfy

$$\Gamma_R \leq \Gamma_{\mathrm{max}}^{q\bar{q}} \frac{s_{\mathrm{tot}}}{s_{q\bar{q}}} \,, \tag{4.47}$$

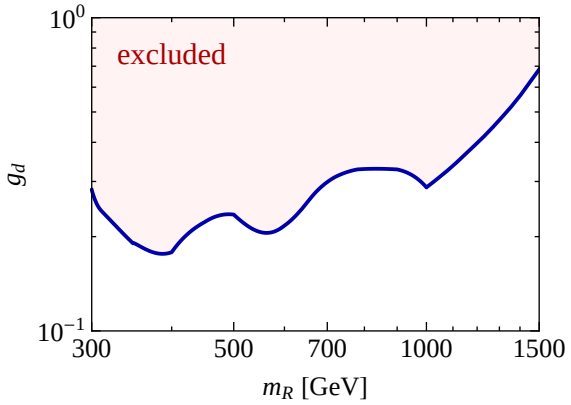

FIG. 4.8. Limit on g_d from the combination of all experimental bounds (see text).

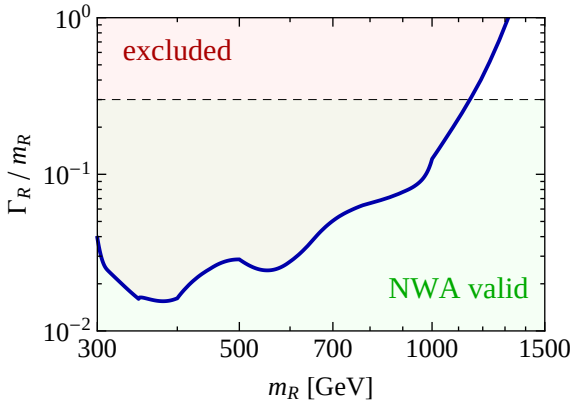

FIG. 4.9. Limit on Γ_R from the combination of all experimental bounds.

where $\Gamma^{q\bar{q}}_{\text{max}}$ is the partial width obtained setting $g_q^2 = s_{\text{tot}}$ and assuming family independent couplings. The resulting bounds are shown in Fig. 4.9.

We observe that up to $m_R \sim 1100\,\text{GeV}$, Γ_R/m_R is constrained to be so small that the NWA stays valid, which is an important consistency requirement for our treatment. We can therefore use the limit on Γ_R from Fig. 4.9 together with Eq. (4.44) to calculate an upper bound on the direct detection cross section. The resulting bounds on the direct detection cross section both as a function of mediator mass and as a function of DM mass are shown in Fig. 4.10. We observe that we can exclude a cross section of $\sigma_p = 2 \times 10^{-40}\,\text{cm}^2$ over the full mass range $300\,\text{GeV} \leq m_R \lesssim 1100\,\text{GeV}$, as long as $m_\chi \ll m_R$.

So far, we have only considered standard SI interactions of DM. For different interactions, such as SD interactions, momentum-dependent interactions, inelastic DM or effective couplings with $f_n \neq f_p$, scattering in the non-relativistic limit is typically strongly suppressed, while the results from LHC searches are not significantly affected (see Secs. 2.4 and 3.3). As a result, in most of these cases the LHC bounds will become much stronger compared to any exclusion limits (or claimed signals) from direct detection experiments. To illustrate this point, we show in Fig. 4.11 the LHC bounds for SD interactions, as well as SI interactions with $f_n/f_p = -0.7$.

Finally, we discuss how our results would change for complex scalar DM (e.g. a scalar technibaryon [40, 243, 244, 247]). In fact, all the experimental limits can be applied in complete analogy, the only difference being that for identical couplings the partial width for decays into scalar DM is smaller by a factor of 4, see Appendix A.6. As a consequence, the bounds on the direct detection

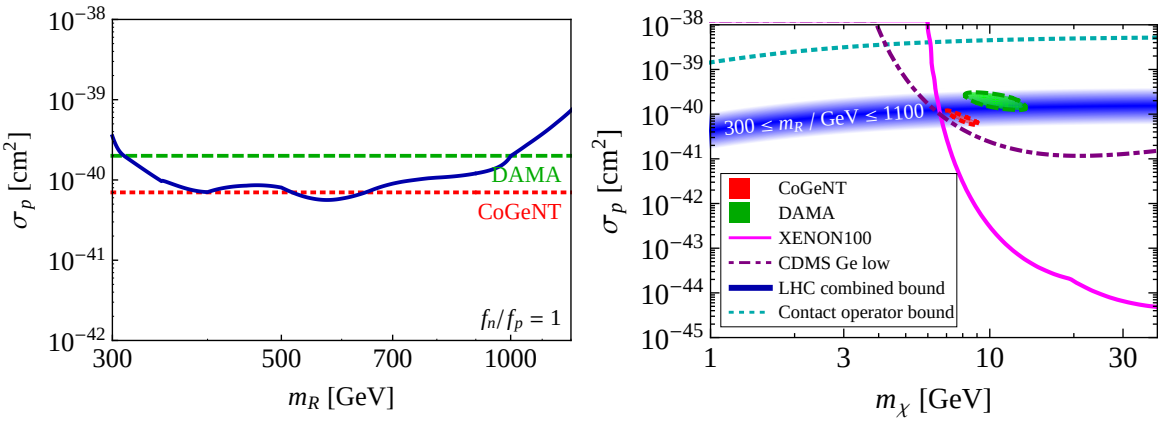

FIG. 4.10. Left: Bound from LHC data on the direct detection cross section as a function of the mediator mass m_R with the DM mass $m_\chi = 10\,\text{GeV}$. Right: Bound on the direct detection cross section from LHC limits as a function of the DM mass m_χ compared to the results from various direct detection experiments. The width of the blue line corresponds to the change of the bound as the mediator mass is varied between 300 and 1100 GeV. For larger or smaller mediator masses, the bound would become weaker. As an example, we show the bound obtained from the contact operator that would arise from integrating out the mediator (see Sec. 2.4).

cross section will be *weaker* by a factor of 4, excluding $\sigma_p > 8 \times 10^{-40}\,\text{cm}^2$ for $m_\chi \ll m_R$ and $300\,\text{GeV} < m_R < 1100\,\text{GeV}$.

To conclude this section, we would like to emphasise once more that it is possible to suppress these collider constraints by making the DM coupling very large compared to the quark couplings. In addition, we have made a number of further assumptions for our analysis. First of all, the DM particle has been assumed to have a mass $m_\chi \ll m_R$. When m_χ becomes larger than $m_R/2$, R can no longer decay into DM particles and therefore monojet signals can only arise when the mediator is produced off-shell. Hence bounds from monojets become much weaker. We do not consider this case further, as LHC bounds on the interactions of heavy DM are significantly less stringent than those obtained from direct detection experiments.

Second, we have assumed family independent fermion couplings (but we allow differences between up-quark and down-quark couplings, and between charged lepton and neutrino couplings). Coupling the mediator predominantly to the third generation would slightly relax the bound from dileptons, but make the already quite strong bound on top quarks even stronger. At the same time, doing so would strongly suppress the direct detection cross section. Consequently, allowing family-dependent couplings would not relax our final constraints.

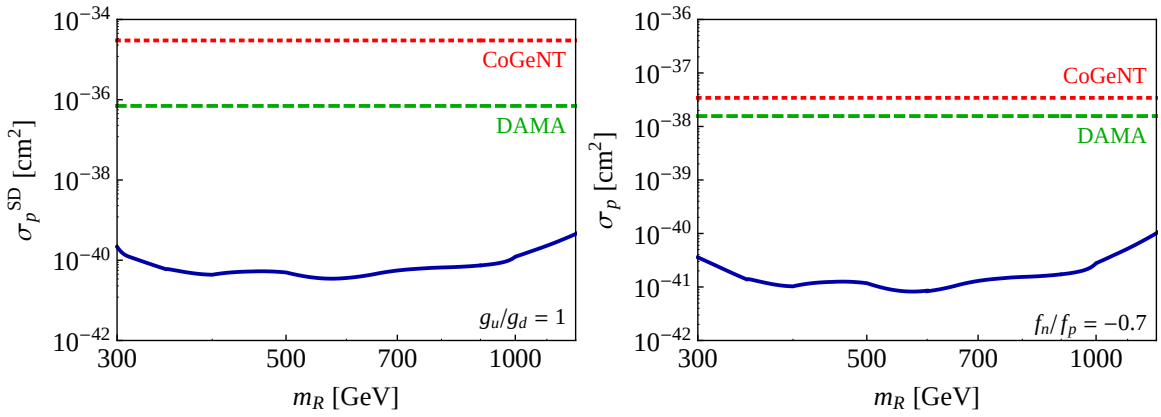

FIG. 4.11. Left: Bound on the SD direct detection cross section from LHC limits as a function of the mediator mass m_R with the DM mass fixed to $m_\chi = 10\,\text{GeV}$. Right: Same but for SI interactions with the isospin-violating couplings $f_n/f_p = -0.7$.

Third, we have only considered the contribution from D-Y production of R. For large m_R, however, the coupling of R to WW is not well constrained, so it could in general be possible to enhance the cross section of VBF production. By neglecting additional contributions to the production of R we give a more conservative bound.

Finally, and most importantly, we have assumed that we can treat R as a narrow resonance and we make extensive use of the NWA to separate the production of R from the subsequent decays. This factorisation is not valid for broad resonances, where we expect a significant contribution from off-shell mediators (see Ref. [222] for a discussion). Moreover, many bounds only apply for a narrow resonance. For example, dijet resonance searches have only been performed for peaks with $\Gamma/m \lesssim 0.3$.

We observe that for $m_R < 1100\text{GeV}$, present experimental results give the constraint $\Gamma_R/m_R < 0.3$. For these values, we expect the NWA to be accurate within a few percent. As m_R increases, the bounds on the individual coupling constants — and therefore the bound on Γ_R — become weaker. For $m_R > 1\,\text{TeV}$, couplings can be of order unity and the width can become so large that neither the experimental limits nor the formalism presented in this chapter can be applied. With increasing energy at the LHC we expect to be able to extend our treatment to larger mediator masses, while at the same time obtaining stronger bounds on the direct detection cross section.

CHAPTER 5

The importance of heavy-quark loops for LHC monojet searches

We have seen in the previous chapter that monojet searches can provide interesting constraints on the DM direct detection cross section, in particular for light DM. How strong these constraints are depends very much on whether the DM interactions lead to SI or SD scattering in direct detection experiments (see Figs. 4.10 and 4.11). In the former case, direct detection experiments are typically more sensitive because of the coherent enhancement proportional to the square of the nucleus mass and monojet searches are only beginning to probe the interesting parameter region. For interactions that are either SD or momentum suppressed, on the other hand, direct detection constraints on the scattering cross section are weakened by many orders of magnitude. In this case LHC bounds are very strong and — at least for heavy mediators — seem to rule out all of the parameter region probed by direct detection.

In this chapter we will look at the comparison between monojet searches and direct detection experiments in more detail and point out that a tree-level calculation is not always sufficient for this purpose. In Sec. 5.1 we consider the exchange of a new heavy scalar or pseudoscalar mediator with Yukawa-like couplings to quarks. In this case, LHC monojet searches give only weak constraints on the DM-proton scattering cross section if only tree-level processes are included in the analysis. The inclusion of heavy-quark loops, however, leads to a dramatic increase in the predicted monojet cross section and therefore a significant improvement of the bounds from LHC searches.

In Sec. 5.2, we study the converse situation, namely the case where LHC monojet searches give very strong bounds at tree level, because direct detection cross sections are SD. We show that loop contributions can significantly boost direct detection bounds whenever they induce SI interactions. In fact, a rigorous classification of DM-nucleon interactions into SI and SD (or

momentum suppressed) is not possible in general, as such a distinction is unstable under radiative corrections. This effect is most striking for tensor and pseudotensor interactions, which induce magnetic and electric dipole moments at loop level. For axialvector and anapole interactions a relevant contribution to direct detection signals arises from loop-induced Yukawa-like couplings between DM and quarks.

We have demonstrated in the previous chapter that it is quite difficult to compare monojet searches with direct detection experiments if the mediator of the interaction can be produced on-shell at the LHC so that monojet cross sections benefit from a resonant enhancement. In this chapter, we want to avoid such complications in order to focus on the effects of heavy-quark loops. We will therefore assume for simplicity that the mediator of the interactions is sufficiently heavy to be integrated out, so that one obtains an effective higher-dimensional operator that describes the low-energy interactions between DM and SM states (see Sec. 2.4). Although this approach has a limited range of applicability, we will argue that the effects discussed here will remain equally important once the mediator of the interaction is reinstated as an active degree of freedom.

5.1 Yukawa-like interactions

In this section, our focus will be on the scalar and pseudoscalar operator introduced in Eq. (2.20), which have the special property that the interactions between DM and quarks are proportional to the SM Yukawa couplings. For these operators the DM pair production proceeds through tree-level diagrams like those shown in the upper row of Fig. 5.1. Using these diagrams alone, the suppression scale Λ in Eq. (2.20) is very difficult to constrain with LHC monojet searches [127–130, 137, 150, 153, 248] since the initial state contains (apart from gluons) only light quarks, which by assumption have small couplings to DM. The situation changes dramatically beyond tree level, since now loop graphs involving virtual top quarks give rise to a $j + \not{E}_T$ signal. Examples of such Feynman diagrams are displayed in the lower row of Fig. 5.1.

5.1.1 Limits from monojet searches

To determine the magnitude of this effect, we again use the results from the CMS monojet search (see Sec. 4.4.3). To calculate the predicted monojet cross section for the operators introduced

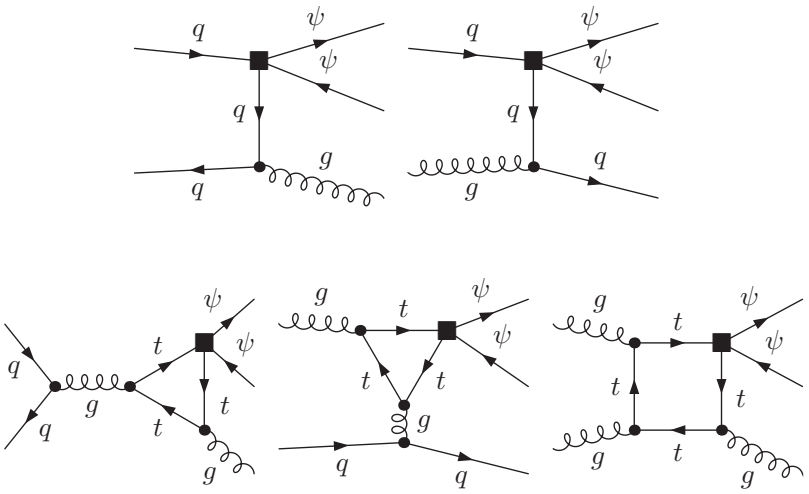

FIG. 5.1. Typical tree-level (upper row) and loop-level (lower row) diagrams leading to monojet events. The black squares denote insertions of four-fermion operators.

above we have implemented each of them in `FeynArts` [249] and performed the computations with `FormCalc` and `LoopTools` [250]. Furthermore, as an independent cross-check, we have verified our findings with `MCFM` [251], modifying the process $p + p \to H\,(A) + j \to \tau^+\tau^- + j$, which is based on the analytical results of Ref. [252] for the scalar Higgs case and Ref. [253] for the pseudoscalar Higgs case. Both computations utilise `MSTW2008LO` PDFs [254]. As before, we do not consider the effects of parton showering and hadronisation or the contribution of additional jets.

Our results are displayed in Fig. 5.2 for the case where DM is either a Dirac fermion or a complex scalar. For Majorana fermion or real scalar DM, the predicted cross sections are larger by a factor of 2 and so the bounds on Λ are stronger by roughly 12%. For the scalar (pseudoscalar) operators we find that including the loop-level processes in the calculation increases the predicted monojet cross sections by a factor of around 500 (900), the precise value depending on the DM mass and the choices of renormalisation (μ_R) and factorisation (μ_F) scales. These numbers translate into an increase of the bounds on Λ by a factor of 2.8 (3.1). Note that the limit on Λ_S that we obtain from tree-level processes alone is already stronger than the one reported in Ref. [126] by about 25%, because we include bottom quarks in the initial state, which we find to give the dominant contribution.

An important question to address is whether the above results could have been obtained without performing a loop calculation, by simply taking the large top-quark mass limit. In this approximation,

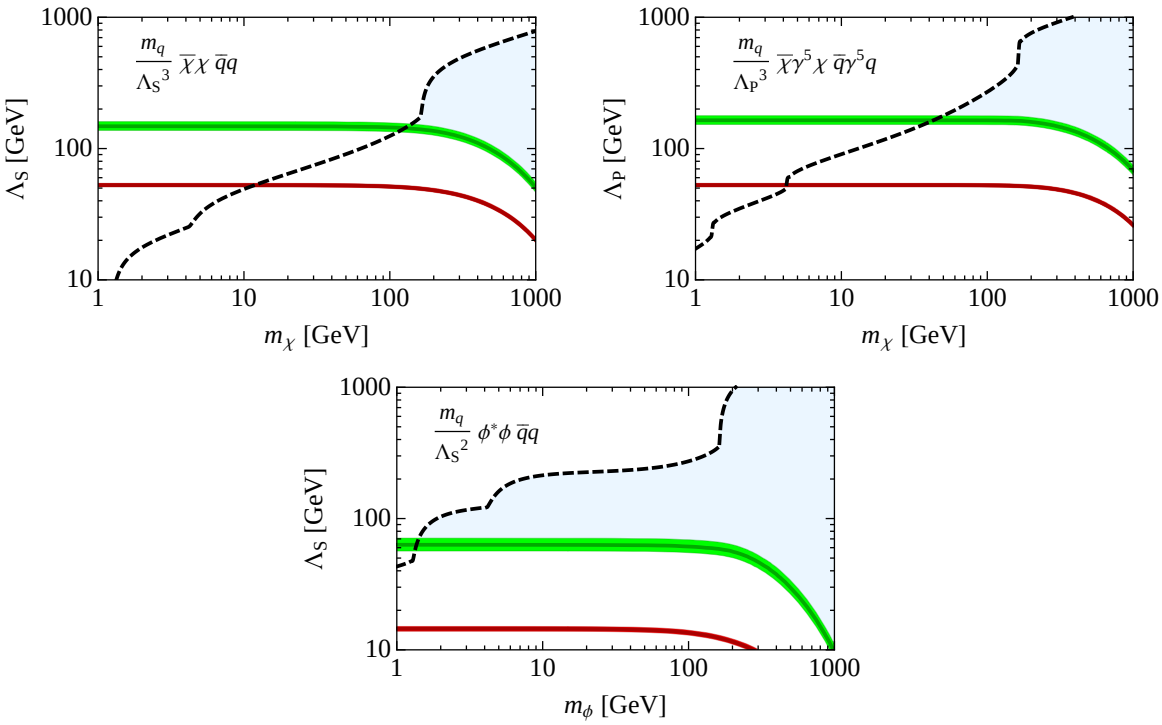

FIG. 5.2. LHC monojet bounds on the scale Λ at tree-level (red) and loop-level (green) for the effective operators $\mathcal{O}_S$ (upper-left panel), $\mathcal{O}_P$ (upper-right panel), and $\mathcal{O}_S^\phi$ (lower panel). The black dashed curves indicate the requirement for the correct relic density. Values of Λ above this curve imply an overproduction of DM in the early universe, while values below are not excluded, leading to allowed parameter regions for large DM masses (indicated by a light blue shading). The width of the bands reflect the scale uncertainties. See text for details.

the effect of heavy-quark loops for the operator $\mathcal{O}_S$ can be described by the effective operator

$$\mathcal{O}_G \equiv \frac{\alpha_s}{4\Lambda_G^3} G^a_{\mu\nu} G^{a\,\mu\nu}\,\bar{\chi}\chi\,. \tag{5.1}$$

The corresponding operator induced by $\mathcal{O}_P$ is obtained by replacing $G^a_{\mu\nu}G^{a\,\mu\nu}$ with $G^a_{\mu\nu}\tilde{G}^{a\,\mu\nu}$, where $\tilde{G}^{a\,\mu\nu} = \epsilon^{\mu\nu\rho\sigma}G^a_{\rho\sigma}$, and $\bar{\chi}\chi$ by $\bar{\chi}\gamma^5\chi$. For scalar DM, one can simply replace $\bar{\chi}\chi$ with $\phi^*\phi$. Effective interactions like Eq. (5.1) have been studied previously in the context of monojet searches [128, 129, 153, 248].

For $m_t \to \infty$ bounds on these operators can be translated into limits on $\mathcal{O}_{S,P}$ and $\mathcal{O}_S^\phi$ by the simple identifications $\Lambda_S = \Lambda_G/(3\pi)^{1/3}$ and $\Lambda_P = \Lambda_G/(2\pi)^{1/3}$. The scales involved in $j + \not{E}_T$ production (i.e. the p_T and the DM mass) are, however, not necessarily small compared to the top-quark mass, which implies that the infinite mass limit is not a good approximation [255]. Numerically, we find that applying the $m_t \to \infty$ limit overestimates the monojet cross sections by

a factor of around 3 for small DM mass and that the quality of the approximation rapidly degrades with increasing p_T cut and DM mass, resulting in errors of up to a factor of 40. These numbers imply that the corresponding limits on Λ would be too strong by a factor of 1.2 (1.9) in the best (worst) case. This consideration clearly shows that one cannot use $\mathcal{O}_{\rm G}$ (or analogous operators) to infer faithful bounds on the quark-DM contact operators.

To assess the theoretical errors in our analysis, we have studied the scale ambiguities of our results. We find the scale μ which determines $\alpha_s(\mu)$ dynamically, i.e. we define $\mu = \xi\, p_T = \mu_R = \mu_F$ and evaluate it on an event-by-event basis. Following common practice, we have varied ξ in the range $[\frac{1}{2}, 2]$. We find that the predictions of the tree-level and loop-level monojet cross sections calculated in this way vary by around $\pm 20\%$ and $\pm 50\%$, respectively. The resulting uncertainties on Λ stay below ± 2 GeV and ± 15 GeV. They are reflected by the width of the coloured bands in Fig. 5.2.

The pronounced scale ambiguity of the loop-level result indicates that NLO corrections might be large. Indeed, the K-factor, representing the ratio between the NLO and LO cross sections of $p + p \to H + j$ evaluated in the $m_t \to \infty$ limit, varies between 1.2 and 1.8 depending on the kinematic region and choice of PDFs [256–258]. Using `MCFM`, we explicitly verified that the same range of K-factors also applies to the monojet signal, although the imposed p_T cut is significantly higher than in the case of Higgs + jet production. Including parton showering and imposing a veto on the number of jets, however, is expected to reduce this K-factor significantly. Including these effects, it was found [227] that the K-factor for the effective gluon operator in Eq. (5.1) is only $K \approx 1.1$.

Nevertheless, the inclusion of NLO corrections and of two-jet events is expected to strengthen the bounds on Λ somewhat. However, it is difficult to estimate the magnitude of this effect in the full calculation with resolved top-quark loops (in particular, for high p_T cut and large DM mass), so we prefer not to include these effects in our results and give a conservative bound. Clearly, a more careful analysis of finite top-quark mass effects at $\mathcal{O}(\alpha_s^4)$ (along the lines of the recent Higgs + jet study [259]) is required to make a more quantitative statement. This study is left for future work.

Finally, we note that the values of Λ that we can exclude with the current data are low compared to typical LHC energies. To discuss the validity of the effective field theory (EFT) approach, let us consider the simplest UV completion, where Eq. (2.20) arises from the full theory after integrating

out a mediator Φ with couplings

$$\mathcal{L} \supset g_\chi^{\mathrm{S}}\, \bar{\chi}\chi\, \Phi + \frac{g_q^{\mathrm{S}}\, m_q}{v} \bar{q}q\, \Phi \quad \text{or} \quad \mathcal{L} \supset g_\chi^{\mathrm{P}}\, \bar{\chi}\gamma^5\chi\, \Phi + \frac{g_q^{\mathrm{P}}\, m_q}{v} \bar{q}\gamma^5 q\, \Phi\,, \tag{5.2}$$

see also Sec. 2.4. We anticipate that the new scalar or pseudoscalar mediator may be produced on-shell in pp collisions, unless the couplings g_q and g_χ are large (see Refs. [129, 142, 153]). In this case the analysis becomes more model-dependent, because the predictions now depend on g_q and g_χ as well as the mass M_Φ and the decay width Γ_Φ of the mediator (see Chapter 4).

The main features of the full theory calculation are captured by including a Breit-Wigner propagator for Φ in the monojet cross section [129]. In particular, the $j + \not{E}_T$ signal is enhanced relative to the EFT result if the s-channel mediator can be produced on-shell. In this case, using an EFT gives a lower bound on the expected monojet cross section. Only if the propagator is forced to be off-shell (because $M_\Phi \lesssim 2m_\chi$) will the full theory predictions be reduced compared to the EFT. More precisely, for the $\not{E}_T$ and p_T cuts that we employ and $m_\chi = 100\,\mathrm{GeV}$, we find that the EFT calculation underestimates the full theory cross section if $M_\Phi \gtrsim 280\,\mathrm{GeV}$ ($M_\Phi \gtrsim 420\,\mathrm{GeV}$) for a decay width $\Gamma_\Phi = M_\Phi/(8\pi)$ ($\Gamma_\Phi = M_\Phi/3$). Such values of M_Φ are perfectly viable (in the sense that the couplings g_q and g_χ are perturbative) given our bounds on Λ_{S} and the relation $M_\Phi^2 = g_q g_\chi \Lambda_{\mathrm{S}}^3/v$. For lighter mediators, on the other hand, the full theory including the Breit-Wigner propagator predicts an essentially constant cross section. The EFT calculation therefore overestimates the result and can no longer be used to give a conservative estimate of the monojet production cross section.

In summary, as long as we focus on low-mass DM particles with $2m_\chi \ll \Lambda$, the EFT is a good approximation that enables us to calculate lower bounds on the $j + \not{E}_T$ cross section. We find that the ratio between loop-level and tree-level cross sections calculated in the full theory is largely insensitive to the precise values of g_q, g_χ, M_Φ and Γ_Φ. In other words, including the contributions of virtual top-quark loops gives an enhancement of more than two orders of magnitude irrespectively of whether the computation is done in the effective or full theory.

5.1.2 Bounds from relic density and direct searches

The suppression scale Λ which can be constrained through monojet searches also enters in the DM annihilation cross section and the DM-proton scattering cross section. Consequently, limits on Λ

can also be inferred from measurements of the relic density and DM direct detection experiments. Here we compare these results with the bounds derived in the previous section.

Two different annihilation channels contribute to the total annihilation cross section. Tree-level annihilation into quarks will be dominant for $m_\chi > m_t$, while annihilation into gluons via heavy-quark loops can give a relevant contribution for lower DM masses. At leading order in the DM velocity v, the annihilation cross sections into quarks for the three operators discussed above are given by (see e.g. Ref. [137])

$$\begin{aligned}
(\sigma_{\rm S} v)_{\bar\chi\chi\to\bar q q} &= \frac{3v^2 m_\chi^4}{8\pi \Lambda_{\rm S}^6} \sum_q z_q \left(1-z_q\right)^{3/2} \,, \\
(\sigma_{\rm P} v)_{\bar\chi\chi\to\bar q q} &= \frac{3m_\chi^4}{2\pi \Lambda_{\rm P}^6} \sum_q z_q \left(1-z_q\right)^{1/2} \,, \\
(\sigma_{\rm S}^\phi v)_{\phi\phi\to\bar q q} &= \frac{3m_\chi^2}{4\pi \Lambda_{\rm S}^4} \sum_q z_q \left(1-z_q\right)^{3/2} \,,
\end{aligned} \tag{5.3}$$

where $z_q = m_q^2/m_\chi^2$ and the sum includes the quarks with $z_q < 1$. The corresponding cross section for annihilation into gluons take the form (see e.g. Ref. [260])

$$\begin{aligned}
(\sigma_{\rm S} v)_{\bar\chi\chi\to gg} &= \frac{v^2 \alpha_s^2 m_\chi^4}{18\pi^3 \Lambda_{\rm S}^6} \sum_q \left|F_{\rm S}(z_q)\right|^2 , \\
(\sigma_{\rm P} v)_{\bar\chi\chi\to gg} &= \frac{\alpha_s^2 m_\chi^4}{2\pi^3 \Lambda_{\rm P}^6} \sum_q \left|F_{\rm P}(z_q)\right|^2 , \\
(\sigma_{\rm S}^\phi v)_{\phi\phi\to gg} &= \frac{\alpha_s^2 m_\chi^2}{9\pi^3 \Lambda_{\rm S}^4} \sum_q \left|F_{\rm S}(z_q)\right|^2 ,
\end{aligned} \tag{5.4}$$

where the sum is over *all* quarks, including those with $z_q > 1$, and

$$F_{\rm S}(z) = \frac{3z}{2}\left[1 + (1-z)\arctan^2\left(\frac{1}{\sqrt{z-1}}\right)\right] , \tag{5.5}$$

$$F_{\rm P}(z) = z\arctan^2\left(\frac{1}{\sqrt{z-1}}\right) \tag{5.6}$$

are the well-known form factors for fermion loops [261]. These form factors are normalised so that $F_{\rm S}(\infty) = F_{\rm P}(\infty) = 1$ in the limit of infinitely heavy quarks.

If we assume that the interactions between the DM particle and SM quarks are the dominant ones at freeze-out, we can determine Λ as a function of m_χ by the requirement that the observed DM relic abundance $\Omega_\chi h^2 \approx 0.12$ [15] is reproduced (see Sec. 1.3). We use Eq. (1.12) and indicate the values of Λ that give the correct relic density by black dashed curves in Fig. 5.2. Larger values

of Λ corresponds to DM overproduction in the early universe, smaller values imply underproduction. Since the former is experimentally excluded, we obtain the following lower bounds on the DM mass from the intersections of the monojet bounds and the relic density constraints:

$$\begin{aligned} \mathcal{O}_{\mathrm{S}}: &\quad m_\chi > 129\ (149)\ \mathrm{GeV}\ , \\ \mathcal{O}_{\mathrm{P}}: &\quad m_\chi > 44\ (55)\ \mathrm{GeV}\ , \\ \mathcal{O}_{\mathrm{S}}^{\phi}: &\quad m_\phi > 1.4\ (1.5)\ \mathrm{GeV}\ . \end{aligned} \tag{5.7}$$

Here the values in brackets apply if DM is a Majorana fermion or a real scalar instead of a Dirac fermion or a complex scalar. It should be noted that these bounds can be weakened if the DM has large annihilation cross sections to other SM states or new hidden sector states. Such additional annihilation channels can in principle significantly reduce the tension between relic density constraints and results from DM searches. Underproduction is generally acceptable, assuming that the particle considered here accounts for only a fraction of the total DM abundance. Moreover, the parameter space that leads to DM underproduction in standard freeze-out can still give the observed relic abundance if the hidden sector carries an particle-antiparticle asymmetry similar to the one in the visible sector (see Sec. 1.4). Since the presence of any asymmetric component necessarily leads to a larger relic density compared to the purely symmetric case, the constraints in Eq. (5.7) provide lower bounds on the DM mass in models of ADM.

For the scalar operators $\mathcal{O}_{\mathrm{S}}$ and $\mathcal{O}_{\mathrm{S}}^{\phi}$, the DM direct detection cross section is given by

$$\sigma_N = f_N^2 \frac{\mu_{N\chi}^2\, m_N^2}{\pi\, \Lambda_{\mathrm{S}}^6}\ , \qquad \sigma_N^{\phi} = f_N^2 \frac{\mu_{N\phi}^2\, m_N^2}{\pi\, \Lambda_{\mathrm{S}}^4\, m_\phi^2}\ , \tag{5.8}$$

where $N = p$, n and $f_n \approx f_p \approx 0.28$ (see Appendix A.5). The scattering cross sections for Majorana or real scalar DM are larger by a factor of 4. Utilising Eq. (5.8), the monojet bounds on Λ can be translated into limits on σ_n, which in turn can be compared to the exclusion limits obtained from XENON100 and CDMS-II as well as to the best-fit regions obtained from DAMA and CoGeNT (see Appendix A.2).

Our final results are shown in Fig. 5.3 for the case where the DM particle is a Dirac fermion. All shown bounds and best-fit regions represent 95% CL ranges. For large values of m_χ, as indicated by the relic density constraints, direct detection experiments give stronger bounds than monojet searches. For $m_\chi \approx 10\,\mathrm{GeV}$, the bounds become comparable, while below this value the bounds

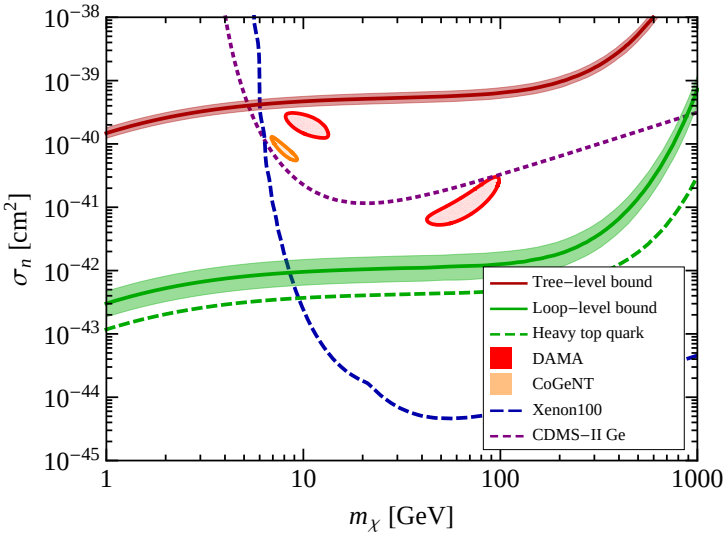

FIG. 5.3. LHC monojet bounds on the DM-proton cross section for the operator $\mathcal{O}_S$ at tree-level (red) and loop-level (green) compared to various results from DM direct detection experiments. While the tree-level monojet bound is too weak to constrain the parameter regions favoured by DAMA and CoGeNT, the loop-level bound clearly excludes these regions.

from LHC searches are far superior. We observe that the inclusion of loop-level processes gives a pertinent improvement of the monojet bounds, in particular because it independently excludes the possibility that the CoGeNT excess or the DAMA modulation arise from the interactions of a heavy scalar mediator with Yukawa-like couplings.

For the pseudoscalar operators the DM direct detection cross section is SD and suppressed by q^4/m_p^4, so that no relevant bounds on Λ_P can be obtained from direct detection experiments. Consequently, the bounds shown in the upper-right panel of Fig. 5.2 are presently the strongest limit on the new-physics scale Λ_P. It is evident from the figure that including loop contributions improves the bound on m_χ inferred from the relic abundance by a factor of about 15.

5.2 Spin-dependent and momentum-suppressed interactions

In this section, we discuss two types of effective operators that lead to either SD or momentum suppressed interactions at tree level, but induce SI interactions once loop contributions are included. For operators with tensor or pseudotensor structure, i.e. $\mathcal{O}_T$ and $\mathcal{O}_{PT}$ as defined in Eq. (2.21), we show that such contributions lead to a magnetic or electric dipole moment of the DM particle, respectively. In other words, the virtual exchange of heavy quarks leads to the effective DM-photon

interactions parameterised by $\mathcal{O}_{\rm M}$ and $\mathcal{O}_{\rm E}$ in Eq. (2.23). While the tree-level interactions are SD or momentum suppressed and therefore pose a challenge for direct detection experiments, the loop-induced interactions lead to an SI part in the differential cross section that is additionally enhanced in the infrared due to the photon pole. This feature makes DM with dipole-type interactions relatively easy to detect in low-energy scattering. For the case of the axialvector and anapole operators defined in Eqs. (2.17) and (2.18), respectively, we consider loop diagrams involving two operator insertions. The resulting corrections generally give rise to SI interactions between DM and quarks. We also discuss the impact of our findings in the context of relic density constraints and existing anomalies in the DM sector.

5.2.1 Tensor and pseudotensor operators

We consider the one-loop diagram shown on the left in Fig. 5.4. A straightforward calculation (outlined in Appendix A.7) shows that the insertion of $\mathcal{O}_{\rm T}$ into this graph induces a contribution to $\mathcal{O}_{\rm M}$ with a magnetic dipole moment (in units $\Lambda_{\rm T}^2$) that is approximately given by

$$\mathcal{C}_{\rm M} \simeq \frac{3eQ_t}{4\pi^2}\, m_t \ln \frac{\Lambda_{\rm T}^2}{m_t^2}\,, \tag{5.9}$$

where $Q_t = 2/3$ and $m_t \approx 163\,\text{GeV}$ are the electric charge and mass of the top quark and we have assumed that $\Lambda_{\rm T} > m_t$. Due to the chiral invariance of QED and QCD the above result also holds for the coefficient $\mathcal{C}_{\rm E}$ that results from the mixing of $\mathcal{O}_{\rm PT}$ into $\mathcal{O}_{\rm E}$. Bottom- and charm-quark loops with an insertion of $\mathcal{O}_{\rm T}$ and $\mathcal{O}_{\rm PT}$ will also induce dipole moments. The corresponding expressions for $\mathcal{C}_{\rm M}$ and $\mathcal{C}_{\rm E}$ are obtained from Eq. (5.9) by the simple replacements $Q_t \to Q_{b,c}$ and $m_t \to m_{b,c}$. These findings agree with the discussion of loop-induced DM dipole moments in the context of leptophilic DM [231].

Direct detection bounds on dipole moments

For the dipole-type operators Eq. (2.23) the scattering in direct detection experiments proceeds through the exchange of a photon, as shown on the right side of Fig. 5.4. In the non-relativistic limit the corresponding differential cross sections are [146, 147]

$$\frac{\mathrm{d}\sigma_{\rm M}}{\mathrm{d}E_{\rm R}} = \frac{4\alpha\mathcal{C}_{\rm M}^2}{\Lambda_{\rm T}^4}\left[Z^2\left(\frac{1}{E_{\rm R}} - \frac{1}{m_\chi v^2} - \frac{1}{2m_N v^2}\right)|F_{\rm c}(E_{\rm R})|^2\right.$$

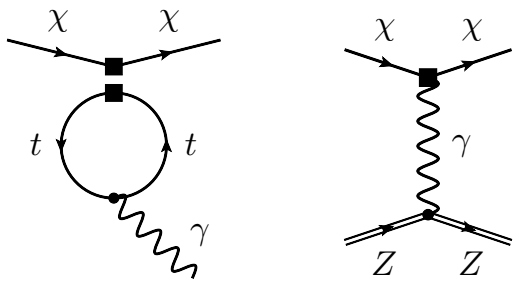

FIG. 5.4. Left: One-loop diagram with a closed top-quark loop that leads to a dipole-type operator. Right: Feynman diagram for elastic DM scattering on a nucleus with electric charge Z. The black squares in both graphs denote an operator insertion.

$$+\frac{2\,(J+1)}{3J}\left(\frac{\mu_N A}{\mu_B}\right)^2\frac{1}{2m_N v^2}\,|F_{\rm s}(E_{\rm R})|^2\Bigg]\,, \tag{5.10}$$

$$\frac{{\rm d}\sigma_{\rm E}}{{\rm d}E_{\rm R}}=\frac{4\alpha\mathcal{C}_{\rm E}^2}{\Lambda_{\rm PT}^4}\frac{Z^2}{v^2E_{\rm R}}\,|F_{\rm c}(E_{\rm R})|^2\,. \tag{5.11}$$

Here $\alpha\approx 1/137$ is the fine-structure constant of electromagnetism, J is the spin of the target nucleus and μ_N/μ_B is its magnetic moment in units of the Bohr magneton $\mu_B=e/(2m_n)$. The form factors $F_{\rm s}(E_{\rm R})$ and $F_{\rm c}(E_{\rm R})$ reflect the distribution of spin and charge in the nucleus as a function of the recoil energy $E_{\rm R}$, and we adopt the parameterisations introduced in Ref. [147] to model these functions. Since most collisions have a momentum transfer small compared to the inverse nuclear radius, uncertainties in the form factors have a negligible effect on our final results. We observe that all terms in the expression for ${\rm d}\sigma_{\rm M}/{\rm d}E_{\rm R}$ are suppressed compared to ${\rm d}\sigma_{\rm E}/{\rm d}E_{\rm R}$ either by a factor of v^2, by a factor of $E_{\rm R}/m_\chi$ or by a factor of $E_{\rm R}/m_N$, which are all typically $\mathcal{O}(10^{-6})$. Consequently, effective operators that induce an electric dipole moment are in general the most severely bounded.

Substituting Eq. (5.10) into Eq. (2.1) and calculating the velocity integral (see e.g. Ref. [146] for details), we can translate bounds on the differential event rate from direct detection experiments into bounds on the magnetic and electric dipole moments $\mathcal{C}_{\rm M}/\Lambda_{\rm T}^2$ and $\mathcal{C}_{\rm E}/\Lambda_{\rm PT}^2$. Using Eq. (5.9) for $\mathcal{C}_{\rm M}$ and an analogous equation for $\mathcal{C}_{\rm E}$, we can further convert these bounds into limits on the new-physics scale Λ entering the definition of the operators $\mathcal{O}_{\rm T}$ and $\mathcal{O}_{\rm PT}$. In our analysis we constrain the suppression scale using results from XENON100, CDMS-II, CRESST-I [262] and PICASSO [263] (see Appendix A.2).

Hadron collider bounds

In order to determine the cross section for a $j + \not{E}_T$ signal associated to the operators in Eq. (2.21), we have implemented each of them in `FeynRules` [264]. The actual computations have been performed at leading order with `MadGraph` 5 [265] utilising `CTEQ6L1` PDFs [266]. We adopt the cuts from the ATLAS monojet search with an integrated luminosity of $4.7\,\text{fb}^{-1}$ at $\sqrt{s} = 7\,\text{TeV}$ [126]. For the signal region 4, comprising events with $\not{E}_T, p_T(j_1) > 500\,\text{GeV}$, the ATLAS results exclude new contributions to the production cross section in excess of 6.9 fb at 95% CL.

While we do include secondary jets in our computation of the signal prediction, we do not consider the effects of parton showering and hadronisation for simplicity, as they do not change our main conclusions qualitatively. In order to assess the theoretical errors in our analysis, we again study the scale ambiguities of our results (see Sec. 5.1). We find that the uncertainties amount to about $\pm 30\%$ at the cross section level.

Results

Our results are displayed in Fig. 5.5. The constraints on the DM dipole moments from direct detection experiments enable us to probe and exclude suppression scales Λ in the range of around $[1.7, 3.7]$ TeV for the tensor operator (upper panel) and in the range of $[66, 159]$ TeV for the pseudotensor operator (lower panel). The black solid curves and grey bands in the two figures correspond to the 95% CL limits from the ATLAS $4.7\,\text{fb}^{-1}$ [126] search for a $j + \not{E}_T$ signal. For DM masses $m_\chi \gtrsim 10\,\text{GeV}$ the resulting bounds are clearly weaker than the constraints obtained from direct detection experiments.

Relic density requirements

Further restrictions on the DM parameter space can be derived by calculating the thermal relic density. As discussed in Sec. 1.3, we can obtain an estimate for Ω_χ by expanding the annihilation cross section in powers of v^2, see Eq. (1.12). For the effective tensor $\mathcal{O}_\text{T}$ and pseudotensor $\mathcal{O}_\text{PT}$ interactions, we find the s-wave coefficients

$$a_\text{T} = \frac{6 m_\chi^2}{\pi \Lambda^4} \sum_f \sqrt{1 - z_f}\,(1 + 2 z_f)\,, \qquad a_\text{PT} = \frac{6 m_\chi^2}{\pi \Lambda^4} \sum_f (1 - z_f)^{3/2}\,, \tag{5.12}$$

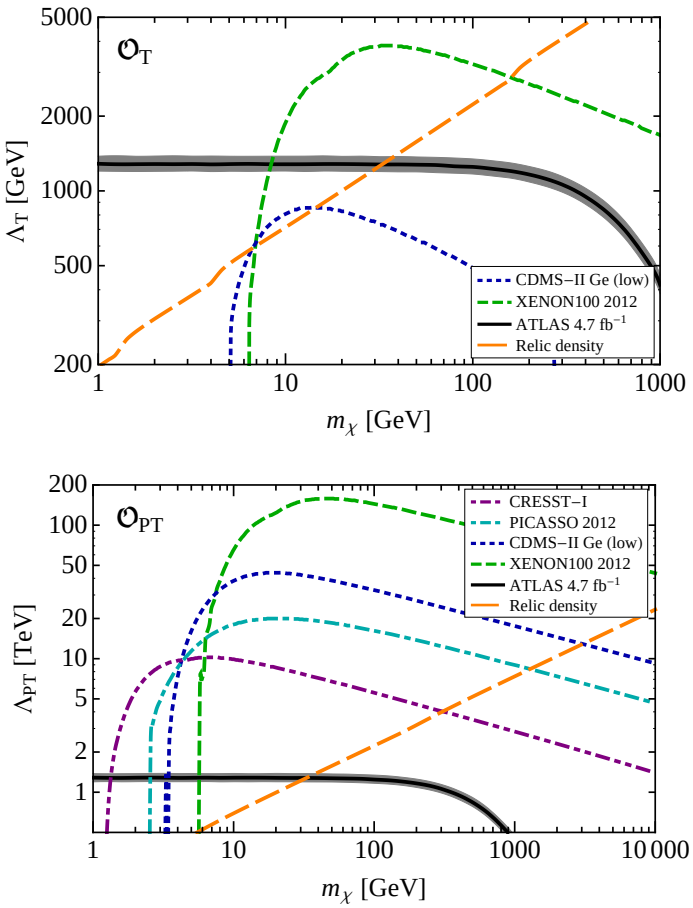

FIG. 5.5. Bounds on the scale Λ suppressing the effective operator $\mathcal{O}_{\rm T}$ (upper panel) and $\mathcal{O}_{\rm PT}$ (lower panel) inferred from constraints on the DM magnetic dipole moment and LHC searches for $j + \not{E}_T$. The orange (long dashed) curve indicates the requirement for the correct relic density. The width of the collider limit indicates scale uncertainties. Note the change of scale between the two panels.

where the sum extends over all quark flavours f with a mass $m_f < m_\chi$ and $z_f \equiv m_f^2/m_\chi^2$. The above results agree with the expressions presented in Ref. [137].

If the interactions due to $\mathcal{O}_{\rm T}$ and $\mathcal{O}_{\rm PT}$ are the only ones at freeze-out, one can determine the suppression scale Λ for fixed m_χ by the requirement to obtain the observed DM relic abundance $\Omega_\chi h^2 \approx 0.12$ [15]. The values of Λ that fulfil this constraint are indicated by the orange dashed curves in Fig. 5.5. The parameter space above (below) this curves corresponds to DM overproduction (underproduction). Combining the direct detection with the relic density constraints then yields a lower bound on the DM mass. We find

$$\mathcal{O}_{\rm T}: \quad m_\chi \gtrsim 160\ \text{GeV}\,, \qquad \mathcal{O}_{\rm PT}: \quad m_\chi \gtrsim 23\ \text{TeV}\,. \tag{5.13}$$

An interesting question in this context is whether the tensor or pseudotensor operator induce observable annihilation into mono-energetic γ-rays at the loop level. If the predicted γ-ray flux is sufficiently large, one could hope to obtain interesting constraints from Fermi-LAT [108], or potentially even to provide an explanation for the claimed observation of a signal at around 130 GeV [267, 268]. However, in order to obtain a visible signal, the suppression scale Λ typically has to be around 400 GeV or smaller [145], which is well below our bounds. In fact, as was pointed out in Refs. [269–271], such a scenario is already excluded just from limits on the diffuse γ-ray emission [109]. Furthermore, it turns out that for the specific case of tensor and pseudotensor operators, the one-loop contribution for annihilation into γ-rays vanishes identically [145] (see also Ref. [272] for a discussion in a non-DM context). The leading contributions to $\bar{\chi}\chi \to \gamma\gamma$ then arise at two loops from one-particle reducible diagrams involving two insertions of $\mathcal{O}_{\rm M}$ or $\mathcal{O}_{\rm E}$. As a result the associated fluxes of mono-energetic γ-rays are suppressed by two powers of Eq. (5.9), rendering them undetectably small.

Direct detection bounds on SD interactions

To conclude the discussion, we want to compare the loop-induced bounds from direct detection experiments to the ones obtained from tree-level scattering. For this purpose we translate the constraints on $\mathcal{O}_{\rm T}$ derived above into bounds on the SD DM-nucleon cross section using Eq. (2.22). Taking the values for $\Delta q^{(N)}$ from Eq. (2.15) we find $a_p \approx a_n \approx 0.32$. We can then compare these 'indirect' bounds on $\sigma_N^{\rm SD}$ with the conventional constraints on SD interactions from direct detection experiments with an odd number of protons or neutrons in the target atoms. Such direct constraints stem from XENON100, CRESST-I, PICASSO, SIMPLE [273], COUPP [274] and KIMS [275] (see Appendix A.2 for details).

The resulting bounds and best-fit regions are shown in Fig. 5.6. The solid red curve indicates the combined bound from loop-induced SI interactions. As expected, if DM interactions proceed via the operator $\mathcal{O}_{\rm T}$, experiments sensitive for SD interactions cannot currently probe the parameter region allowed by LHC monojet searches. Our central observation is, however, that even if we neglect the bounds from the LHC, the accessible parameter region is already excluded by constraints on the DM magnetic dipole moment unless $m_\chi < 5\,\text{GeV}$. In other words, for $m_\chi \geq 5\,\text{GeV}$ there is no need for target nuclei with spin in order to constrain $\mathcal{O}_{\rm T}$. We do not show the corresponding plot for

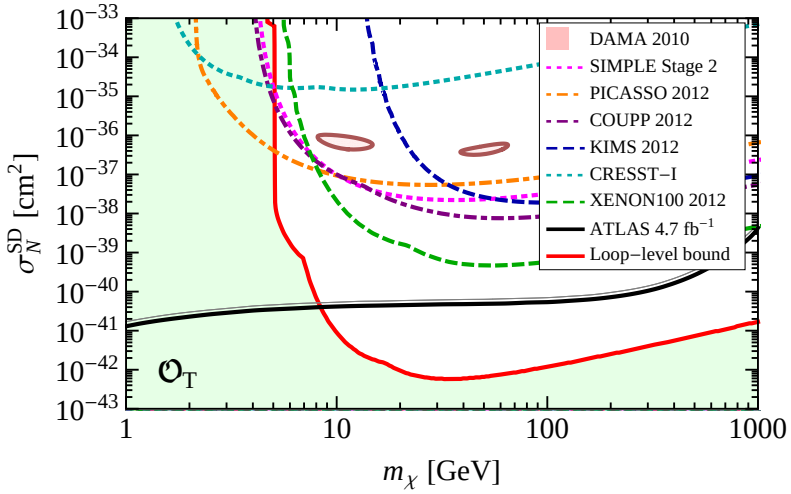

FIG. 5.6. Bounds on the SD DM-nucleon cross section from direct detection experiments compared to the constraints on the operator $\mathcal{O}_{\rm T}$ resulting from loop-induced DM dipole moments and LHC searches for $j + \not{E}_T$. The width of the collider limit indicates scale uncertainties, while the corresponding uncertainties for the dipole moments are not shown.

the pseudotensor operator, because in this case tree-level scattering is momentum suppressed and therefore the corresponding bounds from direct detection experiments do not give any interesting constraint. In other words, all relevant bounds for $\mathcal{O}_{\rm PT}$ are already shown in Fig. 5.5. Note that, in particular, the effective interactions $\mathcal{O}_{\rm T}$ and $\mathcal{O}_{\rm PT}$ cannot provide an explanation for the DAMA modulation.

To conclude this section, let us consider the contribution of bottom and charm quarks to DM dipole moments separately. These contributions are suppressed compared to the one from top quarks because of the smaller quark masses, but they will receive larger logarithmic corrections. For the tensor operator $\mathcal{O}_{\rm T}$, we find numerically that the resulting bounds on Λ are weaker compared to the ones obtained above by a factor of approximately 0.14 for bottom quarks and a factor of approximately 0.12 for charm quarks. For the pseudotensor operator $\mathcal{O}_{\rm PT}$ the limits are weaker by a factor of 0.12 and 0.10, respectively. Thus, in the latter case both bottom- and charm-quark loops alone lead to bounds that significantly exceed the constraints from the LHC.

5.2.2 Axialvector and anapole operators

We now turn to the discussion of the axialvector operator $\mathcal{O}_{\rm AX}$ and the anapole operator $\mathcal{O}_{\rm AN}$. In both cases we consider the one-loop diagrams shown in Fig. 5.7. As has been observed previously in

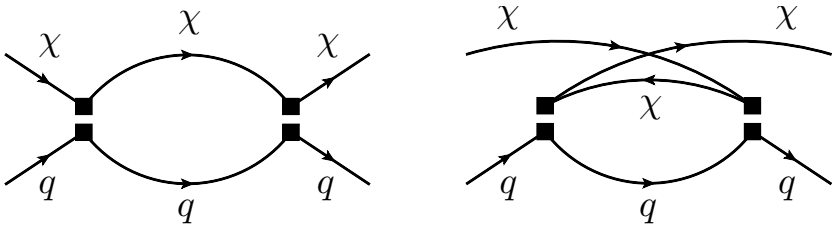

FIG. 5.7. One-loop contributions to the DM-quark scattering amplitude induced by the operators $\mathcal{O}_{\rm AX}$ and $\mathcal{O}_{\rm AN}$. The black squares represent operator insertions.

the literature [231, 276–278], the matrix element resulting from two insertions of the operator $\mathcal{O}_{\rm AX}$ leads to SI scattering, which can be described by the operator $\mathcal{O}_{\rm S}$ defined in Eq. (2.20).[1] Assuming for definiteness $m_\chi < m_t$, the induced coefficient reads (see Appendix A.7 for details)

$$\mathcal{C}_{\rm S} \simeq -\frac{1}{2\pi^2}\frac{m_\chi}{\Lambda_{\rm AX}}\ln\frac{\Lambda_{\rm AX}^2}{m_\chi^2} \tag{5.14}$$

for $q = u, d, s, c, b$ while for $q = t$ the argument of the logarithm is Λ^2/m_t^2. The same result (though with opposite overall sign) holds for two insertions of $\mathcal{O}_{\rm AN}$ instead of $\mathcal{O}_{\rm AX}$.

Bounds on the new-physics scale

Inserting the conventional bounds on $\sigma_N^{\rm SI}$ from various direct detection experiments (see Appendix A.2) into Eq. (5.8) one can constrain $\mathcal{C}_{\rm S}$ and therefore, using Eq. (5.14), the scale Λ appearing in $\mathcal{O}_{\rm AX}$ and $\mathcal{O}_{\rm AN}$.[2] Our results are shown in Fig. 5.8. For DM masses between 10 GeV and 100 GeV, we find bounds in the range of $[50, 100]$ GeV. For smaller values of m_χ, the bounds are suppressed due to the multiplicative factor m_χ in Eq. (5.14), while for larger values the limits deteriorate because m_χ approaches Λ and consequently the logarithm in Eq. (5.14) tends to zero. In practice, we only show bounds that satisfy $\Lambda^2/m_\chi^2 > 2$. Comparing these results to the constraints from LHC searches, we find that the latter give far superior bounds, requiring $\Lambda \gtrsim 700$ GeV.

As before we also calculate the thermal-averaged annihilation cross section into quarks. For the axialvector operator $\mathcal{O}_{\rm AX}$ we find that s-wave annihilation into pairs of quarks is helicity suppressed,

[1] The Feynman diagrams in Fig. 5.7 also lead to a loop-suppressed contribution to $\mathcal{O}_{\rm AX}$, but the corrections to the vector operator $\mathcal{O}_V$ cancel exactly.

[2] Note that, since we find $\Lambda < m_t$, it would be inconsistent to include the contribution to the DM-nucleon couplings that arises from integrating out the top quark. Consequently, following Appendix A.5, we take $f_p \approx f_n \approx 0.21$, which is somewhat smaller than the value used above.

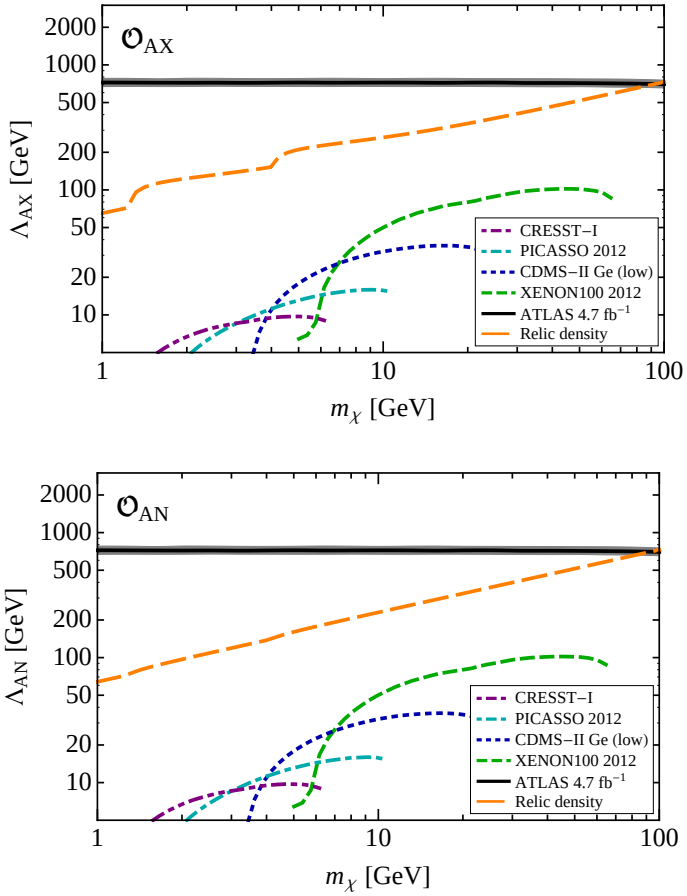

FIG. 5.8. Bounds on the scale Λ suppressing the effective operators $\mathcal{O}_{AX}$ (upper panel) and $\mathcal{O}_{AN}$ (lower panel) inferred from LHC monojet searches and constraints on the SI DM-nucleon cross section. The orange (long dashed) curve in each plot indicates the requirement for the correct relic density. The width of the collider limit indicates scale uncertainties.

so that one has to include the contribution from p-wave annihilation. Explicitly, we get

$$a_{AX} = \frac{3}{2\pi\Lambda_{AX}^4}\sum_f m_f^2\sqrt{1-z_f}\,, \qquad b_{AX} = \frac{3m_\chi^2}{2\pi\Lambda_{AX}^4}\sum_f \sqrt{1-z_f}\,\frac{8-22z_f+17z_f^2}{24\,(1-z_f)}\,. \tag{5.15}$$

In the case of the anapole operator $\mathcal{O}_{AN}$ the annihilation can only proceed via p-wave. The corresponding coefficients are given by

$$a_{AN} = 0\,, \qquad b_{AN} = \frac{m_\chi^2}{4\pi\Lambda_{AN}^4}\sum_f \sqrt{1-z_f}\,(2+z_f)\,. \tag{5.16}$$

Our results in Eqs. (5.15) and (5.16) agree with those given in Ref. [137]. Since annihilation is suppressed for both operators, Λ has to be significantly smaller than for the tensor and pseudotensor operator in order to reproduce the observed relic density. LHC bounds then imply that the required

DM density can only be achieved for $m_\chi \gtrsim 93\,\text{GeV}$ for both the axialvector and the anapole operator.

Because of the helicity suppression for the axialvector operator and the velocity suppression for the anapole operator, constraints from indirect detection are very weak. To calculate these constraints accurately, one would have to take into account both loop-induced annihilation into monoenergetic γ-rays as well as photons arising from the process $\bar{\chi}\chi \to \bar{q}qV$, where V is a SM gauge boson (see e.g. Ref. [279]). We do not perform such a calculation here, because the resulting bounds turn out to be much weaker than existing collider constraints [145, 151]. Moreover, for the anapole operator, the one-loop contribution to annihilation into γ-rays vanishes.[1]

Bounds on the DM scattering cross section

Even though Fig. 5.8 seems to indicate that loop-induced SI scattering cross sections do not lead to relevant constraints on the scale Λ, it is interesting to consider cases where the bounds from LHC searches and the relic density requirement do not apply, for example low-mass ADM interacting with the SM via a mediator that is light compared to LHC scales [137]. In this case, only direct detection experiments can give relevant lower limits on Λ. In this section, we will therefore directly compare the limits from loop-induced SI interactions with the bounds from tree-level SD interactions (for the axialvector operator $\mathcal{O}_{\text{AX}}$) and momentum suppressed interactions (for the anapole operator $\mathcal{O}_{\text{AN}}$) to determine which contribution gives the most stringent constraint.

For the axialvector operator $\mathcal{O}_{\text{AX}}$, the constraints on Λ_{AX} derived above can be translated into bounds on the SD scattering cross section using Eq. (2.13). Our results are shown in the upper panel of Fig. 5.9. As before, the bounds are cut off at large DM masses, because we require $\Lambda^2/m_\chi^2 > 2$. Because of the small Yukawa couplings appearing in Eq. (5.14) these constraints are relatively weak compared to the constraints from SD direct detection experiments. Nevertheless, for some targets with limited sensitivity to SD interactions, such as oxygen, silicon or germanium, the event rate resulting from loop-induced processes becomes comparable to tree-level scattering. Consequently, these effects should be included in a complete analysis of SD interactions.

Let us now turn to the anapole operator $\mathcal{O}_{\text{AN}}$. The differential scattering cross section is given

[1] This finding is in line with the explicit calculation performed in Ref. [272] but disagrees with the results presented in Ref. [145], where a bound on the anapole operator has been inferred using Fermi-LAT data.

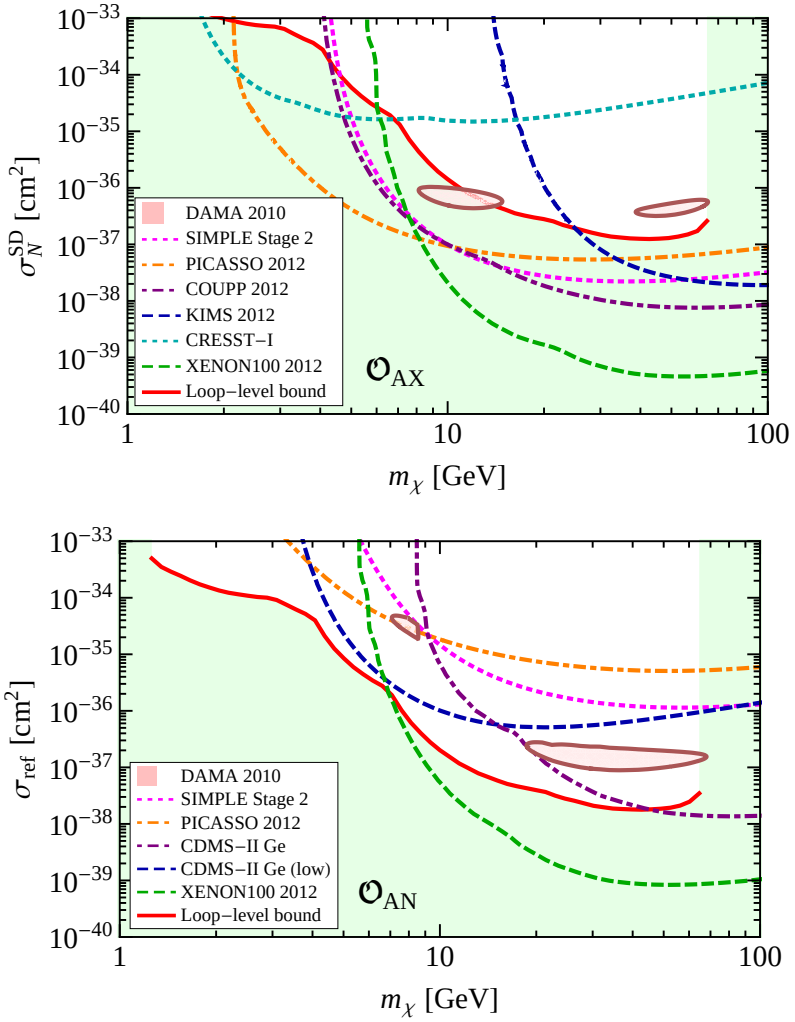

FIG. 5.9. Upper panel: bounds on the SD scattering cross section from tree-level processes compared to the bound from loop-induced SI interactions (solid red curve) for the axialvector operator $\mathcal{O}_{\rm AX}$. Lower panel: corresponding limits on the SI reference cross section for the anapole operator $\mathcal{O}_{\rm AN}$.

by [139]

$$\frac{\mathrm{d}\sigma^{\rm SI}}{\mathrm{d}E_{\rm R}} = \frac{1}{2\pi}\frac{m_N}{\Lambda_{\rm AN}^4}\frac{Z^2}{v^2}\left[v^2 + \frac{q^2}{2m_N^2}\left(1 - \frac{m_N^2}{2\mu_{N\chi}^2}\right)\right] . \tag{5.17}$$

While this cross section is suppressed by powers of v^2 and q^2/m_N^2, there is an enhancement proportional to Z^2 from coherence. Consequently, it is possible to directly constrain Λ for the anapole operator using tree-level scattering in direct detection experiments.

Again, the resulting constraints can be compared to the indirect bounds from loop-induced SI interactions. The resulting bounds in terms of the reference cross section $\sigma_{\rm ref} = \mu_{N\chi}^2/(\pi\,\Lambda_{\rm AN}^4)$ are

shown in the lower panel of Fig. 5.9. We observe that, in contrast to the case of the axialvector operator $\mathcal{O}_{\mathrm{AX}}$, the loop-induced limits for $\mathcal{O}_{\mathrm{AN}}$ are comparable to the bounds obtained from tree-level interactions. In fact, the loop contributions dominate for small DM masses because tree-level interactions are suppressed for small momentum transfer. In other words, in cases where the LHC bounds do not apply, loop-induced processes give the strongest bounds on the DM interactions in this specific region of parameter space.

Our study clearly demonstrates the remarkable complementarity of the different search strategies for DM. For many of the operators we consider, we find that direct detection and collider searches provide comparable bounds, and that different searches dominate for different values of the DM mass. Even in cases where one strategy seems to be inferior to the other when considering interactions only at tree level, loop contributions can change this picture drastically. Consequently, detailed studies of such loop effects will play an essential part in combining the virtues of all different search strategies in order to solve the DM problem.

CHAPTER 6

Conclusions

Good tests kill flawed theories; we remain alive to guess again.

(Karl Popper)

There is clear observational evidence that DM is about five times more abundant in the Universe than ordinary baryonic matter. As we have argued in Chapter 1, DM is likely to be made of new stable particles, implying that there is new BSM physics to be discovered. In fact, there are many viable particle candidates, for example WIMPs, which obtain the appropriate relic density from the freeze-out mechanism. To establish the nature of DM is therefore a key challenge for modern astroparticle physics. Indeed, a large number of experiments now pursue various different strategies to search for WIMPs and similar particles. In Chapter 2, we have presented the wide range of potential experimental signatures and search channels. The topic of this thesis has been to develop new techniques to compare several DM experiments and to exploit the complementarity between different search strategies.

In Chapter 3 our focus has been on direct detection experiments and in particular on the uncertainties arising from the need to assume a DM velocity distribution. We find that contrary to the common expectation, these uncertainties cannot entirely account for disagreements between individual experiments. The key observation is that all nuclear recoil detectors probe the same velocity integral $g(v_{\min})$, although possibly for different values of $v_{\min}$. Both measurements of and constraints on the differential event rate can thus be converted into $v_{\min}$-space to obtain information on $g(v_{\min})$ and compare experiments without any assumptions on astrophysics.

By applying this technique, we have shown that the signals reported by DAMA, CoGeNT and CRESST-II can be brought into agreement by considering a non-standard halo with anisotropy and allowing for a large modulation fraction. Nevertheless, the tension with experimental null results cannot be resolved by varying astrophysical parameters. This conclusion also holds for the tension between CDMS-Si and XENON10/100, which we have examined in more detail, including a discussion of experimental uncertainties related to the ionisation yield in liquid xenon. On the other hand, CDMS-Si and XENON10/100 can be brought into agreement when making different assumptions on the nature of DM scattering, such as different couplings to protons and neutrons (isospin-violating DM) or down-scattering from an excited DM state (exothermic DM).

In recent years, the idea of studying the velocity integral $g(v_{\min})$ in order to gain an understanding of the compatibility or otherwise between different experiments has received an increasing amount of attention. In the present work, we have extended this method to study targets with several different materials and to include annual modulations, and we have proposed a way to constrain the modulation fraction. Recently, the framework has been further extended to include inelastic DM [280], exothermic DM [281] and models with non-standard velocity dependence [282, 283], as well as methods for unbinned analyses [178]. Additional ways to constrain the modulation fraction have been proposed in Refs. [284, 285].

It still remains a major drawback of the method that it is very difficult to quantify the disagreement between two experiments in a statistically meaningful way. To make progress in this regard we have developed a method which enables us to find the best-fit velocity integral for a given set of data. This method can be used very efficiently to determine the DM parameters (such as m_χ and the coupling ratio f_n/f_p) that bring several experiments into agreement and construct confidence regions in a halo-independent way. It is not yet clear, however, how to perform a goodness-of-fit estimate using this method.

Since the completion of Chapter 3, several direct detection experiments have published new results, which affect some of our conclusions. First of all, CoGeNT has published an update of their search for an annual modulation based on more than three years of data [286]. While some evidence for modulation remains, the significance has not grown compared to the previous analysis. Moreover, due to a better understanding of backgrounds from surface events, CoGeNT has significantly reduced its estimate of the absolute rate, so that a modulation fraction between 35%

and 62% is needed in order to explain the signal [170], in significant tension with the expectation (see Sec. 3.1.4). In fact, it has been argued [287] that when taking into account uncertainties in the fraction of surface events, no significant evidence for a DM signal in the absolute rate remains. Similarly, the CRESST-II collaboration has recently presented new data [288], which no longer show an excess at low energies, ruling out the DM interpretation of their previous results.

At the same time LUX [81] and SuperCDMS [97] have recently published new bounds, which are considerably stronger than the previous ones from XENON10 and XENON100. The tension between these constraints and CDMS-Si now is so large that none of the modifications proposed in Sec. 3.3 is sufficient to bring all experiments into agreement [289]. Exothermic scattering no longer relaxes the constraints on the CDMS-Si best-fit region because of the very low energy threshold of SuperCDMS. Similarly, since LUX and SuperCDMS employ different target materials (namely xenon and germanium), it is not possible to tune the ratio f_n/f_p in such a way that bounds from both experiments are sufficiently suppressed (although a marginal compatibility can still be achieved for $f_n/f_p = -0.7$). Only the rather unattractive combination of both exothermic and isospin-violating DM (with $f_n/f_p \approx -0.8$ to suppress SuperCDMS) can fully reconcile all three experiments [290].

In summary, both the experimental sensitivity and the theoretical understanding of direct detection experiments have made significant progress over the past years. As a result, the case for low-mass DM is significantly weaker now than it was in 2011. New experiments with lower backgrounds and larger target masses, on the other hand, will soon begin to probe completely unexplored regions of parameter space. The challenge to interpret upcoming experimental data independently of astrophysical uncertainties and to compare them with results from other search strategies remains as important as ever and it will be of crucial importance to develop appropriate tools. At the same time it is essential that theoretical predictions for non-standard models of DM are explored systematically in order to ensure that the complementarity of different target materials is exploited in the best possible way.

Another idea that has gained considerable momentum over the past few years is the idea of using the LHC, in particular monojet searches, to constrain the DM production cross section. Traditionally, these searches have been interpreted in terms of tree-level production of DM via effective operators. Nevertheless, it has become clear to the community that the range of validity of the effective

operator approach is limited and consequently there is a need for more refined treatments based on simplified models with explicit s-channel and t-channel mediators (see e.g. Refs. [141, 291, 292]).

In Chapter 4, we have considered one particular example for an s-channel mediator, namely a vector mediator coupling to DM and SM particles. Specifically, we have considered the case of a massive Z' arising from a new $U(1)$ gauge group, which couples directly to DM and picks up couplings to SM particles from mixing with the neutral SM gauge bosons. In such a model, DM direct detection cross sections can be large, and negative values for f_n/f_p occur naturally. For Z' masses of a few GeV, the strongest constraints arise from EWPT and Υ decays. For heavier mediators, LHC resonance searches (in particular searches for dilepton resonances) become very constraining. Ongoing and forthcoming searches for Z' gauge bosons at collider experiments will make the bounds on these couplings even tighter. Indeed, recent searches for hidden photons at BABAR [293] already exclude the benchmark parameters considered in Sec. 4.3. To evade these constraints, it is necessary to move to smaller mixing parameters and smaller Z' masses.

We have also considered a more general setup, where we allow for arbitrary couplings between the vector mediator and SM particles. The constraints from LHC searches can be significantly relaxed if the mediator couples more strongly to quarks than to leptons and SM gauge bosons. Using a wide range of LHC searches, in particular monojet searches and dijet resonance searches, it is nevertheless possible to constrain all relevant decay channels for such a general vector mediator and obtain relevant constraints on the DM scattering cross section. Upcoming experimental searches for long-lived hidden sector states and broad resonances will allow us to further relax our assumptions and extend the validity of our analysis.

Another important shortcoming of the conventional analyses of LHC monojet searches is that only tree-level processes have been included in the calculation of both the DM production and the DM scattering cross section. In Chapter 5 we have shown that loop effects, in particular heavy-quark loops, can give important contributions to these cross sections. We have found that for DM-quark interactions arising from the exchange of a new heavy scalar or pseudoscalar mediator with Yukawa-like couplings, the sensitivity of LHC searches has been significantly underestimated. The improvements we find are particularly important for light DM and for the pseudoscalar operator, both of which cannot be constrained by direct detection experiments.

On the other hand, it is not necessarily true that direct detection experiments cannot compete

with LHC searches for interactions that lead to SD or momentum suppressed scattering in the non-relativistic limit, because SI interactions may be induced at loop level. In some cases, for example for loop-induced DM dipole moments, the resulting constraints from direct detection experiments are not only superior to the ones obtained from tree-level processes, but may in fact even surpass the constraints from the LHC. This result is an impressive demonstration both of the power of direct detection experiments as well as of the importance of loop contributions in calculating the expected scattering cross sections.

With increasing centre-of-mass energy and luminosity, the LHC will considerably improve the sensitivity of monojet searches in the future. Moreover, there are many other search channels that the LHC has just begun to explore. Clearly, LHC searches for DM are one of the most exciting aspects of the upcoming run of the LHC and offer bright prospects for the near-term future of the search for DM. The methods outlined in this thesis will be important for further advances in constraining the parameter space of DM-quark interactions and we are looking forward to their implementation in future LHC analyses.

Our analysis of various effective operators and possible UV completions clearly demonstrates the remarkable complementarity of the different search strategies for DM. For many of the operators we consider, we find that direct detection and collider searches provide comparable bounds, and that different searches dominate for different values of the DM mass. Even in cases where one strategy seems to be inferior to the other when considering interactions only at tree level, loop contributions can change this picture drastically. Consequently, detailed studies of such effects will play an essential part in combining the virtues of all different search strategies in order to solve the DM problem.

So far the interactions of DM remain invisible — but the search is gathering speed. With the projected impressive increase in sensitivity in upcoming experiments, we can expect putative signals in the near future rather than just exclusion limits. For an unambiguous detection of DM it will be essential to combine DM signals from more than one type of experiment. Understanding the complementarity and interplay of different search strategies will be the key to drawing robust conclusions of fundamental importance.

Appendices

A.1 Various descriptions of the Galactic dark matter halo

In this appendix we present the velocity distributions considered in Secs. 2.1 and 3.1 and provide the parameter choices used for Figs. 2.2 and 3.2 — for further details we refer to the references. First, we discuss isotropic velocity distributions, where $f(\boldsymbol{v})$ depends only on $|\boldsymbol{v}|$ and there is no preferred direction for DM velocities at the position of the Earth. Then we consider models where the anisotropy parameter [294]

$$\beta(r) \equiv 1 - \frac{\langle v_\theta^2 \rangle + \langle v_\phi^2 \rangle}{2\langle v_r^2 \rangle} \tag{A.1}$$

is non-zero, motivated by numerical simulations, which favour radially biased orbits with $\beta = 0.1$–0.4 at the position of the Earth [295]. Finally, we discuss additional non-halo contributions to the local DM density.

A.1.1 Isotropic models

Standard Halo Model

In the SHM, the velocity distribution function is given by

$$f(\boldsymbol{v}) = \begin{cases} \frac{1}{N}\left[\exp(-v^2/v_0^2) - \exp(-v_{\rm esc}^2/v_0^2)\right] , & |\boldsymbol{v}| < v_{\rm esc} \\ 0 , & |\boldsymbol{v}| \geq v_{\rm esc} \end{cases} , \tag{A.2}$$

where N is a normalisation constant. Possible values for the velocity dispersion v_0 range from $180\,\mathrm{km\,s^{-1}}$ to $280\,\mathrm{km\,s^{-1}}$, while $v_{\rm esc}$ can vary between $450\,\mathrm{km\,s^{-1}}$ and $650\,\mathrm{km\,s^{-1}}$ [86] (see also the left panel of Fig. 2.2). Unless explicitly stated otherwise, we will always assume the standard values $v_0 = 220\,\mathrm{km\,s^{-1}}$ and $v_{\rm esc} = 544\,\mathrm{km\,s^{-1}}$.

King models

The cut-off at $v_{\rm esc}$ is introduced by hand in the SHM, which would otherwise predict particles with infinitely high velocities and an infinite mass for the Galaxy. This problem is addressed in the King model, which provides a cut-off in a self-consistent manner [294]. The velocity distribution is obtained from the distribution function

$$f(\mathcal{E}) = \begin{cases} \frac{1}{N}\left[\exp\left(\mathcal{E}/\sigma^2\right) - 1\right], & \mathcal{E} > 0 \\ 0, & \mathcal{E} \leq 0 \end{cases}, \tag{A.3}$$

where $\mathcal{E} \equiv \Psi(\boldsymbol{x}) - v^2/2$ and $\Psi(\boldsymbol{x})$ is the relative gravitational potential. The local escape velocity at a position $\boldsymbol{x}$ is given by $v_{\rm esc} = \sqrt{2\,\Psi(\boldsymbol{x})}$. At the position of the Earth $f(\boldsymbol{v})$ can be parameterised in the same way as the SHM but the parameter σ is not directly linked to the velocity dispersion and can therefore take values that are much larger than in the SHM [296]. Nevertheless, because of their similarity to the SHM we will not discuss King models further.

Double power-law profiles

A simple modification of the SHM was proposed in Ref. [297]. For double power-law density profiles such as the Navarro-Frenk-White (NFW) profile [298], the following ansatz for the velocity distribution provides a better approximation for the behaviour at high velocities:

$$f(\boldsymbol{v}) = \begin{cases} \frac{1}{N}\left[\exp\left(\frac{v_{\rm esc}^2 - v^2}{k v_0^2}\right) - 1\right]^k, & |\boldsymbol{v}| < v_{\rm esc} \\ 0, & |\boldsymbol{v}| \geq v_{\rm esc} \end{cases}. \tag{A.4}$$

Setting the power-law index k equal to 1 recovers the SHM. The choice $1.5 \leq k \leq 3.5$ however is found to give a better fit to velocity distributions extracted from N-body simulations. We use $k = 2.5$ throughout.

Tsallis model

It was argued in Ref. [299] that the velocity distribution of DM particles in numerical simulations including baryons can be well described by

$$f(\boldsymbol{v}) = \begin{cases} \frac{1}{N}\left[1 - (1-q)\,\frac{\boldsymbol{v}^2}{v_0^2}\right]^{1/(1-q)}, & |\boldsymbol{v}| < v_{\rm esc} \\ 0, & |\boldsymbol{v}| \geq v_{\rm esc} \end{cases}, \tag{A.5}$$

see also Ref. [300]. We adopt the parameters $q = 0.773$, $v_0 = 267.2\,\mathrm{km\,s^{-1}}$ and $v_{\mathrm{esc}} = 560.8\,\mathrm{km\,s^{-1}}$ from Ref. [299].

A.1.2 Anisotropic models

Numerical simulations

A simple anisotropic model has been proposed in Ref. [76] to describe the data from numerical N-body simulations such as Via Lactea [301, 302], GHALO [303] or Aquarius [304]:

$$f(\boldsymbol{v}) = \begin{cases} \frac{1}{N}\left[\exp\left(-(v_r^2/\overline{v}_r^2)^{\alpha_r}\right)\exp\left(-(v_t^2/\overline{v}_t^2)^{\alpha_t}\right)\right], & |\boldsymbol{v}| < v_{\mathrm{esc}} \\ 0\,, & |\boldsymbol{v}| \geq v_{\mathrm{esc}} \end{cases}, \tag{A.6}$$

where $v_t = \sqrt{v_\theta^2 + v_\phi^2}$. For the figures we take the best-fit parameters for the Via Lactea II simulation, namely $v_r = 202.4\,\mathrm{km\,s^{-1}}$, $v_t = 128.9\,\mathrm{km\,s^{-1}}$, $\alpha_r = 0.934$ and $\alpha_t = 0.642$ [76], but we also show the velocity integral and modulation fraction observed in the $\mathrm{GHALO_s}$ simulation.

Logarithmic ellipsoidal model

The simplest triaxial generalisation of the velocity distributions considered above was discussed in Refs. [159, 305, 306]. We allow a different velocity dispersion in all three directions, giving

$$f(\boldsymbol{v}) = \begin{cases} \frac{1}{N}\left[\exp\left(-v_r^2/\overline{v}_r^2 - v_\phi^2/\overline{v}_\phi^2 - v_z^2/\overline{v}_z^2\right)\right], & |\boldsymbol{v}| < v_{\mathrm{esc}} \\ 0\,, & |\boldsymbol{v}| \geq v_{\mathrm{esc}} \end{cases}. \tag{A.7}$$

The three parameters $\overline{v}_r$, $\overline{v}_\phi$ and $\overline{v}_z$ depend on two constants p and q that describe the density distribution and the isotropy parameter γ (as well as v_0). Following Ref. [159], we take $p = 0.9$, $q = 0.8$ and $\gamma = -1.33$ and calculate $\overline{v}_r$, $\overline{v}_\phi$ and $\overline{v}_z$ under the assumption that the Earth is on the major axis.

Distribution functions with $\beta = 0.5$

For a constant anisotropy of $\beta = 0.5$, it is possible to calculate the velocity distribution from a given density profile. In Ref. [307] this was done for centrally cusped density profiles of the form

$$\rho \propto \frac{a^{b-2}}{r(r+a)^{b-1}}\,. \tag{A.8}$$

For $b = 4$, corresponding to the Hernquist density profile [308], the resulting velocity distribution is given by

$$f(\boldsymbol{v}) = \begin{cases} \frac{1}{N} \frac{1}{v_{\rm esc}\sqrt{v_x^2+v_y^2}} \left(1 - \frac{v_x^2+v_y^2+v_z^2}{v_{\rm esc}^2}\right)^2 , & |\boldsymbol{v}| < v_{\rm esc} \\ 0 , & |\boldsymbol{v}| \geq v_{\rm esc} \end{cases} . \tag{A.9}$$

In the plots shown we adopt $a = 10\,\mathrm{kpc}$. For $b = 3$, corresponding to the NFW profile, an analytical expression of the velocity distribution does not exist, but it is straightforward to numerically calculate the velocity distribution from the density profile.

A.1.3 Additional contributions to the local dark matter density

Our discussion of $\tilde{g}(v_{min})$ is quite independent of the origin of the local DM density. Nevertheless, in order to predict the velocity integral (Fig. 2.2) and the modulation amplitude (Fig. 3.2) we have assumed that the local DM density is completely dominated by the contribution from the Galactic DM halo. In general there may be other significant contributions to the local DM density, e.g. from *DM streams* and a *dark disk* (see also Fig. 3.12 and Fig. 3.18). We will now briefly discuss how these can alter the theoretical predictions of $g(v_{\rm min})$ and $A(v_{\rm min})$.

Streams

N-body simulations show that the DM velocity distribution is not a smooth function but instead has a significant amount of sub-structure [309] due to the presence of tidal streams. Such streams can have large velocities relative to the local standard of rest and can therefore contribute to $g(v_{\rm min})$ at large values of $v_{\rm min}$. The result is an edge in the velocity integral (see Fig. 2.1) as well as a significant increase in the modulation fraction [104, 310]. Nevertheless, the bound on the modulation fraction derived in Sec. 3.1.4 remains valid. In other words, a large modulation fraction is always visible as a steep decrease in the velocity integral and can therefore be probed by measuring the differential event rate (see also Ref. [311] for a discussion on how to constrain DM streams with CoGeNT).

Debris flows

A related possibility is the presence of a flow of debris particles, which have been tidally stripped from subhalos falling into the Milky Way. It was suggested [312, 313] that the contribution of such debris flows to the velocity integral can be written as

$$g(v_{\rm min}) = (1-\alpha)\, g(v_{\rm min})_{\rm halo} + \alpha \times \begin{cases} \frac{1}{v_{\rm flow}}\,, & v_{\rm min} < (v_{\rm flow} - v_{\rm E}) \\ \frac{v_{\rm flow}+v_{\rm E}-v_{\rm min}}{2\, v_{\rm flow}\, v_{\rm E}}\,, & (v_{\rm flow} - v_{\rm E}) < v_{\rm min} < (v_{\rm flow} + v_{\rm E}) \\ 0\,, & v_{\rm min} > (v_{\rm flow} + v_{\rm E}) \end{cases}\,, \quad \text{(A.10)}$$

where $v_{\rm flow}$ is the velocity of the flow in the Galactic rest frame and α is the contribution of the debris to the local DM density. For Fig. 3.12 we have chosen $\alpha = 0.2$ and $v_{\rm flow} = 400\,{\rm km\,s^{-1}}$.

Dark disk

Most N-body simulations of the Galactic DM halo neglect the effect of baryons. Baryonic matter can potentially effect the formation of a DM disk that can contribute a similar amount to the local DM density as the halo [197, 299]. Such a dark disk is expected to have a much smaller velocity dispersion than the Galactic halo and to be co-rotating with only a small lag. Consequently, a dark disk will contribute to $\tilde{g}(v_{\rm min})$ only for $v_{\rm min} \leq 250\,{\rm km\,s^{-1}}$ — a region that is irrelevant in the context of light DM [161, 162, 314]. For DM particles with $m_\chi > 50\,{\rm GeV}$, one can however expect a significant increase in both the velocity integral and the modulation fraction at low energies. The velocity distribution of DM particles in the dark disk can be modelled approximately by a M-B distribution, i.e. the parameterisation is formally identical to the one for the SHM. We take $v_0 = 50\,{\rm km\,s^{-1}}$ for the velocity dispersion and $\mathbf{v}_{\rm lag} = (0,\, 50,\, 0)\,{\rm km\,s^{-1}}$ as the lag velocity that replaces the circular velocity of the Sun.

A.2 Overview of direct detection experiments

In this appendix, we discuss the direct detection experiments that we consider for our analysis and state the assumptions that we make. For definitiveness we limit ourselves to experimental results that have appeared before August 2013. A discussion of how more recent results change our conclusions is provided in Chapter 6.

To derive constraints from XENON100, XENON10, CDMS-Ge, CDMS-Si and CRESST-II

we employ the 'maximum gap method' [175], for all other bounds we use the 'binned Poisson' method [74, 176]. For a discussion of these methods, we refer to Ref. [315]. For the CDMS-Si best-fit region we employ the extended maximum likelihood method [174], discussed in detail in Appendix A.3. The other best-fit regions are calculated using a χ^2 parameter estimation method.[1]

XENON100

We take the data based on an exposure of 20.9 kg yr [80], combined with the recent measurements of $\mathcal{L}_{\text{eff}}$ [177]. We calculate the energy resolution under the assumption that it is dominated by Poisson fluctuations in the number of photoelectrons.

XENON10

We consider the $S2$-only analysis presented in Ref. [98]. Unless otherwise specified, we adopt the original choice of $\mathcal{Q}_{\text{y}}$ from Ref. [98], i.e. we assume that $\mathcal{Q}_{\text{y}}$ vanishes for $E_{\text{R}} < 1.4$ keV. Moreover, we take a flat detector acceptance of 0.94 and assume that the energy resolution is given by $\Delta E_{\text{R}} = E_{\text{R}}/\sqrt{E_{\text{R}}\mathcal{Q}_{\text{y}}(E_{\text{R}})}$. It has been suggested that the XENON10 data be analysed by converting recoil spectra to photoelectrons and using Poisson statistics to model the detector response [169]. We find that this procedure gives significantly weaker bounds at low DM mass. Therefore we assume Gaussian fluctuations in order to enable fair comparison with other results in the literature.

CDMS-Si

For our analysis we assume an energy resolution of $\Delta E_{\text{R}} = 0.3$ keV [316] and use the detector acceptance from Ref. [92]. To determine the best-fit region, we take the normalised background distributions from Ref. [317] and rescale the individual contributions in such a way that 0.41, 0.13 and 0.08 events are expected from surface events, neutrons and ^{206}Pb, respectively. We find that varying the normalisation of the background within the range suggested in Ref. [92] while keeping its shape fixed does not sensitively affect the significance of the background+DM hypothesis, nor the shape of the best-fit region. Note that we do not perform a background subtraction when using the CDMS-Si data to obtain a bound.

[1] For CRESST-II we use eq. (13) from Ref. [160] to calculate the best-fit parameter region.

Bin [keVee]	**Event rate in (day kg keVee)$^{-1}$**	**Error in (day kg keVee)$^{-1}$**
0.50 – 0.61	12.8	1.0
0.61 – 0.72	10.1	0.9
0.72 – 0.85	6.7	0.8
0.85 – 1.00	5.5	0.8
1.00 – 1.15	4.5	0.7
Bin [keVee]	**Modulation amplitude in (day kg keVee)$^{-1}$**	**Error in (day kg keVee)$^{-1}$**
0.5 – 1.0	0.75	0.54
1.0 – 2.0	0.51	0.30
2.0 – 3.2	0.26	0.16

TABLE A.1. The CoGeNT event rate and its modulation: the modulation amplitude has been obtained by fitting a cosine with period fixed to 365 days and the phase fixed to $t_0 = 146$ days.

CDMS-Ge

We consider the dedicated low-threshold analysis of the CDMS-Ge data [96] using only the data of the most constraining detector, T1Z5. For our analysis, we adopt an energy resolution of $\Delta E_\mathrm{R} = 0.2\,(E_\mathrm{R} \cdot \mathrm{keV})^{1/2}$ [318].

CoGeNT

We analyse the publicly available data from the CoGeNT experiment taken over the course of 1.2 years [94]. To determine the total event rate, we subtract the L-shell EC contribution and a constant background. We do not attempt to make the subtraction of surface events suggested in Ref. [90]. We use the Lindhard quenching factor and the (corrected) detector resolution from Ref. [319]. The efficiency curve was provided by J. Collar (private communication).

To determine the modulation, we fix the peak date to $t_0 = 146$ days, which is the best-fit value for the DAMA modulation. The bins considered and the resulting event rates and modulation amplitudes are given in Table A.1. Note that the binning of the event rate is chosen in such a way that the corresponding bins in v_min-space are equally sized.

DAMA

We use the combined observed event rates from DAMA/NaI and DAMA/LIBRA [93] for the 8 bins spanning the energy range 2–6 keVee. No significant modulation is observed at higher energies. We assume a quenching factor of 0.3 for Na and 0.09 for I (other values are discussed in Refs. [103, 104]) and no contribution from channelling [320].

CRESST-II

We use the recent results from 730 kg days of data taking [91]. We estimate that the acceptance region corresponds to 86% acceptance for oxygen, 89% for tungsten and 90% for calcium. We take the energy resolution to be $\Delta E_{\mathrm{R}} = 0.3\,\mathrm{keV}$ for each detector. To extract the DM signal, we read off the total number of measured events and the expected background from fig. 11 of Ref. [91] and use the Feldman-Cousins approach [179].

Depending on the application, we bin the CRESST-II data in different ways. In order to calculate best-fit parameter regions, we consider a bin width of 3 keV, rather than a bin width of 1 keV as presented in Ref. [91]. However, if we want to calculate $\tilde{g}(v_{\mathrm{min}})$ using Method 1 from Appendix A.4.2, we have to make sure that the detector efficiency does not vary strongly within a single bin due to the onset of additional detector modules. This condition is fulfilled for the three bins [13 keV – 15 keV], [16 keV – 19 keV] and [19 keV – 22 keV]. Finally, to apply Method 2 from Appendix A.4.2, we need to bin the data in a special way depending on the DM mass. The resulting number of events is shown in Table A.2.

Finally, we also consider the improved constraint from the CRESST-II commissioning run presented in Ref. [321] using the detector efficiencies given there.

CRESST-I

To constrain very low DM masses, we analyse the experimental data from Ref. [262], taking the detector resolution to be $\Delta E = \sqrt{(0.22\,\mathrm{keV})^2 + (0.017\,E_{\mathrm{R}})^2}$.

Bin [keV]	Total events	Expected background	Signal (min)	Signal (max)
10 – 13	9	3.2	3.2	9.6
13 – 16	15	6.1	5.3	13.3
16 – 19	11	7.0	1.2	7.8
19 – 22	8	6.3	0.2	5.0
22 – 25	4	5.2	0	1.8
25 – 28	4	4.6	0	2.2
28 – 31	4	4.3	0	2.5
31 – 34	3	4.0	0	1.5
34 – 37	4	3.7	0	3.0
37 – 40	5	3.5	0.2	4.3
13 – 15	11	3.8	4.0	11.0
16 – 19	11	7.0	1.2	7.8
19 – 22	8	6.3	0.2	5.0
10 – 14	18	5.4	8.4	17.4
12 – 15	19	5.7	9.1	18.1
15 – 21	19	13.7	1.7	10.1
16 – 20	13	9.4	0.9	7.9
17 – 24	17	14.1	0.5	7.7

TABLE A.2. Data from the CRESST-II experiment: total number of events, expected number of background events and 1σ confidence interval for the signal using a Feldman-Cousins approach.

SIMPLE

We do not attempt to combine the results from Stage 1 [322] and Stage 2 [273] but instead consider only the latter. Since the recoil energy is not measured, the experiment can place only an upper limit on the total event rate above the detector threshold of 8 keV. We take the cut acceptance and nucleation efficiency from Ref. [273].

PICASSO

We take the experimental data from Ref. [263] and use $P(E_{\mathrm{R}}, E_{\mathrm{th}}) = 1 - \exp\left[5(1 - E_{\mathrm{R}}/E_{\mathrm{th}})\right]$ for the threshold function.

COUPP

We use the results from Ref. [274] and assume a step function for the nucleation threshold.

KIMS

We calculate our bounds based on the data from Ref. [275], using the detector efficiency from Ref. [323] as suggested in Ref. [68].

A.3 The extended maximum likelihood method

This appendix reviews the extended maximum likelihood method [174], which we use to analyse the data from CDMS-Si. The advantage of this method is that it allows for a parameter estimation without the need to bin the experimental data. The disadvantage (compared to e.g. the standard χ^2 parameter estimation) is that there is no straightforward estimate for the goodness of fit of the best-fit point [324]. Nevertheless, under certain conditions it is still possible to estimate the signal significance using a likelihood ratio [325].

For an experiment with k observed events at energies $E_1, \ldots, E_k$ we define the extended likelihood function by

$$\log \mathcal{L} \equiv \sum_{i=1}^{k} \log \left(\frac{\mathrm{d}R(\mathbf{x})}{\mathrm{d}E_\mathrm{R}}\Big|_{E_i} + \frac{\mathrm{d}B}{\mathrm{d}E_\mathrm{R}}\Big|_{E_i} \right) - \int \left(\frac{\mathrm{d}R(\mathbf{x})}{\mathrm{d}E_\mathrm{R}} + \frac{\mathrm{d}B}{\mathrm{d}E_\mathrm{R}} \right) \mathrm{d}E_\mathrm{R} \,, \tag{A.11}$$

where $\mathrm{d}R(\mathbf{x})/\,\mathrm{d}E_\mathrm{R}$ is the expected recoil spectrum for a DM signal, depending on a set of assumed DM parameters $\mathbf{x}$, and $\mathrm{d}B/\,\mathrm{d}E_\mathrm{R}$ is the known background distribution. We can then determine the best-fit values for the assumed DM parameters, $\hat{\mathbf{x}}$, by minimising $\log \mathcal{L}$.

To determine the allowed parameter region, we can define the test statistic

$$q(\mathbf{x}) \equiv -2 \left(\log \mathcal{L}(\mathbf{x}) - \log \mathcal{L}(\hat{\mathbf{x}}) \right) \,. \tag{A.12}$$

For the true DM parameters of nature (called $\mathbf{x}'$), the test statistic $q(\mathbf{x}')$ is expected to follow a χ^2-distribution with m degrees of freedom, where m is the number of DM parameters. Consequently, given a set of experimental data we can estimate the p-value for a hypothetical value of $\mathbf{x}$ as

$$p(\mathbf{x}) = 1 - F(q(\mathbf{x}), m) \,, \tag{A.13}$$

where $F(x, m)$ is the cumulative distribution function for the χ^2-distribution with m degrees of freedom. In other words, assuming that $\mathbf{x}$ are the true parameters of nature, the probability to find $q(\mathbf{x})$ larger than the observed value is given by $p(\mathbf{x})$. The allowed parameter region at a confidence

level of α is then given by all sets of parameters that satisfy

$$\alpha > 1 - p(\mathbf{x}) = F(q(\mathbf{x}), m) \; . \tag{A.14}$$

In addition we would like to quantify how well the best-fit DM model describes the observed data, i.e. we want to determine how strongly the signal+background hypothesis is preferred over the background-only hypothesis. For this purpose it is convenient to take one of the DM parameters to be the DM-nucleon scattering cross section σ_N. The likelihood of the background-only hypothesis can then be obtained by simply setting $\sigma_N = 0$. We can therefore define

$$q_0 = -2 \left(\log \mathcal{L}(\sigma_N = 0) - \log \mathcal{L}(\hat{\sigma}_N) \right) \; , \tag{A.15}$$

which, if the background-only hypothesis is correct, should have a p-value of

$$p_0 = 1 - F(q_0, 1) \; . \tag{A.16}$$

This value corresponds to the probability that an observed signal is just an upward fluctuation of the background. Consequently, $1 - p_0$ is often quoted as the significance of the signal.

This approach works well if we look for an excess over a large but well-known background distribution. If, on the other hand, the shape of the background distribution is such that very few background events are expected in the signal region the assumption of a χ^2-distribution becomes problematic. To illustrate this problem, let us assume that the signal region is chosen in such a way that the number of expected background events is significantly smaller than 1. Repeating the experiment many times, we would — in the absence of DM interactions — expect most of the data sets to contain no signal-like events. Any such data set will give $\hat{\sigma}_N = 0$, since increasing σ_N will only reduce the likelihood. Consequently, in all of these cases q_0 is exactly zero. If, on the other hand, a signal-like event is observed, this will give very strong evidence for non-zero σ_N and clearly disfavour the background-only hypothesis. In other words, with a small probability q_0 will be very large. Intermediate values, on the other hand, are typically absent. Clearly, for such an experiment q_0 does not follow a χ^2-distribution. In practice, it is therefore often necessary to determine the distribution of q_0 from Monte Carlo simulations of the expected background. For CDMS-Si we find that assuming a χ^2-distribution somewhat overestimates the probability of large fluctuations in q_0 and consequently underestimates p_0.

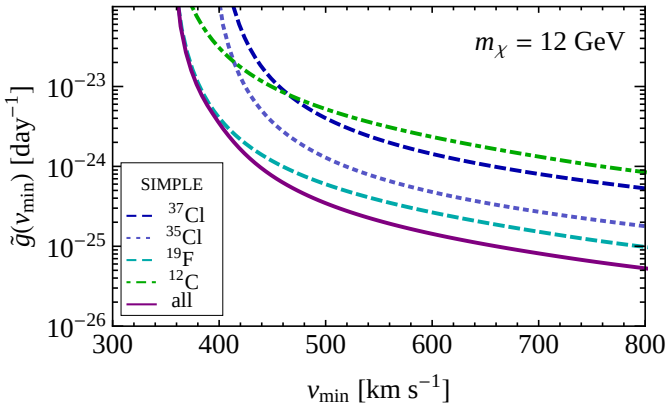

FIG. A.1. The individual bounds on $\tilde{g}(v_{\rm min})$ for the different elements and isotopes present in the target of the SIMPLE experiment as well as the total bound from the combination of these constraints.

A.4 Studying the velocity integral with multiple-element targets

Many experiments, for example SIMPLE and CRESST-II, employ a combination of different elements as target. In this case, a nuclear recoil of a given energy corresponds to different values of $v_{\rm min}$ depending on the recoiling nucleus. In this appendix, we discuss how to disentangle the arising ambiguities. Note that these considerations may also be important for targets consisting of different isotopes of a single element, especially when considering isospin-dependent interactions.

A.4.1 Constraining the velocity integral

First, we discuss how an upper bound can be placed on the velocity integral for a null result from an experiment consisting of more than one element. The most obvious example is the SIMPLE experiment, consisting of C_2ClF_5. To make progress, we apply the method presented in Sec. 3.1.2 separately to each element (or isotope) by requiring that the number of recoil events expected for this element alone does not significantly exceed the total number of events observed.

For each element we thus obtain a bound $\tilde{g}_i^{\rm max}(v_{\rm min})$ on the rescaled velocity integral. In order to obtain a total bound, we can then combine these bounds according to

$$\frac{1}{\tilde{g}^{\rm max}(v_{\rm min})} = \sum_i \frac{1}{\tilde{g}_i^{\rm max}(v_{\rm min})} \,. \tag{A.17}$$

This procedure is illustrated in Fig. A.1.

In fact, it is sufficient to calculate $\tilde{g}_i^{\rm max}(v_{\rm min})$ for only one of the elements in the target, as we

can use this bound to infer the bounds for all other elements. Suppose we have determined the bound $\tilde{g}(v_{\min}) < \tilde{g}_1^{\max}(v_{\min})$ for $v_{\min} = \hat{v}_1$ for an isotope with charge Z_1, mass number A_1 and form factor F_1. For a different isotope, we can now infer the value of the rescaled velocity integral at the minimum velocity $\hat{v}_2$, which satisfies $E_{\mathrm{R}}^{(1)}(\hat{v}_1) = E_{\mathrm{R}}^{(2)}(\hat{v}_2)$, meaning that the two velocities correspond to the same maximum recoil energy on the respective nuclei. The bound from the second isotope is then given by

$$\tilde{g}_2^{\max}(\hat{v}_2) = \frac{c_1 C_{\mathrm{T}}^2(Z_1, A_1) F_1(E_{\mathrm{R}}^{(1)}(\hat{v}_1))^2}{c_2 C_{\mathrm{T}}^2(Z_2, A_2) F_2(E_{\mathrm{R}}^{(2)}(\hat{v}_2))^2} \tilde{g}_1^{\max}(\hat{v}_1) \,, \tag{A.18}$$

where $c_{1,2}$ are the respective mass fractions of the isotopes.

A.4.2 Measuring the velocity integral

We now turn to the more difficult task of inferring information on $\tilde{g}(v_{\min})$ from a potential DM signal in an experiment consisting of several different elements. The obvious application is the CRESST-II experiment, which we will use here for illustration. We consider only the contribution from calcium and oxygen, because for DM masses of 15 GeV and less, nuclear recoils on tungsten have recoil energies well below the threshold of the detector.

The differential event rate in CRESST-II is given by the sum of the differential event rates for the individual elements, i.e.

$$\left(\frac{\mathrm{d}R}{\mathrm{d}E_{\mathrm{R}}}\right)^{\mathrm{tot}} = \left(\frac{\mathrm{d}R}{\mathrm{d}E_{\mathrm{R}}}\right)^{(\mathrm{O})} + \left(\frac{\mathrm{d}R}{\mathrm{d}E_{\mathrm{R}}}\right)^{(\mathrm{Ca})} \,. \tag{A.19}$$

To cause a recoil of energy E_{R}, a DM particle must have a minimum velocity of $v_{\min}^{(\mathrm{O})}(E_{\mathrm{R}})$ for scattering off oxygen and $v_{\min}^{(\mathrm{Ca})}(E_{\mathrm{R}})$ for calcium. Consequently, if we measure the differential event rate at the energy E_{R}, we simultaneously probe the rescaled velocity integral at *both* of these velocities. Therefore, we can only extract information on $\tilde{g}(v_{\min}^{(\mathrm{O})}(E_{\mathrm{R}}))$ if we know the ratio of the differential event rates for scattering off oxygen and calcium

$$\frac{(\mathrm{d}R/\mathrm{d}E_{\mathrm{R}})^{(\mathrm{O})}}{(\mathrm{d}R/\mathrm{d}E_{\mathrm{R}})^{(\mathrm{Ca})}} = \frac{C_{\mathrm{T}}^2(Z^{(\mathrm{O})}, A^{(\mathrm{O})}) \cdot F^{(\mathrm{O})}(E_{\mathrm{R}})^2 \cdot g(v_{\min}^{(\mathrm{O})}(E_{\mathrm{R}}))}{C_{\mathrm{T}}^2(Z^{(\mathrm{Ca})}, A^{(\mathrm{Ca})}) \cdot F^{(\mathrm{Ca})}(E_{\mathrm{R}})^2 \cdot g(v_{\min}^{(\mathrm{Ca})}(E_{\mathrm{R}}))} \,. \tag{A.20}$$

We present two different methods to determine this ratio. The first makes use of the fact that the rescaled velocity integral is a decreasing function of $v_{\min}$ to place a lower bound on the contribution from oxygen. The second method requires a special binning of the data in such a way that the

contribution of calcium can actually be determined from the combined information of several bins. Once we have an estimate of the differential event rate from oxygen alone, we can use the procedure described in Sec. 3.1.1 to obtain the corresponding values of $\tilde{g}(v_{\mathrm{min}})$.

Method 1

Since calcium is the heavier nucleus, $v_{\mathrm{min}}^{(\mathrm{Ca})} > v_{\mathrm{min}}^{(\mathrm{O})}$ for the same recoil energy. We know that $\tilde{g}(v_{\mathrm{min}})$ must decrease as v_{min} increases, so $g(v_{\mathrm{min}}^{(\mathrm{Ca})}(E_{\mathrm{R}})) < g(v_{\mathrm{min}}^{(\mathrm{O})}(E_{\mathrm{R}}))$. Substituting this expression into Eq. (A.20), it is possible to place a lower bound on the contribution of oxygen

$$\left(\frac{\mathrm{d}R}{\mathrm{d}E_{\mathrm{R}}}\right)^{(\mathrm{O})} > \frac{C_{\mathrm{T}}^2(Z^{(\mathrm{O})}, A^{(\mathrm{O})}) \cdot F^{(\mathrm{O})}(E_{\mathrm{R}})^2}{C_{\mathrm{T}}^2(Z^{(\mathrm{Ca})}, A^{(\mathrm{Ca})}) \cdot F^{(\mathrm{Ca})}(E_{\mathrm{R}})^2} \left(\frac{\mathrm{d}R}{\mathrm{d}E_{\mathrm{R}}}\right)^{(\mathrm{Ca})} \equiv S^{(\mathrm{O,Ca})}(E_{\mathrm{R}}) \left(\frac{\mathrm{d}R}{\mathrm{d}E_{\mathrm{R}}}\right)^{(\mathrm{Ca})} . \quad \text{(A.21)}$$

If the differential event rate $(\mathrm{d}R/\mathrm{d}E_{\mathrm{R}})^{\mathrm{tot}}$ is known, we can make use of this inequality and Eq. (A.19) to infer that

$$\left(\frac{\mathrm{d}R}{\mathrm{d}E_{\mathrm{R}}}\right)^{(\mathrm{O})} > \left(\frac{\mathrm{d}R}{\mathrm{d}E_{\mathrm{R}}}\right)^{\mathrm{tot}} \frac{S^{(\mathrm{O,Ca})}(E_{\mathrm{R}})}{1 + S^{(\mathrm{O,Ca})}(E_{\mathrm{R}})} . \quad \text{(A.22)}$$

In practice, additional factors like the target composition and the acceptance for each nuclear recoil need to be included in $S^{(\mathrm{O,Ca})}(E_{\mathrm{R}})$. In the case of CRESST-II, the minimum contribution of oxygen in the relevant energy region is approximately 20%. Note, that this method only constrains but does not actually determine the ratio of oxygen to calcium scatters in each bin. To reflect our ignorance of the true ratio, we do not show central values for the measurements of $\tilde{g}(v_{\mathrm{min}})$ obtained with this method.

Method 2

In order to combine information from several bins, it is useful to construct energy bins of different sizes according to the following rule: Starting from an arbitrary bin $[E_1, E_2]$, we use the heavier target (assumed to be calcium) to convert the boundaries into v_{min}-space and then the lighter target (oxygen) to convert the velocities back into energy space. This way, we obtain a new energy bin $\left[E_{\mathrm{R}}^{(\mathrm{O})}(v_{\mathrm{min}}^{(\mathrm{Ca})}(E_1)), E_{\mathrm{R}}^{(\mathrm{O})}(v_{\mathrm{min}}^{(\mathrm{Ca})}(E_2))\right]$. The two bins thus constructed have the property that calcium recoils with energies in bin 1 probe the *same* region of v_{min}-space as oxygen recoils with energies in bin 2. We can repeat this procedure recursively to obtain additional bins with increasing bin size (see Fig. A.2). It is always possible to choose the first bin in such a way that the different bins do

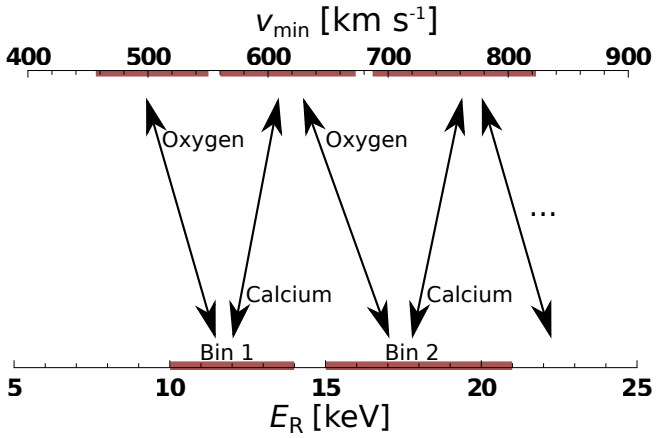

FIG. A.2. An illustration of the method used to construct bins for CRESST-II. The two energy bins constructed in this way have the property that calcium recoils with energies in bin 1 probe the *same* region of $v_{\min}$-space as oxygen recoils with energies in bin 2. For this plot, we have assumed $m_\chi = 9$ GeV.

not overlap.

We only wish to consider bins where a significant excess of signal over expected background is observed, meaning that we abort the iteration as soon as we obtain a bin where the signal is compatible with the background estimate. To give a concrete example, for $m_\chi = 9\,\text{GeV}$ the energy conversion factor between oxygen and calcium is

$$\frac{m_{\text{Ca}}}{\mu^2_{\text{Ca}}}\frac{\mu^2_{\text{O}}}{m_{\text{O}}} = 1.50\,, \tag{A.23}$$

so a possible construction for an experiment like CRESST-II would be [8 – 12], [12 – 18], [18 – 27] (all energies in keV). Unfortunately, the current CRESST-II data reaches down only to 10 keV and we cannot bin the data arbitrarily so we will use only the two bins [10 keV – 14 keV] and [15 keV – 21 keV] here. For different values of m_χ the conversion factor will also change, so different bins must be considered. We present possible choices for different DM masses in Table A.3.

The basic idea is to start by evaluating the highest bin and then work backwards towards bin 1. In the highest bin we can reasonably assume that the observed event rate is completely dominated by the lightest element in the target, because we expect events in this bin to arise from DM particles close to the escape velocity. Under this assumption we can calculate $\tilde{g}(v_{\min})$ for the highest bin in the same way as described in Sec. 3.1.1 for a target consisting of a single element. Now we can exploit the fact that we have constructed the bins in a special way and use the inferred value of

m_χ [GeV]	Conversion factor	Bin 1 [keV]	Bin 2 [keV]
6	1.72	10–14	17–24
9	1.50	10–14	15–21
12	1.34	12–15	16–20
15	1.22	11.5–14	14–17

TABLE A.3. The energy conversion factors between oxygen recoils and calcium recoils for constant $v_{\min}$ and different choices of the DM mass m_χ. The third and fourth column give possible choices for two bins that are related by this conversion factor.

$\tilde{g}(v_{\min})$ to *predict* the number of calcium events in the next lower bin.

We can then subtract the predicted number of calcium events in the next lower bin to obtain the number of events that is due to oxygen scatters alone. Again, we are left with a number of events that correspond to scattering of the lightest element alone. We can use this number to calculate $\tilde{g}(v_{\min})$ in the region of $v_{\min}$-space corresponding to the second to highest bin. Using this measurement to predict the calcium scatters in the next lower bin, we can recursively extract $\tilde{g}(v_{\min})$ for all bins. Compared to the previous method, the advantage is clearly a much more accurate prediction of $\tilde{g}(v_{\min})$. The disadvantage is that we are forced to bin the data in a certain way, which is inconvenient if the energy of each event is not publicly available.

A.5 Scattering cross sections for the scalar operator

In this appendix, we calculate the DM scattering cross section for the operator

$$\mathcal{O}_q = \mathcal{C}_q(\mu)\, m_q\, \bar{\chi}\chi\, \bar{q}q\ , \tag{A.24}$$

where we allow for a scale dependence of the Wilson coefficient $\mathcal{C}_q$. We evolve this coefficient from the scale Λ, where the operator is generated, down to m_t, where we integrate out the top quark. Removing the heavy quark as an active degree of freedom gives rise to a finite threshold correction to the Wilson coefficient of the operator

$$\mathcal{O}_G = \mathcal{C}_G\, \bar{\chi}\chi\, G^{a,\mu\nu} G^a_{\mu\nu}\ , \tag{A.25}$$

where $G^{a,\mu\nu}$ denotes the field strength tensor of QCD. The corresponding matching is captured by the simple replacement [326]

$$m_t\,\bar{\chi}\chi\,\bar{t}t\,\mathcal{C}_t(m_t) \to \bar{\chi}\chi\,G^{a,\mu\nu}G^a_{\mu\nu}\,\mathcal{C}_G(m_t)\;, \tag{A.26}$$

with $\mathcal{C}_G$ given by

$$\mathcal{C}_G(\mu) = -\frac{\alpha_s(\mu)}{12\pi}\,\mathcal{C}_t(m_t)\;. \tag{A.27}$$

At the scales m_b and m_c, the bottom and charm quarks are integrated out, which again results in finite matching corrections to $\mathcal{C}_G$ in full analogy to Eq. (A.27).

At the scale relevant for direct detection, $\mu = m_N \approx 0.939\,\text{GeV}$, we now have to evaluate the matrix elements of the operators $\mathcal{O}_q$ and $\mathcal{O}_G$ between nucleon states N. Following the standard procedure in the DM literature [327], we evaluate these contributions at tree level to obtain

$$\langle N|\mathcal{O}_q|N\rangle \simeq m_N\,f^N_{Tq}\,\mathcal{C}_q(m_N)\;, \tag{A.28}$$

where $q = u,\,d,\,s$ and the scalar form factor f^N_{Tq} is defined via $m_N f^N_{Tq} = \langle N|m_q\bar{q}q|N\rangle$. Furthermore, using the classic tree-level result of Ref. [326] for the operator $\mathcal{O}_G$, one obtains

$$\langle N|\mathcal{O}_G|N\rangle \simeq -\frac{8\pi}{9\alpha_s(m_N)}\,m_N\,f^N_{TG}\,\mathcal{C}_G(m_N)\;, \tag{A.29}$$

where we have introduced the expression $f^N_{TG} = 1 - \sum_q f^N_{Tq}$ for the gluon form factor.

The zero-momentum scattering cross section for $N = p,\,n$ can then be written as

$$\sigma_N = \frac{\mu^2_{\chi N}\,m_N^2}{\pi}\left(f^N\right)^2\;, \tag{A.30}$$

where, combining Eqs. (A.29) and (A.27) one obtains[1]

$$\begin{aligned} m_N\,f^N &= \sum_q \langle N|\mathcal{O}^\chi_q|N\rangle + \langle N|\mathcal{O}^\chi_G|N\rangle \\ &= m_N\left[\sum_{q=u,d,s} f^N_{Tq}\,\mathcal{C}_q(m_N) + \frac{2}{27}\,f^N_{TG}\sum_{q=c,b,t}\mathcal{C}_q(m_q)\right]\;. \end{aligned} \tag{A.31}$$

The light-quark matrix elements f^N_{Tq} can either be determined phenomenologically from baryon masses and meson-baryon scattering data or computed within lattice QCD (see Ref. [278] for a

[1] Note that in contrast to the dimensionless coupling f_N, the coefficient f^N introduced here carries dimension GeV^{-3}.

concise review). We adopt the values

$$\begin{aligned} f_{Tu}^p &\approx 0.023\,, \qquad f_{Td}^p \approx 0.034\,, \qquad f_{Ts}^p \approx 0.013 \\ f_{Tu}^n &\approx 0.019\,, \qquad f_{Td}^n \approx 0.041\,, \qquad f_{Ts}^n \approx 0.013\,. \end{aligned} \tag{A.32}$$

The numbers for f_{Tu}^N and f_{Td}^N have been taken from Ref. [278], whereas f_{Ts}^N has been taken from a recent lattice QCD study in Ref. [328]. Compared to older values of typically $f_{Ts}^N \approx 0.14$ [278] the number given in Eq. (A.32) is notably smaller.

If the dependence of $\mathcal{C}_q$ on the energy scale μ is negligible, we find $f^p \approx f^n \approx 0.28\,\mathcal{C}_q$. For $\Lambda < m_t$, the contribution of the top quark is absent, leading to $f^p \approx f^n \approx 0.21\,\mathcal{C}_q$.

A.6 Decay widths of a vector mediator

In this appendix we present the partial decay widths of a vector mediator R coupling to DM and SM particles, as introduced in Chapter 4:

$$\Gamma(R \to \chi\bar{\chi}) = \frac{m_R}{12\pi}\sqrt{1-\frac{4m_\chi^2}{m_R^2}}\left[(g_\chi^V)^2 + (g_\chi^A)^2 + \frac{m_\chi^2}{m_R^2}(2(g_\chi^V)^2 - 4(g_\chi^A)^2)\right], \tag{A.33}$$

$$\Gamma(R \to \phi\phi^*) = \frac{m_R}{48\pi}\sqrt{1-\frac{4m_\phi^2}{m_R^2}}\, g_{R\phi}^2\,, \tag{A.34}$$

$$\Gamma(R \to f\bar{f}) = \frac{m_R N_c}{12\pi}\sqrt{1-\frac{4m_f^2}{m_R^2}}\left[(g_f^V)^2 + (g_f^A)^2 + \frac{m_f^2}{m_R^2}(2(g_f^V)^2 - 4(g_f^A)^2)\right], \tag{A.35}$$

$$\begin{aligned} \Gamma(R \to W^+W^-) = \frac{1}{192\pi}\, m_R \left(\frac{m_R}{m_W}\right)^4 \left(1-4\frac{m_W^2}{m_R^2}\right)^{1/2} \\ \times \left((g_{WW1}^R)^2 \left[4\frac{m_W^2}{m_R^2} - 4\frac{m_W^4}{m_R^4} - 48\frac{m_W^6}{m_R^6}\right] \right. \\ + g_{WW1}^R\, g_{WW2}^R \left[12\frac{m_W^2}{m_R^2} - 48\frac{m_W^4}{m_R^4}\right] + (g_{WW2}^R)^2\left[1 - 16\frac{m_W^4}{m_R^4}\right] \\ \left. + (g_{WW3}^R)^2\left[4\frac{m_W^2}{m_R^2} - 32\frac{m_W^4}{m_R^4} + 64\frac{m_W^6}{m_R^6}\right]\right), \end{aligned} \tag{A.36}$$

$$\Gamma(R \to ZZ) = \frac{(g^R_{ZZ})^2}{96\pi}\, m_R\, \frac{m_R^2}{m_Z^2} \left(1 - 4\frac{m_Z^2}{m_R^2}\right)^{3/2} \left[1 - 6\frac{m_Z^2}{m_R^2}\right] , \tag{A.37}$$

$$\Gamma(R \to Z\gamma) = \frac{(g^R_{Z\gamma})^2}{96\pi}\, m_R\, \frac{m_R^2}{m_Z^2} \left(1 - \frac{m_Z^2}{m_R^2}\right)^{3} , \tag{A.38}$$

$$\Gamma(R \to ZH) = \frac{(g^R_{ZH})^2}{192\pi\, m_Z^2}\, m_R \sqrt{\lambda(1, x_Z, x_H)}\, (\lambda(1, x_Z, x_H) + 12 x_Z) , \tag{A.39}$$

where $x_Z = (m_Z/m_R)^2$, $x_H = (m_H/m_R)^2$, and $\lambda(x, y, z) = x^2 + y^2 + z^2 - 2xy - 2yz - 2zx$.

A.7 Calculation of one-loop amplitudes

In this appendix we present explicit calculations for the one-loop diagrams in Fig. 5.4 and Fig. 5.7. For an insertion of $\mathcal{O}_{\rm T}$, the graph with a closed top-quark loop shown on the left in Fig. 5.4 yields the amplitude

$$\mathcal{A} = -\frac{i}{(2\pi)^4} \frac{N_c e Q_t}{\Lambda_{\rm T}^2} \left(\bar\chi \sigma_{\mu\nu} \chi\right) \mu^{4-d} \int d^d l\, \frac{texttr\left[\sigma^{\mu\nu} \left(\not{l} - \not{q} + m_t\right) \not{\varepsilon} \left(\not{l} + m_t\right)\right]}{\left((l-q)^2 - m_t^2\right)\left(l^2 - m_t^2\right)} , \tag{A.40}$$

where we have used dimensional regularisation. The factor $N_c = 3$ arises from the trace over colours, μ is the renormalisation scale, while q^μ and ε^μ denote the momentum and the polarisation vector of the photon, respectively. The Dirac trace evaluates to

$$\mathrm{tr}\left[\sigma^{\mu\nu} \left(\not{l} - \not{q} + m_t\right) \not{\varepsilon} \left(\not{l} + m_t\right)\right] = 4 i m_t \left(q^\mu \varepsilon^\nu - q^\nu \varepsilon^\mu\right) . \tag{A.41}$$

We hence find

$$\mathcal{A} = \frac{i}{4\pi^4} \frac{3 e Q_t}{\Lambda_{\rm T}^2}\, m_t \left(\bar\chi \sigma_{\mu\nu} \chi\right) \left(q^\mu \varepsilon^\nu - \varepsilon^\mu q^\nu\right) \int d^d l\, \frac{\mu^{4-d}}{\left((l-q)^2 - m_t^2\right)\left(l^2 - m_t^2\right)} . \tag{A.42}$$

In order to extract the contribution $\mathcal{A}_{\rm M}$ to the magnetic dipole operator, we expand the integrand in powers of q^2 and obtain

$$\mathcal{A}_{\rm M} = \frac{i}{4\pi^4} \frac{3 e Q_t}{\Lambda_{\rm T}^2}\, m_t \left(\bar\chi \sigma_{\mu\nu} \chi\right) \left(q^\mu \varepsilon^\nu - \varepsilon^\mu q^\nu\right) \int d^d l\, \frac{\mu^{4-d}}{\left(l^2 - m_t^2\right)^2} . \tag{A.43}$$

The loop integral in Eq. (A.43) is readily evaluated as a power series in $\epsilon \equiv (4-d)/2$. For energies too low to resolve the four-fermion tensor interactions, there is a UV $1/\epsilon$ pole. We regularise this singularity by the simple replacement

$$\frac{1}{\epsilon} + \ln\frac{\mu^2}{m_t^2} \to \ln\frac{\Lambda_{\rm T}^2}{m_t^2}\,. \tag{A.44}$$

After this replacement and keeping only the logarithmically enhanced terms, we arrive at

$$\mathcal{A}_{\rm M} = -\frac{3eQ_t}{4\pi^2}\frac{m_t}{\Lambda_{\rm T}^2}\,(\bar\chi\sigma_{\mu\nu}\chi)\,(q^\mu\varepsilon^\nu - \varepsilon^\mu q^\nu)\ln\frac{\Lambda_{\rm T}^2}{m_t^2}\,. \tag{A.45}$$

The result Eq. (5.9) is then obtained by replacing $(q^\mu\varepsilon^\nu - \varepsilon^\mu q^\nu)$ with $F^{\mu\nu}$. The calculation of the $\mathcal{O}_{\rm PT}$ insertion proceeds in exactly the same way as described above,[1] and leads to an analogous result.

We now turn to the computation of the two diagrams in Fig. 5.7. In this case we can immediately neglect all external momenta. For the axialvector operator $\mathcal{O}_{\rm AX}$ the sum of the two graphs gives

$$\mathcal{A} = -\frac{1}{(2\pi)^4}\frac{1}{\Lambda_{\rm AX}^4}\,\mu^{4-d}\int d^dl\left[\frac{(\bar\chi\gamma_\mu\gamma_5(\not l + m_\chi)\gamma_\nu\gamma_5\chi)\,(\bar q\gamma^\mu\gamma_5(-\not l + m_q)\gamma^\nu\gamma_5 q)}{\left(l^2-m_\chi^2\right)\left(l^2-m_q^2\right)}\right. \tag{A.46}$$

$$\left. + \frac{(\bar\chi\gamma_\mu\gamma_5(\not l + m_\chi)\gamma_\nu\gamma_5\chi)\,(\bar q\gamma^\nu\gamma_5(\not l + m_q)\gamma^\mu\gamma_5 q)}{\left(l^2-m_\chi^2\right)\left(l^2-m_q^2\right)}\right]. \tag{A.47}$$

After some Dirac algebra, we obtain for the contribution $\mathcal{A}_{\rm S}$ of this amplitude proportional to $\mathcal{O}_{\rm S}$ the result

$$\mathcal{A}_{\rm S} = -\frac{d}{8\pi^4}\frac{m_q m_\chi}{\Lambda_{\rm AX}^4}\,(\bar\chi\chi)\,(\bar qq)\int d^dl\,\frac{\mu^{4-d}}{\left(l^2-m_\chi^2\right)\left(l^2-m_q^2\right)}\,. \tag{A.48}$$

Expanding the resulting expression in ϵ and keeping only the UV pole, we find

$$\mathcal{A}_{\rm S} = -\frac{i}{2\pi^2}\frac{m_q m_\chi}{\Lambda_{\rm AX}^4}\,(\bar\chi\chi)\,(\bar qq)\,\frac{1}{\epsilon}\,. \tag{A.49}$$

Identifying the singularity with the corresponding logarithm, we finally obtain Eq. (5.14). In the case of $\mathcal{O}_{\rm AN}$ the quark Dirac lines in Eq. (A.46) do not contain γ_5 matrices, and in consequence the final result Eq. (A.49) receives the opposite overall sign.

[1] Note that $\sigma^{\mu\nu}\gamma^5 = \frac{i}{2}\epsilon^{\mu\nu\rho\sigma}\sigma_{\rho\sigma}$.

Bibliography

[1] M. T. Frandsen, F. Kahlhoefer, C. McCabe, S. Sarkar, et al., *Resolving astrophysical uncertainties in dark matter direct detection*, *JCAP* **1201** (2012) 024, [arXiv:1111.0292].

[2] M. T. Frandsen, F. Kahlhoefer, C. McCabe, S. Sarkar, et al., *The unbearable lightness of being: CDMS versus XENON*, *JCAP* **1307** (2013) 023, [arXiv:1304.6066].

[3] B. Feldstein and F. Kahlhoefer, *A new halo-independent approach to dark matter direct detection analysis*, arXiv:1403.4606.

[4] M. T. Frandsen, F. Kahlhoefer, S. Sarkar, and K. Schmidt-Hoberg, *Direct detection of dark matter in models with a light Z'*, *JHEP* **1109** (2011) 128, [arXiv:1107.2118].

[5] M. T. Frandsen, F. Kahlhoefer, A. Preston, S. Sarkar, et al., *LHC and Tevatron Bounds on the Dark Matter Direct Detection Cross-Section for Vector Mediators*, *JHEP* **1207** (2012) 123, [arXiv:1204.3839].

[6] U. Haisch, F. Kahlhoefer, and J. Unwin, *The impact of heavy-quark loops on LHC dark matter searches*, *JHEP* **1307** (2013) 125, [arXiv:1208.4605].

[7] U. Haisch and F. Kahlhoefer, *On the importance of loop-induced spin-independent interactions for dark matter direct detection*, *JCAP* **1304** (2013) 050, [arXiv:1302.4454].

[8] V. C. Rubin and W. K. Ford, Jr., *Rotation of the Andromeda Nebula from a Spectroscopic Survey of Emission Regions*, *Astrophys.J.* **159** (1970) 379.

[9] K. Begeman, A. Broeils, and R. Sanders, *Extended rotation curves of spiral galaxies: Dark haloes and modified dynamics*, *Mon.Not.Roy.Astron.Soc.* **249** (1991) 523.

[10] M. Milgrom, *A Modification of the Newtonian dynamics as a possible alternative to the hidden mass hypothesis*, *Astrophys.J.* **270** (1983) 365–370.

[11] A. Aguirre, J. Schaye, and E. Quataert, *Problems for MOND in clusters and the Ly-alpha forest*, *Astrophys.J.* **561** (2001) 550, [astro-ph/0105184].

[12] F. Zwicky, *On the Masses of Nebulae and of Clusters of Nebulae*, *Astrophys.J.* **86** (1937) 217.

[13] D. Clowe, M. Bradac, A. H. Gonzalez, M. Markevitch, et al., *A direct empirical proof of the existence of dark matter*, *Astrophys.J.* **648** (2006) L109–L113, [astro-ph/0608407].

[14] V. Springel, S. D. White, A. Jenkins, C. S. Frenk, et al., *Simulating the joint evolution of quasars, galaxies and their large-scale distribution*, *Nature* **435** (2005) 629–636, [astro-ph/0504097].

[15] **Planck** Collaboration, P. Ade et al., *Planck 2013 results. XVI. Cosmological parameters*, arXiv:1303.5076.

[16] B. Fields and S. Sarkar, *Big-Bang nucleosynthesis (2006 Particle Data Group mini-review)*, astro-ph/0601514.

[17] J. R. Primack, D. Seckel, and B. Sadoulet, *Detection of Cosmic Dark Matter*, *Ann.Rev.Nucl.Part.Sci.* **38** (1988) 751–807.

[18] **MACHO** Collaboration, C. Alcock et al., *The MACHO project: Microlensing results from 5.7 years of LMC observations*, *Astrophys.J.* **542** (2000) 281–307, [astro-ph/0001272].

[19] M. Rauch, J. Miralda-Escude, W. L. Sargent, T. A. Barlow, et al., *The Opacity of the Lyman alpha forest and implications for omega(baryon) and the ionizing background*, *Astrophys.J.* **489** (1997) 7–20, [astro-ph/9612245].

[20] N. Yoshida, V. Springel, S. D. White, and G. Tormen, *Weakly self-interacting dark matter and the structure of dark halos*, *Astrophys.J.* **544** (2000) L87–L90, [astro-ph/0006134].

[21] R. Dave, D. N. Spergel, P. J. Steinhardt, and B. D. Wandelt, *Halo properties in cosmological simulations of selfinteracting cold dark matter*, *Astrophys.J.* **547** (2001) 574–589, [astro-ph/0006218].

[22] J. Miralda-Escude, *A test of the collisional dark matter hypothesis from cluster lensing*, *Astrophys.J.* **564** (2002) 60, [astro-ph/0002050].

[23] M. Markevitch, A. Gonzalez, D. Clowe, A. Vikhlinin, et al., *Direct constraints on the dark matter self-interaction cross-section from the merging galaxy cluster 1E0657-56*, *Astrophys.J.* **606** (2004) 819–824, [astro-ph/0309303].

[24] F. Kahlhoefer, K. Schmidt-Hoberg, M. T. Frandsen, and S. Sarkar, *Colliding clusters and dark matter self-interactions*, *Mon.Not.Roy.Astron.Soc.* **437** (2014) 2865–2881, [arXiv:1308.3419].

[25] E. W. Kolb and M. S. Turner, *The Early Universe*, *Front.Phys.* **69** (1990) 1–547.

[26] D. S. Gorbunov and V. A. Rubakov, *Introduction to the theory of the early universe: Hot big bang theory*. World Scientific, Hackensack, USA, 2011.

[27] G. Gelmini and P. Gondolo, *DM production mechanisms*, in *Particle Dark Matter : Observations, Models and Searches* (G. Bertone, ed.), p. 121. Cambridge University Press, 2010. arXiv:1009.3690.

[28] B. W. Lee and S. Weinberg, *Cosmological lower bound on heavy-neutrino masses*, *Phys. Rev. Lett.* **39** (Jul, 1977) 165–168.

[29] J. R. Ellis, J. Hagelin, D. V. Nanopoulos, K. A. Olive, et al., *Supersymmetric Relics from the Big Bang*, *Nucl.Phys.* **B238** (1984) 453–476.

[30] G. Jungman, M. Kamionkowski, and K. Griest, *Supersymmetric dark matter*, *Phys.Rept.* **267** (1996) 195–373, [hep-ph/9506380].

[31] H.-C. Cheng, K. T. Matchev, and M. Schmaltz, *Radiative corrections to Kaluza-Klein masses*, *Phys.Rev.* **D66** (2002) 036005, [hep-ph/0204342].

[32] K. Griest and D. Seckel, *Three exceptions in the calculation of relic abundances*, *Phys. Rev. D* **43** (1991) 3191–3203.

[33] J. L. Feng and J. Kumar, *The WIMPless Miracle: Dark-Matter Particles without Weak-Scale Masses or Weak Interactions*, *Phys.Rev.Lett.* **101** (2008) 231301, [arXiv:0803.4196].

[34] A. Sakharov, *Violation of CP Invariance, c Asymmetry, and Baryon Asymmetry of the Universe*, *Pisma Zh.Eksp.Teor.Fiz.* **5** (1967) 32–35.

[35] S. Nussinov, *Technocosmology: Could a technibaryon excess provide a 'natural' missing mass candidate?*, *Phys.Lett.* **B165** (1985) 55.

[36] K. Griest and D. Seckel, *Cosmic Asymmetry, Neutrinos and the Sun*, *Nucl.Phys.* **B283** (1987) 681.

[37] S. M. Barr, R. S. Chivukula, and E. Farhi, *Electroweak Fermion Number Violation and the Production of Stable Particles in the Early Universe*, *Phys.Lett.* **B241** (1990) 387–391.

[38] D. B. Kaplan, *A Single explanation for both the baryon and dark matter densities*, *Phys.Rev.Lett.* **68** (1992) 741–743.

[39] D. E. Kaplan, M. A. Luty, and K. M. Zurek, *Asymmetric Dark Matter*, *Phys.Rev.* **D79** (2009) 115016, [arXiv:0901.4117].

[40] M. T. Frandsen, S. Sarkar, and K. Schmidt-Hoberg, *Light asymmetric dark matter from new strong dynamics*, *Phys.Rev.* **D84** (2011) 051703, [arXiv:1103.4350].

[41] J. L. Feng, A. Rajaraman, and F. Takayama, *SuperWIMP dark matter signals from the early universe*, *Phys.Rev.* **D68** (2003) 063504, [hep-ph/0306024].

[42] J. R. Ellis, A. D. Linde, and D. V. Nanopoulos, *Inflation Can Save the Gravitino*, *Phys.Lett.* **B118** (1982) 59.

[43] M. Bolz, A. Brandenburg, and W. Buchmuller, *Thermal production of gravitinos*, *Nucl.Phys.* **B606** (2001) 518–544, [hep-ph/0012052].

[44] L. J. Hall, K. Jedamzik, J. March-Russell, and S. M. West, *Freeze-In Production of FIMP Dark Matter*, *JHEP* **1003** (2010) 080, [arXiv:0911.1120].

[45] R. Peccei and H. R. Quinn, *CP Conservation in the Presence of Instantons*, *Phys.Rev.Lett.* **38** (1977) 1440–1443.

[46] R. Peccei and H. R. Quinn, *Constraints Imposed by CP Conservation in the Presence of Instantons*, *Phys.Rev.* **D16** (1977) 1791–1797.

[47] F. Wilczek, *Problem of Strong p and t Invariance in the Presence of Instantons*, *Phys.Rev.Lett.* **40** (1978) 279–282.

[48] S. Weinberg, *A New Light Boson?*, *Phys.Rev.Lett.* **40** (1978) 223–226.

[49] J. Preskill, M. B. Wise, and F. Wilczek, *Cosmology of the Invisible Axion*, *Phys.Lett.* **B120** (1983) 127–132.

[50] L. Abbott and P. Sikivie, *A Cosmological Bound on the Invisible Axion*, *Phys.Lett.* **B120** (1983) 133–136.

[51] M. Dine and W. Fischler, *The Not So Harmless Axion*, *Phys.Lett.* **B120** (1983) 137–141.

[52] P. Minkowski, *mu → e gamma at a Rate of One Out of 1-Billion Muon Decays?*, *Phys.Lett.* **B67** (1977) 421.

[53] R. N. Mohapatra and G. Senjanovic, *Neutrino Mass and Spontaneous Parity Violation*, *Phys.Rev.Lett.* **44** (1980) 912.

[54] T. Asaka, S. Blanchet, and M. Shaposhnikov, *The nuMSM, dark matter and neutrino masses*, *Phys.Lett.* **B631** (2005) 151–156, [hep-ph/0503065].

[55] A. Boyarsky, O. Ruchayskiy, and M. Shaposhnikov, *The Role of sterile neutrinos in cosmology and astrophysics*, *Ann.Rev.Nucl.Part.Sci.* **59** (2009) 191–214, [arXiv:0901.0011].

[56] R. A. Flores and J. R. Primack, *Observational and theoretical constraints on singular dark matter halos*, *Astrophys.J.* **427** (1994) L1–4, [astro-ph/9402004].

[57] B. Moore, S. Ghigna, F. Governato, G. Lake, et al., *Dark matter substructure within galactic halos*, *Astrophys.J.* **524** (1999) L19–L22, [astro-ph/9907411].

[58] A. A. Klypin, A. V. Kravtsov, O. Valenzuela, and F. Prada, *Where are the missing Galactic satellites?*, *Astrophys.J.* **522** (1999) 82–92, [astro-ph/9901240].

[59] G. Bertone, D. Hooper, and J. Silk, *Particle dark matter: Evidence, candidates and constraints*, *Phys.Rept.* **405** (2005) 279–390, [hep-ph/0404175].

[60] M. Beltran, D. Hooper, E. W. Kolb, and Z. C. Krusberg, *Deducing the nature of dark matter from direct and indirect detection experiments in the absence of collider signatures of new physics*, *Phys.Rev.* **D80** (2009) 043509, [arXiv:0808.3384].

[61] M. W. Goodman and E. Witten, *Detectability of Certain Dark Matter Candidates*, *Phys.Rev.* **D31** (1985) 3059.

[62] P. Smith and J. Lewin, *Dark Matter Detection*, *Phys.Rept.* **187** (1990) 203.

[63] R. Gaitskell, *Direct detection of dark matter*, *Ann.Rev.Nucl.Part.Sci.* **54** (2004) 315–359.

[64] A. H. G. Peter, V. Gluscevic, A. M. Green, B. J. Kavanagh, et al., *WIMP physics with ensembles of direct-detection experiments*, arXiv:1310.7039.

[65] G. Gelmini and P. Gondolo, *WIMP annual modulation with opposite phase in Late-Infall halo models*, *Phys.Rev.* **D64** (2001) 023504, [hep-ph/0012315].

[66] R. Schoenrich, J. Binney, and W. Dehnen, *Local Kinematics and the Local Standard of Rest*, *Mon.Not.Roy.Astron.Soc.* **403** (2010) [arXiv:0912.3693].

[67] C. Savage, P. Gondolo, and K. Freese, *Can WIMP spin dependent couplings explain DAMA data, in light of null results from other experiments?*, *Phys.Rev.* **D70** (2004) 123513, [astro-ph/0408346].

[68] J. Kopp, T. Schwetz, and J. Zupan, *Global interpretation of direct Dark Matter searches after CDMS-II results*, *JCAP* **1002** (2010) 014, [arXiv:0912.4264].

[69] T. Schwetz and J. Zupan, *Dark Matter attempts for CoGeNT and DAMA*, *JCAP* **1108** (2011) 008, [arXiv:1106.6241].

[70] J. Lewin and P. Smith, *Review of mathematics, numerical factors, and corrections for dark matter experiments based on elastic nuclear recoil*, *Astropart.Phys.* **6** (1996) 87–112.

[71] J. Menendez, D. Gazit, and A. Schwenk, *Spin-dependent WIMP scattering off nuclei*, *Phys.Rev.* **D86** (2012) 103511, [arXiv:1208.1094].

[72] P. Toivanen, M. Kortelainen, J. Suhonen, and J. Toivanen, *Large-scale shell-model calculations of elastic and inelastic scattering rates of lightest supersymmetric particles (LSP) on I-127, Xe-129, Xe-131, and Cs-133 nuclei*, *Phys.Rev.* **C79** (2009) 044302.

[73] V. Bednyakov and F. Simkovic, *Nuclear spin structure in dark matter search: The Finite momentum transfer limit*, *Phys.Part.Nucl.* **37** (2006) S106–S128, [hep-ph/0608097].

[74] C. Savage, G. Gelmini, P. Gondolo, and K. Freese, *Compatibility of DAMA/LIBRA dark matter detection with other searches*, *JCAP* **0904** (2009) 010, [arXiv:0808.3607].

[75] P. J. Fox, G. D. Kribs, and T. M. Tait, *Interpreting Dark Matter Direct Detection Independently of the Local Velocity and Density Distribution*, *Phys.Rev.* **D83** (2011) 034007, [arXiv:1011.1910].

[76] M. Kuhlen, N. Weiner, J. Diemand, P. Madau, et al., *Dark Matter Direct Detection with Non-Maxwellian Velocity Structure*, *JCAP* **1002** (2010) 030, [arXiv:0912.2358].

[77] A. Drukier, K. Freese, and D. Spergel, *Detecting Cold Dark Matter Candidates*, *Phys.Rev.* **D33** (1986) 3495–3508.

[78] K. Freese, J. A. Frieman, and A. Gould, *Signal Modulation in Cold Dark Matter Detection*, *Phys.Rev.* **D37** (1988) 3388.

[79] B. Morgan, A. M. Green, and N. J. Spooner, *Directional statistics for WIMP direct detection*, *Phys.Rev.* **D71** (2005) 103507, [astro-ph/0408047].

[80] **XENON100** Collaboration, E. Aprile et al., *Dark Matter Results from 225 Live Days of XENON100 Data*, *Phys.Rev.Lett.* **109** (2012) 181301, [arXiv:1207.5988].

[81] **LUX** Collaboration, D. Akerib et al., *First results from the LUX dark matter experiment at the Sanford Underground Research Facility*, arXiv:1310.8214.

[82] C. Strege, G. Bertone, G. Besjes, S. Caron, et al., *Profile likelihood maps of a 15-dimensional MSSM*, arXiv:1405.0622.

[83] M. Kundera, *The Unbearable Lightness of Being*. Faber & Faber, London, Great Britain, 2000.

[84] C. Savage, G. Gelmini, P. Gondolo, and K. Freese, *XENON10/100 dark matter constraints in comparison with CoGeNT and DAMA: examining the Leff dependence*, *Phys.Rev.* **D83** (2011) 055002, [arXiv:1006.0972].

[85] J. M. Cline, Z. Liu, and W. Xue, *An optimistic CoGeNT analysis*, *Phys.Rev.* **D87** (2013) 015001, [arXiv:1207.3039].

[86] C. McCabe, *The Astrophysical Uncertainties Of Dark Matter Direct Detection Experiments*, *Phys.Rev.* **D82** (2010) 023530, [arXiv:1005.0579].

[87] A. M. Green, *Astrophysical uncertainties on direct detection experiments*, *Mod.Phys.Lett.* **A27** (2012) 1230004, [arXiv:1112.0524].

[88] M. Fairbairn, T. Douce, and J. Swift, *Quantifying Astrophysical Uncertainties on Dark Matter Direct Detection Results*, *Astropart.Phys.* **47** (2013) 45–53, [arXiv:1206.2693].

[89] L. E. Strigari, *Galactic Searches for Dark Matter*, *Phys.Rept.* **531** (2013) 1–88, [arXiv:1211.7090].

[90] **CoGeNT** Collaboration, C. Aalseth et al., *CoGeNT: A Search for Low-Mass Dark Matter using p-type Point Contact Germanium Detectors*, *Phys.Rev.* **D88** (2013), 012002, [arXiv:1208.5737].

[91] G. Angloher, M. Bauer, I. Bavykina, A. Bento, et al., *Results from 730 kg days of the CRESST-II Dark Matter Search*, *Eur.Phys.J.* **C72** (2012) 1971, [arXiv:1109.0702].

[92] **CDMS** Collaboration, R. Agnese et al., *Silicon Detector Dark Matter Results from the Final Exposure of CDMS II*, *Phys.Rev.Lett.* **111** (2013) 251301, [arXiv:1304.4279].

[93] **DAMA/LIBRA** Collaboration, R. Bernabei et al., *New results from DAMA/LIBRA*, *Eur.Phys.J.* **C67** (2010) 39–49, [arXiv:1002.1028].

[94] C. Aalseth, P. Barbeau, J. Colaresi, J. Collar, et al., *Search for an Annual Modulation in a P-type Point Contact Germanium Dark Matter Detector*, *Phys.Rev.Lett.* **107** (2011) 141301, [arXiv:1106.0650].

[95] A. Bottino, F. Donato, N. Fornengo, and S. Scopel, *Light neutralinos and WIMP direct searches*, *Phys.Rev.* **D69** (2004) 037302, [hep-ph/0307303].

[96] **CDMS-II** Collaboration, Z. Ahmed et al., *Results from a Low-Energy Analysis of the CDMS II Germanium Data*, *Phys.Rev.Lett.* **106** (2011) 131302, [arXiv:1011.2482].

[97] **SuperCDMS** Collaboration, R. Agnese et al., *Search for Low-Mass WIMPs with SuperCDMS*, arXiv:1402.7137.

[98] **XENON10** Collaboration, J. Angle et al., *A search for light dark matter in XENON10 data*, *Phys.Rev.Lett.* **107** (2011) 051301, [arXiv:1104.3088].

[99] M. T. Frandsen, F. Kahlhoefer, J. March-Russell, C. McCabe, et al., *On the DAMA and CoGeNT Modulations*, *Phys.Rev.* **D84** (2011) 041301, [arXiv:1105.3734].

[100] M. Farina, D. Pappadopulo, A. Strumia, and T. Volansky, *Can CoGeNT and DAMA Modulations Be Due to Dark Matter?*, *JCAP* **1111** (2011) 010, [arXiv:1107.0715].

[101] P. J. Fox, J. Kopp, M. Lisanti, and N. Weiner, *A CoGeNT Modulation Analysis*, *Phys.Rev.* **D85** (2012) 036008, [arXiv:1107.0717].

[102] C. McCabe, *DAMA and CoGeNT without astrophysical uncertainties*, *Phys.Rev.* **D84** (2011) 043525, [arXiv:1107.0741].

[103] J. Kopp, T. Schwetz, and J. Zupan, *Light Dark Matter in the light of CRESST-II*, *JCAP* **1203** (2012) 001, [arXiv:1110.2721].

[104] C. Kelso, D. Hooper, and M. R. Buckley, *Toward A Consistent Picture For CRESST, CoGeNT and DAMA*, *Phys.Rev.* **D85** (2012) 043515, [arXiv:1110.5338].

[105] M. T. Frandsen, U. Haisch, F. Kahlhoefer, P. Mertsch, et al., *Loop-induced dark matter direct detection signals from gamma-ray lines*, *JCAP* **1210** (2012) 033, [arXiv:1207.3971].

[106] L. Bergstrom, *Radiative Processes in Dark Matter Photino Annihilation*, *Phys.Lett.* **B225** (1989) 372.

[107] M. Cirelli, P. Panci, and P. D. Serpico, *Diffuse gamma ray constraints on annihilating or decaying Dark Matter after Fermi*, *Nucl.Phys.* **B840** (2010) 284–303, [arXiv:0912.0663].

[108] **Fermi-LAT** Collaboration, M. Ackermann et al., *Search for Gamma-ray Spectral Lines with the Fermi Large Area Telescope and Dark Matter Implications*, *Phys.Rev.* **D88** (2013) 082002, [arXiv:1305.5597].

[109] **Fermi-LAT** Collaboration, M. Ackermann et al., *Constraints on the Galactic Halo Dark Matter from Fermi-LAT Diffuse Measurements*, *Astrophys.J.* **761** (2012) 91, [arXiv:1205.6474].

[110] **Fermi-LAT** Collaboration, M. Ackermann et al., *Dark Matter Constraints from Observations of 25 Milky Way Satellite Galaxies with the Fermi Large Area Telescope*, *Phys.Rev.* **D89** (2014) 042001, [arXiv:1310.0828].

[111] A. W. Strong, I. V. Moskalenko, and V. S. Ptuskin, *Cosmic-ray propagation and interactions in the Galaxy*, *Ann.Rev.Nucl.Part.Sci.* **57** (2007) 285–327, [astro-ph/0701517].

[112] P. Mertsch and S. Sarkar, *AMS-02 data confronts acceleration of cosmic ray secondaries in nearby sources*, arXiv:1402.0855.

[113] **PAMELA** Collaboration, O. Adriani et al., *An anomalous positron abundance in cosmic rays with energies 1.5-100 GeV*, *Nature* **458** (2009) 607–609, [arXiv:0810.4995].

[114] **AMS** Collaboration, M. Aguilar et al., *First Result from the Alpha Magnetic Spectrometer on the International Space Station: Precision Measurement of the Positron Fraction in Primary Cosmic Rays of 0.5–350 GeV*, *Phys.Rev.Lett.* **110** (2013) 141102.

[115] F. Donato, N. Fornengo, and P. Salati, *Anti-deuterons as a signature of supersymmetric dark matter*, *Phys.Rev.* **D62** (2000) 043003, [hep-ph/9904481].

[116] **IceCube** Collaboration, M. Aartsen et al., *Search for dark matter annihilations in the Sun with the 79-string IceCube detector*, *Phys.Rev.Lett.* **110** (2013), 131302, [arXiv:1212.4097].

[117] F. Halzen and D. Hooper, *Prospects for detecting dark matter with neutrino telescopes in light of recent results from direct detection experiments*, *Phys.Rev.* **D73** (2006) 123507, [hep-ph/0510048].

[118] R. Kappl and M. W. Winkler, *New Limits on Dark Matter from Super-Kamiokande*, *Nucl.Phys.* **B850** (2011) 505–521, [arXiv:1104.0679].

[119] W. H. Press and D. N. Spergel, *Capture by the sun of a galactic population of weakly interacting massive particles*, *Astrophys.J.* **296** (1985) 679–684.

[120] C. Kouvaris and P. Tinyakov, *Can Neutron stars constrain Dark Matter?*, *Phys.Rev.* **D82** (2010) 063531, [arXiv:1004.0586].

[121] M. T. Frandsen and S. Sarkar, *Asymmetric dark matter and the Sun*, *Phys.Rev.Lett.* **105** (2010) 011301, [arXiv:1003.4505].

[122] S. D. McDermott, H.-B. Yu, and K. M. Zurek, *Constraints on Scalar Asymmetric Dark Matter from Black Hole Formation in Neutron Stars*, *Phys.Rev.* **D85** (2012) 023519, [arXiv:1103.5472].

[123] M. Beltran, D. Hooper, E. W. Kolb, Z. A. Krusberg, et al., *Maverick dark matter at colliders*, *JHEP* **1009** (2010) 037, [arXiv:1002.4137].

[124] **CDF** Collaboration, *Search for Extra Dimensions in Jets+Missing Energy in RunII*, www-cdf.fnal.gov/physics/exotic/r2a/20070322.monojet/public/ykk.html.

[125] **CMS** Collaboration, S. Chatrchyan et al., *Search for dark matter and large extra dimensions in monojet events in pp collisions at* $\sqrt{s} = 7$ *TeV*, *JHEP* **1209** (2012) 094, [arXiv:1206.5663].

[126] **ATLAS** Collaboration, G. Aad et al., *Search for dark matter candidates and large extra dimensions in events with a jet and missing transverse momentum with the ATLAS detector*, *JHEP* **1304** (2013) 075, [arXiv:1210.4491].

[127] Y. Bai, P. J. Fox, and R. Harnik, *The Tevatron at the Frontier of Dark Matter Direct Detection*, *JHEP* **1012** (2010) 048, [arXiv:1005.3797].

[128] J. Goodman, M. Ibe, A. Rajaraman, W. Shepherd, et al., *Constraints on Dark Matter from Colliders*, *Phys.Rev.* **D82** (2010) 116010, [arXiv:1008.1783].

[129] P. J. Fox, R. Harnik, J. Kopp, and Y. Tsai, *Missing Energy Signatures of Dark Matter at the LHC*, *Phys.Rev.* **D85** (2012) 056011, [arXiv:1109.4398].

[130] P. J. Fox, R. Harnik, J. Kopp, and Y. Tsai, *LEP Shines Light on Dark Matter*, *Phys.Rev.* **D84** (2011) 014028, [arXiv:1103.0240].

[131] Y. Bai and T. M. Tait, *Searches with Mono-Leptons*, *Phys.Lett.* **B723** (2013) 384–387, [arXiv:1208.4361].

[132] L. M. Carpenter, A. Nelson, C. Shimmin, T. M. Tait, et al., *Collider searches for dark matter in events with a Z boson and missing energy*, *Phys.Rev.* **D87** (2013), 074005, [arXiv:1212.3352].

[133] N. F. Bell, J. B. Dent, A. J. Galea, T. D. Jacques, et al., *Searching for Dark Matter at the LHC with a Mono-Z*, *Phys.Rev.* **D86** (2012) 096011, [arXiv:1209.0231].

[134] A. Berlin, T. Lin, and L.-T. Wang, *Mono-Higgs Detection of Dark Matter at the LHC*, arXiv:1402.7074.

[135] S. Profumo, W. Shepherd, and T. Tait, *Pitfalls of dark matter crossing symmetries*, *Phys.Rev.* **D88** (2013), 056018, [arXiv:1307.6277].

[136] **Particle Data Group** Collaboration, J. Beringer et al., *Review of Particle Physics (RPP)*, *Phys.Rev.* **D86** (2012) 010001.

[137] J. March-Russell, J. Unwin, and S. M. West, *Closing in on Asymmetric Dark Matter I: Model independent limits for interactions with quarks*, *JHEP* **1208** (2012) 029, [arXiv:1203.4854].

[138] A. L. Fitzpatrick and K. M. Zurek, *Dark Moments and the DAMA-CoGeNT Puzzle*, *Phys.Rev.* **D82** (2010) 075004, [arXiv:1007.5325].

[139] C. M. Ho and R. J. Scherrer, *Anapole Dark Matter*, *Phys.Lett.* **B722** (2013) 341–346, [arXiv:1211.0503].

[140] G. Busoni, A. De Simone, E. Morgante, and A. Riotto, *On the Validity of the Effective Field Theory for Dark Matter Searches at the LHC*, *Phys.Lett.* **B728** (2014) 412–421, [arXiv:1307.2253].

[141] O. Buchmueller, M. J. Dolan, and C. McCabe, *Beyond Effective Field Theory for Dark Matter Searches at the LHC*, *JHEP* **1401** (2014) 025, [arXiv:1308.6799].

[142] I. M. Shoemaker and L. Vecchi, *Unitarity and Monojet Bounds on Models for DAMA, CoGeNT, and CRESST-II*, *Phys.Rev.* **D86** (2012) 015023, [arXiv:1112.5457].

[143] R. Harnik and G. D. Kribs, *An Effective Theory of Dirac Dark Matter*, *Phys.Rev.* **D79** (2009) 095007, [arXiv:0810.5557].

[144] P. Agrawal, Z. Chacko, C. Kilic, and R. K. Mishra, *A Classification of Dark Matter Candidates with Primarily Spin-Dependent Interactions with Matter*, arXiv:1003.1912.

[145] J. Goodman, M. Ibe, A. Rajaraman, W. Shepherd, et al., *Gamma Ray Line Constraints on Effective Theories of Dark Matter*, *Nucl.Phys.* **B844** (2011) 55–68, [arXiv:1009.0008].

[146] V. Barger, W.-Y. Keung, and D. Marfatia, *Electromagnetic properties of dark matter: Dipole moments and charge form factor*, *Phys.Lett.* **B696** (2011) 74–78, [arXiv:1007.4345].

[147] T. Banks, J.-F. Fortin, and S. Thomas, *Direct Detection of Dark Matter Electromagnetic Dipole Moments*, arXiv:1007.5515.

[148] J.-M. Zheng, Z.-H. Yu, J.-W. Shao, X.-J. Bi, et al., *Constraining the interaction strength between dark matter and visible matter: I. fermionic dark matter*, *Nucl.Phys.* **B854** (2012) 350–374, [arXiv:1012.2022].

[149] J.-F. Fortin and T. M. Tait, *Collider Constraints on Dipole-Interacting Dark Matter*, *Phys.Rev.* **D85** (2012) 063506, [arXiv:1103.3289].

[150] A. Rajaraman, W. Shepherd, T. M. Tait, and A. M. Wijangco, *LHC Bounds on Interactions of Dark Matter*, *Phys.Rev.* **D84** (2011) 095013, [arXiv:1108.1196].

[151] K. Cheung, P.-Y. Tseng, and T.-C. Yuan, *Gamma-ray Constraints on Effective Interactions of the Dark Matter*, *JCAP* **1106** (2011) 023, [arXiv:1104.5329].

[152] K. Cheung, P.-Y. Tseng, Y.-L. S. Tsai, and T.-C. Yuan, *Global Constraints on Effective Dark Matter Interactions: Relic Density, Direct Detection, Indirect Detection, and Collider*, *JCAP* **1205** (2012) 001, [arXiv:1201.3402].

[153] P. J. Fox, R. Harnik, R. Primulando, and C.-T. Yu, *Taking a Razor to Dark Matter Parameter Space at the LHC*, *Phys.Rev.* **D86** (2012) 015010, [arXiv:1203.1662].

[154] V. Barger, W.-Y. Keung, D. Marfatia, and P.-Y. Tseng, *Dipole Moment Dark Matter at the LHC*, *Phys.Lett.* **B717** (2012) 219–223, [arXiv:1206.0640].

[155] N. Zhou, D. Berge, and D. Whiteson, *Mono-everything: combined limits on dark matter production at colliders from multiple final states*, *Phys.Rev.* **D87** (2013), 095013, [arXiv:1302.3619].

[156] H. Dreiner, D. Schmeier, and J. Tattersall, *Contact Interactions Probe Effective Dark Matter Models at the LHC*, *Europhys.Lett.* **102** (2013) 51001, [arXiv:1303.3348].

[157] B. Batell, J. Pradler, and M. Spannowsky, *Dark Matter from Minimal Flavor Violation*, *JHEP* **1108** (2011) 038, [arXiv:1105.1781].

[158] M. Kamionkowski and A. Kinkhabwala, *Galactic halo models and particle dark matter detection*, *Phys.Rev.* **D57** (1998) 3256–3263, [hep-ph/9710337].

[159] A. M. Green, *Effect of halo modeling on WIMP exclusion limits*, *Phys.Rev.* **D66** (2002) 083003, [astro-ph/0207366].

[160] M. Fairbairn and T. Schwetz, *Spin-independent elastic WIMP scattering and the DAMA annual modulation signal*, *JCAP* **0901** (2009) 037, [arXiv:0808.0704].

[161] J. March-Russell, C. McCabe, and M. McCullough, *Inelastic Dark Matter, Non-Standard Halos and the DAMA/LIBRA Results*, *JHEP* **0905** (2009) 071, [arXiv:0812.1931].

[162] A. M. Green, *Dependence of direct detection signals on the WIMP velocity distribution*, *JCAP* **1010** (2010) 034, [arXiv:1009.0916].

[163] L. E. Strigari and R. Trotta, *Reconstructing WIMP Properties in Direct Detection Experiments Including Galactic Dark Matter Distribution Uncertainties*, *JCAP* **0911** (2009) 019, [arXiv:0906.5361].

[164] C. Arina, J. Hamann, and Y. Y. Wong, *A Bayesian view of the current status of dark matter direct searches*, *JCAP* **1109** (2011) 022, [arXiv:1105.5121].

[165] A. H. Peter, *Getting the astrophysics and particle physics of dark matter out of next-generation direct detection experiments*, *Phys.Rev.* **D81** (2010) 087301, [arXiv:0910.4765].

[166] A. H. Peter, *WIMP astronomy and particle physics with liquid-noble and cryogenic direct-detection experiments*, *Phys.Rev.* **D83** (2011) 125029, [arXiv:1103.5145].

[167] M. Drees and C.-L. Shan, *Reconstructing the Velocity Distribution of WIMPs from Direct Dark Matter Detection Data*, *JCAP* **0706** (2007) 011, [astro-ph/0703651].

[168] P. J. Fox, J. Liu, and N. Weiner, *Integrating Out Astrophysical Uncertainties*, *Phys.Rev.* **D83** (2011) 103514, [arXiv:1011.1915].

[169] P. Gondolo and G. B. Gelmini, *Halo independent comparison of direct dark matter detection data*, *JCAP* **1212** (2012) 015, [arXiv:1202.6359].

[170] C. Aalseth, P. Barbeau, J. Colaresi, J. D. Leon, et al., *Maximum Likelihood Signal Extraction Method Applied to 3.4 years of CoGeNT Data*, arXiv:1401.6234.

[171] E. Del Nobile, C. Kouvaris, and F. Sannino, *Interfering Composite Asymmetric Dark Matter for DAMA and CoGeNT*, *Phys.Rev.* **D84** (2011) 027301, [arXiv:1105.5431].

[172] J. M. Cline and A. R. Frey, *Minimal hidden sector models for CoGeNT/DAMA events*, *Phys.Rev.* **D84** (2011) 075003, [arXiv:1108.1391].

[173] F. Giuliani, *Isospin conserving Dark Matter with isospin dependent interaction, and reconciliation of contrasting results from direct Dark Matter experiments*, arXiv:1110.4616.

[174] R. J. Barlow, *Extended maximum likelihood*, *Nucl.Instrum.Meth.* **A297** (1990) 496–506.

[175] S. Yellin, *Finding an upper limit in the presence of unknown background*, *Phys.Rev.* **D66** (2002) 032005, [physics/0203002].

[176] A. M. Green, *Calculating exclusion limits for weakly interacting massive particle direct detection experiments without background subtraction*, *Phys.Rev.* **D65** (2002) 023520, [astro-ph/0106555].

[177] **XENON100** Collaboration, E. Aprile et al., *Response of the XENON100 Dark Matter Detector to Nuclear Recoils*, *Phys.Rev.* **D88** (2013) 012006, [arXiv:1304.1427].

[178] P. J. Fox, Y. Kahn, and M. McCullough, *Taking Halo-Independent Dark Matter Methods Out of the Bin*, arXiv:1403.6830.

[179] G. J. Feldman and R. D. Cousins, *A Unified approach to the classical statistical analysis of small signals*, *Phys.Rev.* **D57** (1998) 3873–3889, [physics/9711021].

[180] S. Chang, A. Pierce, and N. Weiner, *Momentum Dependent Dark Matter Scattering*, *JCAP* **1001** (2010) 006, [arXiv:0908.3192].

[181] B. Feldstein, A. L. Fitzpatrick, and E. Katz, *Form Factor Dark Matter*, *JCAP* **1001** (2010) 020, [arXiv:0908.2991].

[182] E. Del Nobile, C. Kouvaris, P. Panci, F. Sannino, et al., *Light Magnetic Dark Matter in Direct Detection Searches*, *JCAP* **1208** (2012) 010, [arXiv:1203.6652].

[183] D. Tucker-Smith and N. Weiner, *Inelastic dark matter*, *Phys.Rev.* **D64** (2001) 043502, [hep-ph/0101138].

[184] A. Kurylov and M. Kamionkowski, *Generalized analysis of weakly interacting massive particle searches*, *Phys.Rev.* **D69** (2004) 063503, [hep-ph/0307185].

[185] F. Giuliani, *Are direct search experiments sensitive to all spin-independent WIMP candidates?*, *Phys.Rev.Lett.* **95** (2005) 101301, [hep-ph/0504157].

[186] S. Chang, J. Liu, A. Pierce, N. Weiner, et al., *CoGeNT Interpretations*, *JCAP* **1008** (2010) 018, [arXiv:1004.0697].

[187] J. L. Feng, J. Kumar, D. Marfatia, and D. Sanford, *Isospin-Violating Dark Matter*, *Phys.Lett.* **B703** (2011) 124–127, [arXiv:1102.4331].

[188] P. W. Graham, R. Harnik, S. Rajendran, and P. Saraswat, *Exothermic Dark Matter*, *Phys.Rev.* **D82** (2010) 063512, [arXiv:1004.0937].

[189] R. Essig, J. Kaplan, P. Schuster, and N. Toro, *On the Origin of Light Dark Matter Species*, arXiv:1004.0691.

[190] V. Cirigliano, M. L. Graesser, and G. Ovanesyan, *WIMP-nucleus scattering in chiral effective theory*, *JHEP* **1210** (2012) 025, [arXiv:1205.2695].

[191] M. Drees and C.-L. Shan, *Model-Independent Determination of the WIMP Mass from Direct Dark Matter Detection Data*, *JCAP* **0806** (2008) 012, [arXiv:0803.4477].

[192] M. Pato, L. Baudis, G. Bertone, R. Ruiz de Austri, et al., *Complementarity of Dark Matter Direct Detection Targets*, *Phys.Rev.* **D83** (2011) 083505, [arXiv:1012.3458].

[193] M. Pato, *What can(not) be measured with ton-scale dark matter direct detection experiments*, *JCAP* **1110** (2011) 035, [arXiv:1106.0743].

[194] M. Pato, L. E. Strigari, R. Trotta, and G. Bertone, *Taming astrophysical bias in direct dark matter searches*, *JCAP* **1302** (2013) 041, [arXiv:1211.7063].

[195] B. J. Kavanagh and A. M. Green, *Improved determination of the WIMP mass from direct detection data*, *Phys.Rev.* **D86** (2012) 065027, [arXiv:1207.2039].

[196] B. J. Kavanagh and A. M. Green, *Model independent determination of the dark matter mass from direct detection experiments*, *Phys.Rev.Lett.* **111** (2013), 031302, [arXiv:1303.6868].

[197] J. Read, L. Mayer, A. Brooks, F. Governato, et al., *A dark matter disc in three cosmological simulations of Milky Way mass galaxies*, *Mon.Not.Roy.Astron.Soc.* **397** (2009) 44–51, [arXiv:0902.0009].

[198] B. J. Kavanagh, *Parametrizing the local dark matter speed distribution: a detailed analysis*, *Phys.Rev.* **D89** (2014) 085026, [arXiv:1312.1852].

[199] B. Feldstein, M. Ibe, and T. T. Yanagida, *Hypercharged Dark Matter and Direct Detection as a Probe of Reheating*, arXiv:1310.7495.

[200] A. Belyaev, M. T. Frandsen, S. Sarkar, and F. Sannino, *Mixed dark matter from technicolor*, *Phys.Rev.* **D83** (2011) 015007, [arXiv:1007.4839].

[201] V. Cirigliano, M. L. Graesser, G. Ovanesyan, and I. M. Shoemaker, *Shining LUX on Isospin-Violating Dark Matter Beyond Leading Order*, arXiv:1311.5886.

[202] E. Del Nobile and F. Sannino, *Dark Matter Effective Theory*, *Int.J.Mod.Phys.* **A27** (2012) 1250065, [arXiv:1102.3116].

[203] B. Holdom, *Two U(1)'s and Epsilon Charge Shifts*, *Phys.Lett.* **B166** (1986) 196.

[204] K. Babu, C. F. Kolda, and J. March-Russell, *Implications of generalized Z-Z' mixing*, *Phys.Rev.* **D57** (1998) 6788–6792, [hep-ph/9710441].

[205] S. Cassel, D. Ghilencea, and G. Ross, *Electroweak and Dark Matter Constraints on a Z' in Models with a Hidden Valley*, *Nucl.Phys.* **B827** (2010) 256–280, [arXiv:0903.1118].

[206] A. Hook, E. Izaguirre, and J. G. Wacker, *Model Independent Bounds on Kinetic Mixing*, *Adv.High Energy Phys.* **2011** (2011) 859762, [arXiv:1006.0973].

[207] Y. Mambrini, *The Kinetic dark-mixing in the light of CoGENT and XENON100*, *JCAP* **1009** (2010) 022, [arXiv:1006.3318].

[208] Z. Kang, T. Li, T. Liu, C. Tong, et al., *Light Dark Matter from the $U(1)_X$ Sector in the NMSSM with Gauge Mediation*, *JCAP* **1101** (2011) 028, [arXiv:1008.5243].

[209] E. J. Chun, J.-C. Park, and S. Scopel, *Dark matter and a new gauge boson through kinetic mixing*, *JHEP* **1102** (2011) 100, [arXiv:1011.3300].

[210] P. J. Fox, J. Liu, D. Tucker-Smith, and N. Weiner, *An Effective Z'*, *Phys.Rev.* **D84** (2011) 115006, [arXiv:1104.4127].

[211] P. Gondolo, P. Ko, and Y. Omura, *Light dark matter in leptophobic Z' models*, *Phys.Rev.* **D85** (2012) 035022, [arXiv:1106.0885].

[212] Y. Mambrini, *The ZZ' kinetic mixing in the light of the recent direct and indirect dark matter searches*, *JCAP* **1107** (2011) 009, [arXiv:1104.4799].

[213] D. Feldman, Z. Liu, and P. Nath, *The Stueckelberg Z' Extension with Kinetic Mixing and Milli-Charged Dark Matter From the Hidden Sector*, *Phys.Rev.* **D75** (2007) 115001, [hep-ph/0702123].

[214] C. D. Carone and H. Murayama, *Possible light U(1) gauge boson coupled to baryon number*, *Phys.Rev.Lett.* **74** (1995) 3122–3125, [hep-ph/9411256].

[215] C. D. Carone and H. Murayama, *Realistic models with a light U(1) gauge boson coupled to baryon number*, *Phys.Rev.* **D52** (1995) 484–493, [hep-ph/9501220].

[216] K. Babu, C. F. Kolda, and J. March-Russell, *Leptophobic U(1)s and the R_b-R_c crisis*, *Phys.Rev.* **D54** (1996) 4635–4647, [hep-ph/9603212].

[217] B. Holdom, *Oblique electroweak corrections and an extra gauge boson*, *Phys.Lett.* **B259** (1991) 329–334.

[218] P. Fayet, *U-boson production in e^+e^- annihilations, ψ and Υ decays, and Light Dark Matter*, *Phys.Rev.* **D75** (2007) 115017, [hep-ph/0702176].

[219] A. Aranda and C. D. Carone, *Limits on a light leptophobic gauge boson*, *Phys.Lett.* **B443** (1998) 352–358, [hep-ph/9809522].

[220] M. Reece and L.-T. Wang, *Searching for the light dark gauge boson in GeV-scale experiments*, *JHEP* **0907** (2009) 051, [arXiv:0904.1743].

[221] M. S. Carena, A. Daleo, B. A. Dobrescu, and T. M. Tait, *Z' gauge bosons at the Tevatron*, *Phys.Rev.* **D70** (2004) 093009, [hep-ph/0408098].

[222] E. Accomando, A. Belyaev, L. Fedeli, S. F. King, et al., *Z' physics with early LHC data*, *Phys.Rev.* **D83** (2011) 075012, [arXiv:1010.6058].

[223] K. Hagiwara, R. Peccei, D. Zeppenfeld, and K. Hikasa, *Probing the Weak Boson Sector in $e^+e^- \to W^+W^-$*, *Nucl.Phys.* **B282** (1987) 253.

[224] W.-Y. Keung, I. Low, and J. Shu, *Landau-Yang Theorem and Decays of a Z' Boson into Two Z Bosons*, *Phys.Rev.Lett.* **101** (2008) 091802, [arXiv:0806.2864].

[225] T. G. Rizzo and R. W. Robinett, *Triple Gauge Boson Decay of New Neutral Gauge Bosons*, *Phys.Lett.* **B226** (1989) 117.

[226] A. Pukhov, *CalcHEP 2.3: MSSM, structure functions, event generation, batchs, and generation of matrix elements for other packages*, hep-ph/0412191.

[227] U. Haisch, F. Kahlhoefer, and E. Re, *QCD effects in mono-jet searches for dark matter*, *JHEP* **1312** (2013) 007, [arXiv:1310.4491].

[228] **DELPHI** Collaboration, J. Abdallah et al., *Search for one large extra dimension with the DELPHI detector at LEP*, *Eur.Phys.J.* **C60** (2009) 17–23, [arXiv:0901.4486].

[229] **ATLAS** Collaboration, G. Aad et al., *Search for dark matter candidates and large extra dimensions in events with a photon and missing transverse momentum in pp collision data at $\sqrt{s} = 7$ TeV with the ATLAS detector*, *Phys.Rev.Lett.* **110** (2013) 011802, [arXiv:1209.4625].

[230] **CMS** Collaboration, S. Chatrchyan et al., *Search for Dark Matter and Large Extra Dimensions in pp Collisions Yielding a Photon and Missing Transverse Energy*, *Phys.Rev.Lett.* **108** (2012) 261803, [arXiv:1204.0821].

[231] J. Kopp, V. Niro, T. Schwetz, and J. Zupan, *DAMA/LIBRA and leptonically interacting Dark Matter*, *Phys.Rev.* **D80** (2009) 083502, [arXiv:0907.3159].

[232] **CMS** Collaboration, S. Chatrchyan et al., *Search for narrow resonances using the dijet mass spectrum in pp collisions at $\sqrt{s} = 8$ TeV*, *Phys.Rev.* **D87** (2013), 114015, [arXiv:1302.4794].

[233] **CMS** Collaboration, *Search for Narrow Resonances using the Dijet Mass Spectrum in pp Collisions at $\sqrt{s} = 7$ TeV*, CMS-PAS-EXO-11-094.

[234] **CDF** Collaboration, T. Aaltonen et al., *Search for new particles decaying into dijets in proton-antiproton collisions at $\sqrt{s} = 1.96$ TeV*, *Phys.Rev.* **D79** (2009) 112002, [arXiv:0812.4036].

[235] **CMS** Collaboration, S. Chatrchyan et al., *Searches for new physics using the $t\bar{t}$ invariant mass distribution in pp collisions at $\sqrt{s} = 8$ TeV*, *Phys.Rev.Lett.* **111** (2013) 211804, [arXiv:1309.2030].

[236] **ATLAS** Collaboration, *Search for high-mass dilepton resonances in 20 fb^{-1} of pp collisions at $\sqrt{s} = 8$ TeV with the ATLAS experiment*, ATLAS-CONF-2013-017, ATLAS-COM-CONF-2013-010.

[237] **CMS** Collaboration, S. Chatrchyan et al., *Search for high mass resonances decaying into τ^- lepton pairs in pp collisions at $\sqrt{s} = 7$ TeV*, *Phys.Lett.* **B716** (2012) 82–102, [arXiv:1206.1725].

[238] **ATLAS** Collaboration, *Search for resonant ZZ production in the $ZZ \to \ell\ell qq$ channel with the ATLAS detector using 7.2 fb^{-1} of $\sqrt{s} = 8$ TeV pp collision data*, ATLAS-CONF-2012-150, ATLAS-COM-CONF-2012-187.

[239] **CMS** Collaboration, *Search for a narrow spin-2 resonance decaying to Z bosons in the semileptonic final state*, CMS-PAS-EXO-12-022.

[240] **ATLAS** Collaboration, *Search for new phenomena in the $WW \to \ell\nu\ell'\nu'$ final state in pp collisions at $\sqrt{s} = 7$ TeV with the ATLAS detector*, ATLAS-CONF-2012-068, ATLAS-COM-CONF-2012-119.

[241] **CMS** Collaboration, *Search for new resonances decaying to $WW \to \ell\nu q\bar{q}'$ in the final state with a lepton, missing transverse energy, and single reconstructed jet*, CMS-PAS-EXO-12-021.

[242] **ATLAS** Collaboration, *Search for the bb decay of the Standard Model Higgs boson in associated W/ZH production with the ATLAS detector*, ATLAS-CONF-2013-079, ATLAS-COM-CONF-2013-080.

[243] R. Foadi, M. T. Frandsen, and F. Sannino, *Technicolor Dark Matter*, *Phys.Rev.* **D80** (2009) 037702, [arXiv:0812.3406].

[244] R. Barbieri, S. Rychkov, and R. Torre, *Signals of composite electroweak-neutral Dark Matter: LHC/Direct Detection interplay*, *Phys.Lett.* **B688** (2010) 212–215, [arXiv:1001.3149].

[245] H. An, X. Ji, and L.-T. Wang, *Light Dark Matter and Z' Dark Force at Colliders*, *JHEP* **1207** (2012) 182, [arXiv:1202.2894].

[246] **ATLAS** Collaboration, G. Aad et al., *ATLAS search for new phenomena in dijet mass and angular distributions using pp collisions at $\sqrt{s} = 7$ TeV*, *JHEP* **1301** (2013) 029, [arXiv:1210.1718].

[247] S. B. Gudnason, C. Kouvaris, and F. Sannino, *Dark Matter from new Technicolor Theories*, *Phys.Rev.* **D74** (2006) 095008, [hep-ph/0608055].

[248] J. Goodman, M. Ibe, A. Rajaraman, W. Shepherd, et al., *Constraints on Light Majorana dark Matter from Colliders*, *Phys.Lett.* **B695** (2011) 185–188, [arXiv:1005.1286].

[249] T. Hahn, *Generating Feynman diagrams and amplitudes with FeynArts 3*, *Comput.Phys.Commun.* **140** (2001) 418–431, [hep-ph/0012260].

[250] T. Hahn and M. Perez-Victoria, *Automatized one loop calculations in four-dimensions and D-dimensions*, *Comput.Phys.Commun.* **118** (1999) 153–165, [hep-ph/9807565].

[251] J. M. Campbell, R. K. Ellis, and C. Williams. http://mcfm.fnal.gov.

[252] R. K. Ellis, I. Hinchliffe, M. Soldate, and J. van der Bij, *Higgs Decay to $\tau^+\tau^-$: A Possible Signature of Intermediate Mass Higgs Bosons at the SSC*, *Nucl.Phys.* **B297** (1988) 221.

[253] M. Spira, A. Djouadi, D. Graudenz, and P. Zerwas, *Higgs boson production at the LHC*, *Nucl.Phys.* **B453** (1995) 17–82, [hep-ph/9504378].

[254] A. Martin, W. Stirling, R. Thorne, and G. Watt, *Parton distributions for the LHC*, *Eur.Phys.J.* **C63** (2009) 189–285, [arXiv:0901.0002].

[255] U. Baur and E. N. Glover, *Higgs Boson Production at Large Transverse Momentum in Hadronic Collisions*, *Nucl.Phys.* **B339** (1990) 38–66.

[256] D. de Florian, M. Grazzini, and Z. Kunszt, *Higgs production with large transverse momentum in hadronic collisions at next-to-leading order*, *Phys.Rev.Lett.* **82** (1999) 5209–5212, [hep-ph/9902483].

[257] V. Ravindran, J. Smith, and W. Van Neerven, *Next-to-leading order QCD corrections to differential distributions of Higgs boson production in hadron hadron collisions*, *Nucl.Phys.* **B634** (2002) 247–290, [hep-ph/0201114].

[258] C. J. Glosser and C. R. Schmidt, *Next-to-leading corrections to the Higgs boson transverse momentum spectrum in gluon fusion*, *JHEP* **0212** (2002) 016, [hep-ph/0209248].

[259] R. V. Harlander, T. Neumann, K. J. Ozeren, and M. Wiesemann, *Top-mass effects in differential Higgs production through gluon fusion at order α_s^4*, *JHEP* **1208** (2012) 139, [arXiv:1206.0157].

[260] X. Chu, T. Hambye, T. Scarna, and M. H. Tytgat, *What if Dark Matter Gamma-Ray Lines come with Gluon Lines?*, *Phys.Rev.* **D86** (2012) 083521, [arXiv:1206.2279].

[261] A. Djouadi, *The Anatomy of electro-weak symmetry breaking. I: The Higgs boson in the standard model*, *Phys.Rept.* **457** (2008) 1–216, [hep-ph/0503172].

[262] M. F. Altmann, G. Angloher, M. Bruckmayer, C. Bucci, et al., *Results and plans of the CRESST dark matter search*, astro-ph/0106314.

[263] **PICASSO** Collaboration, S. Archambault et al., *Constraints on Low-Mass WIMP Interactions on ^{19}F from PICASSO*, *Phys.Lett.* **B711** (2012) 153–161, [arXiv:1202.1240].

[264] N. D. Christensen and C. Duhr, *FeynRules - Feynman rules made easy*, *Comput.Phys.Commun.* **180** (2009) 1614–1641, [arXiv:0806.4194].

[265] J. Alwall, M. Herquet, F. Maltoni, O. Mattelaer, et al., *MadGraph 5 : Going Beyond*, *JHEP* **1106** (2011) 128, [arXiv:1106.0522].

[266] J. Pumplin, D. Stump, J. Huston, H. Lai, et al., *New generation of parton distributions with uncertainties from global QCD analysis*, *JHEP* **0207** (2002) 012, [hep-ph/0201195].

[267] T. Bringmann, X. Huang, A. Ibarra, S. Vogl, et al., *Fermi LAT Search for Internal Bremsstrahlung Signatures from Dark Matter Annihilation*, *JCAP* **1207** (2012) 054, [arXiv:1203.1312].

[268] C. Weniger, *A Tentative Gamma-Ray Line from Dark Matter Annihilation at the Fermi Large Area Telescope*, *JCAP* **1208** (2012) 007, [arXiv:1204.2797].

[269] W. Buchmuller and M. Garny, *Decaying vs Annihilating Dark Matter in Light of a Tentative Gamma-Ray Line*, *JCAP* **1208** (2012) 035, [arXiv:1206.7056].

[270] T. Cohen, M. Lisanti, T. R. Slatyer, and J. G. Wacker, *Illuminating the 130 GeV Gamma Line with Continuum Photons*, *JHEP* **1210** (2012) 134, [arXiv:1207.0800].

[271] I. Cholis, M. Tavakoli, and P. Ullio, *Searching for the continuum spectrum photons correlated to the 130 GeV gamma-ray line*, *Phys.Rev.* **D86** (2012) 083525, [arXiv:1207.1468].

[272] C. Bobeth and U. Haisch, *New Physics in $\Gamma_1 2^s$: $(\bar{s}b)(\bar{\tau}\tau)$ Operators*, *Acta Phys.Polon.* **B44** (2013) 127–176, [arXiv:1109.1826].

[273] M. Felizardo, T. Girard, T. Morlat, A. Fernandes, et al., *Final Analysis and Results of the Phase II SIMPLE Dark Matter Search*, *Phys.Rev.Lett.* **108** (2012) 201302, [arXiv:1106.3014].

[274] **COUPP** Collaboration, E. Behnke et al., *First Dark Matter Search Results from a 4-kg CF_3I Bubble Chamber Operated in a Deep Underground Site*, *Phys.Rev.* **D86** (2012) 052001, [arXiv:1204.3094].

[275] S. Kim, H. Bhang, J. Choi, W. Kang, et al., *New Limits on Interactions between Weakly Interacting Massive Particles and Nucleons Obtained with CsI(Tl) Crystal Detectors*, *Phys.Rev.Lett.* **108** (2012) 181301, [arXiv:1204.2646].

[276] M. Cirelli, N. Fornengo, and A. Strumia, *Minimal dark matter*, *Nucl.Phys.* **B753** (2006) 178–194, [hep-ph/0512090].

[277] R. Essig, *Direct Detection of Non-Chiral Dark Matter*, *Phys.Rev.* **D78** (2008) 015004, [arXiv:0710.1668].

[278] M. Freytsis and Z. Ligeti, *On dark matter models with uniquely spin-dependent detection possibilities*, *Phys.Rev.* **D83** (2011) 115009, [arXiv:1012.5317].

[279] N. F. Bell, J. B. Dent, A. J. Galea, T. D. Jacques, et al., *W/Z Bremsstrahlung as the Dominant Annihilation Channel for Dark Matter, Revisited*, *Phys.Lett.* **B706** (2011) 6–12, [arXiv:1104.3823].

[280] N. Bozorgnia, J. Herrero-Garcia, T. Schwetz, and J. Zupan, *Halo-independent methods for inelastic dark matter scattering*, *JCAP* **1307** (2013) 049, [arXiv:1305.3575].

[281] S. Scopel and K. Yoon, *A systematic halo-independent analysis of direct detection data within the framework of Inelastic Dark Matter*, arXiv:1405.0364.

[282] E. Del Nobile, G. Gelmini, P. Gondolo, and J.-H. Huh, *Generalized Halo Independent Comparison of Direct Dark Matter Detection Data*, *JCAP* **1310** (2013) 048, [arXiv:1306.5273].

[283] E. Del Nobile, G. B. Gelmini, P. Gondolo, and J.-H. Huh, *Direct detection of Light Anapole and Magnetic Dipole DM*, *JCAP* **1406** (2014) 002, [arXiv:1401.4508].

[284] J. Herrero-Garcia, T. Schwetz, and J. Zupan, *On the annual modulation signal in dark matter direct detection*, *JCAP* **1203** (2012) 005, [arXiv:1112.1627].

[285] J. Herrero-Garcia, T. Schwetz, and J. Zupan, *Astrophysics independent bounds on the annual modulation of dark matter signals*, *Phys.Rev.Lett.* **109** (2012) 141301, [arXiv:1205.0134].

[286] **CoGeNT** Collaboration, C. Aalseth et al., *Search for An Annual Modulation in Three Years of CoGeNT Dark Matter Detector Data*, arXiv:1401.3295.

[287] J. H. Davis, C. McCabe, and C. Boehm, *Quantifying the evidence for Dark Matter in CoGeNT data*, arXiv:1405.0495.

[288] **CRESST** Collaboration, G. Angloher et al., *Results on low mass WIMPs using an upgraded CRESST-II detector*, arXiv:1407.3146.

[289] P. J. Fox, G. Jung, P. Sorensen, and N. Weiner, *Dark Matter in Light of LUX*, *Phys.Rev.* **D89** (2014) 103526, [arXiv:1401.0216].

[290] G. B. Gelmini, A. Georgescu, and J.-H. Huh, *Direct Detection of Light "Ge-phobic" Exothermic Dark Matter*, arXiv:1404.7484.

[291] H. An, L.-T. Wang, and H. Zhang, *Dark matter with t-channel mediator: a simple step beyond contact interaction*, arXiv:1308.0592.

[292] A. DiFranzo, K. I. Nagao, A. Rajaraman, and T. M. P. Tait, *Simplified Models for Dark Matter Interacting with Quarks*, *JHEP* **1311** (2013) 014, [arXiv:1308.2679].

[293] **BABAR** Collaboration, J. P. Lees et al., *Search for a dark photon in e^+e^- collisions at BABAR*, arXiv:1406.2980.

[294] J. Binney and S. Tremaine, *Galactic Dynamics: Second Edition*. Princeton University Press, Princeton, USA, 2008.

[295] S. H. Hansen and B. Moore, *A Universal density slope - velocity anisotropy relation for relaxed structures*, *New Astron.* **11** (2006) 333, [astro-ph/0411473].

[296] S. Chaudhury, P. Bhattacharjee, and R. Cowsik, *Direct detection of WIMPs : Implications of a self-consistent truncated isothermal model of the Milky Way's dark matter halo*, *JCAP* **1009** (2010) 020, [arXiv:1006.5588].

[297] M. Lisanti, L. E. Strigari, J. G. Wacker, and R. H. Wechsler, *The Dark Matter at the End of the Galaxy*, *Phys.Rev.* **D83** (2011) 023519, [arXiv:1010.4300].

[298] J. F. Navarro, C. S. Frenk, and S. D. White, *The Structure of cold dark matter halos*, *Astrophys.J.* **462** (1996) 563–575, [astro-ph/9508025].

[299] F. Ling, E. Nezri, E. Athanassoula, and R. Teyssier, *Dark Matter Direct Detection Signals inferred from a Cosmological N-body Simulation with Baryons*, *JCAP* **1002** (2010) 012, [arXiv:0909.2028].

[300] J. Vergados, S. Hansen, and O. Host, *The impact of going beyond the Maxwell distribution in direct dark matter detection rates*, *Phys.Rev.* **D77** (2008) 023509, [arXiv:0711.4895].

[301] J. Diemand, M. Kuhlen, and P. Madau, *Dark matter substructure and gamma-ray annihilation in the Milky Way halo*, *Astrophys.J.* **657** (2007) 262–270, [astro-ph/0611370].

[302] J. Diemand, M. Kuhlen, P. Madau, M. Zemp, et al., *Clumps and streams in the local dark matter distribution*, *Nature* **454** (2008) 735–738, [arXiv:0805.1244].

[303] J. Stadel, D. Potter, B. Moore, J. Diemand, et al., *Quantifying the heart of darkness with GHALO - a multi-billion particle simulation of our galactic halo*, *Mon.Not.Roy.Astron.Soc.* **398** (2009) L21, [arXiv:0808.2981].

[304] V. Springel, J. Wang, M. Vogelsberger, A. Ludlow, et al., *The Aquarius Project: the subhalos of galactic halos*, *Mon.Not.Roy.Astron.Soc.* **391** (2008) 1685–1711, [arXiv:0809.0898].

[305] N. Evans, C. Carollo, and P. de Zeeuw, *Triaxial haloes and particle dark matter detection*, *Mon.Not.Roy.Astron.Soc.* **318** (2000) 1131, [astro-ph/0008156].

[306] P. Belli, R. Cerulli, N. Fornengo, and S. Scopel, *Effect of the galactic halo modeling on the DAMA / NaI annual modulation result: an Extended analysis of the data for WIMPs with a purely spin independent coupling*, *Phys.Rev.* **D66** (2002) 043503, [hep-ph/0203242].

[307] N. W. Evans and J. H. An, *Distribution function of the dark matter*, *Phys.Rev.* **D73** (2006) 023524, [astro-ph/0511687].

[308] L. Hernquist, *An Analytical Model for Spherical Galaxies and Bulges*, *Astrophys.J.* **356** (1990) 359.

[309] M. Vogelsberger, A. Helmi, V. Springel, S. D. White, et al., *Phase-space structure in the local dark matter distribution and its signature in direct detection experiments*, *Mon.Not.Roy.Astron.Soc.* **395** (2009) 797–811, [arXiv:0812.0362].

[310] C. Savage, K. Freese, and P. Gondolo, *Annual Modulation of Dark Matter in the Presence of Streams*, *Phys.Rev.* **D74** (2006) 043531, [astro-ph/0607121].

[311] A. Natarajan, C. Savage, and K. Freese, *Probing dark matter streams with CoGeNT*, *Phys.Rev.* **D84** (2011) 103005, [arXiv:1109.0014].

[312] M. Lisanti and D. N. Spergel, *Dark Matter Debris Flows in the Milky Way*, *Phys.Dark Univ.* **1** (2012) 155–161, [arXiv:1105.4166].

[313] M. Kuhlen, M. Lisanti, and D. N. Spergel, *Direct Detection of Dark Matter Debris Flows*, *Phys.Rev.* **D86** (2012) 063505, [arXiv:1202.0007].

[314] T. Bruch, J. Read, L. Baudis, and G. Lake, *Detecting the Milky Way's Dark Disk*, *Astrophys.J.* **696** (2009) 920–923, [arXiv:0804.2896].

[315] C. McCabe, *Aspects of dark matter phenomenology*. PhD thesis, University of Oxford, 2011.

[316] **CDMS** Collaboration, D. Akerib et al., *A low-threshold analysis of CDMS shallow-site data*, *Phys.Rev.* **D82** (2010) 122004, [arXiv:1010.4290].

[317] K. A. McCarthy, "Dark matter search results from the silicon detectors of the cryogenic dark matter search experiment." Presented at the APS Physics Meeting, Denver, Colorado, 2013.

[318] K. Schmidt-Hoberg and M. W. Winkler, *Improved Constraints on Inelastic Dark Matter*, *JCAP* **0909** (2009) 010, [arXiv:0907.3940].

[319] **CoGeNT** Collaboration, C. Aalseth et al., *Experimental constraints on a dark matter origin for the DAMA annual modulation effect*, *Phys.Rev.Lett.* **101** (2008) 251301, [arXiv:0807.0879].

[320] N. Bozorgnia, G. B. Gelmini, and P. Gondolo, *Channeling in direct dark matter detection I: channeling fraction in NaI (Tl) crystals*, *JCAP* **1011** (2010) 019, [arXiv:1006.3110].

[321] A. Brown, S. Henry, H. Kraus, and C. McCabe, *Extending the CRESST-II commissioning run limits to lower masses*, *Phys.Rev.* **D85** (2012) 021301, [arXiv:1109.2589].

[322] M. Felizardo, T. Morlat, A. Fernandes, T. Girard, et al., *First Results of the Phase II SIMPLE Dark Matter Search*, *Phys.Rev.Lett.* **105** (2010) 211301, [arXiv:1003.2987].

[323] **KIMS** Collaboration, H. Lee et al., *Limits on WIMP-nucleon cross section with CsI(Tl) crystal detectors*, *Phys.Rev.Lett.* **99** (2007) 091301, [arXiv:0704.0423].

[324] J. Heinrich, *Pitfalls of Goodness-of-Fit from Likelihood*, *eConf* **C030908** (2003) MOCT001, [physics/0310167].

[325] G. Cowan, K. Cranmer, E. Gross, and O. Vitells, *Asymptotic formulae for likelihood-based tests of new physics*, *Eur.Phys.J.* **C71** (2011) 1554, [arXiv:1007.1727].

[326] M. A. Shifman, A. Vainshtein, and V. I. Zakharov, *Remarks on Higgs Boson Interactions with Nucleons*, *Phys.Lett.* **B78** (1978) 443.

[327] M. Drees and M. M. Nojiri, *New contributions to coherent neutralino - nucleus scattering*, *Phys.Rev.* **D47** (1993) 4226–4232, [hep-ph/9210272].

[328] **JLQCD** Collaboration, K. Takeda et al., *Nucleon strange quark content in 2+1-flavor QCD*, *PoS* **LATTICE2010** (2010) 160, [arXiv:1012.1907].